# Modelling cell–matrix interactions in airway smooth muscle cells

Linda Irons

Thesis submitted to The University of Nottingham
for the degree of Doctor of Philosophy

October 2018

# Abstract

Tissues, in both humans and animals, consist of cells embedded in a dynamic scaffold known as the extracellular matrix (ECM). Cells interact with the ECM through the process of cell–matrix adhesion, and these interactions, mediated by transmembrane proteins called integrins, are fundamental in regulating a diverse range of physiological processes. The focus of this thesis is on airway smooth muscle (ASM) cell–matrix adhesion, which regulates the transmission of contractile forces generated within ASM cells to the ECM. This is of particular importance in the context of asthma, where contraction of ASM cells, and the subsequent transmission of contractile forces to the surrounding tissue, leads to a narrowing of the airways called bronchoconstriction. In this thesis, we develop mathematical models of ASM cell–matrix adhesion; our objective is to investigate how integrin-mediated adhesions are affected by the dynamic mechanical environment of the *in vivo* airway. In particular, we aim to gain insight into how integrins respond to tidal breathing and deep inspirations (DIs), since changes in integrin dynamics may affect the extent of airway narrowing during bronchoconstriction.

Firstly, we develop a discrete stochastic–elastic model and a multiscale continuum model (Chapter 2), both able to account for detailed integrin binding kinetics alongside material deformations at the cell level. With these models we observe two distinct adhesion regimes in response to oscillatory loading, where either adhesion formation or adhesion rupture dominate (Chapter 3). For intermediate oscillation amplitudes we observe bistability due to shared loading and, as a result, we find that perturbations in the loading amplitude, mimicking DIs, can lead to different outcomes for the level of adhesion. This will affect the level of attainable force transmission during ASM cell contraction, and we discuss the possible consequences for airway narrowing. There is strong qualitative agreement between our discrete and continuum model results, and we consider several extensions of the continuum model (Chapter 4) to allow for activation, diffusion and strain-dependent reinforcement of integrins.

In addition to theoretical results, we present and analyse experimental data from atomic force microscopy experiments (Chapter 5). In the experiments, cells were subject to vertical oscillatory loading of varying amplitudes. By extending the continuum model to support vertical motion, we mimic the experimental protocol and, in agreement with the data, we obtain two distinct temporal patterns in adhesion force. Our simulations provide insight into the underlying integrin dynamics and the resulting cell deformation; these cannot currently be measured by experiments but are predicted by the model. We use cluster analysis techniques to study force timecourses from individual cells and, in some cases, we observe switching behaviours that could be an indicator for bistability.

The integrin response to oscillatory loading affects how contractile forces are transmitted from ASM cells to the ECM. However, it is also known that oscillatory loading affects the generation of contractile force (which is mediated by actomyosin crossbridges within the cell). In order to fully understand the consequences for bronchoconstriction, it is therefore important to consider how these processes interact. To investigate this, we couple our model of cell–matrix adhesion to a well-established model of contractile force generation (Chapter 6). Our results demonstrate a close mechanical coupling between the two processes and show that both force transmission (via integrins) and force generation (via crossbridges) are modulated by oscillatory loading. Moreover, there is feedback between the two processes and a regulatory mechanism due to negative feedback. We observe two regions of bistability: one as reported in our earlier results, due to shared loading between integrins, and a second due to analogous mechanisms for the crossbridges. These both introduce hysteresis and can result, in each case, in reduced levels of total contractile force after large amplitude oscillations. It is known from experiments that deep inspirations can induce either transient or sustained bronchodilation, and that these responses differ in asthmatics and non-asthmatics. Because of the hysteresis in total contractile force, we hypothesise that bistability could be an underlying mechanism by which sustained bronchodilation occurs. Furthermore, we show that the bistability can be lost for changes in the passive cell stiffness or in the relative crossbridge to integrin strength; a loss of bistability would result in an inability to obtain sustained reductions in contractile force, which could correspond to the transient bronchodilation seen in asthmatics.

# Acknowledgements

Primarily, I would like to thank my supervisors, Bindi Brook, Markus Owen and Reuben O'Dea, for all their help, guidance and enthusiasm over the past three years. It has been an absolute pleasure to work and learn from them, and their advice has been invaluable to both the research and writing of this thesis.

My thanks extend to Gerald Meininger for helpful discussions regarding AFM experiments, and to his lab members and colleagues at the University of Missouri (Leike Xie, Vladislav Glinsky and Huang Huang) for the data in Chapters 4 and 5.

I would also like to acknowledge the School of Mathematical Sciences, University of Nottingham, for funding this project; the IT and administrative staff there for ensuring that everything ran smoothly; and my fellow PhD students, past and present, for making it so much fun.

Finally, a special thank you to my parents and family, for their support and encouragement throughout.

# List of publications

This thesis includes results from the following original publications.

**Chapter 3**

L. Irons, M. R. Owen, R. D. O'Dea, and B. S. Brook (2018) 'Effect of loading history on airway smooth muscle cell–matrix adhesions'. *Biophysical Journal*, 114(11):2679–2690.

**Chapter 5**

L. Irons, L. Xie, M. Owen, M. A. Hill, L. A. Martinez-Lemus, O. Glinski, V. V. Glinsky, R. O'Dea, B. Brook, and G. A. Meininger (2017) 'Utilization of mechano-biological models to predict cell adhesion interactions between bone marrow endothelial cells and breast cancer cells'. *The FASEB Journal 2017*, 31:1_Supplement, 860.1.

# Contents


**1 Introduction** **1**

1.1 Asthma . . . . . 1

1.1.1 Airway physiology . . . . . 2

1.1.2 Asthmatic airways . . . . . 3

1.2 An overview of cell adhesion . . . . . 8

1.2.1 Cell adhesion molecules . . . . . 8

1.2.2 Integrin structure and focal adhesions . . . . . 9

1.2.3 Experimental techniques for measuring cell adhesion . . . . . 11

1.3 Existing modelling approaches . . . . . 14

1.3.1 Stochastic models of cell–ECM adhesion . . . . . 14

1.3.2 Continuum models of cell–ECM adhesion . . . . . 17

1.3.3 Models of contractile force generation . . . . . 19

1.4 Thesis overview and structure . . . . . 20

**2 Discrete and continuum models of cell–matrix adhesion** **22**

2.1 Discrete model formulation . . . . . 22

2.2 Continuum model formulation . . . . . 28

2.2.1 Microscale integrin binding dynamics . . . . . 28

2.2.2 Analytical results from the microscale formulation . . . . . 31

2.2.3 Multiple ECM binding sites . . . . . 39

2.2.4 Coupling to a macroscale model of cell deformation . . . . . 40

2.2.5 Numerical solution of the continuum model . . . . . 44

2.3 Summary . . . . . 46

**3 Effect of oscillatory loading on cell–matrix adhesion 47**

3.1 Varying the amplitude of oscillation . . . . . 48

3.1.1 Effect of varying the model parameters . . . . . 55

3.1.2 Effect of varying the input waveform . . . . . 58

3.2 Perturbations due to deep inspirations . . . . . 61

3.3 Conclusions . . . . . 64

**4 Modelling integrin activation, diffusion and strengthening 67**

4.1 Integrin diffusion and activation . . . . . 68

4.2 Force-dependent strengthening . . . . . 79

4.3 Investigating the duration between DIs and integrin recovery rate . . . 90

4.3.1 Experimental protocol and results . . . . . 90

4.3.2 Numerical experiments . . . . . 92

4.4 Conclusions . . . . . 98

**5 Vertical oscillations: models and experimental data 101**

5.1 Model formulation . . . . . 102

5.1.1 A 3-spring model for material deformations . . . . . 102

5.1.2 Model of integrin binding dynamics . . . . . 105

5.1.3 Numerical results . . . . . 107

5.2 Experimental protocol for vertical oscillations . . . . . 115

5.2.1 Vascular smooth muscle cells . . . . . 115

5.2.2 Experimental methods . . . . . 117

5.2.3 Experimental results . . . . . 118

5.3 Conclusions . . . . . 133

**6 Coupling cell–matrix adhesion to contractile force generation 135**

6.1 Huxley–Hai–Murphy (HHM) model . . . . . 135

6.2 Coupling to the 3-spring framework . . . . . 138

6.3 Coupled crossbridge and integrin dynamics . . . . . 145
6.3.1 Crossbridge response to oscillatory loading . . . . . 146
6.3.2 Interacting crossbridge and integrin dynamics . . . . . 149
6.4 Conclusions . . . . . 158

**7 Conclusions** **161**
7.1 Summary of main findings . . . . . 161
7.2 Scope for future work . . . . . 167

**A Analytical solutions for the single-site model** **170**
A.1 Steady state distributions with a constant relative velocity . . . . . 170
A.2 Method of characteristics for piecewise-linear binding rates . . . . . 175

**B Parameter values** **188**
B.1 Parameter values for Chapter 3 . . . . . 188
B.1.1 Dimensionless parameter values . . . . . 188
B.1.2 Dimensional parameter values . . . . . 189
B.2 Parameter values for Chapter 4 . . . . . 191
B.2.1 Integrin diffusion and activation . . . . . 191
B.2.2 Force-dependent strengthening . . . . . 192
B.3 Parameter values for Chapter 5 . . . . . 193
B.3.1 Retraction curves . . . . . 193
B.3.2 Vertical oscillations: qualitative study . . . . . 194
B.4 Parameter values for Chapter 6 . . . . . 194

**References** **197**

# Chapter 1

# Introduction

## 1.1 Asthma

Asthma is a chronic respiratory disease affecting over 300 million individuals worldwide [11]. In the UK, over 5.4 million people are affected [7], equating to more than 1 in 12 of the population. There is currently no cure and treatments can only relieve the symptoms. Common symptoms include chest tightness, shortness of breath, wheezing and coughing [74], which can interfere with daily activities and significantly affect quality of life. In severe asthmatics, whose symptoms are poorly controlled, asthma is responsible for a large number of hospital admissions and over 250,000 deaths annually [11]. Additionally, there are high costs associated with the management of asthma. Directly, there are costs associated with hospital resources and care, estimated to be in excess of £1.1 billion per year in the UK [7]. Indirectly, there is wider impact due to increased absences from work; for the UK this reportedly reaches 20 million days per year [103].

Asthma has three defining characteristics: inflammation, airway hyperresponsiveness and airway remodelling. Inflammation of the airway tissue occurs in response to inhaling allergens and leads to an obstruction of airflow. Additionally, a series of biochemical responses are triggered, a result of which is the secretion of contractile agonists such as histamine [21]. This causes further problems since contractile agonists trigger airway smooth muscle (ASM) cell contraction, which results in bronchoconstriction, a narrowing of the airways that further restricts airflow [113]. In addition to inflammation, asthmatics also exhibit airway hyperresponsiveness, which is defined as an increased sensitivity to contractile agonists; ASM cell contraction is more

severe and occurs at relatively low doses of agonist [113]. The third characteristic, airway remodelling, constitutes the longer term structural changes seen in asthmatic airways. These changes include excess collagen deposition and increased ASM mass [22], and result in altered material properties such as changes in tissue stiffness and contractility.

In this thesis we develop mathematical models to better understand cell-level mechanisms of relevance to asthma, with a particular focus on the mechanisms influencing bronchoconstriction. We begin by presenting an overview of respiratory and airway physiology before discussing the characteristics of asthmatic airways in more detail. In Section 1.2 we then introduce an key process in regulating bronchoconstriction, which is the process of cell–matrix adhesion. Cell–matrix adhesion regulates the transmission of contractile forces generated by ASM cells to the surrounding tissue, and is therefore an important area of study. In Section 1.3 we review the existing modelling and experimental literature relevant to cell–matrix adhesion and to ASM cell contraction, and in Section 1.4 we summarise the key objectives and structure of this work.

### 1.1.1 Airway physiology

The lungs are the primary organs of the human respiratory system and are responsible for gas exchange during respiration. Specifically, they control the uptake of oxygen and the removal of carbon dioxide from the bloodstream. To enable this, air enters the respiratory system through either the nose or the mouth before passing through the trachea and main bronchi (Fig. 1.1). The main bronchi divides into the left and right bronchi, through which the air travels to reach each of the lungs. Within the lungs the branching of airways continues; firstly with bronchi directed into each of five lobes in the lungs (three in the right lung, two in the left) before dividing for a further 21 generations [109]. At each division the airways become narrower and less stiff.

The first 16 generations in the branched structure are known as the conducting zone, where no gas exchange occurs. Further generations form the transitional and respiratory zones, where bronchioles divide into smaller respiratory bronchioles, alveolar ducts and alveolar sacs. Here the branched structures terminate in approximately 300 million alveoli, allowing for efficient gas exchange since it provides an extremely large

surface area. Gas exchange occurs by diffusion between the alveoli and surrounding capillaries.

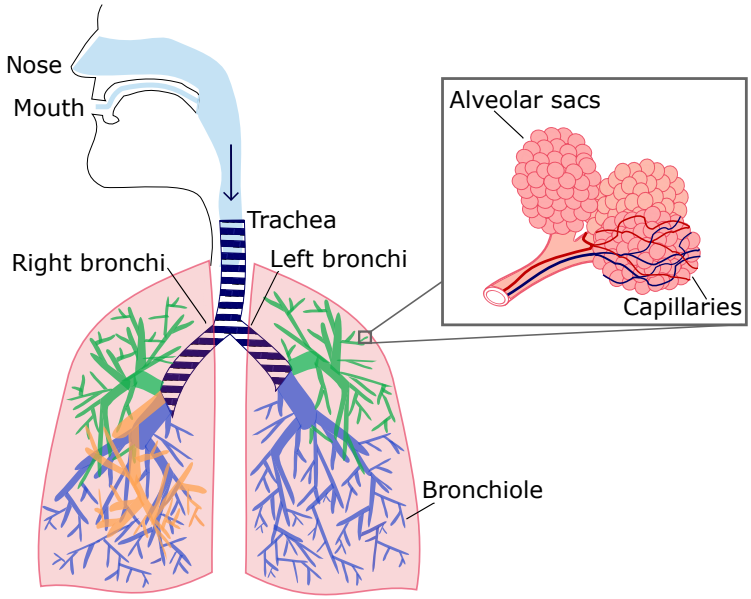


**Figure 1.1:** Schematic of the key components in the respiratory system. Air inhaled through the nose or mouth travels through the trachea, bronchi, into one of five lobes (coloured) and through the branched structure of airways in the lungs. Gas exchange occurs in the smaller respiratory bronchioles where oxygen and carbon dioxide diffuse between alveoli and capillaries. (Image adapted from en.wikipedia.org/wiki/Respiratory_system).

### 1.1.2 Asthmatic airways

There are three defining characteristics of asthmatic airways: inflammation, airway hyperresponsiveness and airway remodelling [21, 107]. Together, these factors contribute to airway obstruction, reduced airflow and an overall decline in lung function.

#### Inflammation

In asthmatics, the inhalation of allergens induces an inflammatory response. As part of the inflammatory response there is production, recruitment and activation of inflammatory cells [21, 79]. The activated inflammatory cells secrete proinflammatory mediators such as histamine [75], a contractile agonist, triggering ASM cell contraction and bronchoconstriction. During the inflammatory response there is also an increased secretion of mucus from goblet cells which line the airway walls [21], causing

further obstruction of the airways. Inflammatory events additionally have long term consequences for asthmatics by promoting airway remodelling. In particular, a type of inflammatory cell called eosinophils can secrete growth factors, including the pro-remodelling growth factor TGF$\beta$ [57].

### Bronchoconstriction and airway hyperresponsiveness

Bronchoconstriction (Fig. 1.2), occurs in response to contractile agonists. Exposure to agonists triggers the generation of contractile force within ASM cells, resulting in contraction of individual cells (Fig. 1.3) [54]. These forces are transmitted to the surrounding airway tissue by a type of transmembrane protein called integrins (Section 1.2.2) [153], and the combination of these two processes leads to narrowing of the whole airway. A key characteristic of asthma is airway hyperresponsiveness, which is an increased sensitivity to contractile agonist. This means that ASM cell contraction (and the resulting bronchoconstriction) is triggered at relatively low exposures to agonist. Furthermore, when subject to the same dose of agonist, the degree of contraction is observed to increase with the severity of asthma [104].

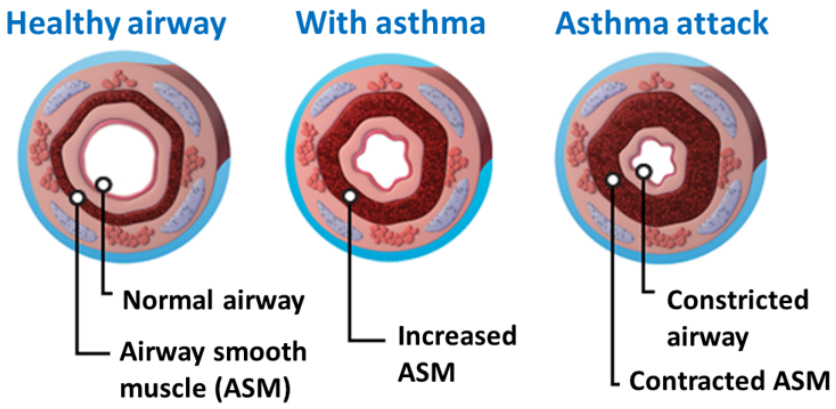


**Figure 1.2:** Airway smooth muscle (ASM) is present in healthy airways (left). In asthmatic airways (middle), the ASM mass is increased due to airway remodelling. During bronchoconstriction (right), contractile force generated within ASM cells leads to airway narrowing. This restricts airflow through the airways and makes breathing difficult. (Image from houstonlungclinic.com/bronchial-thermoplasty).

Contractile force is generated by intracellular proteins called actin and myosin [54]. Intracellular actin and myosin filaments slide over each other, when triggered, to cause contraction of the whole ASM cell (Fig. 1.3). The thicker myosin filaments have

protruding myosin heads that bind to sites on nearby actin filaments (F-actin), to form crossbridges. Myosin heads bind at an angle and induce a small relative motion of the actin filament, where the crossbridges repeatedly detach and rebind to actin sites further along the filament. This cycle of unbinding and rebinding is called crossbridge cycling, and produces the sliding motion behind all types of muscle contraction [118].

Within the cell, chains of actomyosin filaments form longer pathways along which contractile force is transmitted (Fig. 1.3) [54]. Additionally, actin filaments adhere to the surrounding extracellular matrix (ECM) via integrins, which will be described in detail in Section 1.2.2. Due to integrin-mediated adhesion, the contractile force generated within the cell by crossbridge cycling leads to ECM deformation [123]. Integrins therefore regulate the transmission of contractile force between ASM cells and the airway tissue, and will be an important factor to investigate in the study of bronchoconstriction.

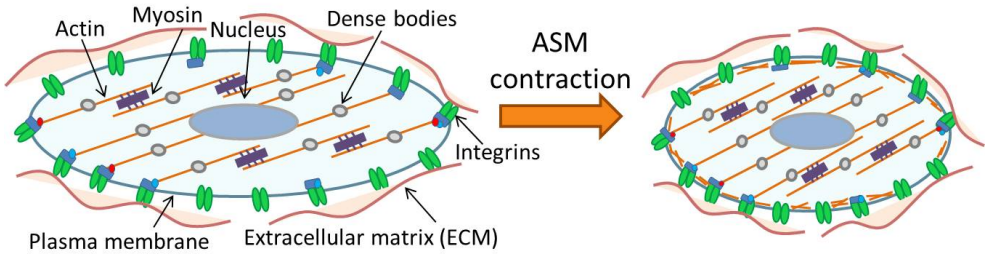


**Figure 1.3:** A representation of an ASM cell and the contractile machinery within the cell. Chains of actomyosin filaments form force transmission pathways, along which contractile force is transmitted during crossbridge cycling. Contractile forces are transmitted to the ECM when ECM ligands are connected to the cytoskeleton via integrin-mediated adhesions. In reality the actomyosin network and integrins are far more dense than depicted. (Image adapted from [54])

The lung provides an inherently dynamic environment for ASM cells due to breathing. As well as regular 'tidal breathing', there are variations in breathing patterns over time. A key example is the act of sighing which happens involuntarily approximately 12 times an hour. A sigh is a type of deep inspiration (DI), classified by a large increase in the volume of air inhaled (approximately 2–5 times that of tidal volume) and is a reflex that reinflates alveoli that may have collapsed during tidal breathing [93].

There have been several experimental studies which look at the relationship between taking deep inspirations (DIs) and the reversal of bronchoconstriction. In healthy subjects DIs are known to promote bronchodilation, but this effect is either transient or non-existent in asthmatics [33, 78, 125]. Further experimental studies show that DIs are in fact a crucial mechanism for the regulation of normal lung function. This is evidenced in several studies where healthy subjects purposely refrain from sighing for a period of time [98, 129, 130]. In each of these studies, after withholding DIs, healthy individuals were observed to experience airway hyperresponsiveness on a similar level to asthmatic subjects. Withholding from DIs also results in reduced lung compliance and increased airway resistance [93].

The reasons behind DI-induced bronchodilation are not fully understood, but a key aspect to understand is how the fluctuating mechanical environment of the lung during breathing affects contractile force generation and ASM cell–matrix adhesion dynamics. A common hypothesis is that DIs lead to the disruption of actin-myosin crossbridges [125] which mediate contractile force generation within the cell. Under this hypothesis, it becomes necessary to understand what can cause differences in crossbridge dynamics in asthmatics and non-asthmatics, whose response to DIs differ [33, 78, 125]. However, since the transmission of intracellular contractile forces to the extracellular domain is reliant on cell–matrix adhesions [123], the density and dynamics of adhesions in asthmatic and non-asthmatic cases could also play an important role. The response of ASM cell–matrix adhesions to the oscillatory environment in the lung has so far not been studied, and will be considered in this work.

#### Airway remodelling

A number of long term physiological and structural changes occur in asthmatic airways due to a process known as airway remodelling; these changes are illustrated and described in Fig. 1.4. In a healthy airway, the flow of air is unobstructed through the lumen. In asthmatic airways, a number of factors lead to obstruction of airflow. Firstly, there are abnormal increases in the number of goblet cells, which are interspersed between epithelial cells and line the airway. These secrete excess mucus into the lumen [116]. Due to remodelling, there is also an increase in the number of blood vessels in the airway wall (through angiogenesis), with the new blood vessels reported to be hyperpermeable. As a result, excess fluid can leak into the surrounding tissue, known as edema, which results in swelling and further airway obstruction

[21]. An important feature of airway remodelling is an increase in ASM mass [22]. There is also increased collagen deposition and thickening of the basement membrane (Fig. 1.4), all of which result in a stiffening of the airway tissue. These structural changes are thought to be irreversible and over time lead to permanently obstructed airflow and a decline in lung function. The extent of airway remodelling will be patient-specific and depend on the severity of the asthma.

Inflammatory events promote airway remodelling; however, they are not the sole contributor. During bronchoconstriction, the contraction of ASM cells is known to activate the growth factor TGF$\beta$ [51], which can induce changes in the epithelial layer and increase the proliferation rate of ASM [57]. Activation of TGF$\beta$, which otherwise remains latent in the ECM, is triggered by local deformations generated by the transmission of contractile forces to the surrounding ECM via integrin-mediated adhesions [105, 136, 146]. This evidence provides further motivation to study integrins and the transmission of contractile force to the ECM in the context of asthma.

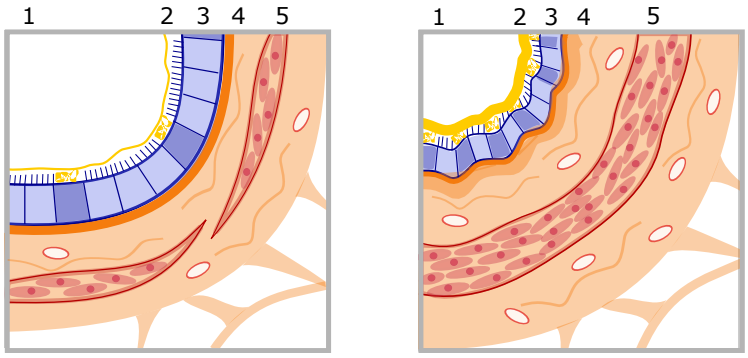


**Figure 1.4:** Diagram of physiological changes that occur in an asthmatic airway compared to a healthy airway. In a healthy airway (left), (1) Air flows through the lumen. (2) There is a thin layer of mucus, secreted by goblet cells. (3) Goblet cells (dark blue) are interspersed between epithelial cells (light blue) which line the airway. (4) The basement membrane (orange) separates the epithelial layer from the rest of the airway wall components, which include collagen fibres, blood vessels and (5) a circumferential layer of airway smooth muscle (ASM). In an asthmatic airway (right) changes include a reduced diameter of the lumen and increased levels of mucus due to goblet cell hyperplasia. There is also increased collagen deposition and thickening of the basement membrane. Furthermore, there is an increase in the number of blood vessels and an increased ASM mass. (Image adapted from [116]).

## 1.2 An overview of cell adhesion

In Section 1.2.1 we provide an overview of cell adhesion. Of particular importance to this work is cell–matrix adhesion via integrins, which is discussed in detail in Section 1.2.2. Integrins transmit the contractile forces generated within airway smooth muscle (ASM) cells to the surrounding airway tissue [153]; together with contractile force generation, cell–matrix adhesion is therefore a key process to understand in the study of bronchoconstriction. In Section 1.2.3 we discuss some experimental techniques that are currently used for measuring cell adhesion *in vitro*. One such technique is atomic force microscopy (AFM), and we will be considering data from AFM experiments in Chapters 4 and 5.

### 1.2.1 Cell adhesion molecules

Interactions between cells, or between a cell and the extracellular matrix (ECM), are mediated by the process of cell adhesion. These interactions regulate a diverse range of physiological processes by affecting cell migration, shape and the cell cycle. As a result, cell adhesion is central to the formation and maintenance of tissues [52], morphogenesis [52, 134], tumour metastasis [15, 50], virus attachment to host cells [18] and inflammation [39]. In addition to providing the necessary surface attachments for these processes, transmembrane proteins associated with cell adhesion mediate bidirectional chemical and mechanical signalling [5, 120, 124]. In the context of asthma and ASM cells, cell–matrix adhesion between ASM cells and the surrounding ECM is important in regulating the extent of airway narrowing during bronchoconstriction (Section 1.1.2).

The transmembrane proteins that are essential for cell–cell or cell–matrix adhesion are known as cell adhesion molecules (CAMs) and undergo specific binding by a lock and key mechanism. The binding is either homophilic (to molecules of the same type) or heterophilic (to molecules of a different type). CAMs are grouped into four main superfamilies: cadherins, selectins, immunoglobulins and integrins. Cadherins are homophilic and bind to the extracellular domain of other cadherins to mediate cell–cell adhesion. Collectively they are able to form strong connections between neighbouring cells, known as adherens junctions. Since CAMs are transmembrane proteins they also have an intracellular domain. The intracellular domains of cadherins bind to catenins, a family of proteins that further bind to the actin cytoskeleton of the cell [5].

The selectin superfamily is made up of L-, E-, and P-selectins and mediates adhesion involving leukocytes, endothelial cells and platelets respectively. Selectins initiate adhesion by recognising and binding heterophilically to selected carbohydrate groups on the surface of other cells [2]. The immunoglobulin superfamily are also involved in cell–cell adhesion and use both homophilic and heterophilic binding. The final superfamily, integrins, mediate cell–matrix adhesion and are the type of CAMs considered in this work. Their binding is heterophilic: the extracellular domain of integrins bind to ligands in the ECM such as fibronectin, vitronectin, laminin or collagen [111]. Integrins, and the large focal adhesions that they form, are capable of transmitting and responding to mechanical forces between a cell and its environment and are known to be highly dynamic structures due to their sensitivity to environmental cues [67, 71, 123, 132, 148]. Their dynamic behaviour is most notably studied in the context of cell migration, which is induced by traction generated by adhesions at the leading edge of a cell. Due to their sensitivity to environmental cues, an important aspect to understand is the response of ASM cell–matrix adhesions to the oscillatory mechanical environment in the lung.

### 1.2.2 Integrin structure and focal adhesions

Integrins are heterodimeric and consist of an $\alpha$ and $\beta$ subunit, each of which has an extracellular, transmembrane, and cytoplasmic domain. In mammals there are 18 known $\alpha$ subunits, 8 known $\beta$ subunits, and 24 recorded combinations and integrin types. The specific subunits of an integrin depend on cell type, and additionally determine properties and functions of the integrin including binding affinity for particular ligands in the ECM [71]. To enable signal transduction between the cell and the ECM, a sequence of molecular events must take place to physically connect the integrin to both the intracellular and extracellular regions of the cell; these events are described below and sketched in Fig. 1.5.

In their inactive state, integrins take on a bent conformation which leaves them close to the cell membrane and with a low-affinity for binding to ligands in the ECM (Fig. 1.5). Activation mechanisms involve a sequence of regulatory events within the cell [9, 27, 60]. An important and final stage of this so-called 'inside-out' activation involves the binding of adaptor proteins—commonly talin—to the $\beta$-subunit cytoplasmic tail [27]. The active integrin then extends into an upright high-affinity conformation where it is more readily available for binding to ligands in the ECM. The adaptor

proteins additionally form the link between the integrin and the actin cytoskeletal network within the cell. In some cases, integrins in the bent conformation can be activated by binding to ligands in the ECM—in particular, Adair *et al.* [1] show that, under certain biochemical conditions in the extracellular domain, an outside-in activation of integrins occurs.

When active integrins become bound to both adaptor proteins within the cell and to ligands in the ECM they form a physical link between intra- and extracellular domains. From this state bi-directional mechanical signals can be transduced, and larger adhesive complexes may develop. At various stages in its development, the adhesive complex can be roughly classified according to its size as well its the molecular composition. The diameter of a single integrin is 6-10nm. Small clusters of integrins are considered to be nascent adhesions and typically have lifetimes of 10s of seconds. If additional proteins are successfully recruited, nascent adhesions can mature into a slightly larger focal complexes (of typical diameter 1$\mu$m) [106]. These focal complexes survive for a few minutes and will either disassemble or form stable focal adhesions (FAs) through additional protein recruitment; zyxin has been identified as a protein present only in this final stage of FA maturation [152]. Stable FAs are typically 2$\mu$m wide and 3-10$\mu$m in length, have lifetimes of tens of minutes, and consist of a large protein complex within the cell. The formation of stable FAs is hierarchical and involves the organised recruitment of over 100 proteins within the cell. Some important components of the protein complex, in addition to talin, include focal adhesion kinase (FAK), vinculin, $\alpha$-actinin, paxillin, filamin and tensin [152]. FAs provide a stronger attachment between the actin cytoskeleton and the ECM and allow for large mechanical forces to be transferred between individual cells and the ECM. Even in this mature state, there are still dynamic processes occuring within the FA—the integrins can cycle between states and proteins are replaced.

As well as facilitating the transmission of mechanical forces, integrins are highly mechanosensitive. In response to the extracellular environment, experiments have shown that the substrate stiffness can influence the size and strength of integrin-mediated adhesions [32, 76, 110]. In response to intracellular forces, which are generated by actomyosin filaments attached via talin to the integrin tail, adhesions can recruit additional proteins to strengthen the adhesion. In this case, a conformal change in the talin protein is induced under tension such that cryptic binding sites for vinculin are exposed [67]. Vinculin can then bind to talin and also to the actin cytoskele-

ton to strengthen the adhesion (Fig. 1.5). Several other positive feedback mechanisms related to the growth and strengthening of integrin adhesions have been identified or hypothesised, including a mechanical advantage of integrin clustering due to co-operativity [108, 151], and upregulation of integrin activation through biochemical signalling pathways [26, 144, 149].

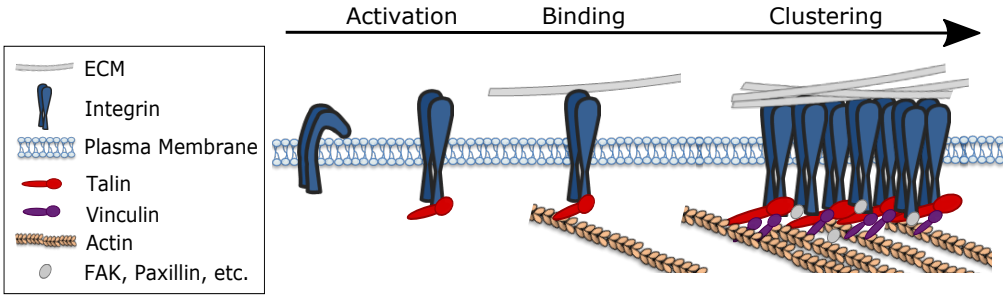


**Figure 1.5:** Sketch of the key stages involved in cell–matrix adhesion. Inactive integrins have a bent conformation with a low-affinity for binding to ligands in the ECM. Adaptor proteins (commonly talin), bind to the cytoplasmic tail and lead to integrin activation; the integrin then extends into an upright high-affinity conformation [27]. Additionally, adaptor proteins connect the integrins to the actin cytoskeleton. In the active state, integrins readily bind to ligands in the ECM, by which they create a physical link between intracellular and extracellular domains. As adhesions mature, integrins begin to cluster. Large protein complexes are formed within the cell; this can involve over 100 proteins, including focal adhesion kinase (FAK), vinculin, $\alpha$-actinin, paxillin, filamin and tensin [152].

### 1.2.3 Experimental techniques for measuring cell adhesion

Detailed experimental study of cell adhesion requires high precision techniques that are capable of measuring forces starting at the order of piconewtons. Force spectroscopy methods have been used to achieve this, and include the use of magnetic tweezers, optical tweezers, microneedles, traction force microscopy and atomic force microscopy [43, 99, 102, 135]. These techniques, amongst those reviewed recently by Wu *et al.* [150], are able to provide force measurements at the level of single molecules, as well as measuring adhesive properties at the whole cell level. For integrins, clusters of adhesion molecules are known to reorganise and strengthen in response to external forces [67, 119]. Single-molecule studies could therefore be beneficial when

interested in quantifying individual integrin properties; the accuracy and implementation of single molecule force spectroscopy using optical and magnetic tweezers and atomic force microscopy are reviewed in detail in [102]. In other cases it is the collective behaviour of adhesions that is of interest, such as during cell migration via traction forces [43, 99, 135] or the strength and dynamics of larger focal adhesions [133]. Cell adhesion molecules are load bearing and quantities that are often of interest to measure include bond energies and lifetimes under an applied load, the distribution of rupture forces, and total adhesion strength.

Atomic force microscopy (AFM) can exert a larger range of forces than optical or magnetic tweezers [102] and can be used to either study the rupture of single molecules and bonds or to measure the collective behaviour of larger focal adhesions. AFM provides extremely high resolution measurements, and is able to detect forces as small as $10^{-15}$N at room temperature [19]. The technology uses photodiode detectors and a laser to track the deflection of a metal cantilever as it interacts with the surface of a cell (illustrated in Fig. 1.6). The position of the cantilever relative to the cell is controlled by a piezoelectric scanner (Fig. 1.6a), and the cantilever could either have a small tip functionalised with ligands for integrins to bind to, be attached to a larger substrate-coated microbead, or be attached to another cell. To measure adhesion dynamics, the cantilever is lowered vertically to the cell surface where adhesion occurs. It is later retracted, and the upward motion of the cantilever is resisted by the adhesions that have formed, causing the cantilever to bend (Fig. 1.6b). The cantilever is of known mechanical properties and its deflection can therefore be used to calculate adhesion forces throughout the process. This information can be plotted in 'approach-retract' force curves (Fig. 1.6b), which are also used to detect events where individual bonds rupture; when the bonds break there are abrupt changes in adhesion force, seen by jumps in the retraction curve. The scanners are also able to move laterally and this method is often used to produce images and high resolution information about cell surface topography and to determine local mechanical properties such as variations in cell elasticity [85, 90, 140].

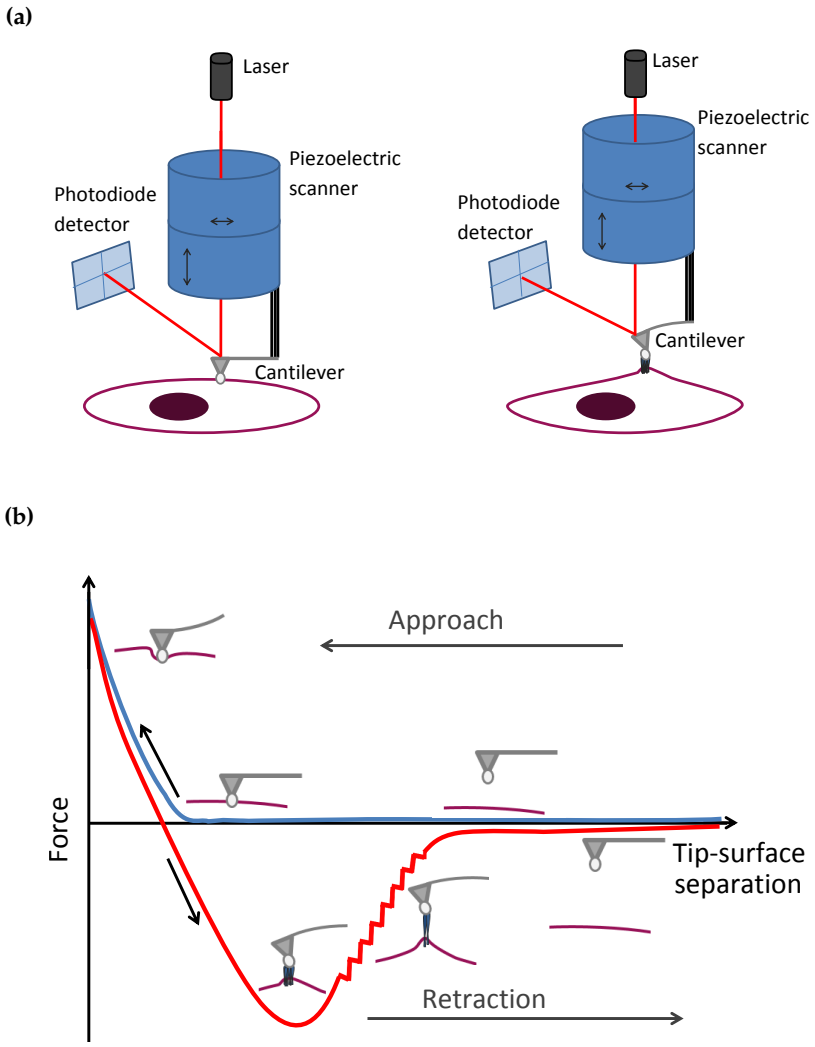


**Figure 1.6:** (a) Experimental set-up for atomic force microscopy (AFM) measurements. The position of a metal cantilever relative to the cell is controlled by a piezoelectric scanner which can move laterally or vertically. The deflection of the cantilever as it interacts with the surface of a cell is tracked by a laser and photodiode detectors. Deflection is used to calculate adhesion forces since the mechanical properties of the cantilever are known. (b) Sketch of the approach-retract curves obtained by measuring cantilever deflection as the cantilever is first lowered to the cell surface (blue curve) and then retracted (red curve) once adhesions have formed. Cantilever deflection shows whether the force is repulsive (positive) or attractive (negative), and jumps in the retraction curve indicate adhesion rupture events.

## 1.3 Existing modelling approaches

Here we discuss some existing approaches to modelling cell–ECM adhesion. A common choice is to use stochastic, individual-based models due to the relative ease of incorporating detailed binding kinetics for individual integrin–ligand pairs. Continuum models accounting for integrin binding have also been developed; however, capturing the detailed response of individual integrins to mechanical cues in this setting remains a challenge.

### 1.3.1 Stochastic models of cell–ECM adhesion

A common modelling approach is to simulate the stochastic binding dynamics of individual integrin–ligand bonds using Monte Carlo simulations. In the simplest description a bond can be described as open (not bound to the ligand) or closed (bound to the ligand). Rupture and binding events are equivalent to transitions between the two states and can therefore be modelled stochastically using master equations. Similarly to the experimental methods used in force spectroscopy, the simulated bonds are often subject to an applied load for which quantities such as bond lifetimes and rupture forces are calculated. In order to simulate these responses, suitable rate functions for the transition between closed and open bonds must be chosen.

An early model for bond rupture under constant force is the Bell model [14], where the rupture rate of a bond is assumed to increase exponentially with force according to

$$k_{off}(F) = k_0 \exp(\gamma F/kT). \tag{1.3.1}$$

The parameters $k_0$, $k$, and $T$ are the unstressed unbinding rate, the Boltzmann constant and the absolute temperature respectively, and $F$ is the total force on the bond. The parameter $\gamma$ is an empirical constant that depends on material properties. This relationship originates from observations on the strength of macroscopic solids under stress [154], but can also be derived theoretically, *e.g.* from the Arrhenius equation [143] and as a low force approximation of Kramers theory [141]. Other forms for rupture rates have since been suggested [40, 41, 83, 114], and precise measurements for individual ligand-receptor bonds using single force spectroscopy [44, 102] remain an area of ongoing research. Within stochastic models of cell adhesion, there is flexibility to include and investigate these different force-dependent functions for bond rupture. A number of studies use a stochastic implementation of the Bell model to investigate

the stochastic rupture of parallel bonds under shared loading [36, 37, 126]. Erdmann and Schwarz [36] consider a cluster of bonds between two parallel surfaces where a constant, perpendicular, external loading is applied to one surface (Fig. 1.7). The cluster lifetime is measured for different loading values and is seen to be dependent on the initial number of closed bonds and the rebinding rate. It is shown that the rebinding of ruptured bonds is necessary in order to obtain physiological cluster lifetimes. In a later study, the same authors further investigate the properties of the bound and unbound adhesion states [37]. By modelling the individual bonds as Hookean springs which can resist the external loading, two positive feedback mechanisms are seen. There is a decrease in distance between the two surfaces due to binding events and an increase in separation when unbinding occurs, which further promote binding and unbinding respectively. Since the initial adhesion state influences the separation of the two surfaces, these feedback mechanisms lead to the existence of bistability for some loading values; the outcome could either be bound or unbound clusters. It is hypothesised that this bistability could be related to the switch between transient and firm adhesions seen in early adhesion formation.

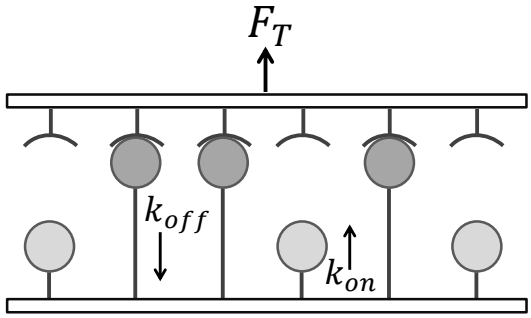


**Figure 1.7:** Figure adapted from [36], showing open and closed bonds under a constant loading $F_T$. Each bond experiences a force $F = \frac{F_T}{N_C}$ where $N_C$ is the number of closed bonds. Stochastic transitions between open and closed states occur with the rates $k_{on}$ and $k_{off}(F)$.

Since cell–matrix adhesions exert traction forces, studies considering friction generated by discrete bonds in more general contexts are also relevant. Filippov *et al.* [42] consider stochastic transitions of discrete molecular bonds that form between two rigid surfaces in the presence of a low and high relative motion of the surfaces. In each of the two cases, known macroscopic friction properties are successfully simulated. In contrast to the above studies, the motion that they apply is parallel (rather than perpendicular) to the surface.

Qian *et al.* [115] extend the initial studies of shared loading between parallel bonds by considering bonds that experience stress non-uniformly due to the loading being applied at an angle. In addition to changing the loading angle, they couple the stochastic integrin binding dynamics to a mechanistic model of the cell and the ECM. Within the mechanistic model, they investigate the effect of different ECM and cytoskeletal stiffnesses and show, in agreement with previous experimental observation, that with cytoskeletal stiffening and a low angle of applied load the adhesion lifetime is significantly increased.

Due to the fluctuating mechanical environment of airways *in vivo*, studies that consider the effect of dynamic, rather than static, loading on adhesion stability are of particular relevance to the work in this thesis. Kong *et al.* [81] consider the stochastic rupture of adhesion clusters under an oscillatory strain applied to the extracellular substrate. In their model, stochastic binding dynamics are coupled to a viscoelastic description of actin stress fibres, which are attached to the intracellular domain of the focal adhesions. Starting from a high adhesion state, a threshold strain is observed past which adhesions quickly rupture. Additionally it is seen that the oscillation frequency, the stress fibre stiffness and the stress fibre relaxation time further influence the threshold strains that adhesion clusters can withstand.

In addition to the rupture of bonds, the initial formation of focal adhesions is an area of interest. In a related stochastic modelling framework, Paszek *et al.* [108] successfully use stochastic lattice spring models (LSMs) and a stochastic simulation algorithm for modelling integrin–ligand bonds, called Adhesive Dynamics [58, 59], to simulate the formation of integrin clusters. Spatial clustering of integrins is an important prerequisite for focal adhesion formation and it is shown that a mechanical feedback due to resistance provided by the glycocalyx (an additional layer between the membrane and ECM) can drive clustering by promoting cooperativity. The model consists of a spring network to model the cell and ECM interface, separated by parallel springs representing the glycocalyx. They simulate stochastic binding and rupture events between the cell and the ECM and the integrin distributions respond to changes in the rest length of the glycocalyx springs. When the width of the glycocalyx is larger than the integrin rest length a mechanical cooperativity is seen; binding creates a local deformation that promotes further binding due to the reduced distance between the integrins and their ligands. This study was not concerned with external loading, but their discrete LSM approach can accommodate high levels of microscopic

detail both in terms of binding kinetics and mechanics.

Other physical factors that have been observed experimentally to affect integrin dynamics include ECM stiffness, ligand density, and actin fibre orientation. The first two of these factors have been tested in the computational model of Paszek *et al.* [108] and in a number of other stochastic–elastic models that are reviewed further by Gao *et al.* [48]. Chan and Odde [30] and Walcott *et al.* [142] both use stochastic models to investigate differing adhesion dynamics on stiff and compliant ECM, and obtain results in agreement with experimental studies. Walcott *et al.* [142] show that these mechanosensitive adhesion properties emerge naturally with the inclusion of load dependent reaction rates. It is evident that there are multiple factors capable of influencing integrin dynamics, which are likely to be acting in combination. Their relative importance and the full underlying mechanisms are still not clear, but these types of models have been able to reproduce, and begin to help explain, a wide range of experimental results.

### 1.3.2 Continuum models of cell–ECM adhesion

Despite their popularity, stochastic models quickly become prohibitive for larger scale simulations given the potentially large number of integrins present on the cell surface (densities have been reported to reach $900\mu\text{m}^{-2}$ in mature adhesions [147]). Continuum models would therefore be beneficial in such cases, and additionally allow for more efficient coupling to larger scale (e.g. cell and tissue level) models.

A model that couples a continuum description of integrin dynamics to a cell-level mechanical model is that of Alt *et al.* [4], who consider integrin clustering in the context of cell migration. They consider integrins in one of 4 states (unbound, bound to the ECM, bound to the cytoskeleton, and double-bound to both the ECM and cytoskeleton) and model integrin binding reactions as reversible state transitions using mass action kinetics. Within the cell a two-phase flow model is used for the cytoskeleton and the cytosol, and actin-bound integrins are advected with the cytoskeletal flow. The advection-reaction-diffusion description of integrin binding dynamics is additionally coupled to force-balance equations at the leading edge of the cell, where double-bound integrins produce a frictional force between the cell and the ECM, enabling migration. In their study, the focus is on the resulting migration patterns, rather than the detailed biochemical mechanisms behind cluster formation.

Welf *et al.* [144] develop a more detailed continuum model for integrin binding and the formation of integrin clusters by considering a reaction-diffusion system that incorporates biochemical feedback. A biochemical feedback loop in the activation of talin is incorporated, which subsequently leads to positive feedback in the activation of integrins. Their results show that this feedback is sufficient to induce a spatial clustering of integrins, which are activated during a reaction of inactive integrins with diffusing talin. In their model the actin cytoskeleton and mechanical effects are not considered and the ECM is assumed stationary. Block *et al.* [20] also investigate cluster formation using a reaction-diffusion model for integrin binding and, similarly to Welf *et al.* [144], they model the changes between different integrin states using mass action kinetics. However, due to the mechanosensitive nature of integrin-based adhesion complexes [67, 71, 123, 132, 148] and the spatial constraints experienced by each bond, it is necessary to develop descriptions and binding rate functions that can also accommodate the response to local mechanical cues. In an effort to capture the mechanosensitive nature of integrins, Cao et al. [28, 29] have developed continuum models that allow for investigation of the effect of substrate and cell nucleus stiffness on focal adhesion size. The timescale of interest in their studies (focal adhesion growth, occuring over minutes) is relatively large compared to the timescale associated with individual integrin binding reactions, so a quasi-static approximation for the density of integrins is used.

Motivated by the stochastic–elastic model of Paszek *et al.* [108], Yuan *et al.* [151] have developed a mechanistic continuum model for integrin clustering. They model the cell membrane as an infinitely extended elastic plate that is separated from the ECM by a further elastic layer, representing the glycocalyx. Their results, in agreement with Paszek *et al.* [108], demonstrate that such a repulsive layer promotes integrin clustering since bound integrins (of length smaller than the width of the repulsive layer) produce small deformations that make reductions in integrin separation energetically favourable.

In a more general friction study, closely related to the stochastic model of Filippov *et al.* [42], Srinivasan and Walcott [131] consider a continuum approximation to friction generated by discrete bonds through the use of the Lacker–Peskin model [86]. This model is formulated in terms of a local spatial variable that considers the bond displacements from a reference alignment, rather than their individual positions. This formulation allows for the inclusion of binding rates that incorporate local spatial

constraints; Srinivasan and Walcott [131] use the Bell model for bond rupture, as commonly used in stochastic simulations. A necessary assumption in this study is that the two surfaces are rigid and parallel so that the displacement of each bond is sufficient to determine the total traction force. In the presence of a relative velocity between the two layers, the distributions are then governed by advection–reaction equations. Using this model, well-known macroscopic friction behaviours are successfully simulated.

### 1.3.3 Models of contractile force generation

In order to fully understand the tissue-level behaviour that occurs during bronchoconstriction, models of contractile force transmission via integrins will need to be coupled to models of contractile force generation within the cell. Models that incorporate both cell–matrix adhesion and descriptions of the intracellular contractile machinery will also be relevant to other applications, including cell migration, where dynamic integrin turnover occurs alongside the motion of actin filaments [4].

For ASM cells an important factor is how a fluctuating environment due to tidal breathing affects both the contractile force generation and the adhesion dynamics. A number of experimental and theoretical studies have investigated the effect of a dynamic environment on ASM contractile force generation [12, 13, 24, 46, 53, 88, 89]. In an experimental study, Gunst [53] applied length oscillations to bronchial and trachealis tissue strips that are initially in different contractile states. Experimental measurements show how force varies throughout the cycle and it is additionally observed that the mean contractile force is reduced during dynamic stretching in comparison to the isometric force obtained at equivalent static lengths. It has been proposed that contractile force could be reduced due to disruptions in the binding of actin to myosin during length fluctuations [89]. To more accurately quantify length and airway calibre changes that occur in an *in vivo* environment, Latourelle *et al.* [89] and LaPrad *et al.* [88] applied force and pressure oscillations to tissue strips and isolated airways respectively, rather than length oscillations. In this more recent experimental framework the muscle length changes freely and the nonlinear response of length to pressure oscillations can also be measured.

In theoretical models of contractile force generation, the sliding filament model of Huxley [70] has been combined with the kinetic scheme of Hai and Murphy [55, 56]

to investigate crossbridge cycling and the phosphorylation and dephosphorylation of myosin crossbridges. This Huxley–Hai–Murphy (HHM) model developed by Fredberg *et al.* [47] and Mijailovich *et al.* [97] is able to capture the reduced contractile force seen during ASM length oscillations, but does not explain all of the experimental observations on the behaviour of whole tissue strips. To address this, further studies incorporate the HHM model into cell and tissue level models [24, 64, 65, 112]; Brook [24] showed that the cell-level behaviour is likely to be further influenced by the reorganisation of contractile units due to disruptions in the acto-myosin network during the length oscillations.

The dynamic environment of the airway *in vivo* is known to affect contractile force generation; however, since integrins are also sensitive to mechanical cues, we believe that coupling of models of contractile force generation to models of contractile force transmission (via integrins) is a necessary step towards fully understanding tissue-level dynamics during bronchoconstriction.

## 1.4 Thesis overview and structure

The aim of this thesis is to investigate how airway smooth muscle (ASM) cell–matrix adhesions are affected by dynamic mechanical environments. In particular, we aim to understand how integrins respond to tidal breathing and deep inspirations. We develop two mathematical models for this purpose in Chapter 2; a discrete stochastic–elastic model and a multiscale continuum model. Both of these models are able to support local spatial constraints in the descriptions of integrin binding and rupture, allowing us to consider detailed binding kinetics at the integrin level alongside cell level material deformations. In the multiscale formulation, the integrin level and cell level are considered to be the microscale and macroscale respectively.

In Chapter 3, we present numerical results from the discrete and continuum models, where we investigate how an oscillatory loading of the extracellular matrix (ECM) affects integrin binding dynamics. We consider loading conditions that represent tidal breathing and deep inspirations, and show the effect of varying parameters such as material stiffnesses, oscillation frequency and binding affinities. There is strong qualitative agreement between our continuum and discrete results, and in Chapter 4 we focus on extending the more tractable continuum model. We consider activation and

diffusion of free integrins, and a strain-dependent reinforcement of integrins, occuring due to vinculin binding to cryptic sites on talin.

In Chapters 2–4, we only consider horizontal motion between the cell and ECM. In Chapter 5, we modify the microscale description to additionally allow for vertical motion. We then couple this to a 3-spring description of the cell, integrins and ECM, with which we replicate an experimental atomic force microscopy (AFM) protocol. In the experiments, a cantilever (with substrate-coated bead attached) repeatedly approached and retracted from a cell whilst the adhesion forces were measured in time. We compare our model results to the experimental data, provided by Prof. Gerald Meininger and Huang Huang (University of Missouri), and use cluster analysis techniques to identify differing patterns in adhesion force.

In Chapter 6, we investigate the interacting dynamics of integrin-mediated adhesions and actomyosin crossbridges by coupling our adhesion model to a description of intracellular contractile force generation. The cell, previously modelled as a passive material, is extended to include active contractile components that follow a 4-state Huxley–Hai–Murphy model for crossbridge cycling and phosphorylation [97]. ASM cells are subject to constant fluctuations in their mechanical environment, and both contractile force generation and contractile force transmission could be modulated. In our coupled model, we investigate the combined response of crossbridges and integrins when the cell is subject to oscillatory length fluctuations.

The conclusions drawn from these investigations are summarised in Chapter 7, where we discuss our main findings and suggest directions for future work.

# Chapter 2

# Discrete and continuum models of cell–matrix adhesion

In this chapter we introduce two models of cell–matrix adhesion. In the first model (Section 2.1) we develop an example of a discrete stochastic model of integrins transitioning between bound and unbound states. By using a stochastic-elastic framework we additionally capture the local mechanical response to the binding reactions. A discrete approach, however, is computationally intensive for large scale simulations and the number of integrins on a cell surface is often high. We therefore develop a second, multiscale, continuum model (Section 2.2), which aims to capture similar amounts of integrin-level detail. By using a novel two-scale approach, our continuum framework supports local spatial constraints for the integrins at the microscale and supports spatial binding rate functions of the type typically implemented in discrete stochastic simulations.

## 2.1 Discrete model formulation

The early stages of FA formation (see Section 1.2.2) can be summarised by reversible state transitions where we classify integrins by the following states (Fig. 2.1):

(i) $I_U$: Inactive, unbound, and freely diffusing in the plasma membrane

(ii) $I$: Active, unbound, and freely diffusing in the plasma membrane

(iii) $I_A$: Active and bound, via adaptor proteins, to the intracellular actin cytoskeleton

(iv) $I_E$: Active and bound to ligands in the ECM

(v) $B$: Bound to both the actin cytoskeleton and to ligands in the ECM.

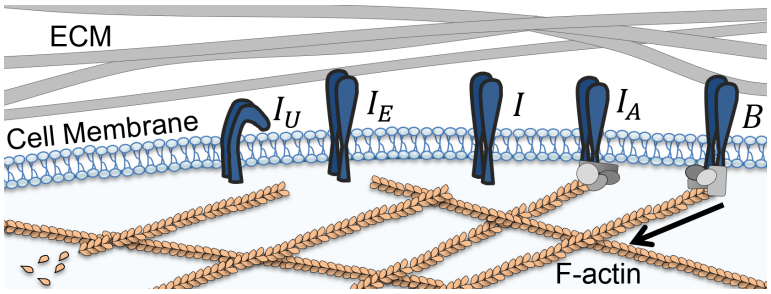


**Figure 2.1:** A representation of the five possible integrin states. Inactive ($I_U$) and active ($I$) integrins diffuse in the membrane. Active integrins may become actin-bound ($I_A$) via adaptor proteins, bound to ligands in the ECM ($I_E$) or double-bound to both the actin cytoskelton and the ECM ($B$).

In our discrete model we consider a simplified reaction scheme in which the integrin activation processes are assumed to have already occurred. We therefore assume that integrins are already attached to the actin cytoskeleton within the cell and undergo reversible reactions to become bound to the ECM and able to transmit force (i.e. $I_A$ binds reversibly to $B$; Fig. 2.1). We assume that the actin cytoskeleton, integrins and ECM form an evolving spring network in which actin-bound integrins, $I_A$, and 'potential binding sites' on the ECM fibre, $E$, are modelled as individual nodes, indexed by $I_{A_j}$ and $E_i$, respectively (Fig. 2.2). We denote the number of ECM nodes by $N$ and the number of actin-bound integrin nodes by $M$, where $N$ and $M$ do not need to be equal. Hookean springs between the neighbouring $I_A$ and $E$ nodes represent the cytoskeleton and ECM, respectively, and are each assigned a spring stiffness ($\kappa_a$ and $\kappa_e$, shown in blue and red). We additionally allow for stochastic binding reactions (described below) between integrins and the ECM, dependent on the proximity and availability of binding sites, where each node is considered to be an individual species. This allows reaction propensities to depend on the pairwise distances between integrins and the ECM binding sites; pairs of compatible nodes may undergo stochastic transitions to form double-bound integrins ($B$) according to the following reaction

$$I_A + E \underset{\hat{k}_u(\hat{x})}{\overset{\hat{k}_b(\hat{x})}{\rightleftharpoons}} B, \tag{2.1.1}$$

where $\hat{x}$ is a spatial variable local to each integrin. The local variable $\hat{x}$ measures the horizontal distance between each pair of $I_A$ and $E$ nodes (see Fig. 2.2) and is effectively a measure of how far each integrin head is from its unstressed position, $\hat{x} = 0$. Throughout, hats indicate dimensional quantities. In this model, every combination of $I_A$ and $E$ nodes are considered as a possible pair, and pairwise distances $\hat{x}$ are

stored in an $N \times M$ distance matrix. Based on these distances, binding and unbinding propensities are calculated for each pair (Eqs. 2.1.2, 2.1.3). There will therefore be $NM$ possible binding reactions and a further $NM$ possible unbinding reactions. In accordance with the chosen stochastic binding reactions we add or remove a third spring-type (black), representing double-bound integrins with stiffness $\kappa_b$, between the $I_A$ and $E$ nodes selected to bind. We additionally include springs with stiffness $\kappa_r$ (green) from the $I_A$ nodes to a fixed configuration of 'anchor' nodes, as a representation of the restoring forces by, and attachments to, the cytoskeletal network within the cell.

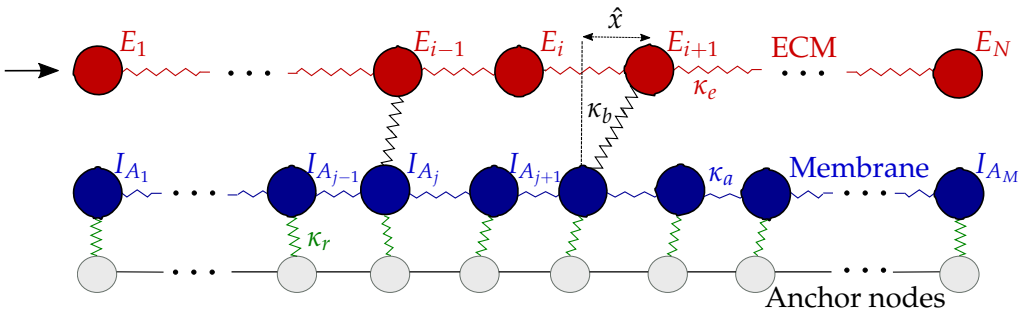


**Figure 2.2:** Structure of the discrete spring network. Actin-bound integrins ($I_A$, blue) and ECM binding sites ($E$, red) are considered as individual nodes, connected to their neighbours by linear springs with stiffness constants $\kappa_a$ and $\kappa_e$ respectively. Bound integrins ($B$, black) are represented by removable springs between the two sets of nodes, with spring constant $\kappa_b$. The local variable $\hat{x}$ measures horizontal distances between each pairwise combination of integrin and ECM binding site nodes, to be stored in an $N \times M$ distance matrix and used to inform binding propensities. We additionally include horizontal restoring forces for the $I_A$ nodes to a fixed configuration of anchor nodes via springs with stiffness $\kappa_r$ (green). In this model the vertical movement is constrained and we only consider horizontal motion, imposed via displacement conditions on $E_1$.

To simulate the reversible binding events in Eq. 2.1.1 we must first specify binding and unbinding propensities, valid for each pair of $I_A$ and $E$ nodes. Our chosen spatial binding rates are piecewise linear functions (Fig. 2.3) given by

$$\hat{k}_b(\hat{x}) = \begin{cases} \hat{f}_1 \left(1 - \frac{|\hat{x}|}{\hat{h}}\right) & |\hat{x}| \leq \hat{h}, \\ 0 & \text{otherwise}, \end{cases} \tag{2.1.2}$$

and

$$\hat{k}_u(\hat{x}) = \begin{cases} \hat{g}_1 + \frac{\hat{g}_2|\hat{x}|}{\hat{h}} & |\hat{x}| \leq \hat{s}, \\ \hat{g}_3 & \text{otherwise.} \end{cases} \tag{2.1.3}$$

A maximum binding rate $\hat{f}_1 > 0$ occurs at $\hat{x} = 0$, after which the binding propensity decreases linearly to zero within a finite binding range, $\hat{h}$. The unbinding rate when $\hat{x} = 0$ is given by $\hat{g}_1 > 0$, and increases linearly with $\hat{x}$. Beyond a maximum horizontal distance of $\hat{s} > \hat{h}$, any remaining bonds rupture quickly with a high rate $\hat{g}_3 > 0$. We note that these rate functions approximate those which can be derived using detailed balance (see e.g. [62], Fig. 9c and [131], Fig. 2), by which pairs of reaction rates are constrained to ensure thermodynamic reversibility. Within this modelling framework there is flexibility in the choice of rate functions, and alternative forms can easily be accommodated.

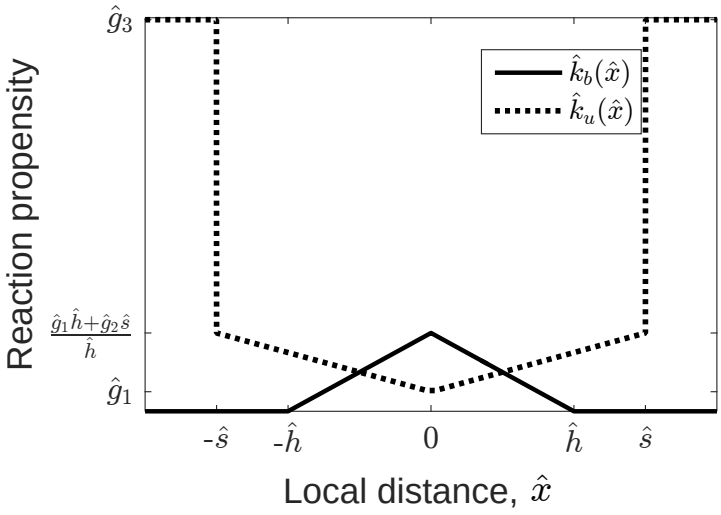


**Figure 2.3:** Sketch of the chosen form of piecewise linear binding ($\hat{k}_b$, Eq. 2.1.2) and unbinding ($\hat{k}_u$, Eq. 2.1.3) functions. The local variable $\hat{x}$ measures the local distance between pairs of ECM and actin-bound integrin nodes (see Fig. 2.2) and is therefore effectively a measure of how far each integrin head is from its unstressed position, $\hat{x} = 0$.

After calculating the binding and unbinding propensities for each combination of $I_A$ and $E$ nodes (a total of $2NM$ reactions), we select the reaction that is to occur using a stochastic first reaction algorithm [49]. The time, $\hat{\tau}$, until the next reaction occurs is

found by calculating

$$\hat{\tau} = \frac{1}{a_0} \ln\left(\frac{1}{r_1}\right), \tag{2.1.4}$$

where $r_1$ is a uniformly distributed random number drawn from $(0,1)$ and where $a_0$ is the sum of all reaction propensities. The time between events is therefore exponentially distributed with mean $1/a_0$, the accuracy of which is derived and discussed by Gillespie [49] and further detailed by Erban *et al.* [35]. Next, we must identify which reaction occured at this time. To do so, a second uniformly distributed random number $r_2 \in (0,1)$ is generated. We select the reaction, indexed by an integer $\mu$, such that $\sum_{i=1}^{\mu-1} a_i < a_0 r_2 \leq \sum_{i=1}^{\mu} a_i$ is satisfied, where $a_i$ are the individual reaction propensities and where $1 \leq \mu \leq 2NM$. This process can be thought of as dividing $(0, a_0)$ into subintervals for each of the $2NM$ reactions. The length of each subinterval is given by its reaction propensity, and a random point $a_0 r_2 \in (0, a_0)$ has higher probability of landing in the larger subintervals. This step therefore ensures that the probability of choosing a given reaction is proportional to its propensity. Note that whilst a node is already bound, further binding propensities for that node are set to be zero. Additionally, if a node is not bound, the unbinding propensity is zero.

The stochastic reactions govern bond formation and rupture and are used to update the structure of the mechanical spring network (Fig. 2.2). To then implement a position update of the network we consider the net force acting on each node, $\hat{\boldsymbol{F}}_k$. There are contributions due to neighbouring springs, $\hat{\boldsymbol{F}}_{N_k}$, and forces due to integrin bonds between species, $\hat{\boldsymbol{F}}_{B_k}$. In this model, electrostatic interactions and inertia are assumed to be negligible. We therefore take $\hat{\boldsymbol{F}}_k = \hat{\boldsymbol{F}}_{N_k} + \hat{\boldsymbol{F}}_{B_k}$ and solve the equilibrium equation $\Sigma \hat{\boldsymbol{F}}_k = \boldsymbol{0}$ on the network at each timestep, to provide updates for node positions. We also ensure that this equilibrium condition is satisfied in the initial configuration, in which there are no bound integrins and where the $I_A$ and $E$ nodes are equally spaced.

In order to investigate the effect of a dynamic environment, we allow for external forcing to the ECM via time-dependent displacements of the boundary node

$$\hat{U}_{E_1}(\hat{t}) = \hat{f}(\hat{t}), \tag{2.1.5}$$

for a function $\hat{f}(\hat{t})$ to be specified, and where $\hat{U}_{E_i}$ denotes the displacement of the $i$th ECM node (see Fig. 2.2) from its rest position. Eq. 2.1.5 provides a Dirichlet boundary condition for the force balance equations. We note that the first reaction algorithm used to determine the binding reactions [49] generates an event-based timestep. As

we also wish to allow for external forcing and time-dependent displacements, we introduce a maximum timestep $\hat{\tau}_{max}$ such that, in the case that no reaction occurs within this timestep, a position update of the network is induced and reaction propensities are recalculated. We summarise the computational model in Algorithm 2.1.1.

---

**Algorithm 2.1.1** Discrete stochastic–elastic model

1: Initialise actin and ECM spring networks and relax to mechanical equilibrium.
2: **while** $\hat{t} < \hat{T}$ **do**
3: Calculate binding and unbinding propensities, $a_i$, based on pairwise distances (where $i \in [1, ...n]$ and $n$ denotes the number of possible reactions).
4: Generate a uniformly distributed random number, $r_1$, from the interval $(0, 1)$, to calculate the time elapsed before the next reaction, $\hat{\tau} = \frac{1}{a_0}\ln(1/r_1)$. The constant $a_0$ is the sum of all reaction propensities, $a_0 = \sum_{i=1}^{n} a_i$.
5: **if** $\hat{\tau} < \hat{\tau}_{max}$ **then**
6: Generate a second uniformly distributed random number, $r_2 \in (0, 1)$, and select the reaction, indexed by $\mu$, such that $\sum_{i=1}^{\mu-1} a_i < a_0 r_2 \leq \sum_{i=1}^{\mu} a_i$ is satisfied.
7: Update the structure of the spring network according to chosen reaction.
8: **end if**
9: Set $\hat{t} = \hat{t} + \min\{\hat{\tau}, \hat{\tau}_{max}\}$. Calculate net forces acting on each point and update positions by solving $\Sigma \hat{\boldsymbol{F}}_i = \boldsymbol{0}$, subject to boundary constraints.
10: **end while**

---

This stochastic framework can easily be extended to allow for integrin diffusion and integrin activation. Integrin diffusion via random walks can be incorporated into the position update (Step 9) of Algorithm 2.1.1, and integrin activation can be included by adding an additional set of pairwise reaction propensities between diffusing integrins and actin nodes into Step 3.

We will show numerical results from the discrete model in Chapter 3, where we compare the model to an analogous continuum model developed in Section 2.2. The two models will be used to investigate the integrin response to an oscillatory displacement of the ECM, representing the effect of tidal breathing *in vivo*.

## 2.2 Continuum model formulation

We now develop a multiscale continuum model of cell–matrix adhesion which will form the basis of the rest of the models in this thesis. Our multiscale approach allows for the inclusion of local spatial constraints for the integrins at the microscale, and this key feature allows us to capture detailed microscale binding kinetics and mechanics in a manner similar to individual-based stochastic models. At the macroscale, we model the cell and ECM as linearly elastic materials; however, the framework that we develop can be generalised to support more complicated macroscale descriptions. Our continuum approach to modelling cell–matrix adhesion will also allow for coupling to other continuum models, such as those used for contractile force generation (considered in Chapter 6). A continuum approach is also beneficial in terms of computational efficiency, which will be especially important in larger scale simulations.

### 2.2.1 Microscale integrin binding dynamics

We begin by introducing the microscale model of integrin binding dynamics which will later be extended and coupled to a macroscale model of cell deformation (Section 2.2.4). At the microscale we adapt the Huxley crossbridge model [70]. As in the discrete model (Section 2.1), we consider a simplified reaction scheme where the integrin activation processes described in Section 1.2.2 are assumed to have already occurred. We therefore assume that integrins are attached to the actin cytoskeleton within the cell and undergo reversible reactions to become bound to the ECM and able to transmit force (*i.e.* $I_A$ binds reversibly to $B$, see Fig. 2.1). A microscale coordinate, $\hat{x}$, that is local to each double-bound integrin ($B$) and measures the horizontal distance between the points of cytoskeletal and ECM attachment (see Fig. 2.4); an integrin in a vertical position therefore has a distance of $\hat{x} = 0$.

In order to study the collective behaviour of the integrins we consider a distribution, $b(\hat{x}, \hat{t})$, which denotes the fraction of double-bound integrins that are bound with horizontal distance $\hat{x}$ at time $\hat{t}$. As in the Huxley model [70], we assume that each actin-bound integrin has a single ECM binding site within its binding range, which means that integrins in the actin-bound ($I_A$) state are also associated with a unique $\hat{x}$–distance measured to their nearest binding site. The actin-bound integrins can therefore also be described by a distribution, $u(\hat{x}, \hat{t})$, denoting the fraction of actin-bound integrins with a distance $\hat{x}$ to the nearest binding site at time $\hat{t}$. In our model, integrins

can be in only one of these two states, and therefore $b(\hat{x},\hat{t}) + u(\hat{x},\hat{t}) = 1$.

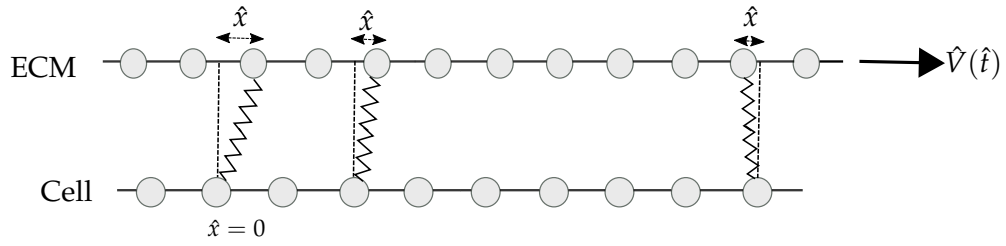


**Figure 2.4:** Sketch of the microscale formulation, based on the Huxley crossbridge model [70]. The microscale variable $\hat{x}$ is local to each integrin and measures horizontal distance from the point of cytoskeletal attachment to the nearest ECM binding site. Cell and ECM layers have relative velocity $\hat{V}$.

To derive the governing equations for the distributions, we consider the conservation of double-bound integrins in an arbitrary region $[\hat{x}_0, \hat{x}_0 + \Delta\hat{x}]$. The total number of double-bound integrins in this region is given by the integral $\int_{\hat{x}_0}^{\hat{x}_0+\Delta\hat{x}} \hat{\rho} b(\hat{x},\hat{t}) d\hat{x}$, where $\hat{\rho}$ denotes the total number of integrins per unit length, assumed constant with respect to $\hat{x}$. In the presence of a relative velocity between the ECM and cell membrane, $\hat{V}(\hat{t})$ (Fig. 2.4), the conservation equation is

$$\begin{aligned}\frac{\partial}{\partial \hat{t}} \int_{\hat{x}_0}^{\hat{x}_0+\Delta\hat{x}} \hat{\rho} b(\hat{x},\hat{t}) d\hat{x} =& \hat{\rho} \int_{\hat{x}_0}^{\hat{x}_0+\Delta\hat{x}} \hat{k}_b(\hat{x}) u(\hat{x},\hat{t}) d\hat{x} - \hat{\rho} \int_{\hat{x}_0}^{\hat{x}_0+\Delta\hat{x}} \hat{k}_u(\hat{x}) b(\hat{x},\hat{t}) d\hat{x} \\ &+ \hat{\rho}\hat{V}(\hat{t}) b(\hat{x}_0,\hat{t}) - \hat{\rho}\hat{V}(\hat{t}) b(\hat{x}_0+\Delta\hat{x},\hat{t}).\end{aligned} \tag{2.2.1}$$

The first two terms on the right hand side of Eq. 2.2.1 account for the binding and unbinding of integrins from the ECM, via spatial binding and unbinding functions $\hat{k}_b(\hat{x})$ and $\hat{k}_u(\hat{x})$ respectively. The functional form for $\hat{k}_b(\hat{x})$ and $\hat{k}_u(\hat{x})$ will be specified later. The last two terms in Eq. 2.2.1 account for advection of double-bound integrins into and out of the region, respectively, with relative velocity $\hat{V}(\hat{t})$. By using the mean value theorem and taking the limit as $\Delta\hat{x} \to 0$ we obtain the advection–reaction equation

$$\frac{\partial b(\hat{x},\hat{t})}{\partial \hat{t}} + \hat{V}(\hat{t}) \frac{\partial b(\hat{x},\hat{t})}{\partial \hat{x}} = \hat{k}_b(\hat{x})(1 - b(\hat{x},\hat{t})) - \hat{k}_u(\hat{x}) b(\hat{x},\hat{t}), \tag{2.2.2}$$

where $b(\hat{x},\hat{t}) + u(\hat{x},\hat{t}) = 1$ has additionally been used.

Bound integrins are represented by linear springs, which act in parallel to generate a drag force between the cell and the ECM, given by

$$\hat{F}(\hat{t}) = \hat{\rho}\hat{\lambda}_b \int_{-\infty}^{\infty} \hat{x} b(\hat{x},\hat{t}) d\hat{x}, \tag{2.2.3}$$

for the integrin spring constant $\hat{\lambda}_b$. We assume that the cell and ECM are rigid in the

microscale model; however, we will later allow for macroscopic deformations in the fully-coupled multiscale model (discussed in Section 2.2.4).

### Binding rate functions

To evolve Eq. 2.2.2 the forms of the spatial binding and unbinding functions need to be specified. In the original crossbridge model [70], asymmetric piecewise linear functions are used where binding only occurs for positive $\hat{x}$ and is biased toward the point where the site first comes into range. This asymmetry does not apply to the integrin model, and we use a maximum binding rate at $\hat{x} = 0$ which decreases symmetrically to zero as $|\hat{x}|$ increases. This is enforced through the same binding function, $\hat{k}_b(\hat{x})$, as in the discrete model (Eq. 2.1.2). Similarly, we use the same unbinding rate function, $\hat{k}_u(\hat{x})$ (Eq. 2.1.3, Fig. 2.3). There is flexibility in the choice of rate functions, and alternatives will be discussed in Section 3.3. These piecewise-linear functions allow us to obtain analytical results for Eq. 2.2.2 (shown in Section 2.2.2).

### Nondimensionalisation

We nondimensionalise the microscale governing equation (Eq. 2.2.2) with the scalings

$$x = \hat{x}/\hat{h}, \quad t = \hat{f}_1\hat{t}, \quad V = \hat{V}/\hat{f}_1\hat{h}, \quad F = \hat{F}/\hat{\rho}\hat{h}\hat{\lambda}_b, \quad \rho = \hat{\rho}\hat{h}. \tag{2.2.4}$$

The dimensionless microscale governing equation is the advection–reaction equation

$$\frac{\partial b(x,t)}{\partial t} + V\frac{\partial b(x,t)}{\partial x} = k_b(x)(1 - b(x,t)) - k_u(x)b(x,t), \tag{2.2.5}$$

where the dimensionless rate functions (from Eqs. 2.1.2–2.1.3) are

$$k_b(x) = \begin{cases} 1 - |x| & 0 \leq |x| \leq 1 \\ 0 & \text{otherwise} \end{cases} \tag{2.2.6}$$

and

$$k_u(x) = \begin{cases} h_1 + h_2|x| & 0 \leq |x| \leq s \\ h_3 & \text{otherwise.} \end{cases} \tag{2.2.7}$$

The constants $h_i = \hat{g}_i/\hat{f}_1$ are ratios of the unbinding rates to the maximum binding rate, and $s = \hat{s}/\hat{h}$. We assume that all rate constants are positive and that the unbinding range ($\hat{s}$) is larger than the binding range ($\hat{h}$), giving $h_i > 0$ and $s > 1$. The dimensionless drag force generated by double-bound integrins is given by

$$F(t) = \int_{-\infty}^{\infty} xb(x,t)dx. \tag{2.2.8}$$

Additionally, we note that the total fraction of double-bound integrins is given by

$$B = \int_{-\infty}^{\infty} b(x,t)dx. \tag{2.2.9}$$

### 2.2.2 Analytical results from the microscale formulation

#### Steady state distribution with a zero relative velocity

At first we consider the case when the relative velocity $V = 0$. The distribution of double-bound integrins then varies according to

$$\frac{\partial b(x,t)}{\partial t} = k_b(x)(1 - b(x,t)) - k_u(x)b(x,t). \tag{2.2.10}$$

At steady state, denoted $b_s(x)$, we have the steady distribution

$$b_s(x) = \frac{k_b(x)}{k_b(x) + k_u(x)}. \tag{2.2.11}$$

With use of Eqs. 2.2.6 and 2.2.7 we obtain

$$b_s(x) = \begin{cases} \frac{1-|x|}{(1+h_1)-(1-h_2)|x|} & |x| \leq 1, \\ 0 & \text{otherwise.} \end{cases} \tag{2.2.12}$$

The steady distribution, plotted in Fig. 2.5, takes a maximum value of $1/(1+h_1)$ at $x = 0$ and decreases symmetrically to zero at the maximum binding range, $x = \pm 1$. This symmetry results in a zero net drag force generated by the integrins (see Eq. 2.2.8 and Fig. 2.5), consistent with a zero relative velocity, $V = 0$, between cell and ECM.

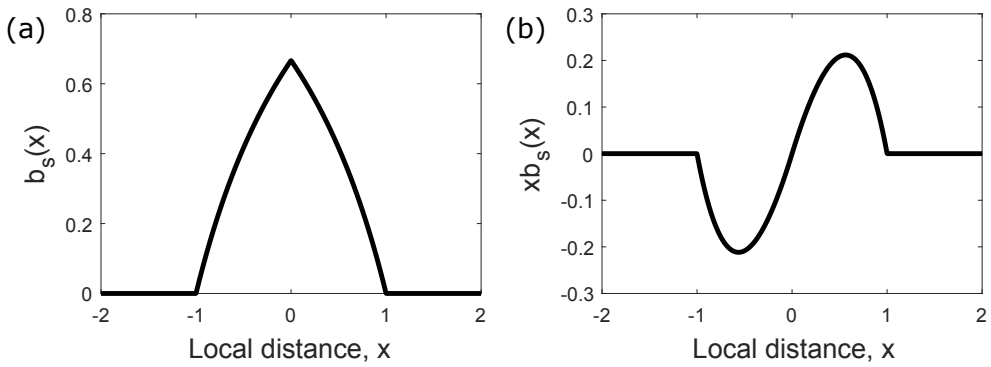


**Figure 2.5:** (a) The symmetric steady distribution $b_s(x)$ when $V = 0$. (b) The function $xb_s(x)$ is an odd function, meaning that the total drag force generated by integrins (see Eq. 2.2.8) will be zero.

**Steady state distribution with a constant relative velocity**

We now consider steady state solutions when $V$ is a positive constant. The piecewise linear binding and unbinding functions (Eqs. 2.2.6, 2.2.7) suggest consideration of Eq. 2.2.5 at steady state in each of the following six regions:

(i) $x < -s$, (ii) $-s \leq x < -1$, (iii) $-1 \leq x < 0$, (iv) $0 \leq x \leq 1$, (v) $1 < x \leq s$, (vi) $x > s$.

The resulting six ODEs for $b_s(x)$ are either separable (regions (i), (ii), (v), (vi)) or solved using integrating factors (regions (iii), (iv)) to give

$$\text{(i), (ii)} \qquad b_s(x) = 0, \tag{2.2.13a}$$

$$\text{(iii)} \qquad b_s(x) = \left(\frac{1-\gamma}{2V}\sqrt{\frac{\pi}{\beta}}\text{erfi}(\sqrt{\beta}(x+\gamma)) + A\right)e^{-\beta(x+\gamma)^2} + \frac{1}{2\beta V}, \tag{2.2.13b}$$

$$\text{(iv)} \qquad b_s(x) = \left(\frac{1-\gamma}{2V}\sqrt{\frac{\pi}{\beta}}\text{erf}(\sqrt{\beta}(x-\gamma)) + B\right)e^{\beta(x-\gamma)^2} + \frac{1}{2\beta V}, \tag{2.2.13c}$$

$$\text{(v)} \qquad b_s(x) = Ce^{-\frac{1}{V}\left(h_1 x + \frac{h_2}{2}x^2\right)}, \tag{2.2.13d}$$

$$\text{(vi)} \qquad b_s(x) = De^{-\frac{h_3}{V}x}, \tag{2.2.13e}$$

in the regions (i)–(vi) respectively. Here $\beta = \frac{(1-h_2)}{2V}$, $\gamma = \frac{1+h_1}{1-h_2}$, and the constants $A$–$D$, determined by continuity of $b_s(x)$ at each interface, are given by

$$A = \frac{\gamma-1}{2V}\sqrt{\frac{\pi}{\beta}}\text{erfi}(\sqrt{\beta}(\gamma-1)) - \frac{1}{2\beta V}e^{\beta(\gamma-1)^2}, \tag{2.2.14a}$$

$$B = \left(\frac{1-\gamma}{2V}\sqrt{\frac{\pi}{\beta}}\text{erfi}(\sqrt{\beta}\gamma) + A\right)e^{-2\beta\gamma^2} - \frac{1-\gamma}{2V}\sqrt{\frac{\pi}{\beta}}\text{erf}(-\sqrt{\beta}\gamma), \tag{2.2.14b}$$

$$C = \left(\left(\frac{1-\gamma}{2V}\sqrt{\frac{\pi}{\beta}}\text{erf}(\sqrt{\beta}(1-\gamma)) + B\right)e^{\beta(1-\gamma)^2} + \frac{1}{2\beta V}\right)e^{\frac{1}{V}\left(h_1+\frac{h_2}{2}\right)}, \tag{2.2.14c}$$

$$D = \left(\left(\frac{1-\gamma}{2V}\sqrt{\frac{\pi}{\beta}}\text{erf}(\sqrt{\beta}(1-\gamma)) + B\right)e^{\beta(1-\gamma)^2} + \frac{1}{2\beta V}\right)e^{\frac{h_3 s^2}{V^3}\left(h_1+\frac{h_2}{2}s\right)\left(h_1+\frac{h_2}{2}\right)}. \tag{2.2.14d}$$

In the above, erf and erfi are the error function and imaginary error function respectively, defined by

$$\text{erf}(z) = \frac{2}{\sqrt{\pi}}\int e^{-z^2}dz \quad \text{and} \quad \text{erfi}(z) = \frac{2}{\sqrt{\pi}}\int e^{z^2}dz. \tag{2.2.15}$$

Full steps for obtaining these solutions are provided in Appendix A.1. The steady state distributions corresponding to increasing relative velocities $V$ are shown in Fig. 2.6(a). The bound integrin distributions become increasingly skewed as $V$ increases, with a sharp decrease to zero occuring at $x = s$ due to the high (and discontinuous) unbinding rate there (Eq. 2.2.7). As $V$ increases, the position of the peak drag

force (Fig. 2.6(b)) is also shifted. The corresponding total drag forces generated at steady state are shown in Fig. 2.7, calculated from Eq. 2.2.8. For small velocities the drag force increases as the relative velocity increases, as the distributions begin to skew. As the relative velocity continues to increase there is a decrease in the total drag force, due to the reduced number of integrins that remain bound (seen by decreasing the height of the distributions in Fig. 2.6(a)). Note that the steady distributions (Eqs. 2.2.13, 2.2.14) are reflected symmetrically about $x = 0$ if $V < 0$.

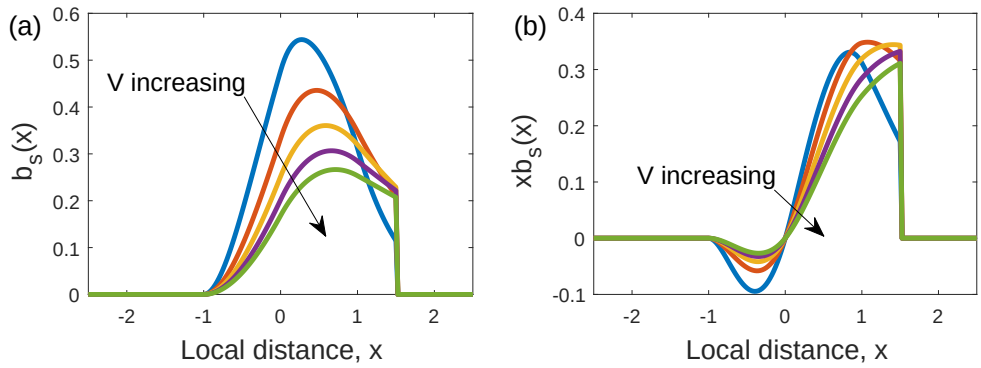


**Figure 2.6:** (a) Steady state distributions, $b_s(x)$, for increasing relative velocities $V = 0.5, 1, 1.5, 2, 2.5$. (b) Corresponding distributions of drag force; the total drag force generated by integrins is given by the area under this curve (see Eq. 2.2.8). The area increases between $V = 0.5$ and $V = 1$, before reducing for larger $V$ (see Fig. 2.7). Parameter values: $h_1 = 0.5$, $h_2 = 0.4$, $h_3 = 50$, $s = 1.5$ (in Eqs. 2.2.13, 2.2.14).

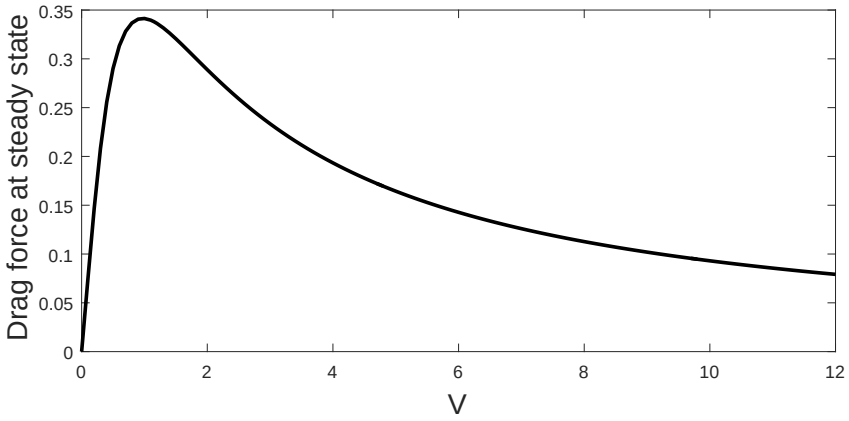


**Figure 2.7:** Total drag force, $F$ (see Eq. 2.2.8), generated by double-bound integrins at steady state as a function of the relative velocity $V$. Parameter values: $h_1 = 0.5$, $h_2 = 0.4$, $h_3 = 50$, $s = 1.5$ (in Eqs. 2.2.13, 2.2.14).

### Effect of varying the model parameters

We now consider the effect of varying the model parameters. We first vary the horizontal distance, $s$ (Eq. 2.2.7), at which the high unbinding of integrins occurs (Fig. 2.8). We see that by increasing $s$ the integrins remain bound at larger displacements, and will therefore generate a higher drag force. Next, we vary the rate, $h_3$, of the high unbinding in $x > s$ (Fig. 2.9). As $h_3$ increases, the survival rate of integrins in the region $x > s$ decreases, and the total drag force will decrease. From Eq. 2.2.13e, the fraction of bound integrins with displacements $x > s$ will approach zero as $h_3 \to \infty$.

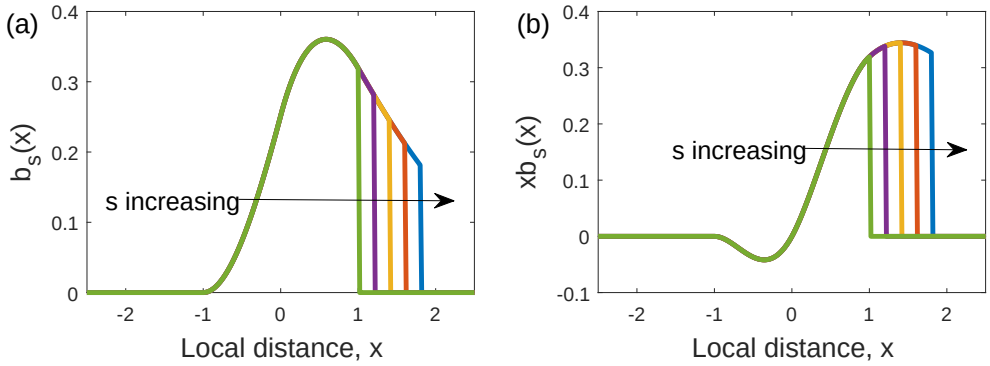


**Figure 2.8:** (a) Steady state distributions as the threshold for high unbinding, $s$ (Eq. 2.2.7), increases ($s = 1, 1.2, 1.4, 1.6, 1.8$). (b) By examining the area under this curve (see Eq. 2.2.8), an increase in $s$ leads to an increase in the total drag force generated by double-bound integrins. Parameter values: $h_1 = 0.5$, $h_2 = 0.4$, $h_3 = 50$, $V = 1.5$ (in Eqs. 2.2.13, 2.2.14).

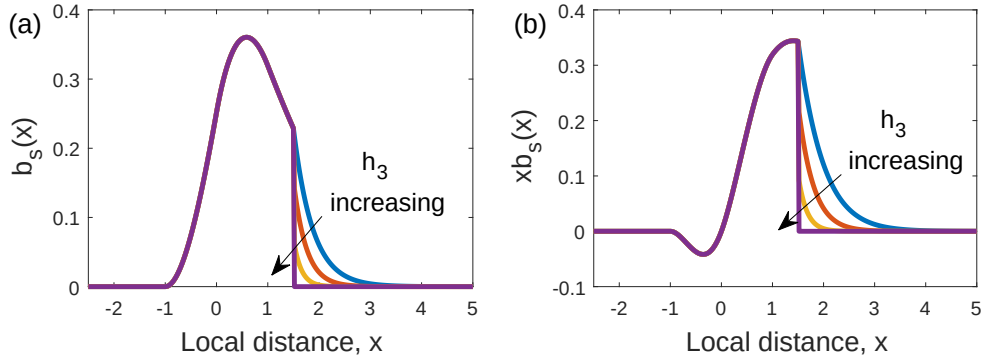


**Figure 2.9:** (a) Steady state distributions as the high unbinding rate, $h_3$ (Eq. 2.2.7), increases ($h_3 = 4, 6, 10, 50$). (b) By examining the area under this curve (see Eq. 2.2.8), an increase in $h_3$ leads to an reduction in the total drag force generated by double-bound integrins. Parameter values: $h_1 = 0.5$, $h_2 = 0.4$, $s = 1.5$, $V = 1.5$ (in Eqs. 2.2.13, 2.2.14).

**Time-dependent distributions for a zero relative velocity**

We now consider the time-dependent solution for the double-bound integrin distribution governed by Eq. 2.2.5. As in the previous section, we solve the governing equation separately in each of six regions of $x$, corresponding to the ranges of the piecewise linear binding and unbinding rates. We again begin by considering the case where the relative velocity $V$ is zero, which requires the solution of six first order linear PDEs, subject to the initial condition $b(x,0) = b_0(x)$. The general solutions are

$$b(x,t) = b_0(x)e^{-h_3 t}, \qquad x < -s, \tag{2.2.16a}$$

$$b(x,t) = b_0(x)e^{-(h_1-h_2 x)t}, \qquad -s \le x < -1, \tag{2.2.16b}$$

$$b(x,t) = \frac{(1+x)}{1+h_1+(1-h_2)x} + C(x)e^{-(1+h_1+(1-h_2)x)t}, \qquad -1 \le x < 0, \tag{2.2.16c}$$

$$b(x,t) = \frac{(1-x)}{1+h_1-(1-h_2)x} + D(x)e^{-(1+h_1-(1-h_2)x)t}, \qquad 0 \le x \le 1, \tag{2.2.16d}$$

$$b(x,t) = b_0(x)e^{-(h_1+h_2 x)t}, \qquad 1 < x \le s, \tag{2.2.16e}$$

$$b(x,t) = b_0(x)e^{-h_3 t}, \qquad x > s, \tag{2.2.16f}$$

where

$$C(x) = b_0(x) - \frac{(1+x)}{1+h_1+(1-h_2)x}, \tag{2.2.17a}$$

$$D(x) = b_0(x) - \frac{(1-x)}{1+h_1-(1-h_2)x}. \tag{2.2.17b}$$

The spatio-temporal evolution of the double-bound integrin distribution from a zero initial condition, $b_0(x) = 0$, is shown in Fig. 2.10. From this initial condition, there is binding of integrins to the ECM and, for all $|x| < 1$, we observe a monotonic increase in the fraction of bound integrins until the symmetric steady state distribution seen in Fig. 2.5 is reached. Due to the symmetry of $b_0(x,t)$ and of the rate functions (Eqs. 2.2.6, 2.2.7), the distributions are always symmetric about $x = 0$; the total drag force $F(t)$ (Eq. 2.2.8) is therefore zero throughout. If, instead, we start from a uniform non-zero initial condition, $b_0(x) = 0.25$ (Fig. 2.11), we see decay as well as growth to obtain the steady state distribution, due to unbinding of integrins from the ECM when $|x| > 1$. For $1 < |x| < s$ the rate of unbinding increases with $|x|$, and when $|x| > s$ the unbinding is extremely rapid. The distribution settles to the steady state distribution of Fig. 2.10, producing a zero total drag force due to symmetry. Additionally, we show that the total bound fraction, $B$ (Eq. 2.2.9) converges to the same steady value from both the zero (Fig. 2.10) and non-zero (Fig. 2.11) initial conditions (Fig. 2.12).

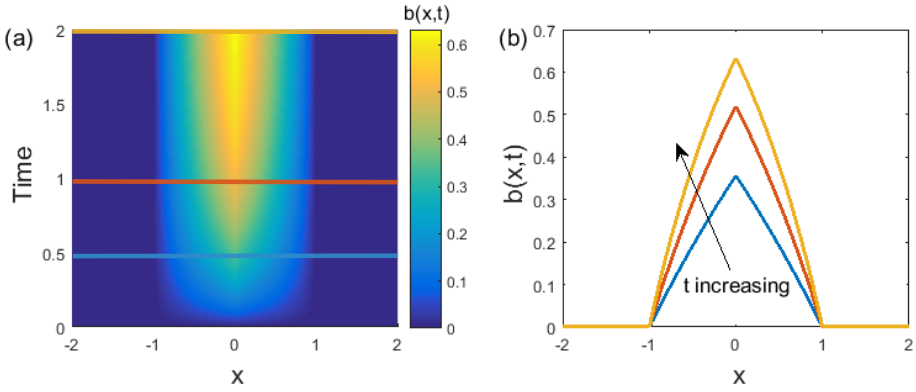


**Figure 2.10:** (a) Time-dependent evolution of the double-bound integrin distribution, $b(x,t)$, for $V = 0$, and $b_0(x,t) = 0$. (b) Sample distributions at $t = 0.5$, $t = 1$, and $t = 2$. By $t = 2$ the steady state distribution (Fig. 2.5 and Eq. 2.2.12) has been obtained. Parameter values: $V = 0$, $h_1 = 0.5$, $h_2 = 0.4$, $h_3 = 50$, $s = 1.5$ (in Eqs. 2.2.16, 2.2.17).

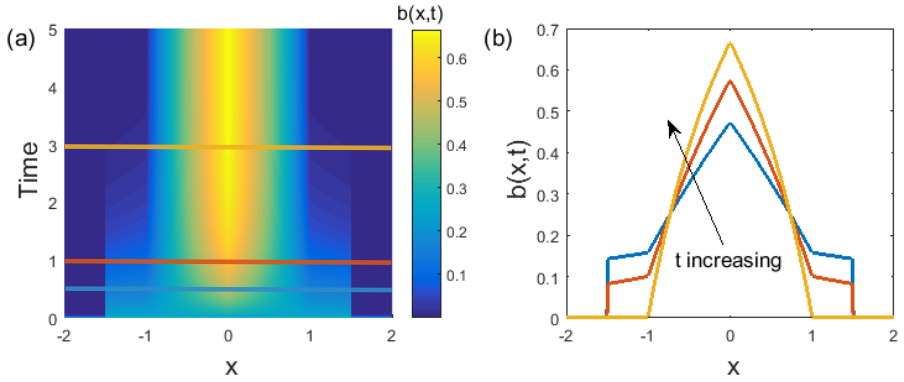


**Figure 2.11:** (a) Time-dependent evolution of the double-bound integrin distribution, $b(x,t)$, for $V = 0$, and $b_0(x,t) = 0.25$. (b) Sample distributions at $t = 0.5$, $t = 1$, and $t = 3$, which are converging to the steady state distribution, shown in Fig. 2.5 and Eq. 2.2.12. Parameter values: $V = 0$, $h_1 = 0.5$, $h_2 = 0.4$, $h_3 = 50$, $s = 1.5$ (in Eqs. 2.2.16, 2.2.17).

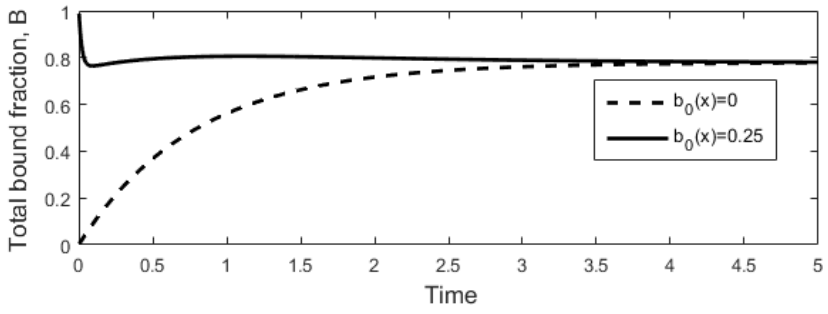


**Figure 2.12:** Timecourses for the bound fraction, $B$ (Eq. 2.2.9), for $b_0(x,t) = 0$ and $b_0(x,t) = 0.25$ (Figs. 2.10 and 2.11), converge to a steady value, associated with the steady state distribution (Eq. 2.2.12, shown in Fig. 2.5).

### Time-dependent distributions for non-zero relative velocities

In the case where $V$ is non-zero, time-dependent general solutions for Eq. 2.2.5 can, in some cases, be obtained by using the method of characteristics. For our chosen piecewise-linear reaction rates, it is possible to solve the PDEs in Eq. 2.2.5 for constant values of $V$ by partitioning the characteristic space into 21 regions (see Appendix A.2), which take into account the changing forms of $k_b(x)$ and $k_u(x)$ and the regions through which the solution has propagated. The solutions from each region must then be matched on the boundaries. Solutions can also be obtained for some choices of time-dependent $V(t)$, discussed in Appendix A.2, and for which a simpler example can be found in [8]. We provide the general solution of Eq. 2.2.5 for constant relative velocities in Appendix A.2, and show the result for $V = 1.5$ and a zero initial condition, $b_0(x) = 0$, in Fig. 2.13. We observe an increase in the distribution of double-bound integrins to an asymmetric steady state, which is consistent with the steady state distribution obtained in Fig. 2.6. The resulting drag force in time, calculated from Eq. 2.2.8, increases from zero to a maximum steady state (Fig. 2.14).

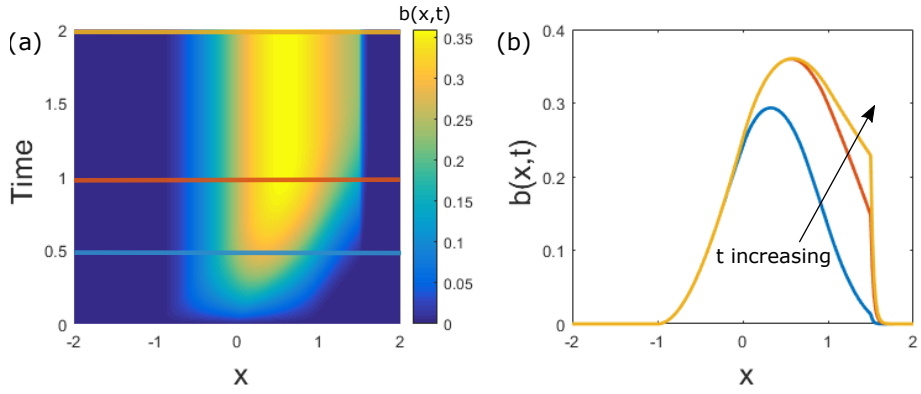


**Figure 2.13:** (a) Evolution of the double-bound integrin distribution, $b(x,t)$, for $V = 1.5$, starting from a zero initial distribution. (b) Sample distributions at $t = 0.5$, $t = 1$, and $t = 2$. By $t = 2$ the steady state distribution, shown in Fig. 2.6 with $V = 1.5$, has been obtained. Parameter values: $V = 1.5$, $h_1 = 0.5$, $h_2 = 0.4$, $h_3 = 50$, $s = 1.5$ (in Eqs. 2.2.5 and 2.2.7).

### Numerical simulation of the microscale advection–reaction equation

The microscale advection–reaction equation (Eq. 2.2.5) can also be evolved numerically by using an upwind finite difference scheme (described in Section 2.2.4). The evolution of the bound integrin distributions, calculated numerically, is shown in Fig. 2.15(a) for $V = 1.5$ and a zero initial condition for bound integrins. The numerical re-

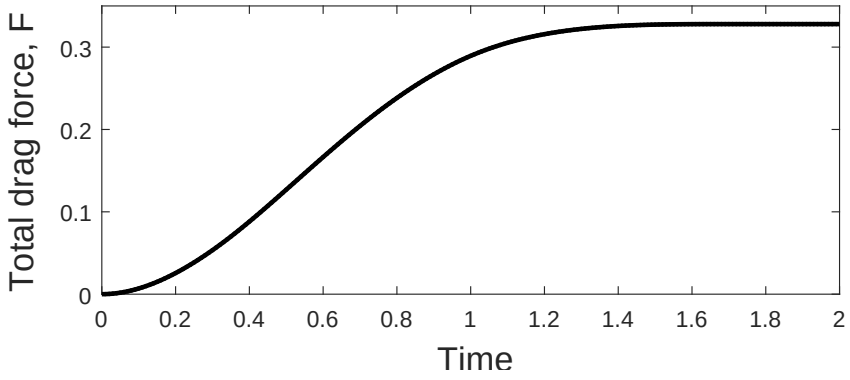


**Figure 2.14:** Total drag force, $F$ (Eq. 2.2.8), generated by the evolving distribution of double-bound integrins in Fig. 2.13. A relative velocity leads to asymmetric distributions and therefore a non-zero drag force. The steady value obtained corresponds to the steady state distribution shown in Fig. 2.6 with $V = 1.5$.

sult is in agreement with the analytical solution (Fig. 2.13(a)) and, since the two methods produce equivalent results, we use numerical simulations to solve Eq. 2.2.5 from this point onwards. Numerical simulation will easily accommodate time-dependent changes in $V$, whereas it is not always possible to obtain analytical solutions for $V(t)$. In the cases where it is possible, finding the solution via the method of characteristics (Appendix A.2) is a long process.

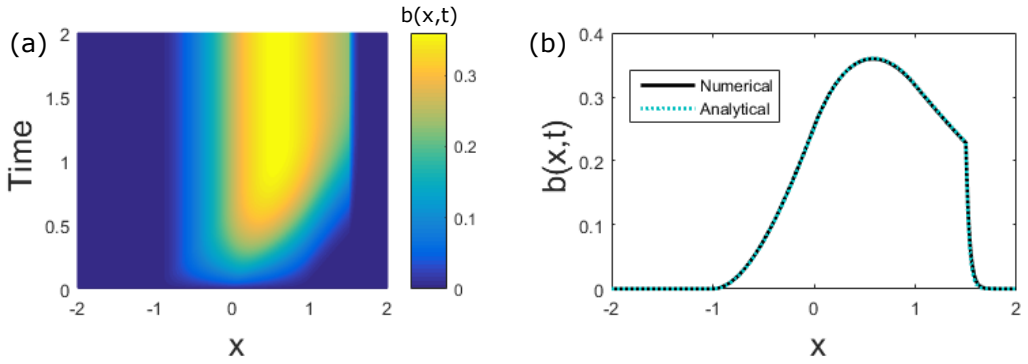


**Figure 2.15:** (a) The evolution of the double-bound integrin distribution obtained numerically for $V = 1.5$ is in agreement with the analytical solution in Fig. 2.13. (b) There is also agreement between the analytical and numerical solutions at steady state ($t = 2$). Parameter values: $V = 1.5$, $h_1 = 0.5$, $h_2 = 0.4$, $h_3 = 50$, $s = 1.5$ (in Eqs. 2.2.16a–2.2.17b).

### 2.2.3 Multiple ECM binding sites

In Section 2.2.1, we made an assumption that each actin-bound integrin had a single ECM binding site within its binding range. In the more general case there could be a discrete set of $N$ binding sites within range of each actin-bound integrin (Fig. 2.16), and in this case the model is altered slightly.

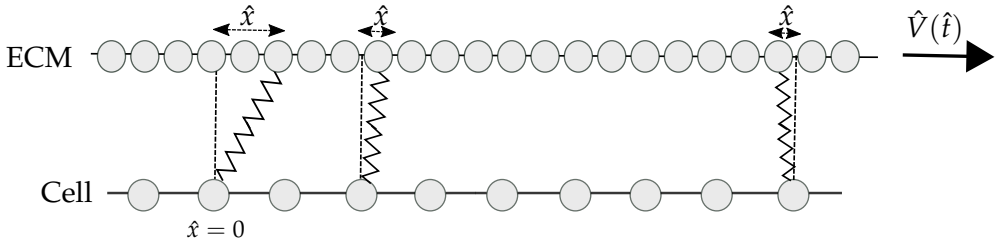


**Figure 2.16:** Sketch of the microscale formulation when there is more than one ECM binding site within range (determined by the binding function) of each actin-bound integrin. The microscale variable $\hat{x}$ is local to each integrin and again measures horizontal distances from the point of cytoskeletal attachment to the ECM binding sites. Cell and ECM layers have relative velocity $\hat{V}$.

The governing equation in Eq. 2.2.2 remains largely the same, except now the binding term must take into account the sum of all of the possible binding reactions. The governing equation becomes

$$\frac{\partial b}{\partial \hat{t}} + \hat{V}\frac{\partial b}{\partial \hat{x}} = \hat{k}_b(\hat{x})\left(1 - \sum_{i=-\infty}^{\infty} b(\hat{x} + i\hat{l}, \hat{t})\right) - \hat{k}_u(\hat{x})b(\hat{x}, \hat{t}), \tag{2.2.18}$$

where $\hat{l}$, assumed constant, is the spacing between ECM binding sites. Note that, although the sum is for $i \in (-\infty, \infty)$, there will only be $N$ non-zero terms; once $|\hat{x} + i\hat{l}|$ is larger than the integrin range, the values of $b$ are zero. If $\hat{l}$ is large relative to the binding range, so that there is only one binding site within range, then $b(\hat{x}, \hat{t})$ will be the only non-zero term in the sum and the single-site model in Section 2.2.1 (and Eq. 2.2.2) is recovered. In the other extreme, referred to as the Lacker–Peskin model [86], we assume that the ECM binding sites are abundant and continuously distributed across the domain, which is the limit as $\hat{l} \to 0$ (or $N \to \infty$). To arrive at the Lacker–Peskin model from the discrete binding site model, we first divide Eq. 2.2.18 by the binding site spacing, $\hat{l}$, to obtain

$$\frac{\partial (b/\hat{l})}{\partial \hat{t}} + \hat{V}\frac{\partial (b/\hat{l})}{\partial \hat{x}} = \frac{\hat{k}_b(\hat{x})}{\hat{l}}\left(1 - \hat{l}\sum_{i=-\infty}^{\infty} (b(\hat{x} + i\hat{l}, \hat{t})/\hat{l})\right) - \hat{k}_u(\hat{x})(b/\hat{l}). \tag{2.2.19}$$

For small $\hat{l}$, the sum in Eq. 2.2.19 is approximated by an integral to obtain the advection–reaction equation

$$\frac{\partial \hat{b}}{\partial \hat{t}} + \hat{V}\frac{\partial \hat{b}}{\partial \hat{x}} = \frac{\hat{k}_b(\hat{x})}{\hat{l}}\left(1 - \int_{-\infty}^{\infty} \hat{b}(\hat{x},\hat{t})d\hat{x}\right) - \hat{k}_u(\hat{x})\hat{b}(\hat{x},\hat{t}). \tag{2.2.20}$$

The distributions, $\hat{b}(\hat{x},\hat{t}) = b(\hat{x},\hat{t})/\hat{l}$, in the Lacker–Peskin model are therefore dimensional quantities (with dimension 1/length), from which the fraction of integrins bound with displacements in a range $[\hat{x}, \hat{x}+\Delta\hat{x}]$ at time $\hat{t}$ is calculated via the integral $\int_{\hat{x}}^{\hat{x}+\Delta\hat{x}} \hat{b}(\hat{x},\hat{t})d\hat{x}$. The total bound fraction of integrins is given by

$$B = \int_{-\infty}^{\infty} \hat{b}(\hat{x},\hat{t})d\hat{x}, \tag{2.2.21}$$

where, as in the single-site model (Eq. 2.2.9), $B \in [0,1]$. The extensions of the original Huxley model [70] to discrete and continuous binding sites are well-established and further discussions can be found in [80, 86, 131].

### 2.2.4 Coupling to a macroscale model of cell deformation

We now couple our microscale, integrin-level, description for bond formation and rupture (Eq. 2.2.20) to a macroscale model of cell and ECM deformation. We consider the cell and ECM to be linearly elastic materials, with deformations denoted by $\hat{U}_A(\hat{X},\hat{t})$ and $\hat{U}_E(\hat{X},\hat{t})$, respectively. Here, $\hat{X}$ is a macroscale spatial coordinate and $\hat{t}$ is time. At each point in $\hat{X}$, the deformation occurs as a result of the adhesive drag force, $\hat{F}(\hat{X},\hat{t})$, which is generated by integrins cycling between bound and unbound states at the microscale. An inherent assumption is that these two spatial scales are well-separated. Here we choose to use the multiple ECM binding sites model (Eq. 2.2.20) and the microscale advection–reaction equations are now parameterised by the macroscale coordinate $\hat{X}$; the multiscale coupling is illustrated in Fig. 2.17.

#### Macroscale governing equations

The macroscale velocity of the ECM relative to the cell membrane can be written as

$$\hat{V}(\hat{X},\hat{t}) = \frac{\partial \hat{U}_E(\hat{X},\hat{t})}{\partial \hat{t}} - \frac{\partial \hat{U}_A(\hat{X},\hat{t})}{\partial \hat{t}}, \tag{2.2.22}$$

which is coupled to the microscale distributions of bound integrins (see Fig. 2.17) via Eq. 2.2.20.

We assume that the drag forces, $\hat{F}(\hat{X},\hat{t})$, due to bound integrins are body forces acting

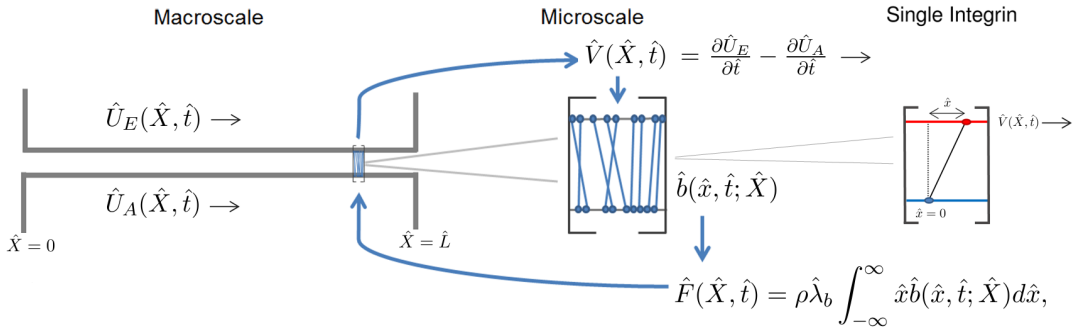


**Figure 2.17:** Schematic diagram of the multiscale coupling. A relative velocity $\hat{V}(\hat{X},\hat{t})$, arising from macroscale deformation, influences the binding dynamics and distribution of bonds, $\hat{b}(\hat{x},\hat{t};\hat{X})$, in a corresponding microscale problem (Eq. 2.2.20). The variable $\hat{x}$ is local to each integrin and measures the horizontal distance from the cytoskeletal attachment to the binding site on the ECM, as shown. Microscale distributions determine the horizontal drag force, $\hat{F}(\hat{X},\hat{t})$, which is used to update the displacements $\hat{U}_A$ and $\hat{U}_E$ and thereby $\hat{V}(\hat{X},\hat{t})$ (via Eqs. 2.2.22–2.2.23).

in equal and opposite directions on the two materials and, as in the discrete model (Algorithm 2.1.1), we assume that inertial effects are negligible. The macroscale governing equations are therefore the quasi-static equilibrium conditions

$$\frac{\partial^2 \hat{U}_A}{\partial \hat{X}^2} = -\frac{1}{\hat{K}_A}\hat{F}, \qquad \frac{\partial^2 \hat{U}_E}{\partial \hat{X}^2} = \frac{1}{\hat{K}_E}\hat{F}, \tag{2.2.23}$$

where the constants $\hat{K}_A$ and $\hat{K}_E$ are stiffness-like parameters for the cell layer and for the ECM respectively.

### Boundary Conditions

The cell displacement is assumed to be zero at $\hat{X} = 0$ and $\hat{X} = \hat{L}$ so that

$$\hat{U}_A(0,\hat{t}) = 0, \qquad \hat{U}_A(\hat{L},\hat{t}) = 0. \tag{2.2.24}$$

However, changes to these boundary conditions can easily be implemented in the numerical solution of the model (discussed in Section 2.2.5). For the ECM, we apply a time-dependent displacement at $\hat{X} = 0$ and zero strain at $\hat{X} = \hat{L}$

$$\hat{U}_E(0,\hat{t}) = \hat{f}(\hat{t}), \qquad \frac{\partial \hat{U}_E(\hat{L},\hat{t})}{\partial \hat{X}} = 0, \tag{2.2.25}$$

where $\hat{f}(\hat{t})$ is a function to be specified, as in the discrete model (Eq. 2.1.5). The zero strain condition allows for unconstrained movement of the ECM at $\hat{X} = \hat{L}$; alternative

choices, such as fixed Dirichlet conditions for $\hat{U}_E(\hat{L},\hat{t})$, are not shown here but are easily implemented.

**Nondimensionalisation**

The governing equations and boundary conditions are nondimensionalised with the scalings

$$\begin{aligned} &x = \hat{x}/\hat{h}, \quad t = \hat{f}_1\hat{t}, \quad U_A = \hat{U}_A/\hat{L}, \quad U_E = \hat{U}_E/\hat{L}, \\ &b = \hat{b}\hat{h}, \quad X = \hat{X}/\hat{L}, \quad V = \hat{V}/\hat{f}_1\hat{L}, \quad F = \hat{F}/\hat{\rho}\hat{h}\hat{\lambda}_b, \end{aligned} \tag{2.2.26}$$

where $\hat{f}_1$ is the maximum binding rate and $\hat{h}$ is the integrin binding range. For simplicity we assume that $\hat{\rho}$ is uniform, but an extension to a non-uniform (but constant) $\hat{\rho}(\hat{X})$ is easily incorporated. The dimensionless microscale governing equations are

$$\frac{\partial b}{\partial t} + \frac{V}{\delta}\frac{\partial b}{\partial x} = \eta k_b(x)\left(1 - \int_{-\infty}^{\infty} b(x,t;X)dx\right) - k_u(x)b(x,t;X), \tag{2.2.27}$$

where the dimensionless parameters $\delta = \hat{h}/\hat{L}$ and $\eta = \hat{h}/\hat{l}$ are the ratios of the integrin binding range to the macroscale length scale and to the microscale binding site separation, respectively. The microscale advection–reaction equations are coupled to the macroscale equations via the macroscale velocity $V(X,t)$.

The dimensionless binding rate functions are

$$k_b(x) = \begin{cases} 1 - |x| & |x| \leq 1, \\ 0 & \text{otherwise}, \end{cases} \tag{2.2.28}$$

and

$$k_u(x) = \begin{cases} h_1 + h_2|x| & |x| \leq s, \\ h_3 & \text{otherwise}, \end{cases} \tag{2.2.29}$$

where $h_i = \hat{g}_i/\hat{f}_1$ are the ratios of unbinding rates to the maximum binding rate, and $s = \hat{s}/\hat{h}$. The dimensionless drag force

$$F(X,t) = \int_{-\infty}^{\infty} xb(x,t;X)dx, \tag{2.2.30}$$

features at the macroscale, where the dimensionless governing equations become

$$\frac{\partial^2 U_A}{\partial X^2} = -\frac{1}{K_A}F, \qquad \frac{\partial^2 U_E}{\partial X^2} = \frac{1}{K_E}F, \tag{2.2.31}$$

where

$$K_A = \hat{K}_A/\hat{\rho}\hat{h}\hat{\lambda}_b\hat{L} \quad \text{and} \quad K_E = \hat{K}_E/\hat{\rho}\hat{h}\hat{\lambda}_b\hat{L}. \tag{2.2.32}$$

The dimensionless boundary conditions for the cell and ECM are

$$\begin{aligned} &\text{(i)} \;\; U_A(0,t) = 0, && U_A(1,t) = 0, \\ &\text{(ii)} \;\; U_E(0,t) = f(t), && \tfrac{\partial U_E(1,t)}{\partial X} = 0, \end{aligned} \tag{2.2.33}$$

respectively, for a time-dependent displacement condition, $f(t)$, to be specified.

**Implementation**

To solve the advection–reaction system (Eq. 2.2.27), we differentiate the macroscale governing equations (Eq. 2.2.31) with respect to time and use Eq. 2.2.22 to obtain

$$\frac{\partial^2 V}{\partial X^2} = \left(\frac{1}{K_E} + \frac{1}{K_A}\right)\frac{\partial F}{\partial t}. \tag{2.2.34}$$

From the definition of $F(X,t)$ (Eq. 2.2.30),

$$\frac{\partial F}{\partial t} = \int_{-\infty}^{\infty} x\frac{\partial b}{\partial t}dx, \tag{2.2.35}$$

and by substituting this into Eq. 2.2.34, using Eq. 2.2.27 and integrating the resulting expression by parts, we arrive at the following second order PDE for $V(X,t)$

$$\frac{\partial^2 V}{\partial X^2} = \gamma H + \frac{\gamma}{\delta}VB, \tag{2.2.36}$$

where

$$H = \int_{-\infty}^{\infty} x f(b)\, dx, \;\; B = \int_{-\infty}^{\infty} b\, dx, \;\; \gamma = \left(\tfrac{1}{K_E} + \tfrac{1}{K_A}\right), \tag{2.2.37}$$

and

$$f(b) = \eta k_b(x)\,(1-B) - k_u(x)b. \tag{2.2.38}$$

To arrive at this final form, we must also note that $xb \to 0$ as $x \to \pm\infty$. The coupled system of equations (Eqs. 2.2.27 and 2.2.36) are solved numerically, as detailed in Section 2.2.5, below, subject to

$$V(0,t) = f'(t), \qquad \frac{\partial V}{\partial X}(1,t) = 0, \tag{2.2.39}$$

which are consistent with Eq. 2.2.33.

By integrating the macroscale governing equations (Eq. 2.2.31) twice and using the

boundary conditions in Eq. 2.2.33, we obtain the cell and ECM deformation, $U_A(X,t)$ and $U_E(X,t)$, respectively in terms of $F(X,t)$, given by

$$U_A = -\frac{1}{K_A}\int_0^X \int_0^\zeta F d\xi d\zeta + \frac{X}{K_A}\int_0^1 \int_0^\zeta F d\xi d\zeta, \tag{2.2.40}$$

and

$$U_E = \frac{1}{K_E}\int_0^X \int_0^\zeta F d\xi d\zeta - \frac{X}{K_E}\int_0^1 F d\xi + f(t). \tag{2.2.41}$$

### 2.2.5 Numerical solution of the continuum model

In this section we describe the numerical solution of the multiscale continuum model, which comprises a microscale advection–reaction system (Eq. 2.2.27) coupled to a second order macroscale PDE (Eq. 2.2.36).

The macroscale PDE is solved using a finite difference scheme, subject to the boundary conditions in Eq. 2.2.39. We discretise the macroscale domain, $X \in [0,1]$, into $N$ points with an equal spacing of $\Delta X = 1/(N-1)$. Macroscale variables $V$, $H$, and $B$ (defined in Eqs. 2.2.22, 2.2.37) are spatially discretised into the vectors $\boldsymbol{v} = (V_1, V_2, ..., V_N)^T$, $\boldsymbol{h} = (H_1, H_2, ..., H_N)^T$, and $\boldsymbol{b} = (B_1, B_2, ..., B_N)^T$, respectively, where the built-in MATLAB function `trapz` is used to calculate the elements of $\boldsymbol{h}$ and $\boldsymbol{b}$ from microscale distributions (see Eq. 2.2.37). Using a second order central difference, we approximate the macroscale spatial derivative in Eq. 2.2.36 by

$$\frac{\partial^2 V_i}{\partial X^2} = \frac{V_{i+1} - 2V_i + V_{i-1}}{\Delta X^2} \tag{2.2.42}$$

and solve for $\boldsymbol{v}$ through a matrix equation of the form

$$\boldsymbol{v} = \boldsymbol{A}^{-1}\boldsymbol{p}, \tag{2.2.43}$$

where the vector $\boldsymbol{p}$ is given by

$$\boldsymbol{p} = \left(f'(t), \gamma H_2, ..., \gamma H_N\right)^T, \tag{2.2.44}$$

and where the matrix $\boldsymbol{A}$ is

$$\boldsymbol{A} = \begin{pmatrix} 1 & 0 & 0 & 0 & 0 & \dots & 0 \\ \frac{1}{\Delta X^2} & D_2 & \frac{1}{\Delta X^2} & 0 & 0 & \dots & 0 \\ 0 & \frac{1}{\Delta X^2} & D_3 & \frac{1}{\Delta X^2} & 0 & \dots & 0 \\ \vdots & \ddots & \ddots & \ddots & \ddots & \ddots & \vdots \\ 0 & \dots & 0 & \frac{1}{\Delta X^2} & D_{N-2} & \frac{1}{\Delta X^2} & 0 \\ 0 & \dots & 0 & 0 & \frac{1}{\Delta X^2} & D_{N-1} & \frac{1}{\Delta X^2} \\ 0 & \dots & 0 & 0 & 0 & \frac{2}{\Delta X^2} & D_N \end{pmatrix}. \tag{2.2.45}$$

The diagonal elements, $D_2, ..., D_N$, are given by $D_i = -\frac{2}{\Delta X^2} - \frac{\gamma}{\delta} B_i$, for $i \in \{2, ..., N\}$, where $B_i$ are elements of the discretised bound fraction vector, $\boldsymbol{b}$, as defined above. The first and last rows of $\boldsymbol{A}$ enforce the Dirichlet and zero strain boundary conditions for $V_1$ and $V_N$ (Eq. 2.2.39) respectively.

Eq. 2.2.43 is solved alongside the microscale advection–reaction system (Eq. 2.2.27), for which we evolve spatially discretised microscale distributions, $b(x, t; X)$, using the method of lines [122] and the built-in MATLAB function `ode15s`. Since Eq. 2.2.27 is hyperbolic, the choice of finite difference approximation for the spatial derivative, $\frac{\partial b}{\partial x}$, must be chosen adaptively at each timestep depending on the sign of $V(X)$. This is known as an upwind scheme [122], and is necessary due to propogation of the solutions as a wave. Information must therefore be taken from the 'upwind' side of the wave, and here we use the first order scheme

$$\frac{\partial b_i}{\partial x} = \begin{cases} (b_i - b_{i-1})/\Delta x, & V(X) > 0, \\ (b_{i+1} - b_i)/\Delta x, & V(X) < 0, \end{cases} \tag{2.2.46}$$

where a backward difference is taken if $V(X)$ is positive and a forward difference is taken if $V(X)$ is negative.

To allow for more efficient computation, we discretise the microscale spatial domain with a variable step size. A finer mesh (with step size $\Delta x_1$) is required in $|x| \leq s$ (see Eq. 2.2.7), whereas a step size of $\Delta x_2 = \lambda \Delta x_1$, where $\lambda > 1$, is used for $|x| > s$. Microscale distributions are evolved at each of the $N$ (macroscale) discretised points, and distributions are coupled through the solution of $v$. The computational cost is therefore dependent on the choice of $N$, $\Delta x_1$ and $\lambda$. In the simulations in Chapter 3, we use $N = 31$, $\Delta x_1 = 0.025$ and $\lambda = 10$. To arrive at these choices, we considered fixed reductions in mesh sizes and measured the Euclidean norm between successive solution vectors. Solutions began to converge, detected by a point where this measure started to decrease monotonically toward zero. From here, discretisations were chosen by selecting values where further reductions in mesh spacing produced negligible differences in the solution vectors. In general, this requires a decision to be made based on the trade-off between numerical error and efficiency.

## 2.3 Summary

In this chapter we introduced a discrete stochastic-elastic model (Section 2.1) and a multiscale continuum model (Section 2.2) of cell–matrix adhesion. The discrete model consists of an evolving network of linear springs, with stochastic reactions governing binding and unbinding of integrins from the ECM. The individual-based nature of the discrete model supports local spatial constraints on the integrin binding reactions; additionally, the local mechanical response to the bound integrins is accounted for. The stochastic simulation algorithm for this model is given in Algorithm 2.1.1. Since large-scale discrete simulations are computationally intensive, we additionally developed a novel multiscale continuum model that allows for similar consideration of local spatial constraints in the integrin binding reactions. To achieve this we used a two-scale approach, considering firstly a microscale model of the integrin binding dynamics (Section 2.2.1). The microscale model is an adaptation of the Huxley cross-bridge model [70], and we discussed the model derivation alongside some analytical and numerical results. In Section 2.2.4, we then coupled the microscale formulation to a macroscale description of cell and ECM deformation and presented the governing equations, nondimensionalisation and numerical scheme required to solve the fully coupled system. Numerical results from both the discrete and multiscale continuum models will now be shown in Chapter 3.

# Chapter 3

# Effect of oscillatory loading on cell–matrix adhesion

As a result of tidal breathing, ASM cells and the extracellular matrix are subjected to regular mechanical fluctuations. Since it is well established that integrins are responsive to mechanical and environmental cues (Section 1.2), an important consideration is how the dynamic environment of an airway *in vivo* affects adhesion strength and dynamics. We expect the resulting integrin dynamics to influence the level of contractile force transmission attainable between ASM cells and the ECM during bronchoconstriction, and hence to regulate the extent of airway narrowing.

In this chapter we use both the discrete (Section 2.1) and continuum models (Section 2.2) to investigate integrin binding and adhesion dynamics in response to an oscillatory loading of the ECM, representing tidal breathing. Firstly we consider the discrete stochastic-elastic model and investigate how tidal breathing could influence the formation and survival of adhesions. We then replicate these simulations with the multiscale continuum model, which couples microscale binding reactions to the macroscale mechanical environment. We find good qualitative agreement between the continuum model and the stochastic simulations; with the more tractable continuum model we investigate the importance of parameters of relevance to asthmatic and non-asthmatic airways. These include material stiffnesses, oscillation frequency and binding affinities. We also consider the effect of varying the waveform of the oscillation and the ratio between inhalation and exhalation times. Motivated by experimental observations about the possible bronchodilatory effect of taking deep inspirations (DIs), we then investigate the effect of perturbations to the amplitude of

oscillatory loading, representing DIs. The majority of the results in this chapter have been published in Irons *et al.* [72].

## 3.1 Varying the amplitude of oscillation

### Boundary conditions

In order to represent fluctuations that occur due to tidal breathing, we impose an external, oscillatory, loading to the ECM. In the discrete model this is imposed through Eq. 2.1.5, where the chosen time-dependent displacement of the ECM boundary node follows

$$\hat{U}_{E_1}(\hat{t}) = \hat{A}\sin(\hat{\omega}\hat{t}), \tag{3.1.1}$$

for amplitude $\hat{A}$, frequency $\frac{\hat{\omega}}{2\pi}$, and where $\hat{U}_{E_i}$ denotes the displacement of the $i$th ECM node from its rest position (see Fig. 2.2).

In the continuum model, we apply the same time-dependent displacement to the ECM at $\hat{X} = 0$ and zero strain at $\hat{X} = \hat{L}$. The boundary conditions are therefore

$$\hat{U}_E(0,\hat{t}) = \hat{A}\sin(\hat{\omega}\hat{t}) \quad \text{and} \quad \frac{\partial \hat{U}_E(\hat{L},\hat{t})}{\partial \hat{X}} = 0, \tag{3.1.2}$$

or in dimensionless form

$$U_E(0,t) = A\sin(\omega t) \quad \text{and} \quad \frac{\partial U_E(1,t)}{\partial X} = 0, \tag{3.1.3}$$

where the scalings in Eq 2.2.26, along with $A = \hat{A}/\hat{L}$ and $\omega = \hat{\omega}/\hat{f}_1$, have been used.

In both models the cell membrane is constrained at $\hat{X} = 0$ and $\hat{X} = \hat{L}$, as described in Section 2.2.4, by using zero-displacement Dirichlet conditions (Eq. 2.2.24).

### Initial conditions

In the simulations that follow we will consider two initial conditions: (i) a zero state with no pre-existing bound integrins, and (ii) a saturated high steady state of bound integrins, obtained in the absence of external forcing. In the discrete model, this saturated state is found by running the simulation with $A = 0$ until the fraction of bound integrins reaches an approximate steady state; in the continuum model the steady

state is obtained by solving Eq. 2.2.27 with $V = 0$, and is given by

$$b_s(x,0) = \frac{\eta k_b(x)}{k_u(x)} \left( \frac{1}{1 + \int_{-\infty}^{\infty} \frac{\eta k_b(x)}{k_u(x)} dx} \right). \tag{3.1.4}$$

### Numerical results

We first investigate the effect of varying the amplitude, $A$ (Eq. 3.1.3), of the oscillatory loading in both the discrete and continuum models. We show representative time courses from both models (Fig. 3.1) for the fraction of integrins that become double-bound under low, intermediate and high amplitude oscillatory loading. In the continuum model the total macroscale bound fraction is found from

$$B_{tot}(t) = \int_0^1 B(X,t) dX, \tag{3.1.5}$$

where $B(X,t)$ is given by Eq. 2.2.37.

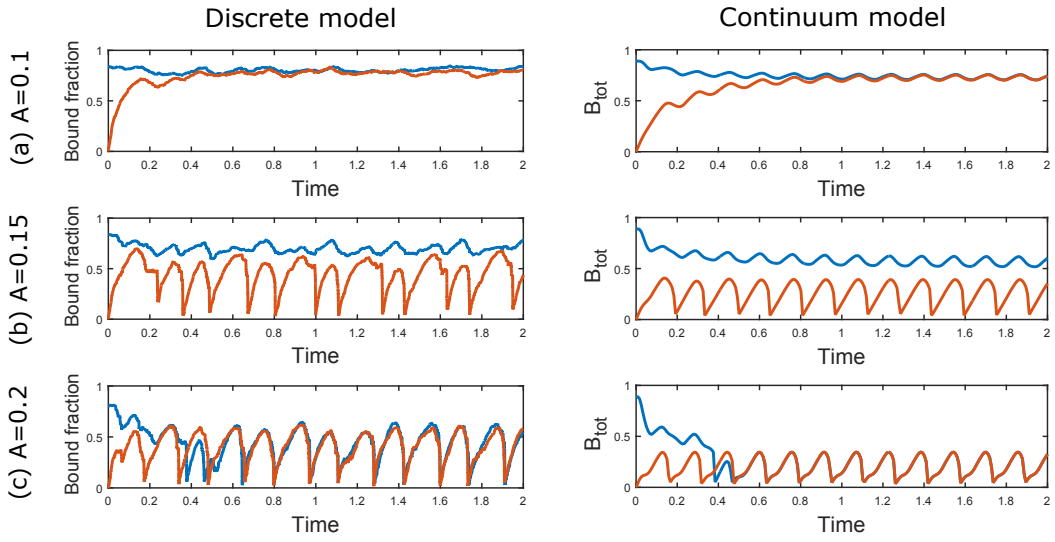


**Figure 3.1:** Representative time courses from the discrete stochastic simulation (Section 2.1) and continuum model (Section 2.2), shown in the left and right columns respectively, illustrating the responses of bound integrins (Eq. 3.1.5) to (a) low, (b) intermediate and (c) high amplitude oscillatory loading. Parameter values in Eqs. 3.1.1 or 3.1.3 are $\omega = 20$ and the amplitudes $A = 0.1$, $A = 0.15$, and $A = 0.2$ respectively. In each case we consider zero (orange) and saturated (blue) initial conditions (Eq. 3.1.4). A full list of parameter values is given in Appendix B.

For the lowest amplitude oscillation, in both models (Fig. 3.1(a)), we find that both the zero and saturated initial conditions converge to a pattern of high adhesion subject to

small fluctuations as a result of a low, sustainable, turnover of bound integrins. For the highest amplitude loading (Fig. 3.1(c)), in both models and for both the zero and saturated initial conditions, the result is a lower oscillatory state for the total bound integrin fraction, in which significant bond rupture leads to a lower mean (approximately 0.2–0.3) and larger amplitude fluctuations. For an intermediate oscillation amplitude (Fig. 3.1(b)) we observe bistability, occuring due to mechanical cooperativity, where the initial condition determines which of these two adhesion states occur; if adhesions are present when oscillations begin, then shared loading and increased traction prevent high levels of rupture under applied strain. Due to the stochastic nature of the discrete model, under high amplitude oscillations we sometimes observe small variations in the time of collapse from the high to the low state (not shown). Similarly, it is possible to observe stochastic switching (as shown in Fig. 3.2) between the two adhesion states when bistable behaviour is present.

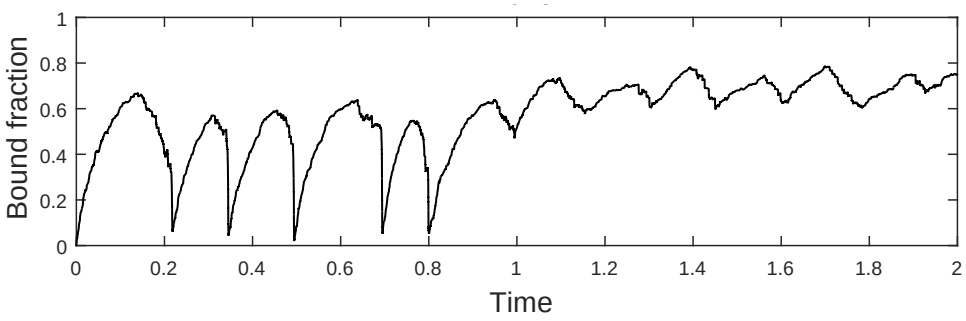


**Figure 3.2:** Example timecourse from the discrete stochastic simulation (Section 2.1) where stochastic switching from low to high adhesion states is observed. The amplitude of oscillatory loading (Eq. 3.1.1) is $A = 0.15$, which exhibits bistable behaviour (Fig. 3.1). A full list of parameter values is given in Appendix B.

In each adhesion state, the different underlying behaviours of the bound integrins can be seen by sampling microscale distributions from the continuum model. We sample distributions across the macroscale domain for $A = 0.1$ and $A = 0.15$ from a zero initial condition (Fig. 3.3). When $A = 0.1$ a high adhesion state occurs and the integrins mostly remain bound with a low turnover. This is seen at $X = 0.5$ and $X = 1$ (Fig. 3.3) where the bound fraction stays high but the local displacements, $x$, of the bound integrins follow the applied oscillatory ECM displacement. At $X = 1$, the bound fraction is highest and the amplitude of the oscillations decrease due to an increased drag force. Since the oscillatory loading is applied at $X = 0$ (Eq. 3.1.3), the disturbance is higher and here the integrins are seen to rupture and rebind at each

cycle. In the low adhesion state ($A = 0.15$), this cyclic rupture and rebinding occurs across the whole domain. However, a similar damping of the oscillatory loading is still seen, shown by the increasing peak value and reduced width of $b(x,t;X)$ as $X$ increases. The damping will be affected by material stiffnesses; the effect of varying these (via $\gamma$, Eq. 2.2.37) on the bound integrin fraction is shown later.

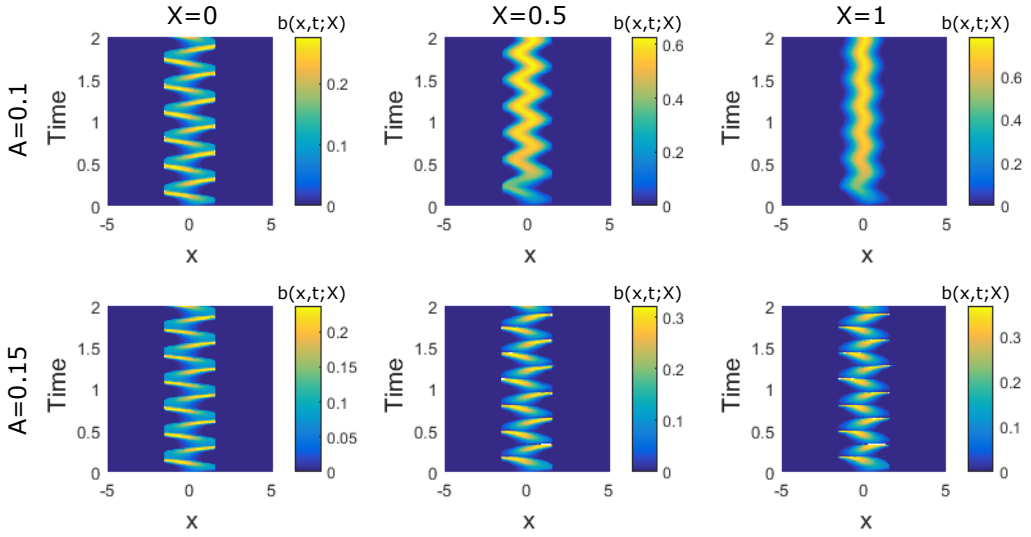


**Figure 3.3:** Microscale bound integrin distributions, $b(x,t;X)$, sampled at $X = 0$, $X = 0.5$ and $X = 1$ for $A = 0.1$ and $A = 0.15$ from a zero initial condition. These distributions show the underlying bound integrin behaviour corresponding to the high and low oscillatory adhesion states in Fig. 3.1(a) and (b). Due to damping, the peak value of $b(x,t;X)$ increases as $X$ increases; note the different scales on the colorbars.

As illustrated by the timecourses in Fig. 3.1, the discrete and continuum models display qualitatively similar behaviour, and we therefore exploit the deterministic nature of the continuum model to comprehensively investigate the bistability. We present the bound integrin densities obtained for a full range of oscillation amplitudes (Fig. 3.4), again using both the zero and saturated initial conditions. Since the states under consideration are oscillatory, once the behaviour has converged to its periodic steady state, we plot the time-averaged adhesion density given by

$$\langle B(X)\rangle = \frac{1}{T}\int^{T} B(X,t)dt, \tag{3.1.6}$$

where $T = 2\pi/\omega$ is the oscillation period. As shown by the microscale distributions in Fig. 3.3, there is variation in $\langle B(X)\rangle$ across the macroscale domain, $X \in [0,1]$, and we observe a significantly lower adhesion density near $X = 0$ where the oscillation is applied.

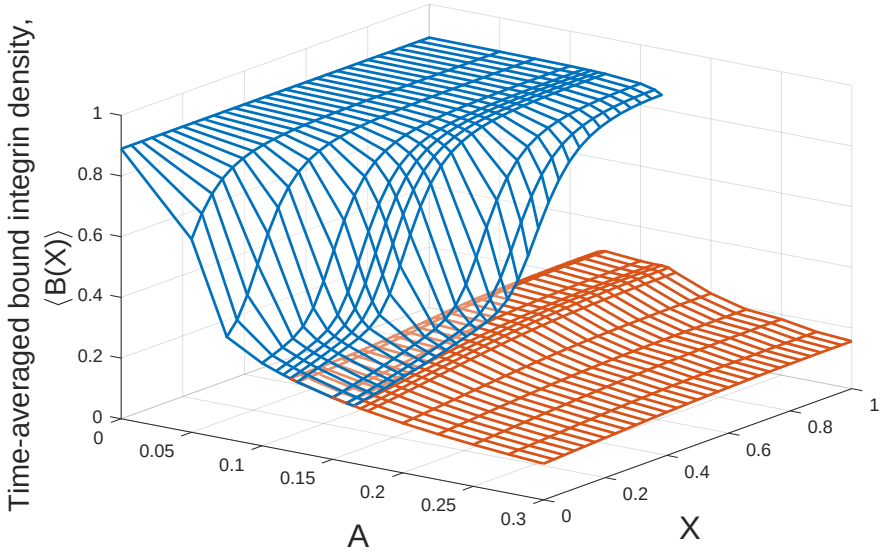


**Figure 3.4:** High (blue) and low (orange) solution surfaces across the macroscale domain, $X$, indicating stable states of the time-averaged adhesion density $\langle B(X)\rangle$ (Eq. 3.1.6) for a range of oscillation amplitudes, $A$ (Eq. 3.1.3). Solutions were obtained by considering zero (orange) and saturated (blue) initial conditions (Eq. 3.1.4) in the continuum model. For intermediate amplitudes there is bistability. Parameters are as in Fig. 3.1 and Table S1.

The time-averaged adhesion density plotted in Fig. 3.4, $\langle B(X)\rangle$, is additionally averaged over $X$ to calculate the total time-averaged density $\langle B_{tot}\rangle$ (Eq. 3.1.5), which is used to generate a bifurcation diagram in Fig. 3.5. Stable branches, indicated by the solid lines, confirm, as in Fig. 3.4, that for low amplitude oscillations we expect solutions to converge to a high averaged bound integrin state regardless of initial conditions, while for high amplitude oscillations the solutions converge to a low bound integrin state. For an intermediate range of oscillation amplitudes we observe a window of bistability where the initial condition, in relation to an unstable branch (dashed line), determines which of the two stable outcomes occurs. The position of the unstable branch is estimated as the mean of two points that are observed to converge to the upper and lower solutions (green and red markers, respectively). The unstable and stable branches appear to meet in a pair of saddle node bifurcations. As marked in Fig. 3.5, when starting on the upper stable branch, an increase in $A$ would lead to a jump from the upper to the lower stable solution at the bifurcation point. The value of $A$ at this point corresponds to a threshold loading at which adhesions quickly rupture. On the other hand a decrease in $A$ from the lower branch leads to a jump from the lower to upper branch at a different amplitude, following a different path, thereby generating a hysteresis loop (blue dotted line).

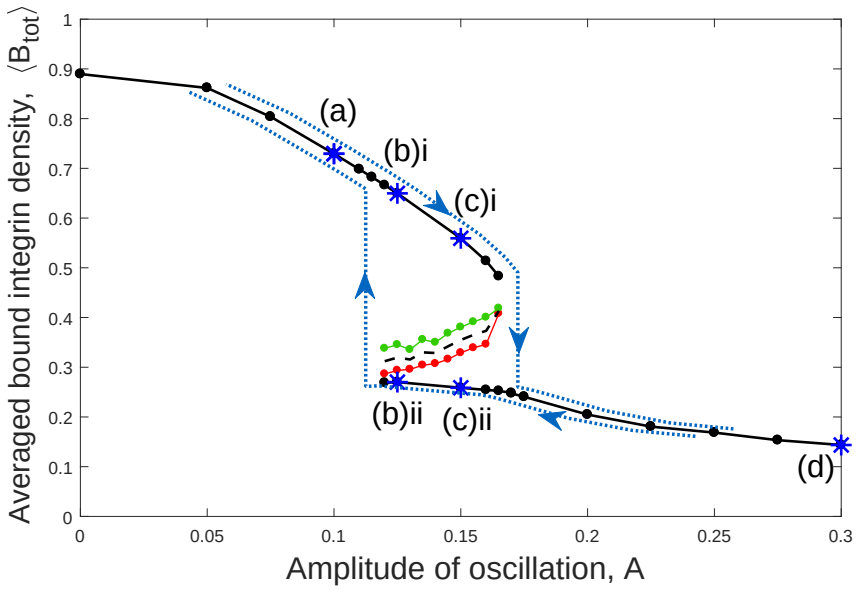


**Figure 3.5:** Bifurcation diagram indicating steady states of the time-averaged total adhesion density $\langle B_{tot} \rangle$ (Eqs. 3.1.5, 3.1.6) for a range of oscillation amplitudes, $A$ (Eq. 3.1.3). Stable branches are indicated by solid lines separated by the dashed, unstable branch. The position of the unstable branch is bounded by points known to converge to the upper and lower solutions, in green and red respectively. Blue markers highlight example monostable ((a) $A = 0.1$, (d) $A = 0.3$) and bistable ((b) $A = 0.125$, (c) $A = 0.15$) regimes, and a hysteresis loop is seen (blue dotted line). The path taken as $A$ increases ((a)→(b)i →(c)i→(d)) differs to the path followed as $A$ decreases ((d)→(c)ii →(b)ii→(a)).

In addition to considering the bound integrin densities, we examine the spatio-temporal cell deformation resulting from oscillatory loading. We show this for both the discrete and continuum models in each stable regime (Fig. 3.6). In the high bound integrin regime (i.e. low amplitude oscillations), adhesions persist and in both models there are smooth transitions between positive and negative cell deformations across the domain (Figs. 3.6(a), (c)). These appear as wide bands that follow the movement of the ECM. In the low bound integrin regime (high amplitude oscillations), the bands narrow and exhibit sharp boundaries due to greater numbers of rupture events at each cycle (Figs. 3.6(b), (d)).

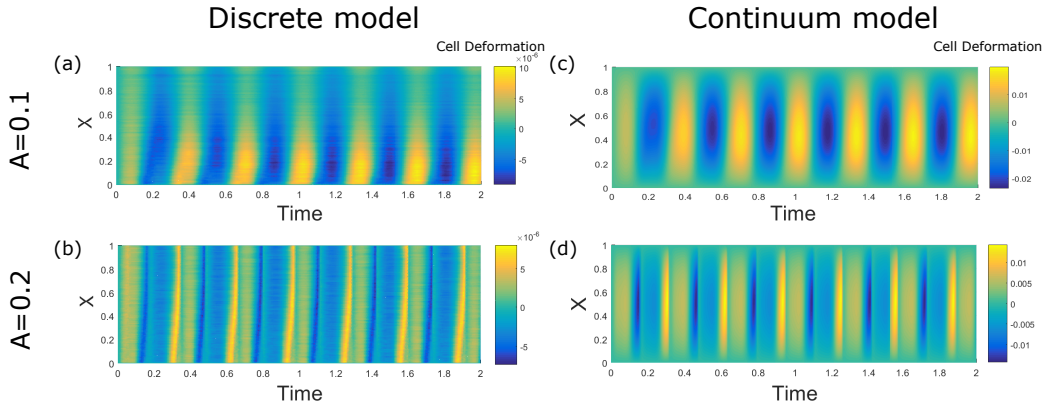


**Figure 3.6:** Cell deformation, $U_A(X,t)$, (indicated by colour) plotted as functions of the position in the cell domain, $X$, and time, $t$, obtained in the discrete (a,b) and continuum (c,d) models in the cases where adhesion formation (a,c) and adhesion rupture (b,d) dominate under oscillatory loading. Simulations are carried out from a zero initial condition, and oscillation amplitudes are $A = 0.1$ and $A = 0.2$ in Eq. 3.1.1 and Eq. 3.1.3. Eq. 3.1.1 has been nondimensionalised using the scalings in Eqs. 2.2.26, 2.2.32. In (a,b) the results have been averaged over 150 simulations, and the spatial positions are presented on a scaled domain $X \in [0,1]$.

The differences in deformation that result from low and high amplitude oscillations correspond to differences in the total drag force generated by bound integrins, shown in Fig. 3.7. The total drag force in the continuum model, $F_{tot}$, is defined analogously to $B_{tot}$ (Eq. 3.1.5). Note that, although the total drag forces are qualitatively similar in both models, there are some significant differences in the spatial propagation of the deformation applied at $X = 0$ (Fig. 3.6) arising due to differences between the two modelling approaches. In particular, individual springs between each node in the discrete model (Fig. 2.2) produce altered damping properties in comparison to

the simplified formulation of the continuum model, where local rigidity is assumed at the microscale (Section 2.2.1). Since bond rupture is directly affected by the level of deformation, the total bound fractions (Fig. 3.1) also differ slightly in magnitude between the two models; however, there is still a striking qualitative agreement for the averaged macroscale quantities of interest ($B_{tot}$, $F_{tot}$, in Figs. 3.1, 3.7). Since we are primarily interested in the qualitative behaviour, in the following sections we continue to exploit the efficiency of the continuum model in place of discrete stochastic simulations to investigate the dependence of the averaged bound integrin density, $B_{tot}$, on parameters of relevance to ASM cells and tidal breathing.

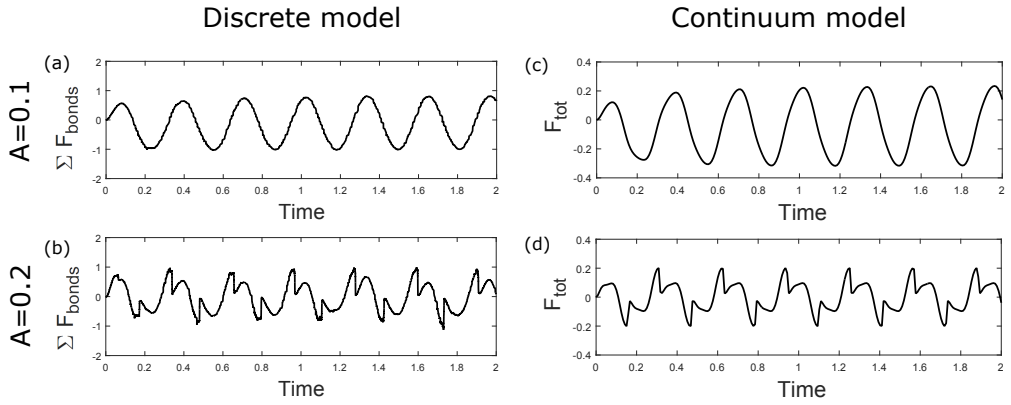


**Figure 3.7:** Total adhesive drag forces, $F_{tot}$, in the discrete (a,b) and continuum (c,d) models corresponding to the deformations in Fig. 3.6. (a,c). $A = 0.1$ in Eq. 3.1.1 and Eq. 3.1.3 and adhesion formation dominates. (b,d). $A = 0.2$ and there is increased rupture and a constant turnover of bound integrins under oscillatory loading. Eq. 3.1.1 has been nondimensionalised using the scalings in Eqs. 2.2.26, 2.2.32. As in Fig. 3.6, simulations are carried out from a zero initial condition. The results in (a,b) are from one sample discrete simulation.

### 3.1.1 Effect of varying the model parameters

We now investigate the effect of varying parameters that could differ between individuals and between asthmatics and non-asthmatics. These include the frequency of oscillations, material stiffnesses and binding affinities. An increase in the frequency of applied oscillations is shown to result in a decrease in the averaged bound integrin density, $\langle B_{tot} \rangle$, on both stable branches (Fig. 3.8(a)). This is due to reduced contact times for integrin binding. The most significant shift occurs in the lower branch where rupture and rebinding must occur at each cycle; the increased frequency pre-

vents significant binding. The location and size of the bistable window are also affected; for higher frequencies the lower branch persists for lower amplitudes, $A$, and the bistable region widens. The end points of the high and low branches have been calculated to the nearest 0.005, giving the widths of the bistable region to be in the ranges $[0.03, 0.04]$, $[0.045, 0.055]$, and $[0.055, 0.065]$ for $\omega = 10$, 20, and 30 respectively.

The material stiffnesses $K_A$ and $K_E$ influence the microscale distributions through the parameter $\gamma$ that appears in the macroscale relative velocity (Eqs. 2.2.36, 2.2.37). As seen by Eq. 2.2.37, the value of $\gamma$ decreases (increases) when either $K_A$ or $K_E$ are increased (reduced). Without loss of generality, in Fig. 3.8(b) we present results corresponding to variations in the cell stiffness, $K_A$. We observe that an increased cell or ECM stiffness (i.e. reduced $\gamma$) leads to a narrowing of the bistable region and a significant downward shift in the amplitude of forcing at which the saddle node bifurcations occur, and where the high branch exists. This is due to increased propagation of the forcing across the macroscale domain; increased material stiffnesses result in a reduced attenuation of the oscillatory load. For stiffer cells a lower oscillation amplitude can therefore result in the same degree of bond rupture.

Since binding affinities are specific to integrin type and can vary due to integrin activation and intracellular signalling [69, 71], we also investigate how the stable adhesion states respond to variations in binding affinities. In Eq. 2.2.29 the rupture rates involve parameters $h_1$, $h_2$, $h_3$, the ratios of unbinding rates $\hat{g}_1$, $\hat{g}_2$, $\hat{g}_3$ to the maximum binding rate $\hat{f}_1$ (see Eqs. 2.2.6, 2.2.7). Here we vary $h_1$, the unbinding rate when integrins are at $x = 0$. We find that the magnitudes of the upper stable states decrease with increased $h_1$ (Fig. 3.8(c)), since this state is obtained when adhesion formation and rupture balance, and when the system is subject to only small fluctuations. Since deformation-induced rupture will occur under lower values of loading if the bound fraction $\langle B_{tot} \rangle$ is reduced, the bifurcation point on the upper branch shifts to a lower value of $A$ as $h_1$ increases. Shifting of the stable branches is most notable in the upper branch since the high equilibrium bound state is more sensitive to $h_1$ than the low oscillatory rupture state; on the lower branch, the integrins are generally further from $x = 0$ and the effect of $h_2$ and $h_3$, which control the unbinding of integrins in a stressed state (see Eq. 15), are dominant. The separation of the lower branch becomes more apparent when the frequency of oscillatory loading is reduced (see Fig. 3.9), since the integrins will then spend more time near $x = 0$.

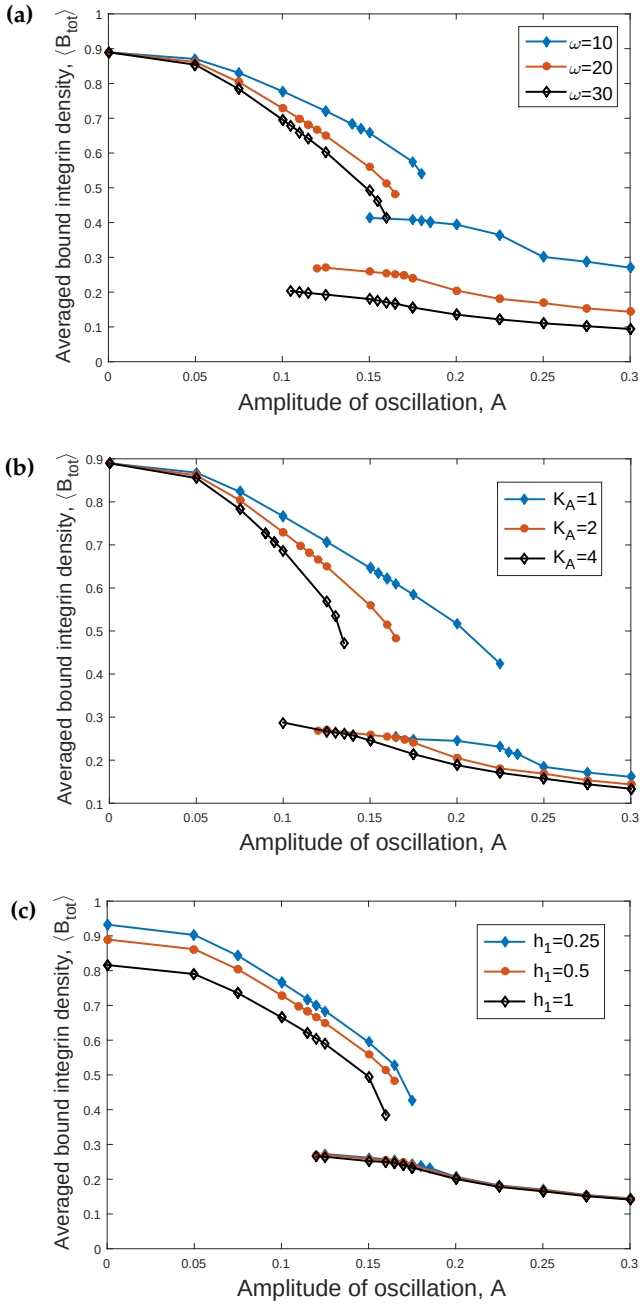


**Figure 3.8:** Stable branches in the continuum model indicating the values of $\langle B_{tot} \rangle$ (Eqs. 3.1.5, 3.1.6) for: (a) varying frequencies of the oscillatory loading, $\omega = 10, 20$, and 30 (Eq. 3.1.3); (b) varying cell stiffnesses, $K_A = 1, 2$, and 4; and (c) varying integrin binding affinities $h_1 = 0.25, 0.5$ and 1 (Eq. 2.2.29) with $\omega = 20$. For increased frequencies, contact times for integrin binding are reduced, leading to lower averaged bound integrin densities. For increased stiffnesses, there is a significant downward shift in the amplitude of oscillation at which the saddle node bifurcations occur. Binding affinities affect the magnitude of the stable adhesion states, most notably the upper branch, as well as the position and width of the bistable region. Unless otherwise stated, parameter values are as in Appendix B.

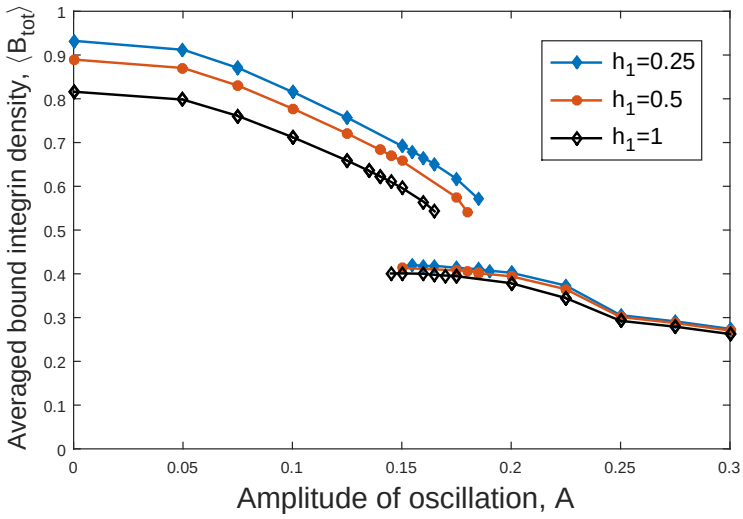


**Figure 3.9:** Stable branches indicating the values of $\langle B_{tot} \rangle$ (Eqs. 3.1.5) as a function of oscillation amplitude, A, for different $h_1 = 0.25$, 0.5 and 1 in Eq. 2.2.7 for $\omega = 10$. The lower branches separate (compared to in Fig. 3.8(c) with $\omega = 20$) due to the lower frequency of oscillations.

### 3.1.2 Effect of varying the input waveform

Sinusoidal waveforms are commonly used to represent tidal breathing in both theoretical and experimental studies [13, 61, 95, 117]; however, breathing is not perfectly sinusoidal with, for example, a longer time spent on exhalation than inhalation [145]. In this section we consider how an asymmetric waveform (accounting for physiological differences in inhalation and exhalation times) may affect the bound integrins, compared to the sinusoidal waveform used in the previous section. We implement the asymmetry by replacing the sinusoidal displacement condition in Eq. 3.1.3 by a boundary condition of the form

$$U_E(0,t) = A\sin(\omega t + \alpha \sin(\omega t)), \tag{3.1.7}$$

where $A$ and $\omega$ control the amplitude and frequency of oscillation, respectively, and $\alpha$ is a skewness parameter. The waveform in Eq. 3.1.7 is shown in Fig. 3.10, where we have chosen to use $\alpha = 0.4$. Denoting the inhalation and exhalation times by $t_I$ and $t_E$, respectively, this gives $t_I/t_E \approx 0.62$, which is within the range of ratios reported during tidal breathing in [145]. Note that in the sinusoidal case presented previously (Eq. 3.1.3), this ratio was $t_I/t_E = 1$.

Since the model is driven by the relative velocity at $X = 0$ (see Eq. 2.2.39), we differ-

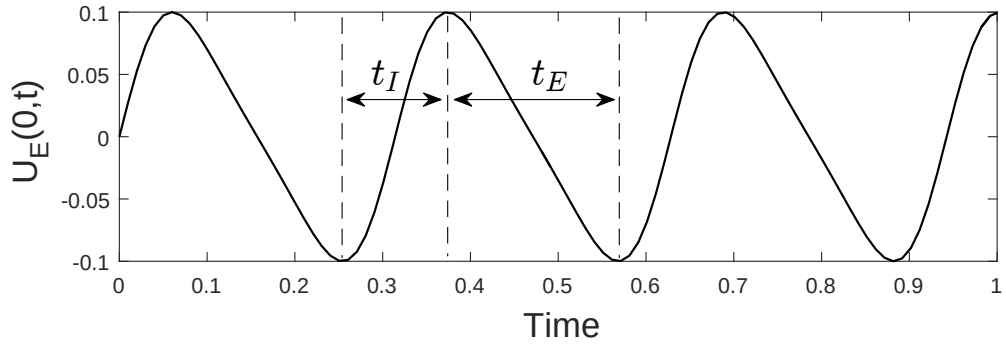


**Figure 3.10:** Plot of the asymmetric waveform used for $U_E(0,t)$, given by Eq. 3.1.7 with $\alpha = 0.4$, $A = 0.1$ and $\omega = 20$. The times $t_I$ and $t_E$ represent inhalation and exhalation, respectively, and in this case $t_I/t_E \approx 0.62$.

entiate Eq. 3.1.7 with respect to time to obtain the boundary condition

$$V(0,t) = A\omega(1 + \alpha\cos(\omega t))(\cos(\omega t + \alpha\sin(\omega t))). \tag{3.1.8}$$

The remaining boundary conditions for the cell and ECM are unchanged (Eq. 2.2.33).

Timecourses of the total bound fraction, $B_{tot}$, (Eq. 3.1.5) are shown in Fig. 3.11 as the oscillation amplitude, $A$, varies. For each amplitude of oscillation we consider a zero (orange) and saturated (blue) initial condition (Eq. 3.1.4), as in Fig. 3.1. Since the oscillations are now asymmetric (Fig. 3.10), the oscillations in the total bound fraction also exhibit asymmetry; there is more adhesion formation during the longer exhalation period, and the bound fraction therefore reaches a higher peak than during inhalation. As the $t_I/t_E$ value decreases from 1 (corresponding to the symmetric case), the asymmetry in the bound fraction timecourses will become increasingly apparent. As in Fig. 3.1, for low oscillation amplitudes we find that adhesion formation dominates and a high bound integrin state is obtained. For high oscillation amplitudes, adhesion rupture dominates, resulting in a lower bound integrin regime. For intermediate oscillation amplitudes, bistability is again observed due to shared loading between integrins; the outcome depends on the initial condition.

The stable solution surfaces for a range of amplitudes of oscillatory loading are shown in Fig. 3.12, which we compare to the result from the symmetric case (Fig. 3.4). Since the results are time-averaged over a full cycle, the symmetric and asymmetric cases exhibit only slight differences. In the asymmetric case, the bistable window is slightly wider (with a 12.5% increase).

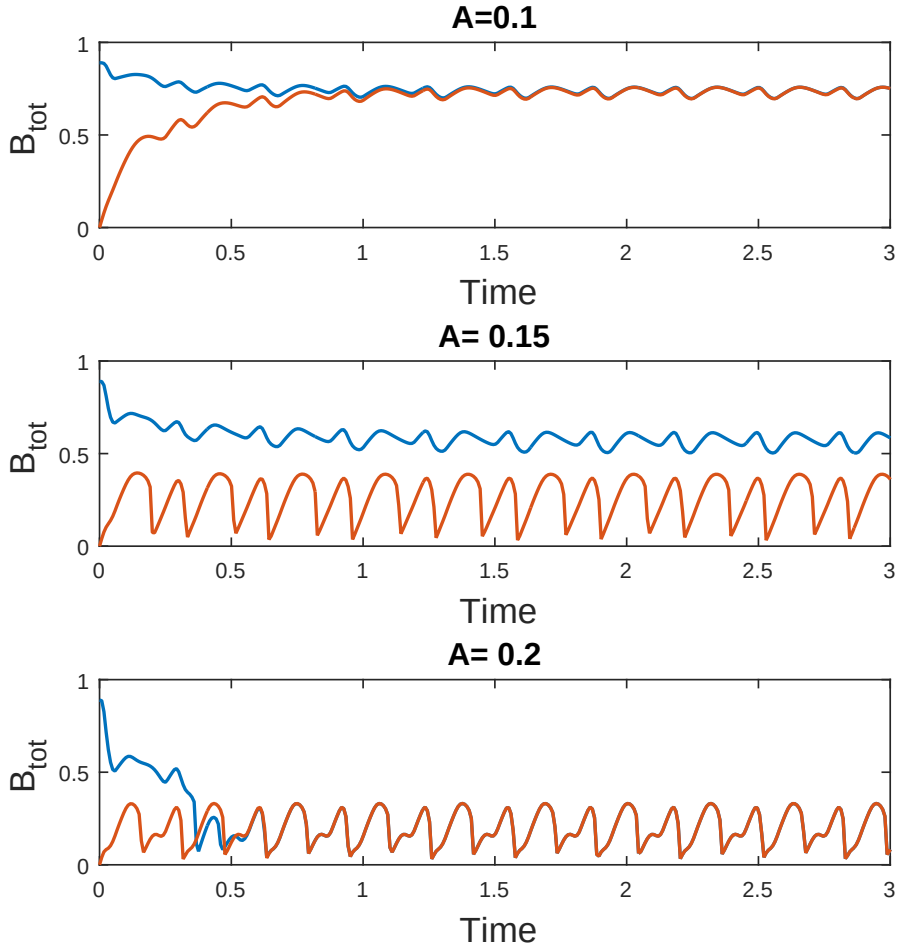


**Figure 3.11:** Timecourses illustrating the responses of total bound integrin fractions (Eq. 3.1.5) to low ($A = 0.1$), intermediate ($A = 0.15$) and high ($A = 0.2$) amplitude oscillatory loading for the boundary conditions in Eq. 3.1.8 with $\omega = 20$ and $\alpha = 0.4$. In each case we consider a zero (orange) and a saturated (blue) initial condition (Eq. 3.1.4).

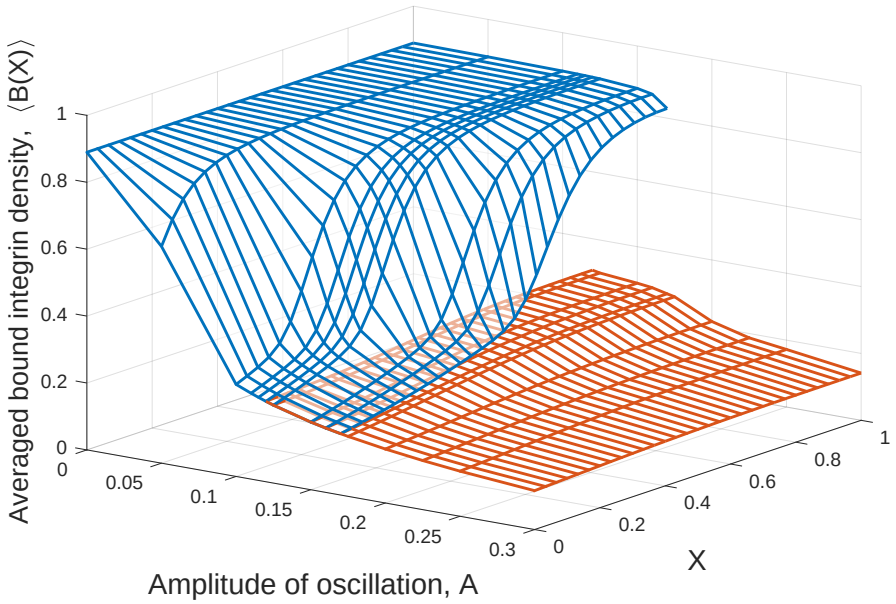


**Figure 3.12:** Upper (blue) and lower (orange) stable solution surfaces for the asymmetric waveform in Equation 3.1.7, with $\omega = 20$ and $\alpha = 0.4$, which also exhibits bistability for intermediate values of $A$. The corresponding result with a symmetric waveform is shown in Fig. 3.4; there are only slight differences as $\langle B(X) \rangle$ is time-averaged over a full cycle.

## 3.2 Perturbations due to deep inspirations

In both non-asthmatics and asthmatics, breathing patterns exhibit variations over time. Motivated by experimental observations about deep inspiration (DI)-induced bronchodilation (Section 1.1.2 and [33, 78, 125]), we now investigate the effect of transient perturbations to the amplitude of oscillatory loading on the bound integrin dynamics. These perturbations are designed to mimic the strain imposed on ASM cells and the ECM that may result from taking a DI during a period of regular breathing. Starting from the saturated initial condition (Eq. 3.1.4), we allow the bound integrin fraction to settle to its periodic high steady state before perturbing the amplitude of the oscillation for one cycle. We now return to sinusoidal oscillations, and to replicate a single DI we impose

$$U_E(0,t) = \begin{cases} A_2 \sin(\omega t), & \frac{8\pi}{\omega} < t < \frac{10\pi}{\omega}, \\ A_1 \sin(\omega t), & \text{otherwise}, \end{cases} \tag{3.2.1}$$

for baseline oscillation amplitude $A_1$, DI amplitude $A_2$ (where $A_2 > A_1$) and oscillation frequency $\frac{\omega}{2\pi}$ (Fig. 3.13).

We consider two different baseline oscillation amplitudes ($A_1 = 0.1$, $A_1 = 0.125$, marked by (a) and (b) in Fig. 3.5). This choice is motivated by variations in the amplitude of tidal breathing that may arise between individuals; pressure-driven oscillations *in vivo* would lead to smaller strains for greater material stiffnesses [64, 88]. The differences in $A_1$ could therefore correspond to asthmatic (stiff) and healthy (compliant) airways. We investigate the response to a small perturbation ($A_2 = 0.15$, point (c) in Fig. 3.5) and a DI that is large enough to induce significant rupture of adhesions ($A_2 = 0.3$, point (d) in Fig. 3.5), and find that for a starting amplitude $A_1 = 0.1$, there is recovery to the high adhesion state regardless of the amplitude of the perturbation (Fig. 3.13(a)). For a starting amplitude $A_1 = 0.125$ there are two possible responses depending on the amplitude of the DI perturbation (Fig. 3.13(b)). As shown by the blue markers in Fig. 3.5, for $A_1 = 0.1$ the high adhesion state is the only stable solution and a high density of bound integrins therefore persists after a perturbation. In contrast, $A_1 = 0.125$ lies within the bistable window and if the DI perturbation is large enough to drive the system into the basin of attraction of the low adhesion state, there is a transition to a low bound integrin density which persists even after the oscillation returns to its initial amplitude. This behaviour can be observed for any values of $A_1$ within the bistable window.

These responses demonstrate the possible consequences of bistability and the importance of loading history, since an event such as a DI perturbation may alter the future state of adhesion when bistability is present. Persistence of the previous state depends on the amplitude of the DI and on where the bistable window (Fig. 3.5) lies in relation to the baseline oscillation amplitude, $A_1$. Physiologically, this will be influenced by differences in the amplitude of the baseline oscillatory displacement, representing tidal breathing, and differences in parameters such as the oscillation frequency, material stiffnesses and binding affinities. These factors could all vary between asthmatics and non-asthmatics and are seen to shift the location of the bistable window (Fig. 3.8).

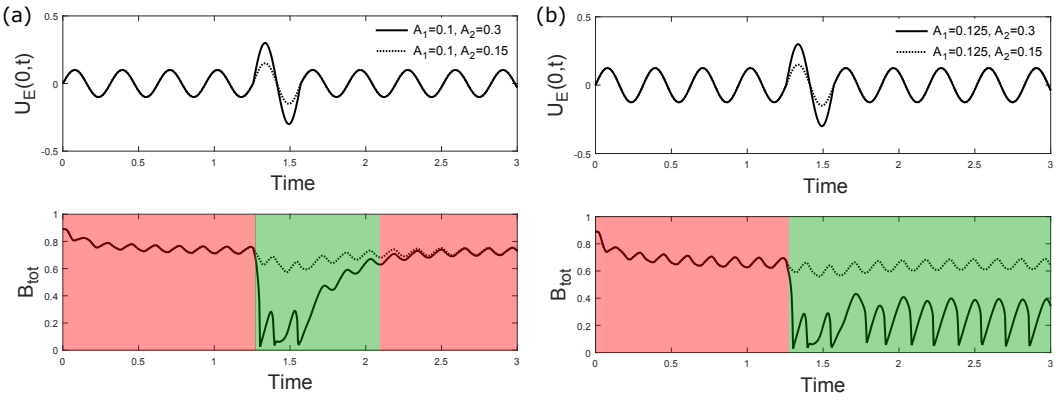


**Figure 3.13:** Different amplitude baseline oscillations and DI-like perturbations may lead to a switch in adhesion states. We show the applied oscillatory displacement, $U_E(0,t)$, and the total bound fraction of integrins, $B_{tot}(t)$, (see Eq. 3.2.1 and Eq. 3.1.5), when $\omega = 20$. (a) For $A_1 = 0.1$, $A_2 = 0.3$ (solid line) and $A_1 = 0.1$, $A_2 = 0.15$ (dashed line), the high adhesion state (red) persists after both DI perturbations, since for $A_1 = 0.1$ this is the only steady state. (b) For $A_1 = 0.125$, $A_2 = 0.3$ (solid line), there is a transition to a low adhesion state (green), since $A_1 = 0.125$ is within the bistable window (see Fig. 3.5) and the DI is sufficiently large to drive the system into the basin of attraction of the low state. For a smaller amplitude perturbation, $A_2 = 0.15$ (dashed line), the high fraction of bound integrins persists.

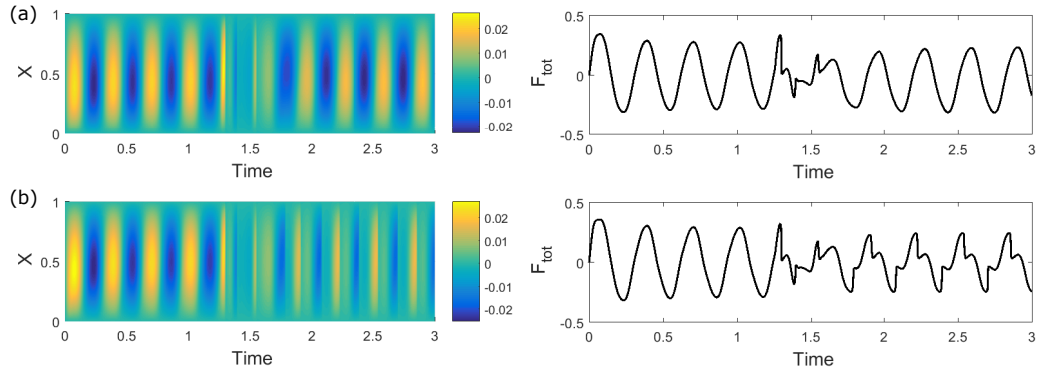


**Figure 3.14:** Cell deformations, $U_A(X,t)$, and total drag forces, $F_{tot}$, corresponding to two of the outcomes shown in Fig. 3.13. In (a) $A_1 = 0.1$ and $A_2 = 0.3$ and the DI results in a transient decrease in bound integrin fraction. This has a temporary effect on the level of deformation and total drag force. In (b) $A_1 = 0.125$ and $A_2 = 0.3$ and the reduction in bound integrin fraction after a DI is sustained. Here there is a permanent switch in adhesion states, with corresponding reductions in $U_A$ and $F_{tot}$.

## 3.3 Conclusions

In this chapter we used the discrete stochastic-elastic model and the multiscale continuum model developed in Chapter 2 to investigate the effect of oscillatory loading, representing deformations due to tidal breathing and deep inspirations (DIs), on the dynamics of ASM cell–matrix adhesions. To date, the consideration of mechanical ASM-ECM interactions via integrins has been neglected in investigations on the effect of tidal breathing and DIs in asthma. Our results indicate that the density of adhesions can be heavily influenced by dynamic loading and also by the loading history. In particular, we observe two distinct regimes where either adhesion formation or adhesion rupture dominate, resulting in large differences in the steady state densities of bound integrins (Fig. 3.1). Moreover, a window of bistability exists for intermediate loading amplitudes (Fig. 3.5) due to mechanical cooperativity; shared loading between pre-existing adhesions allows the high density state to persist when rupture would otherwise dominate. This bistability generates a hysteresis loop and we see that the loading history and events such as perturbations representing deep inspirations can significantly alter the future adhesion dynamics (Fig. 3.13). We have investigated the effect of varying the model parameters (Fig. 3.8) and of varying the input waveform (Fig. 3.11) and observe robustness of these dynamics. Due to their role in transmitting mechanical strains, we expect the high and low adhesion densities to significantly affect the level of contractile force that can be transmitted between intracellular and extracellular domains during ASM cell contraction. This could directly affect the extent of airway narrowing that occurs during bronchoconstriction, and we hypothesise that the high and low adhesion states could correspond to contracted and dilated airways respectively. In addition to the differences in bound integrin densities seen in the two regimes, cell deformations and adhesive drag forces also differ significantly in each case, both in terms of magnitude and dynamics (Figs. 3.6, 3.7).

In previous studies [108, 128], similar instances of mechanical integrin cooperativity have been observed; shared loading between integrins aids initial cluster formation. The existence of a threshold at which integrin rupture dominates over adhesion formation is in agreement with the Monte Carlo simulations in a previous study [81], where an oscillatory strain is applied to an initially fully-bound substrate. Our model assumptions differ in some respects to those of Kong *et al.* [81], but sudden rupture occurs in both when the oscillation amplitude is increased. In our model, we addition-

ally observe bistability and hysteresis. The two adhesion states that we report appear to behave similarly to transient and firm adhesions, observed in other contexts; the high state exhibits persistence of bound integrins, whereas the low state shows cyclic breaking and reattachment of a significant fraction of integrins. Integrin-mediated adhesions can function as either dynamic or stable structures [67] and, in the context of cell migration, switching between transient and firm adhesion states (mediated by biochemical signalling) facilitates migration by altering the traction properties between cells and the ECM. Mechanical signals, in addition to biochemical signals, are known to be able to modulate focal adhesion size and dynamics [100], making further study into how the mechanical environment of ASM affects focal adhesions worthwhile.

Motivated by experimental observations about the bronchodilatory effect of DIs (Section 1.1.2), we used the more tractable continuum model to investigate the effect of transient perturbations to the amplitude of oscillations. After a large DI-like perturbation, our results show either persistence of the high adhesion state or a transition from the high to the low adhesion states (Fig. 3.13). This result provides a possible mechanism for why the bronchodilatory effect after a DI is transient in asthmatics yet sustained in non-asthmatic subjects [33, 78, 125]. The ability of a DI to induce a switch between states is influenced by a difference in either: (i) the position of the bistable region, which shifts in response to changes in material parameters such as oscillation frequency, material stiffnesses and binding affinities (Fig. 3.8); (ii) the amplitude of the unperturbed oscillatory displacement, which we use to represent the magnitude of tidal breathing; or (iii) the magnitude of the DI. All of these factors could differ between individuals, as well as between asthmatics and non-asthmatics. In particular, we expect asthmatics to have stiffer airways and to experience lower amplitude displacements during both tidal breathing and DIs. As demonstrated in Fig. 3.13, lower amplitudes of tidal breathing could lead to an inability to switch to a low adhesion state after a DI. We hypothesise that this switch could correspond to recovering from a contracted to a dilated state. To fully understand the bronchodilatory effect of DIs, it will be crucial to consider the dynamics of actin-myosin crossbridges as well as integrins; we expect them both to contribute, but their relative importance will only become clear when considered together. Results in this vein are presented in Chapter 6, where we develop a coupled model of both integrin and crossbridge dynamics.

Our initial results were obtained in the stochastic-elastic computational model and

then replicated in the multiscale continuum model. Due to the inclusion of detailed microscale binding rates, we find that our continuum model produces similar qualitative behaviour to the discrete model. Whilst the discrete model is advantageous for incorporating large amounts of individual detail, the continuum model is more efficient for a large number of integrins. The continuum model can also more easily be coupled to existing models of contractile force generation, for example [24], in which crossbridge cycling and disruption to actin-myosin contractile units (in response to cell length changes) are considered. Extending the model to include this will allow for the investigation of the combined dynamics of crossbridges and integrins during DIs. As discussed in Section 1.1.2, further motivation for understanding contractile force transmission between ASM cells and the ECM in the context of asthma is to understand the force-dependent activation of TGF$\beta$, a growth factor which otherwise remains latent in the ECM. In order to fully understand the consequence of different adhesion states on the activation of TGF$\beta$ the extension to higher dimensions, where the constraint on vertical motion can be relaxed, will again be needed. Within the continuum framework, it is possible to address simplifications made during initial model development; in particular, one can consider nonlinear elastic materials in order to accommodate large deformations, a more complete reaction sequence including integrin diffusion and activation (Chapter 4), and different forms for spatial binding and rupture rates. Instead of our simplified piecewise linear rates, a more commonly used description for bond rupture under force is the Bell model [14], in which rupture rates increase exponentially with force. A similar observation of bistability due to mechanical cooperativity has been seen in a previous model with a Bell rate for unbinding [37]. Other rate functions, including a power law relation, have also been presented [40, 41], and obtaining precise measurements for individual integrins, using techniques such as atomic force microscopy [44], remains an area of ongoing research. As we explicitly account for binding and unbinding rates that depend on microscale distance, both our discrete and continuum models can accommodate any of these choices.

# Chapter 4

# Modelling integrin activation, diffusion and strengthening

In this chapter we extend the multiscale continuum model presented in Chapters 2 and 3. In the initial model we assumed that integrins were already activated and actin-bound; we now consider diffusion and activation of free integrins, which are processes that occur upstream of integrin binding to ECM. These processes are accounted for in a macroscale reaction–diffusion system, presented in Section 4.1. Using this extended reaction sequence we investigate the different system behaviours that occur when activation and deactivation rate constants are varied. We also explore the idea of a time-dependent activation rate to represent intracellular signalling processes that occur during initial adhesion formation. AFM experiments show a non-monotonic increase in adhesion strength during early adhesion formation and, using the model, we find that a Hill function activation rate, chosen to represent a delay in signalling, could explain these observations.

In Section 4.2 we further extend the model to allow for a force-dependent strengthening of adhesions, which is known to occur through additional protein recruitment within the cell. Integrin-mediated adhesions can be reinforced through the binding of the protein vinculin to cryptic binding sites on talin, which is the primary adaptor protein bound to integrin tails (Section 1.2.2). These binding sites are only exposed when the integrins and talin are under strain. We model this process by adapting the microscale model; bound integrins can undergo an additional strengthening stage, again dependent on a local spatial coordinate. The model is extended to include vinculin-bound integrins as a separate species, and their dynamics are modelled by

a second system of advection–reaction equations. These equations are coupled to the binding reactions and advection–reaction system of the previous microscale formulation (Chapter 2).

In Section 4.3, we explore whether our model extensions can account for behaviours observed in a recent experimental study by Mailhot-Larouche *et al.* [95]. The *in vitro* study was designed to investigate how the time between deep inspirations (DIs) affects airway renarrowing following a DI. A reduced time interval between DIs was observed to increase both the magnitude and the rate of recovery to the contractile state.

## 4.1 Integrin diffusion and activation

In addition to the reversible binding of active actin-bound integrins ($I_A$) to the ECM to form double-bound integrins ($B$), we now consider the binding of integrins ($I$) to adaptor proteins ($A$) within the cell. The notation for the different integrin states are as shown in Fig. 4.1. The adaptor proteins, which include talin, connect the integrins to the actin cytoskeleton and also facilitate inside-out integrin activation (see Section 1.2.2). Activation and binding reactions occur across the macroscale domain, where the extended reaction sequence is now

$$I(X,t) + A(X,t) \underset{k_D}{\overset{k_A}{\rightleftharpoons}} I_A(X,t) \underset{k_{off}}{\overset{k_{on}}{\rightleftharpoons}} B(X,t). \tag{4.1.1}$$

Initially, the rates $k_A$ and $k_D$ in Eq. 4.1.1 will be treated as positive constants, but there is freedom to include dependencies on time or on the macroscale variables. The integrin binding reactions follow our previous microscale model (Section 2.2); the macroscale reaction rates $k_{on}$ and $k_{off}$ are therefore to be determined by underlying microscale bound integrin distributions and local rate functions, $k_b(x)$ and $k_u(x)$. Within this formulation we will also allow for the diffusion of the unbound integrins ($I$). The extended reaction sequence that we consider is sketched in Fig. 4.1.

To nondimensionalise the system, each macroscale species is scaled by the total adaptor protein concentration. This is conserved across the different states at each macroscale point $X$, to give the dimensionless relation $I_A + A + B = 1$. The dimensionless model

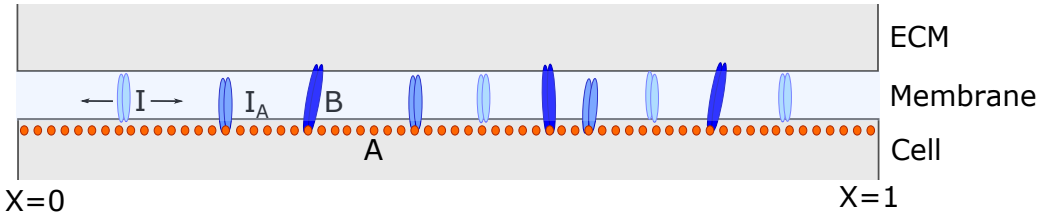


**Figure 4.1:** Sketch of the integrin states involved in the extended reaction sequence. Freely diffusing integrins ($I$) bind to adaptor proteins ($A$) to form active, actin-bound integrins ($I_A$). These integrins bind to the ECM to form double-bound integrins ($B$). The macroscale domain is defined as in Section 2.2.4 and is far more dense than depicted (see Fig. 2.17).

equations are

$$\frac{\partial A}{\partial t} = -k_A I A + k_D(1 - A - B), \tag{4.1.2}$$

$$\frac{\partial I}{\partial t} = D\nabla_X^2 I - k_A I A + k_D(1 - A - B), \tag{4.1.3}$$

$$\frac{\partial b(x,t;X)}{\partial t} + \frac{V(X,t)}{\delta}\frac{\partial b(x,t;X)}{\partial x} = \eta k_b(x)(1 - A - B) - k_u(x)b(x,t;X), \tag{4.1.4}$$

where $b(x,t;X)$ is the microscale distribution as defined in Section 2.2.3 and $D$ is the integrin diffusion constant. The nondimensionalisation uses identical scalings to the previous model (as given in Eq. 2.2.26), with the additional scalings

$$k_A = \hat{k}_A/\hat{f}_1, \qquad k_D = \hat{k}_D/\hat{f}_1, \qquad D = \hat{D}/\hat{f}_1\hat{L}^2, \tag{4.1.5}$$

for the activation rate, deactivation rate and diffusion coefficient respectively. Here $\hat{f}_1$ and $\hat{L}$ are the maximum integrin binding rate (Eq. 2.1.2) and macroscale length (Fig. 2.17), respectively. The dimensionless parameters $\delta = \hat{h}/\hat{L}$ and $\eta = \hat{h}/\hat{l}$ are defined as before (Section 2.2.3) and $B(X,t) = \int_{-\infty}^{\infty} b(x,t;X)dx$ denotes the bound fraction of integrins at each macroscale point. As in the earlier model, $k_b(x)$ and $k_u(x)$ are local binding and unbinding rates and, throughout this chapter, these will be defined as in Eqs. 2.2.6 and 2.2.7.

We note that there are two equivalent ways of writing the system of governing equations; Eq. 4.1.4 could also be written as the following macroscale reaction equation

$$\frac{\partial B}{\partial t} = k_{on} I_A - k_{off} B, \tag{4.1.6}$$

where

$$k_{on} = \eta \int_{-\infty}^{\infty} k_b(x)dx \quad \text{and} \quad k_{off}(X) = \frac{\int_{-\infty}^{\infty} k_u(x)b(x,t;X)dx}{\int_{-\infty}^{\infty} b(x,t;X)dx}. \tag{4.1.7}$$

This alternative form is obtained by integrating Eq. 4.1.4 over $x \in (-\infty, \infty)$, where we note that the advection term disappears since the bound integrin distributions, $b(x,t;X)$, are always zero at the tails. Since $k_{on}$ and $k_{off}$ depend on the microscale distributions, this cannot be solved independently of the microscale advection–reaction system (Eq. 4.1.4); we therefore solve the system as given in Eqs. 4.1.2–4.1.4.

In all of the numerical simulations that follow, we impose zero flux boundary conditions for the diffusing integrins at $X = 0$ and $X = 1$; the total number of integrins is therefore conserved over the macroscale domain. The zero flux conditions are

$$\frac{\partial I}{\partial X}(0,t) = 0, \qquad \frac{\partial I}{\partial X}(1,t) = 0. \tag{4.1.8}$$

An alternative could be to consider periodic boundary conditions. Since we consider the macroscale domain to be a section of the cell membrane, both zero flux and periodic boundary conditions are simplifications. In reality, integrins could diffuse away from (and into) this region, and conservation is not guaranteed. We have also not included source and sink terms for $I$ and $A$ elsewhere across the domain. The number of integrins expressed on the cell surface could vary due to delivery of integrins to and from the membrane [148] and adaptor proteins are known to be continually replaced; however, we assume here that there is a balance between production and decay.

The numerical implementation and discretisation are the same as in Chapter 3 (discussed in Section 2.2.5), with the addition of two vectors, $\mathbf{I} = (I_1, I_2, ...I_N)^T$ and $\mathbf{A} = (A_1, A_2, ...A_N)^T$ for the macroscale variables. The spatial derivative for diffusion is approximated with a second order central difference (analogously to Eq. 2.2.42), and the discretised reaction equations are evolved alongside the microscale advection–reaction system.

### Numerical results: no external forcing

We first consider the evolution of each of the 4 species when there is no external forcing applied to the cell or to the ECM, and for the case where the activation rate, $k_A$, is higher than the deactivation rate, $k_D$ (Fig. 4.2). The initial conditions for the adaptor proteins, actin-bound integrins and double-bound integrins are chosen to be the uniform distributions

$$A(X,0) = 1, \qquad I_A(X,0) = 0, \qquad B(X,0) = 0. \tag{4.1.9}$$

For the unbound integrins, which freely diffuse, we use a Gaussian initial condition

$$I(X,0) = \exp\left(-\frac{(X-\mu)^2}{2\sigma^2}\right), \tag{4.1.10}$$

with mean $\mu$ and standard deviation $\sigma$. We see a sequential activation and then binding of integrins (which transition from $I$ to $I_A$ to $B$ states). Over time, the remaining free integrins diffuse to a near-zero, spatially uniform, state (Fig. 4.2(a)); however, the bound integrins (Fig. 4.2(d)) remain most concentrated near the centre of the domain, $X = 0.5$, where the integrin density was initially highest.

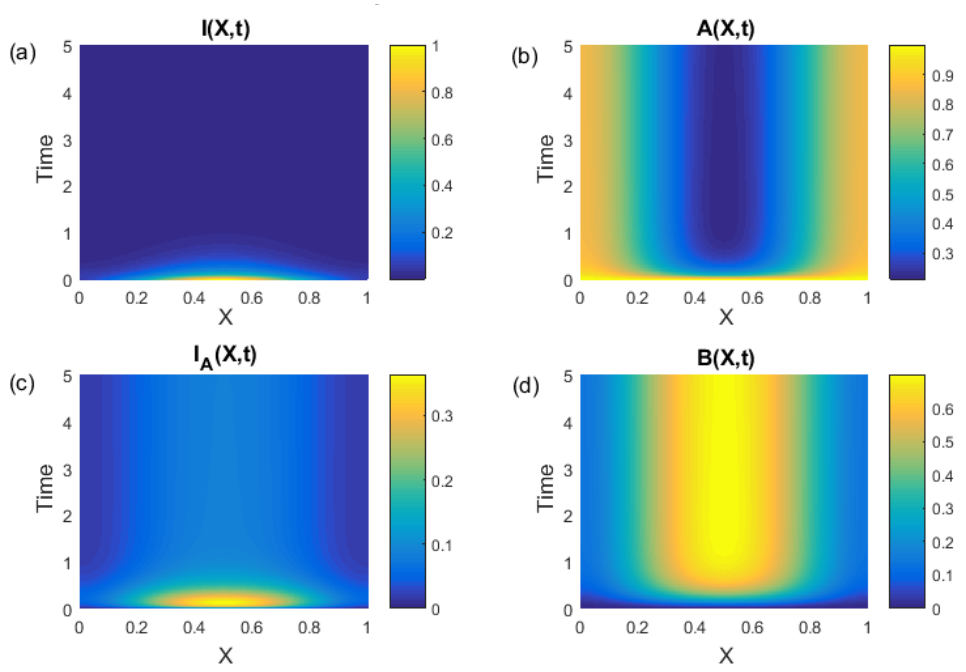


**Figure 4.2:** Spatiotemporal evolutions of each of the macroscale species (Eqs. 4.1.2–4.1.4) when $D = 0.05$, $k_A = 10$ and $k_D = 0.1$. Free integrins ($I$) are firstly activated and actin-bound ($I_A$) and then become double-bound ($B$). In the initial Gaussian distribution of unbound integrins (Eq. 4.1.10), the mean and standard deviation are $\mu = 0.5$ and $\sigma = 0.2$ respectively.

Next we sample three corresponding microscale distributions of bound integrins at $X = 0$, $X = 0.5$ and $X = 1$ (Fig. 4.3). The microscale bound-integrin distributions exhibit the same spatial inhomogeneity seen in the macroscale variables, as indicated by distributions that peak at higher values at $X = 0.5$.

In the case where the deactivation rate is higher than the activation rate (Fig. 4.4), we obtain a very low concentration of actin-bound and double-bound integrins (Fig. 4.4(c), (d)). A low, rather than zero, density of bound integrins occurs since there is

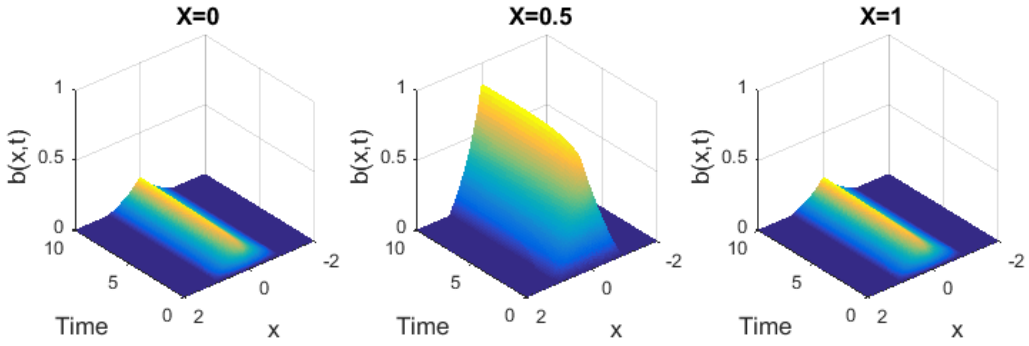


**Figure 4.3:** Sample microscale bound integrin distributions corresponding to the macroscale system in Fig. 4.2. Due to the initial Gaussian distribution of integrins, bound integrins have a higher density at $X = 0.5$.

a balance between the binding of actin-bound ($I_A$) integrins and deactivation: due to the ordered reaction sequence considered here, if actin-bound integrins become double-bound then they must unbind from the ECM before deactivation. Due to the low value of bound integrins, the density of freely diffusing integrins, $I$, (Fig. 4.4(a)) is much higher than in Fig. 4.2(a) (where the activation rate is higher than the deactivation rate) but has again become spatially uniform.

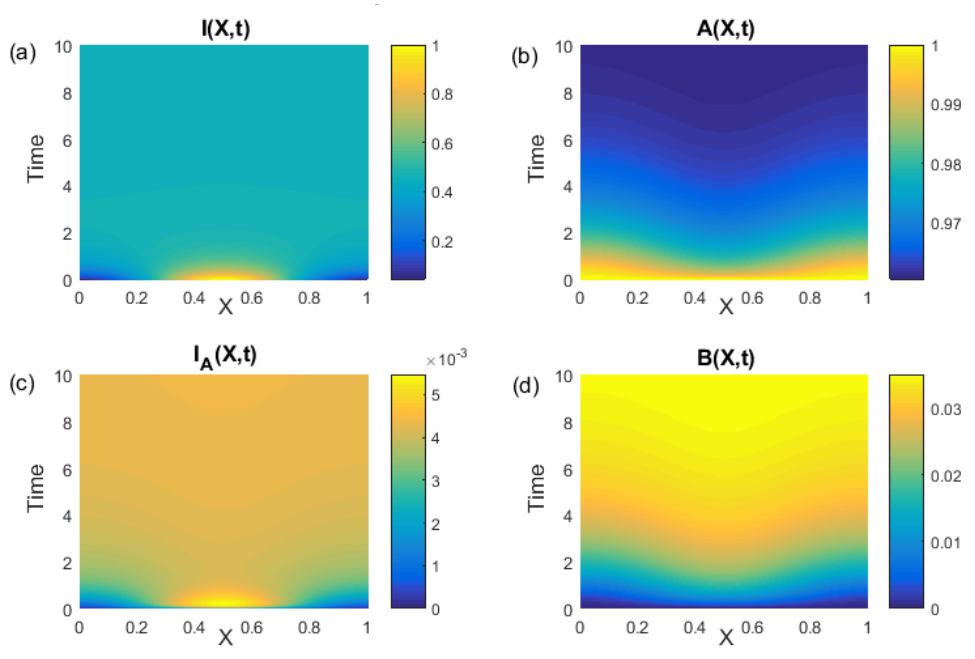


**Figure 4.4:** Spatiotemporal evolutions of each of the macroscale species (Eqs. 4.1.2–4.1.4) when $D = 0.05$, $k_A = 0.1$ and $k_D = 10$. In the initial distribution of unbound integrins (Eq. 4.1.10), we use $\mu = 0.5$ and $\sigma = 0.2$. A low density of integrins achieve the actin-bound and double-bound states.

It may be more realistic to consider an initial condition where some of the integrins are already active and actin-bound ($I_A$). We examine the case where deactivation dominates (Fig. 4.5), but with the following initial conditions

$$A(X,0) = 0.5, \qquad I_A(X,0) = 0.5, \qquad B(X,0) = 0, \tag{4.1.11}$$

and with $I(X,0)$ as in Eq. 4.1.10. The outcome is similar to Fig. 4.4; however, in this case, there is an initial growth of $B$ (due to an initial uptake of $I_A$ integrins) before decay to a low bound state. The four species settle towards a state with a low concentration of both types of bound integrins (Fig. 4.5(c),(d)) and a uniformly high concentration of unbound integrins and adaptor proteins (Fig. 4.5(a),(b)). These differ slightly in magnitude to the steady distributions in Fig. 4.4 due to the increased number of integrins introduced by the initial conditions in Eq. 4.1.11 (Fig. 4.5).

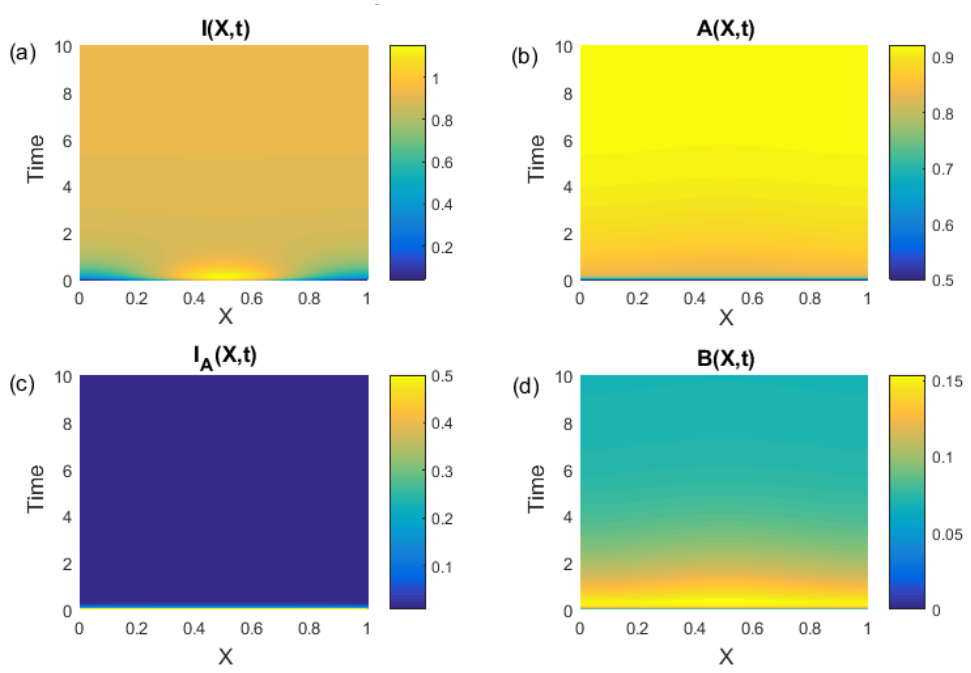


**Figure 4.5:** Spatiotemporal evolutions of each of the macroscale species (Eqs. 4.1.2–4.1.4) when $D = 0.05$, $k_A = 0.1$ and $k_D = 10$. With a non-zero initial concentration of $I_A$ (Eq. 4.1.11) the bound integrins decay rather than grow to a low state (cf. Fig. 4.4).

### Time-dependent integrin activation

The formation of mature focal adhesions is a complex process, involving numerous signalling cascades and a heirarchical recruitment of intracellular proteins [152]. Here we consider a recent experimental result (provided by Prof. Gerald Meininger, Dr.

Leike Xie and Dr. Vladislav Glinsky, University of Missouri) obtained using atomic force microscopy (AFM) techniques (Section 1.2.3) which showed a non-monotonic increase in adhesion strength between an endothelial cell and AFM probe *in vitro* (Fig. 4.6). In the experiments, a coated bead (described below) was lowered to the cell and held stationary for a range of contact times. By then retracting the AFM probe, adhesion strengths were measured (by tracking the deflection of the probe, see Section 1.2.3) for four different bead coatings. The coatings were chosen such that they would allow for different amounts of integrin binding. Firstly, the beads were coated in polyethylene glycol (PEG), which is strongly adhesive and, as such, has previously been used as a linker protein to attach different substrates (e.g. fibronectin) to the glass beads [68]. Following this, beads were either coated with an anti-Galectin-3 antibody (Gal-3 Ab, the base case), bovine serum albumin (BSA, a negative control), or left as PEG (a positive control, since PEG binds both to integrins and non-specifically to other proteins on the cell surface). For a further negative control, an uncoated bead was used. In general, adhesion strength increased with contact time; however, for each of four coatings there was a consistent 'dip' in measured adhesion force, occuring at approximately the same contact times early in the adhesion formation (Fig. 4.6). A hypothesis for this behaviour is that intracellular signalling, triggered by mechanical or biochemical cues upon initial bond formation, has an intrinsic delay before inducing reinforcement and commitment to firm adhesion. During this delay, initial bonds could begin to disassociate. In support of the observed behaviour being related to intracellular signalling (rather than, for example, external mechanical factors) the dip appears to be systematic: it occurs at the same timepoint for each bead coating. Here we will investigate this behaviour phenomenologically by incorporating a delay in integrin activation, modelling the activation rate as a Hill function (Eq. 4.1.12 and Fig. 4.7).

A possible choice to represent a delay in intracellular signalling is the time-dependent activation rate

$$k_A(t) = \kappa_A + \frac{\alpha t^3}{t^3 + 100}, \tag{4.1.12}$$

which is shown in Fig. 4.7. The constant $\kappa_A$ denotes a background activation rate, which will increase to the value $\kappa_A + \alpha$ as $t \to \infty$. The key species of interest are the double-bound integrins, $B$, (Fig. 4.8) which we expect to correlate with adhesion strength. In the model, we can measure this quantity directly. In the AFM experiments, the number of bound integrins cannot be measured and retraction of the AFM probe is required to infer the adhesion strength indirectly. We observe that, while the

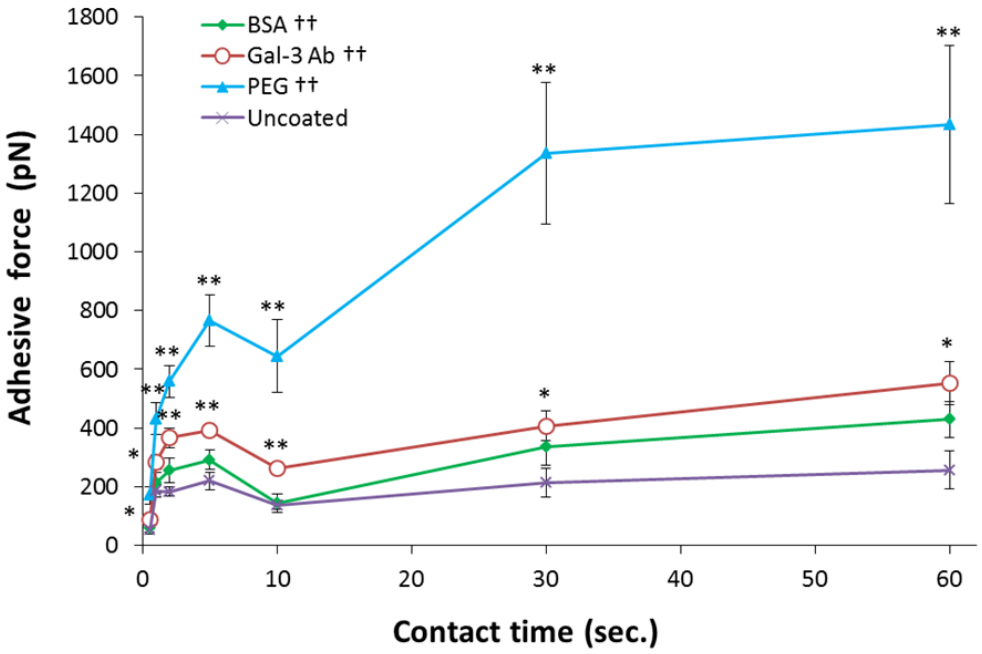


† p< 0.05; †† p< 0.01, Anova analysis on every coated group, n ≥ 6.
* p< 0.05; ** p< 0.01, vs uncoated. There are no statistical differences between BSA coated group and the uncoated group at all contact-time points.

**Figure 4.6:** Experimental AFM data of the maximum adhesion force obtained between cells and coated microbeads. Adhesion force is measured for a range of contact times for 4 bead coatings: anti-Galectin-3 antibody (Gal-3 Ab), polyethylene glycol (PEG, a positive control), bovine serum albumin (BSA, a negative control), and uncoated. Data was provided by Prof. Gerald Meininger, Dr. Leike Xie and Dr. Vladislav Glinsky, University of Missouri.

activation rate is near zero, the number of bound integrins begins to decrease after an initial uptake (Fig. 4.8). However, as the activation rate increases, inactive integrins are encouraged to transition to an active state, allowing for rebinding and thereby increasing the fraction of double-bound integrins. In these simulations, we have used the uniform initial conditions in Eq. 4.1.11; before contact with the substrate-coated bead we expect integrins to be in either the inactive or active, actin-bound state. In the *in vitro* set-up, the bead is initially far away from the cell; the initial double-bound distribution will therefore be zero. Due to the uniform initial conditions, we do not see spatial variation in the solution.

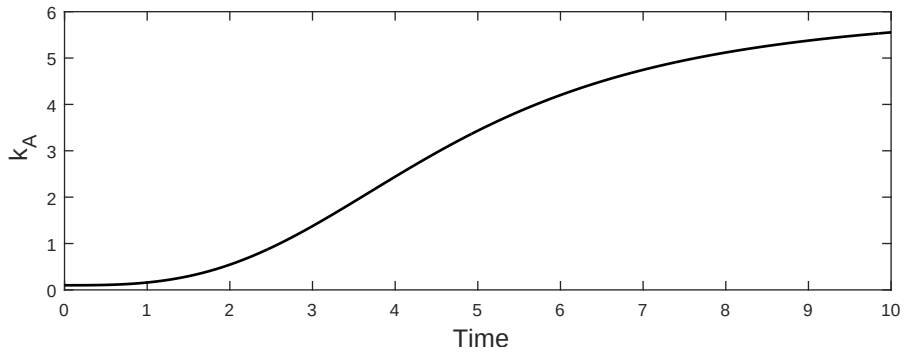


**Figure 4.7:** The time-dependent activation rate, $k_A(t)$, given by Eq. 4.1.12 with $\kappa_A = 0.1$ and $\alpha = 6$.

Since the activation rate is low at early times, the 'dip' behaviour resulting from a delay in integrin activation rate (Eq. 4.1.12) can be understood by comparing Fig. 4.8 to the behaviour that occurs when deactivation dominates (Fig. 4.5). We compare timecourses for the $I_A$ and $B$ integrins in Fig. 4.9. In the case where deactivation dominates, after the same initial binding of actin-bound integrins to the ECM, the majority of $I_A$ integrins transition to an inactive state. As the concentration of $I_A$ integrins decreases, the equilibrium between $I_A$ and $B$ integrins is affected; there is then a corresponding decrease in the number of double-bound integrins. In contrast, the delayed increase in activation rate triggers the reactivation of unbound integrins, which can then recover to a high bound state (similar to Fig. 4.2). Non-monotonic behaviour can therefore arise from a transition between regimes where deactivation and then activation of integrins dominate.

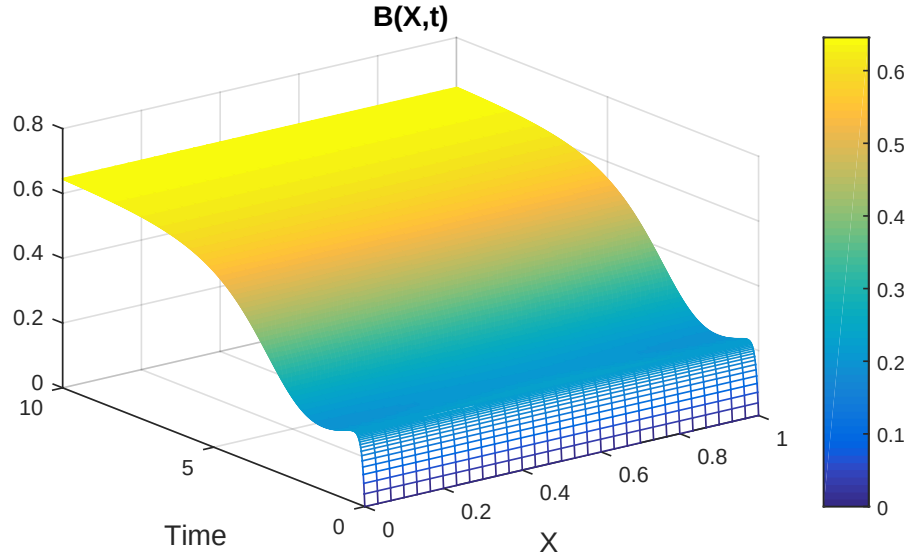


**Figure 4.8:** Spatiotemporal evolution of the macroscale bound integrins, $B$, when $D = 0.05$, $k_D = 5$ and $k_A$ is a Hill function, defined in Eq. 4.1.12 and Fig. 4.7. There is a non-monotonic increase in the double-bound integrins ($B$), due to a temporary 'dip' occuring when the activation rate is low. This is similar to behaviour seen during early adhesion formation in experiments (Fig. 4.6).

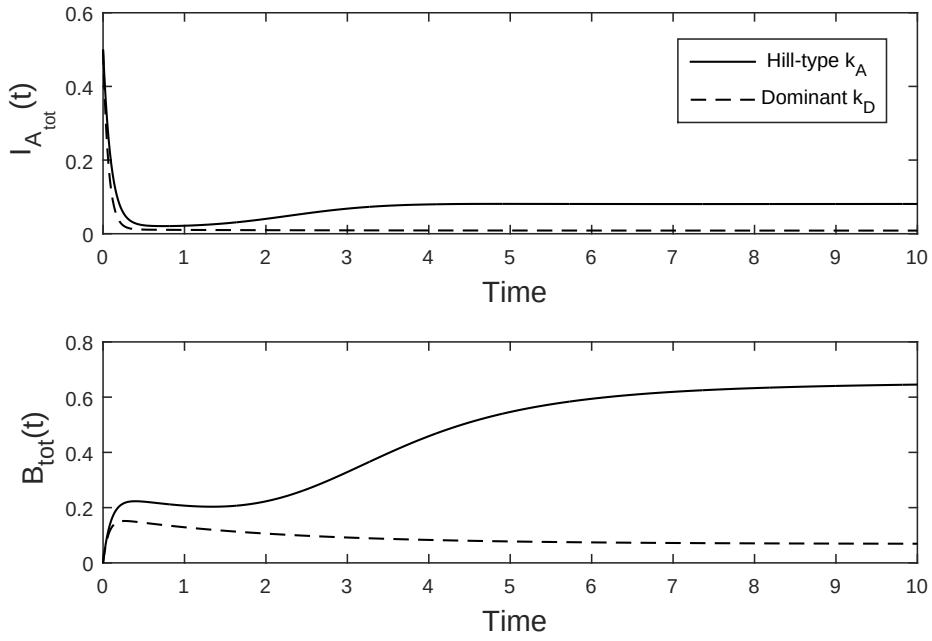


**Figure 4.9:** Total actin-bound fraction, $I_{A_{tot}}(t)$, and double-bound integrin fraction, $B_{tot}(t)$ (Eq. 3.1.5), when (solid line) $k_D = 5$ and $k_A$ is a Hill function, defined in Eq. 4.1.12 and (dashed line) when $k_D = 10$ and $k_A = 0.1$. These correspond to Figs 4.5 and 4.8.

In this model we have extended the previous reaction sequence to allow for the activation and deactivation of integrins. For $k_D \neq 0$, our results show that a constant background rate of activation or reinforcement in a time-dependent manner (for example due to intracellular signalling), leads to a high density of bound integrins. Different behaviours are seen depending on whether activation or deactivation of integrins dominate (Figs. 4.2, 4.4, 4.5) and a non-monotonic increase in the number of bound integrins is obtained when there is a time-dependent transition between the two cases via a Hill function for the activation rate (Fig. 4.8). Similar non-monotonic trends in the adhesion strength have been observed in early adhesion formation in experiments (Fig. 4.6), and consistent experimental results for different substrates support the idea that this behaviour could be related to intracellular signalling. Furthermore, in a previous study of chemokine-triggered inside-out integrin activation [17], the transition of integrins from low to high affinity (active) states was measured both experimentally and simulated with a model of the relevant signalling pathways. A rapid increase of high affinity integrins was observed at $\sim$20 seconds (Fig. 2B in [17]). In the experimental data in Fig. 4.6, the dip in adhesion strength occurs at $\sim$10 seconds, which we hypothesised to occur during a delay during signalling. Taken together, this further suggests that inside-out signalling could be a relevant consideration at this timescale. Within our model framework, models of signalling pathways can in future be incorporated, which could be used to inform the activation rates and to more thoroughly investigate mechanisms behind a delay. In addition to considering integrin activation, this model supports macroscale integrin diffusion and non-uniform initial conditions for the distribution of integrins across $X$. In many contexts, spatial clustering of integrins is a phenomenon of interest, and extensions of this framework could also be used to investigate mechanisms and consequences of spatial patterning.

### Numerical results: oscillatory loading

We now briefly consider the same oscillatory loading as investigated in Chapter 3 (imposed through the boundary conditions in Eq. 3.1.3) to see if the results are affected by the additional reactions. Initial conditions for the free integrins and adaptor proteins were chosen to be the uniform distributions

$$A(X,0) = 0.5, \qquad I(X,0) = 0.5, \tag{4.1.13}$$

and for each (high and zero) initial condition of $B$, the initial distribution of single-bound integrins was calculated from $I_A = 1 - A - B$. It remains the case that there

are two distinct adhesion states and a region of bistability, within which the eventual number of bound integrins $B_{tot}$ (Eq. 3.1.5) depends on the initial condition. An example of bistable behaviour, obtained when the amplitude of oscillation is $A = 0.1$, is shown in Fig. 4.10. Timecourses for the double-bound integrins ($B$) and the corresponding behaviour of the single-bound integrins ($I_A$), free integrins ($I$) and adaptor proteins ($A$) are shown when starting from zero and high initial conditions. In the case of the low adhesion state (following from the zero initial condition on $B$), we observe increased concentrations of both $I$ and $A$ at steady state (Fig. 4.10(a),(b)). This results from increased rupture and therefore an increased concentration of single-bound integrins, $I_A$, which may then become inactive. In both adhesion states, there is an oscillatory cycling between $I_A$ and $B$ integrins, with the amplitude of these oscillations corresponding to the amount of force-induced rupture that occurs.

## 4.2 Force-dependent strengthening

In addition to biochemical signalling within the cell, adhesion maturation is known to be facilitated by a force-dependent strengthening process. When integrins and talin undergo strain, cryptic binding sites on talin are exposed (Section 1.2.2). Vinculin, which is a key focal adhesion protein, can bind to these cryptic sites and also to the actin cytoskeleton, thereby reinforcing the link between integrins and the intracellular domain. This reinforcement is illustrated in Fig. 4.11 and discussed, for example, in [16, 66, 67].

To model this process we now consider two subpopulations of double-bound integrins. As in our previous model, there are double-bound integrins that are not reinforced by vinculin, represented by microscale distributions $b(x,t;X)$. Additionally we will consider microscale distributions of reinforced integrins, $b_v(x,t;X)$, which obey a second set of microscale advection–reaction equations. Since transitions between the two subpopulations depend on individual strains, we again use the local coordinate $x$ to represent the displacement of reinforced integrins from a zero stress position. At the macroscale, the reinforced integrins are denoted by $B_V(X,t)$, defined by

$$B_V(X,t) = \int_{-\infty}^{\infty} b_v(x,t;X)dx. \tag{4.2.1}$$

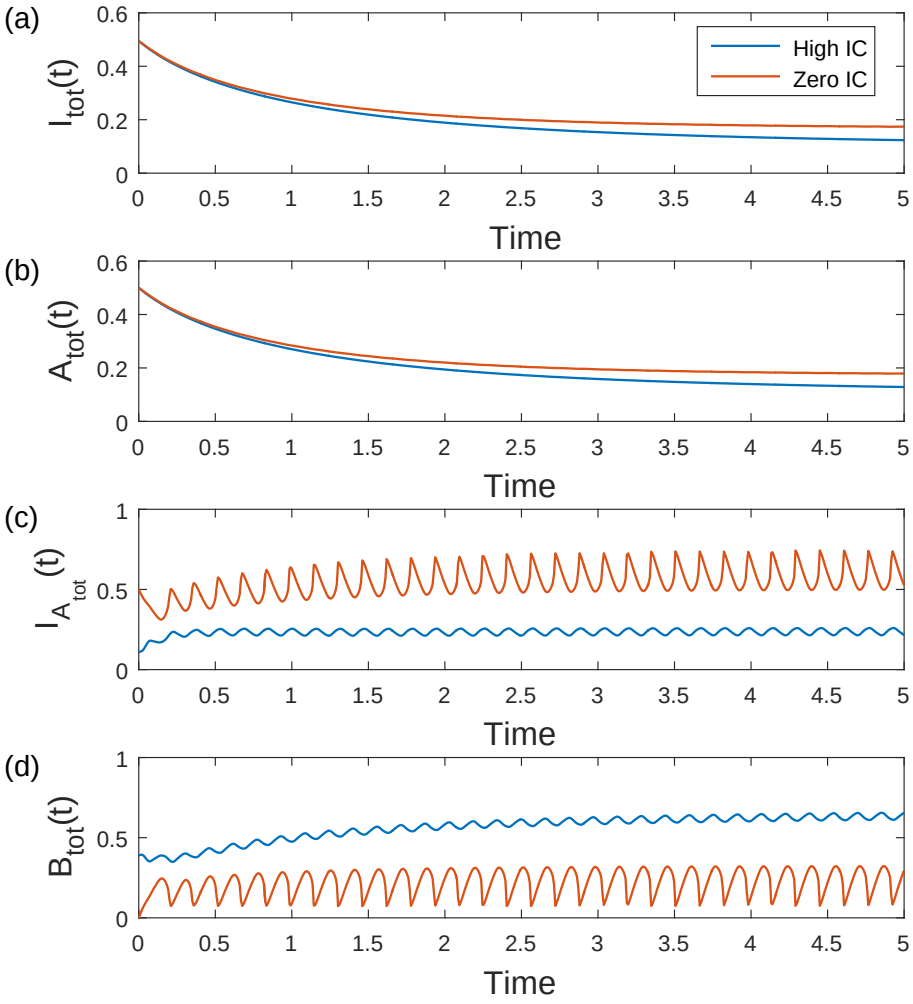


**Figure 4.10:** Timecourses for each of the 4 species: (a) free integrins, $I$, (b) adaptor proteins, $A$, (c) single-bound integrins, $I_A$, and (d) double-bound integrins, $B$, under an oscillatory loading with amplitude $A = 0.1$ (Eq. 3.1.3). The behaviours resulting from high and zero initial conditions for the number of double-bound integrins ($B$) are shown in blue and orange respectively, and bistability is observed. Total concentrations of each species are defined analogously to $B_{tot}$ in Eq. 3.1.5, and model parameters are given in full in Appendix B.

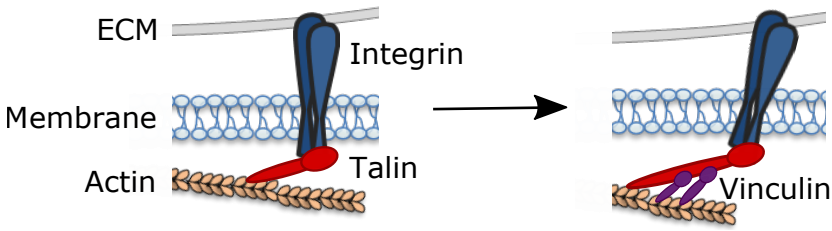


**Figure 4.11:** The adaptor protein talin connects integrin tails to actin. Under tension, talin unfolding takes place and cryptic binding sites are exposed. Vinculin can then bind to talin and to the actin cytoskeleton, reinforcing the link between integrins and the actin cytoskeleton.

The reaction schematic (cf. Eq. 4.1.1) is now

$$I + A \underset{k_D}{\overset{k_A}{\rightleftharpoons}} I_A \underset{k_{off}}{\overset{k_{on}}{\rightleftharpoons}} B \qquad B \underset{k_{weak}}{\overset{k_{str}}{\rightleftharpoons}} B_V \qquad B \xrightarrow{k_{off}} \varnothing \tag{4.2.2}$$

where the reaction rates $k_{on}$, $k_{off}$, $k_{str}$ and $k_{weak}$ all depend on microscale binding reactions, which have spatial rates $k_b(x)$, $k_u(x)$, $k_s(x)$ and $k_w(x)$ respectively. The first two of these are as described in Chapter 2; the remaining two will be described below.

The governing equations in dimensionless form are

$$\frac{\partial A}{\partial t} = -k_A I A + k_D(1 - A - B - B_V), \tag{4.2.3}$$

$$\frac{\partial I}{\partial t} = D\nabla_X^2 I - k_A I A + k_D(1 - A - B - B_V), \tag{4.2.4}$$

$$\frac{\partial b}{\partial t} + \frac{V(X,t)}{\delta}\frac{\partial b}{\partial x} = \eta k_b(x)(1 - A - B - B_V) - k_u(x)b - k_s(x)b + k_w(x)b_v, \tag{4.2.5}$$

$$\frac{\partial b_v}{\partial t} + \frac{V(X,t)}{\delta}\frac{\partial b_v}{\partial x} = k_s(x)b - k_w(x)b_v - k_u(x)b_v, \tag{4.2.6}$$

where $k_s(x)$ denotes the rate function (at the microscale) for transitions from $b$ to $b_v$-type integrins, and $k_w(x)$ regulates the reverse rate. The transition terms cancel when considering the distribution of all double-bound integrins, given by $b_{tot}(x,t;X) = b(x,t;X) + b_v(x,t;X)$, which results in $b_{tot}$ obeying the previous governing equation in Eq. 4.1.4. The nondimensionalisation is similar to previous models; we have used the scalings in Eq. 2.2.26 and Eq. 4.1.5 along with

$$k_s = \hat{k}_s/\hat{f}_1, \qquad k_w = \hat{k}_w/\hat{f}_1, \tag{4.2.7}$$

for the maximum integrin binding rate $\hat{f}_1$ (Eq. 2.1.2). Even though the $b_v$-type integrins have a reinforced connection to the actin cytoskeleton via vinculin, they are still able to unbind from the ECM. We model this by the same spatial unbinding function $k_u(x)$ as used for the $b$-type integrins (Eq. 2.2.7) and allow $b_v$-type integrins to transition directly to $I_A$ integrins. This introduces the simplification that vinculin can only be attached to double-bound integrins; after the unbinding of $b_v$ to $I_A$-type integrins the reinforcement is therefore lost. The conservation of adaptor proteins now requires $I_A + A + B + B_V = 1$.

To represent the strain-dependent adhesion strengthening as cryptic binding sites are exposed, we use the piecewise linear function

$$k_s(x) = \begin{cases} s_1\left(|x| - 1\right), & |x| > 1, \\ 0, & \text{otherwise.} \end{cases} \tag{4.2.8}$$

Within the integrin binding range (see Eq. 2.2.6), there is no additional strengthening. However, the strengthening rate increases linearly at rate $s_1 > 0$ as the extension $|x|$ exceeds this binding range and cryptic sites are revealed. In reality this rate will not increase indefinitely, but since bound integrins unbind at a finite maximum extension (Eq. 2.2.7) we do not enforce an extra condition for large $|x|$.

For the reverse transition ($b_v$ to $b$-type integrins) we assume a low uniform degradation rate

$$k_w(x) = w_1, \tag{4.2.9}$$

for rate constant $w_1 > 0$.

In our model formulation, the bound integrin population at each macroscale point $X$ behaves as a linear spring that connects the actin cytoskeleton to the ECM. The effective spring constant of this linear spring changes with the bound integrin distribution, $b(x, t; X)$. Since vinculin binding leads to an additional physical link between integrins and the cytoskeleton (Fig. 4.11), the reinforced integrin complexes will have an increased effective stiffness and generate an increased drag force between the cytoskeleton and the ECM. We therefore define a spring constant, $\kappa\lambda_b$, for individual integrins of $b_v$-type where $\lambda_b$ is the spring constant for individual $b$-type integrins (without vinculin-reinforcement) and $\kappa > 1$ is a constant scale factor. The dimension-

less equation for the drag force (cf. Eq. 2.2.30) is therefore

$$F(X,t) = \int_{-\infty}^{\infty} x\left(b(x,t;X) + \kappa b_v(x,t;X)\right) dx, \tag{4.2.10}$$

which will replace Eq. 2.2.30 in the solution of the macroscale governing equations (Eq. 2.2.31). The solution of the macroscale system otherwise remains the same.

### Response to shear

Due to the strain-dependent strengthening rate (Eq. 4.2.8), vinculin binding cannot occur without some external forcing. Numerical tests confirm that this is the case; in the absence of external forcing the results (not shown) are identical to those in the previous section. In order to investigate force-dependent strengthening, we therefore must impose a relative motion between the cell and the ECM. To begin with, we investigate the effect of a simple shear. This is imposed through the boundary condition

$$U_E(0,t) = \alpha t, \tag{4.2.11}$$

where $\alpha$ controls the magnitude of the shear. The temporal evolution of microscale distributions of the $b$- and $b_v$-type integrins (Fig. 4.12), sampled at $X = 0.5$ when $\alpha = 0.2$ (Eq. 4.2.11) show that both distributions are skewed towards positive $x$ values; however, the distribution of $b(x,t;0.5)$ decreases in height within the range $1 < x < 1.5$ as the integrins undergo strain and transition into $b_v$- type integrins.

Steady state microscale distributions of the $b$- and $b_v$-type integrins, sampled at $X = 1$ (Fig. 4.13), show that both types of distributions become increasingly skewed for increasing shear magnitude. Although the double-bound integrin distributions, $b(x,t)$, decrease monotonically in height as $\alpha$ increases, the vinculin-reinforced integrin distributions, $b_v(x,t)$, initially increase and then decrease in height. Strengthening of integrins is induced under small strains. These then begin to rupture after an optimum (or threshold) strain is reached. This behaviour is mirrored in the macroscale vinculin-bound integrin density, $B_{V_{tot}}$ (defined analogously to Eq. 3.1.5), shown in Fig. 4.14. The non-monotonic behaviour is reminiscent of catch bond behaviour, where adhesions have been observed to first strengthen and then rupture under force [83].

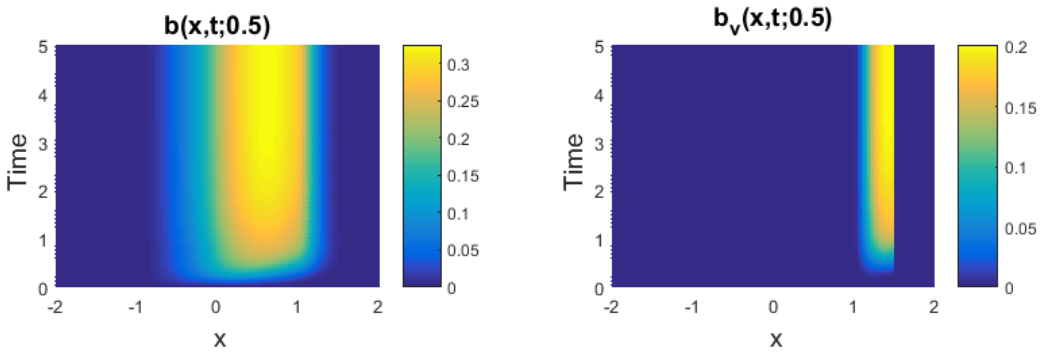


**Figure 4.12:** Evolution of the microscale distributions of $b$- and $b_v$-type integrins, sampled at $X = 0.5$ with a shear amplitude $\alpha = 0.2$ (Eq. 4.2.11). The relative stiffness of $b_v$-type integrins was set to $\kappa = 2$ (Eq. 4.2.10).

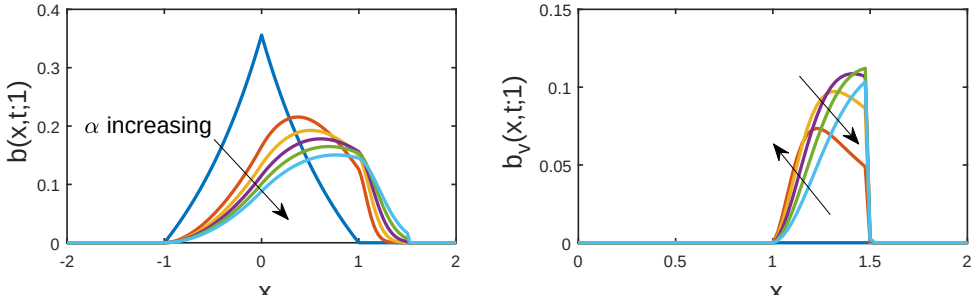


**Figure 4.13:** Steady state microscale distributions of the $b$- and $b_v$-type integrins, sampled at $X = 1$, for varying amplitudes, $\alpha$, of shear (Eq. 4.2.11). Here the relative stiffness of $b_v$- and $b$-type integrins is $\kappa = 2$ (Eq. 4.2.10).

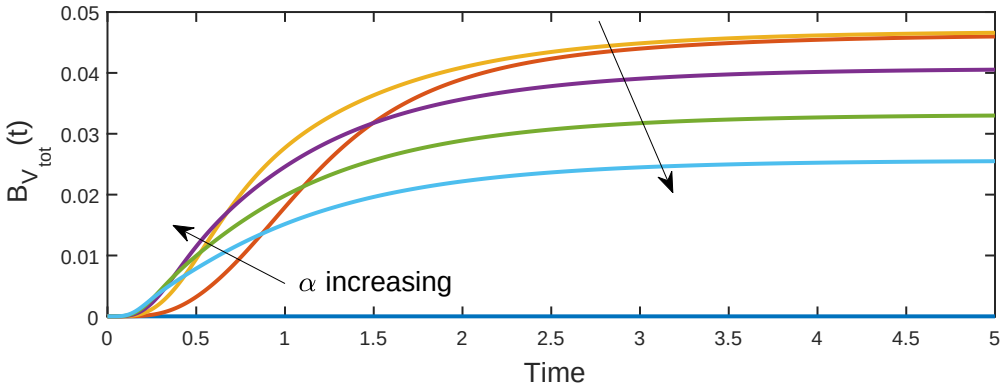


**Figure 4.14:** Macroscale vinculin-bound integrin density, $B_{V_{tot}}$ (defined analogously to Eq. 3.1.5), for $\alpha$ increasing from 0 to 0.5 in steps of 0.1 (Eq. 4.2.11). Under small strains, there is first an increase in density due to strengthening of integrins. For larger strains, these begin to rupture and the densities decrease. Full parameter values are given in Appendix B.

### Response to oscillatory loading

We now reintroduce tidal oscillations of the ECM using the boundary conditions in Eq. 3.1.3. We will examine the behaviour of both subpopulations of double-bound integrins as the amplitude, $A$, of oscillation varies. In addition to the bound integrin response, the effect of oscillations on each of the species in the extended reaction sequence (Section 4.1) is shown.

Due to the oscillations, there is some low amplitude oscillatory cycling between actin-bound ($I_A$) and double-bound ($B$) integrin states (Fig. 4.15). The Gaussian initial distribution of unbound integrins (Eq. 4.1.10) we have used produces an increased density of bound integrins near the centre of the domain (as in Fig. 4.2). However, since the binding of vinculin to cryptic talin binding sites is strain-dependent, the reinforced bound integrins ($B_V$) are concentrated close to $X = 0$, where the load is applied. The peak concentration of $B_V$ occurs at approximately $X = 0.2$, rather than at $X = 0$, as a result of a trade-off between strain-dependent bond strengthening and bond rupture.

Microscale distributions of the reinforced integrins, $b_v(x,t)$, at $X = 0$, $X = 0.5$ and $X = 1$ (Fig. 4.16) show that they initially bind in the range $1 < |x| < s$ (see Eqs. 4.2.8, 2.2.7). At $X = 0$ the relative motion of the cell and ECM is the highest. There is a large amount of rupture, and the low number of remaining bonds are advected back-and-forth across the full range of $|x| \leq s$ values. At $X = 0.5$, damping of the oscillatory load allows for a higher survival of $b_v$-type integrins. Unlike at $X = 0$, the distributions no longer span the full range of $|x| \leq s$; two distinct peaks in the distributions are seen for positive and negative $x$ and these remain separated due to reduced advection. At $X = 1$ there is further damping, which continues to reduce the advection of the distribution. This time, however, the damping results in a lower density of $b_v$-type integrins because of the smaller strain. We see that there is a trade-off between the amount of strain required for the formation and for the survival of $b_v$-type integrins; in this case the optimum, seen in Fig. 4.15, occurs at approximately $X = 0.2$.

Under high amplitude oscillatory loading of the ECM (Fig. 4.17) we observe the rupture regime, rather than the high adhesion regime (Chapter 3). This results in much clearer cycling between $I_A$ and $B$ integrin states. Even though there is damping of the

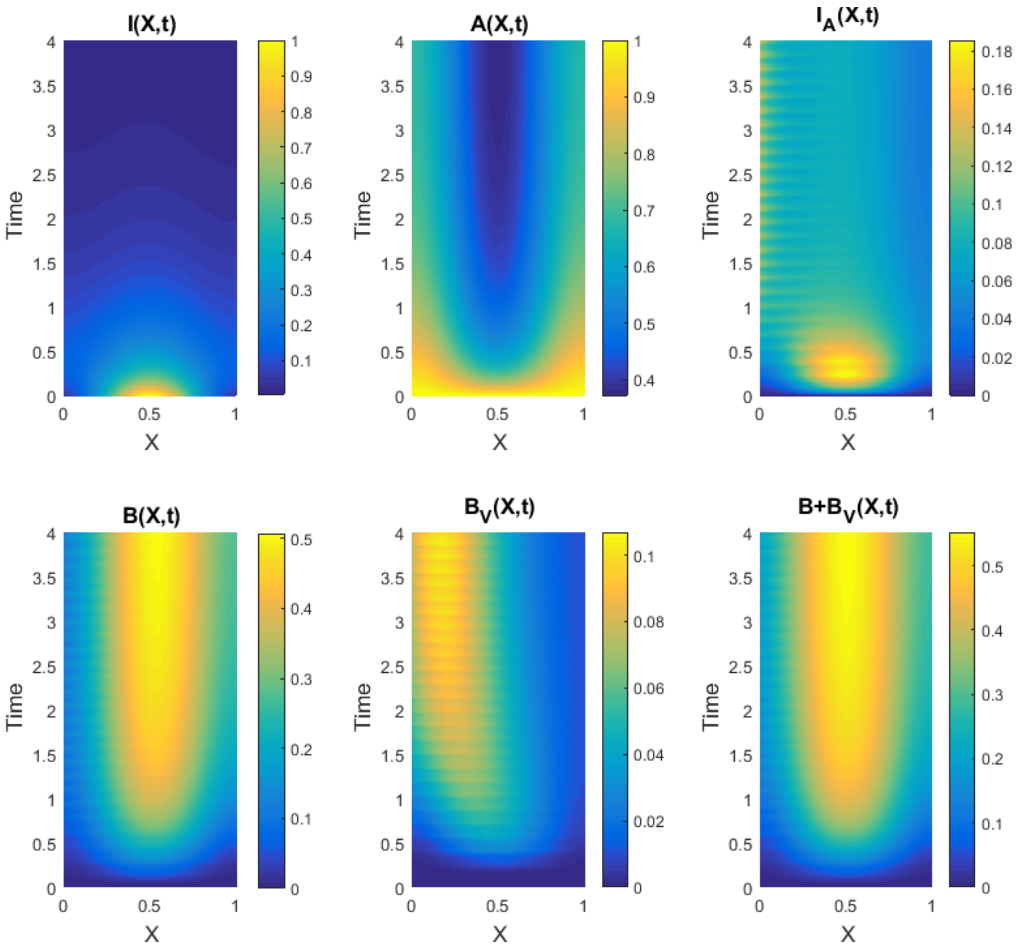


**Figure 4.15:** Spatiotemporal evolutions of each of the macroscale species (Eqs. 4.2.3–4.2.6) with $\kappa = 2$, $s_1 = 50$, $k_A = 2$, $k_D = 0.1$, $D = 0.05$ and a low amplitude oscillatory loading of the ECM ($A = 0.05$ in Eq. 3.1.3). In the initial Gaussian distribution of unbound integrins (Eq. 4.1.10), $\mu = 0.5$ and $\sigma = 0.2$. In Eq. 2.2.7, we have used $s = 1.5$.

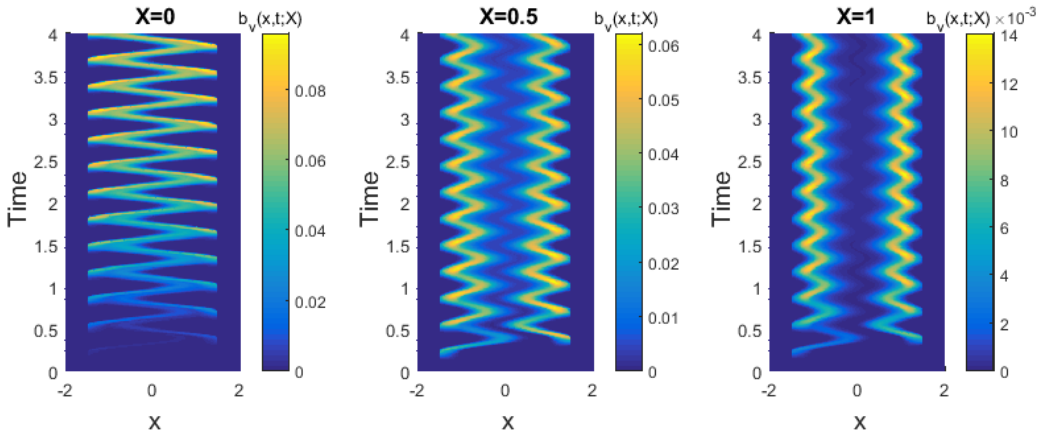


**Figure 4.16:** Microscale distributions of reinforced integrins, $b_v(x,t;X)$, sampled at $X = 0$, $X = 0.5$ and $X = 1$ under low amplitude oscillatory loading, $A = 0.05$, of the ECM. Distributions correspond to the macroscale species $B_V$ in Fig. 4.15; lower values of $b_v(x,t;X)$ are seen as $X$ increases.

oscillatory load across $X$, cycling between $I_A$ and $B$ states occurs throughout the domain, indicating that high amounts of force are experienced across $X$. There is therefore no longer a higher concentration of reinforced integrins ($B_V$) near $X = 0$, and the macroscale distribution of $B_V(X,t)$ is instead approximately proportional to the macroscale distribution of bound integrins, $B(X,t)$. A slight asymmetry is observed, with increased survival of integrins for larger $X$, due to an increase in damping (and therefore reduced rupture) with $X$.

The corresponding microscale distributions of the reinforced integrins, $b_v(x,t)$, (Fig. 4.18) show that the concentrations of reinforced integrins are highest within the range $1 < |x| < s$, where vinculin binding occurs (see Eqs. 4.2.8, 2.2.7). However, due to larger amplitude oscillations, there is now advection of bonds across the whole range of $|x| \leq s$ values. These distributions therefore no longer exhibit two distinct peaks (*e.g.* as seen in the distributions in Fig. 4.16), and a separation between positive and negative $x$ values is not seen.

The level of strain experienced by integrins will be affected by material parameters such as cell and substrate stiffnesses. We therefore investigate the effect of substrate stiffness on the averaged density, $\langle B_{V_{tot}} \rangle$ (defined analogously to $\langle B_{tot} \rangle$ in Eqs. 3.1.5, 3.1.6), of vinculin-reinforced integrins at steady state for a range of oscillation amplitudes, $A$ (Fig. 4.19). We find that increased substrate stiffness increases the density of

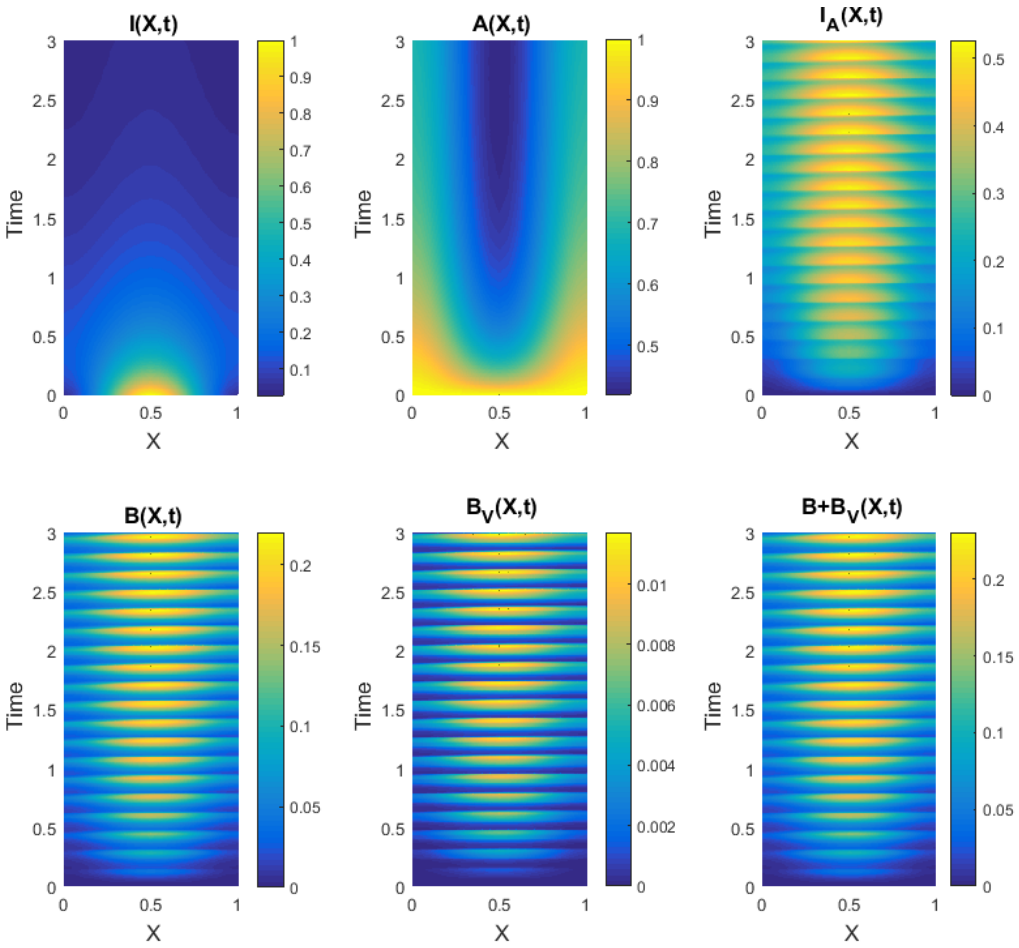


**Figure 4.17:** Spatiotemporal evolutions of each of the macroscale species (Eqs. 4.2.3–4.2.6) with $\kappa = 2$, $s_1 = 50$, $k_A = 2$, $k_D = 0.1$ and $D = 0.05$ and an oscillatory loading of the ECM (Eq. 3.1.3 with $A = 0.15$). In the initial Gaussian distribution of unbound integrins (Eq. 4.1.10), $\mu = 0.5$ and $\sigma = 0.2$ respectively. In Eq. 2.2.7, $s = 1.5$.

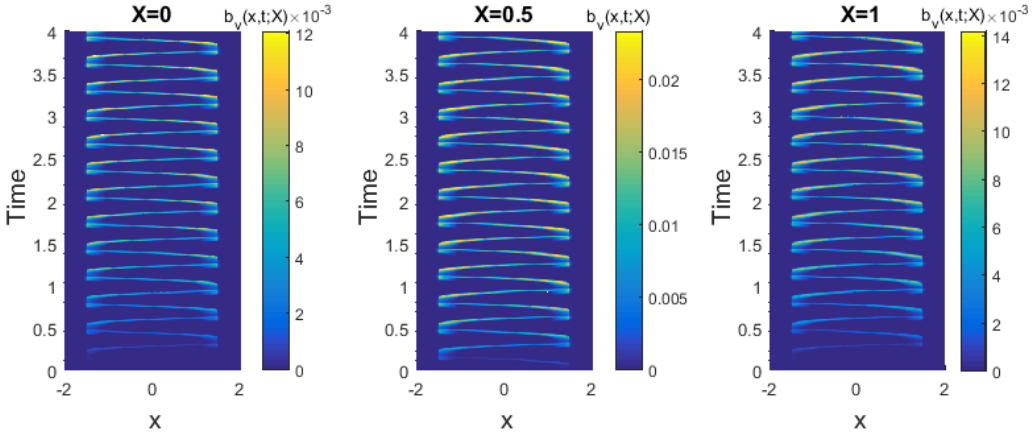


**Figure 4.18:** Microscale distributions of reinforced integrins, $b_v(x,t;X)$, sampled at $X = 0$, $X = 0.5$ and $X = 1$ under higher amplitude oscillatory loading, $A = 0.15$. Distributions correspond to $B_V$ in Fig. 4.17.

vinculin-bound integrins for low oscillation amplitudes, since enhanced propagation of the oscillatory load leads to increased strain. Cryptic binding sites will therefore be revealed at lower values of $A$ compared to the case with a more compliant substrate. Also due to increased force propagation, the threshold for rupture occurs at a lower value of $A$ for stiff substrates.

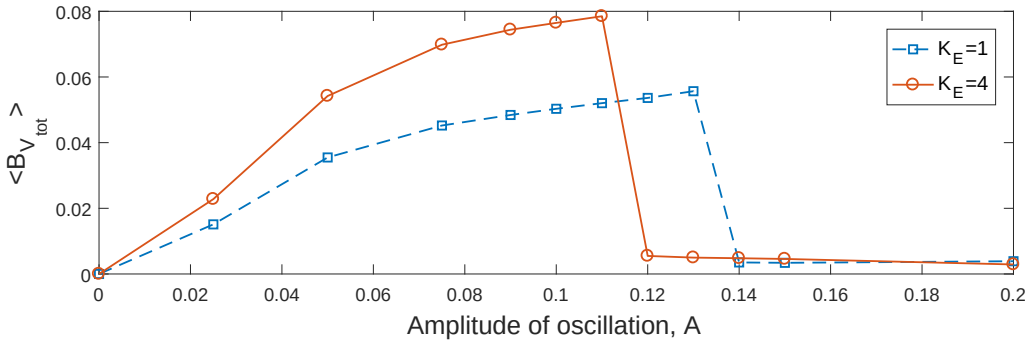


**Figure 4.19:** Averaged density, $\langle B_{V_{tot}} \rangle$, of vinculin-reinforced integrins at steady state for a range of oscillation amplitudes, $A$, from a zero initial condition. We consider two substrate stiffnesses: $K_E = 4$ (solid line) and $K_E = 1$ (dashed). The quantity $\langle B_{V_{tot}} \rangle$ is defined analogously to $\langle B_{tot} \rangle$ in Eqs. 3.1.5 and 3.1.6. Full parameter values are detailed in Appendix B.

In this section, we have shown that, with the inclusion of the vinculin-mediated force-dependent strengthening mechanism, more complex behaviours are observed in response to deformation. Due to competition between adhesion rupture and reinforcement, small amounts of deformation can now encourage the persistence of adhesions

(Fig. 4.14). This non-monotonic response to load is well-known to occur [67, 83] and is an example of the mechanosensitive (as well as mechanotransductive) nature of integrins. With this mechanism present, integrins are sensitive to environmental factors such as cell and substrate stiffness (Fig. 4.19). These types of phenomena can be studied further in our multiscale framework due to the ability to include strain-dependent integrin dynamics in the microscale description. In the context of the lung, deformations and material properties will vary spatially as well as temporally at both the cell and tissue level. Additionally there will be differences in material stiffnesses between healthy and asthmatic airways. As demonstrated in these preliminary results, adhesions will be sensitive to these changes, highlighting the need for future consideration of microscale adhesion dynamics in tissue-level mechanical models.

## 4.3 Investigating the duration between DIs and integrin recovery rate

In this section, we discuss a recent experimental result by Mailhot-Larouche *et al.* [95] from an *in vitro* study designed to investigate how the duration between deep inspirations (DIs) affects the rate of airway renarrowing after a DI (Section 1.1.2). We then explore whether our existing modelling frameworks can account for the observed behaviours or if further model extensions are required.

### 4.3.1 Experimental protocol and results

In the *in vitro* study of Mailhot-Larouche *et al.* [95], sinusoidal length oscillations were applied to isolated guinea pig bronchi to mimic tidal breathing and DIs. The goal of their study was to investigate how the time between large amplitude oscillations representing DIs affected the return of ASM to its initial contractile state. To initialise the experiment, three large amplitude oscillations were administered, which were described to correct for any history effects. Following this, lower amplitude oscillations representing tidal breathing were applied for a period of time, $T_1$, before a further large amplitude oscillation representing a DI. After this, the procedure (of simulating tidal breathing and then a single DI) was repeated for three further time intervals, $T_2$–$T_4$ of tidal breathing. The time intervals $T_1$–$T_4$ were chosen in a random order from $T = 2$, 5, 10 and 30 minutes. Length changes for tidal breathing and DIs were chosen as 6% and 36% of the original length respectively and, throughout the process, the contractile force generated by ASM was recorded. A schematic of the

oscillation protocol is shown in Fig. 4.20.

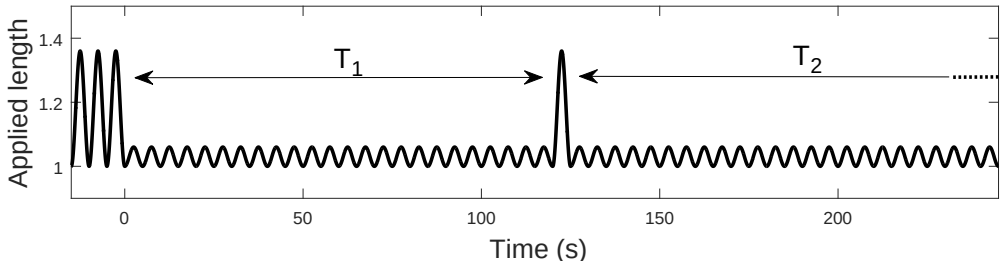


**Figure 4.20:** Schematic of the length oscillations applied in the experimental protocol of Mailhot-Larouche *et al.* [95]. Sinusoidal oscillations have frequency 0.2Hz and tidal breathing and DIs are represented by length changes of 6% and 36% respectively. Times, $T_1$–$T_4$, between DIs (shown here with $T_1 = 2$ minutes) were chosen in a random order from $T = 2$, 5, 10 and 30 minutes.

For the experiment described above, two differing contractile states induced by either methacholine (a contractile agonist) or isoproterenol (a relaxant) were used. In each contractile state, the bronchodilatory ability of the DI was observed to be unaffected by the interval, $T$, between DIs (Fig. 4.20). However, in the contracted state, the interval between DIs did have an effect on the rate of recovery of contractile force post-DI. Interestingly, and perhaps counterintuitively, a faster return to the initial contractile state was observed when the interval between DIs was reduced, suggesting that more frequent DIs provide shorter periods of bronchodilatory relief compared to those taken further apart. In addition to a faster recovery to a contracted state, the extent of force recovery was also higher. The authors emphasise that the mechanisms behind this result cannot be identified from their study; however, they suggest that both the actomyosin contractile units responsible for force generation and the physical link responsible for transmitting these forces to the ECM (i.e. cell–matrix adhesions) could play a role. They suggest that any of these components could be disrupted during DIs and that their rate of repair would correlate with the rate of return to the contractile state. The authors further hypothesise that the relevant machinery for repair may still be active shortly after DIs, thereby leading to faster force recovery when there is a shorter duration between subsequent DIs.

In our Chapter 3 results, simulated DIs induced adhesion rupture to a low bound integrin state followed by a recovery to a high bound state (Fig. 3.13(a)). Motivated by the experimental observations of Mailhot-Larouche *et al.* [95], we now investigate if any factors in our models can influence the rate at which this recovery occurs.

### 4.3.2 Numerical experiments

In the following simulations, we use the 4 species model introduced in Section 4.1. We replicate the protocol for the first DI in Fig. 4.20 by applying the boundary condition

$$U_E(0,t) = \begin{cases} \alpha_2 \sin(\omega t) & t < \frac{6\pi}{\omega}, \\ \alpha_2 \sin(\omega t) & \frac{2\beta\pi}{\omega} < t \leq \frac{2(\beta+1)\pi}{\omega}, \\ \alpha_1 \sin(\omega t) & \text{otherwise}, \end{cases} \tag{4.3.1}$$

where $\alpha_1$ and $\alpha_2$ are amplitudes simulating tidal breathing and DIs respectively, and $\omega/2\pi$ is the frequency of the oscillations. The DIs are applied for the first 3 cycles and then for one further cycle at a later time, controlled by the parameter $\beta$. The time interval before the DI is given by $T = \frac{2(\beta-3)\pi}{\omega}$. In the experiments, further DIs are applied for a sequence of time intervals, selected in a random order (Fig. 4.20). Their results are treated independently of order; we therefore simulate the first DI only, for varying times $T$. For the initial conditions we assume that the double-bound integrins, $B(X,0)$, are uniform and at a saturated steady state, corresponding to the steady state distribution in Eq. 3.1.4. We set $I_A(X,0) = 0$ and, to ensure conservation of adaptor proteins, $A(X,0)$ is then calculated from $A = 1 - I_A - B$.

In the first instance we consider the case where the activation and deactivation rates, $k_A$ and $k_D$, are zero. This reduces the model to the continuum model of Chapter 2, where there are transitions between actin-bound ($I_A$) and double-bound ($B$) integrins only. The response of both of these species to the boundary condition in Eq. 4.3.1 when $\beta = 12$, 18 and 24 (Fig. 4.21) shows unbinding of bound integrins after DIs (seen by increases in the concentration of $I_{A_{tot}}$ and reductions in $B_{tot}$) followed by a return to the pre-DI (oscillatory) steady state. For each of the three values of $\beta$ the behaviour appears to be very similar. Overlaying each of the timecourses post-DI (Fig. 4.22) shows that the recovery is in fact identical in both rate and amplitude. This can be understood from Fig. 4.21 since the $I_A$ and $B$ integrins are seen to have reached an equilibrium long before the $\beta = 12$ DI is applied. DIs at any subsequent times would therefore have the same initial condition and induce the same response. In this model, the conservation law $A + I_A + B = 1$ holds. Since $A$ is constant when $k_A = k_D = 0$, there is also conservation of $I_A + B$. After the DI-induced transition of $B$ to $I_A$, the actin-bound integrins $I_A$ are therefore readily available for rebinding, which is seen here to occur over just a few cycles. This conservation means that the magnitude of bound integrin recovery cannot differ. Due to the lack of activation or deactivation

in the 2-state model, differing recovery rates via the type of mechanism proposed by Mailhot-Larouche *et al.* [95] cannot be achieved; we therefore now consider the effect of including activation and deactivation of the integrins.

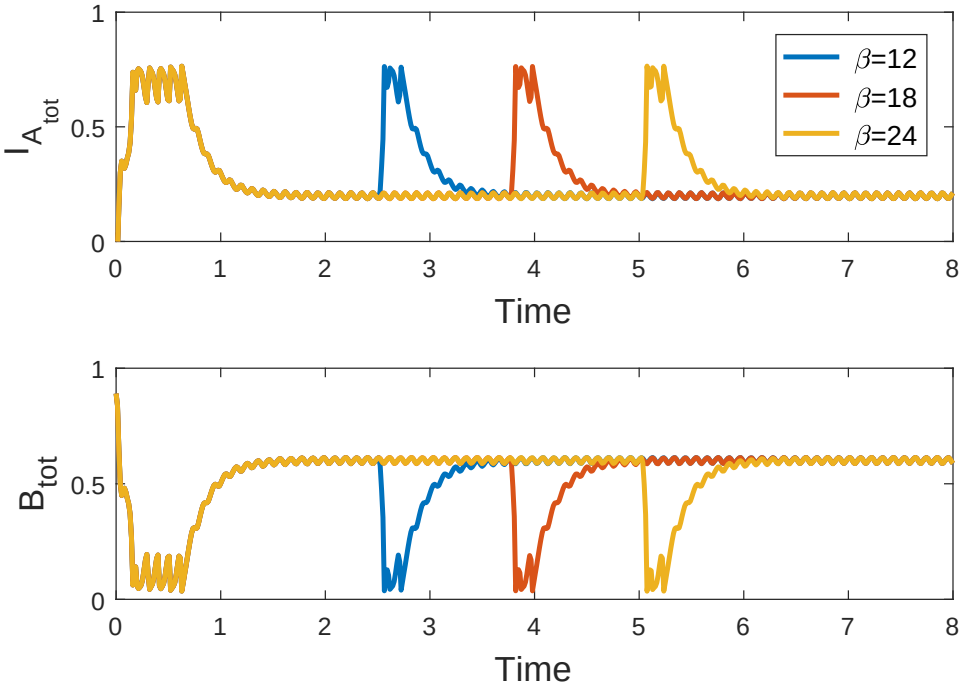


**Figure 4.21:** Timecourses for the total concentrations of actin-bound ($I_A$) and double-bound ($B$) integrins when the ECM is subject to the boundary conditions in Eq. 4.3.1 and there is no activation or deactivation ($k_A = k_D = 0$).

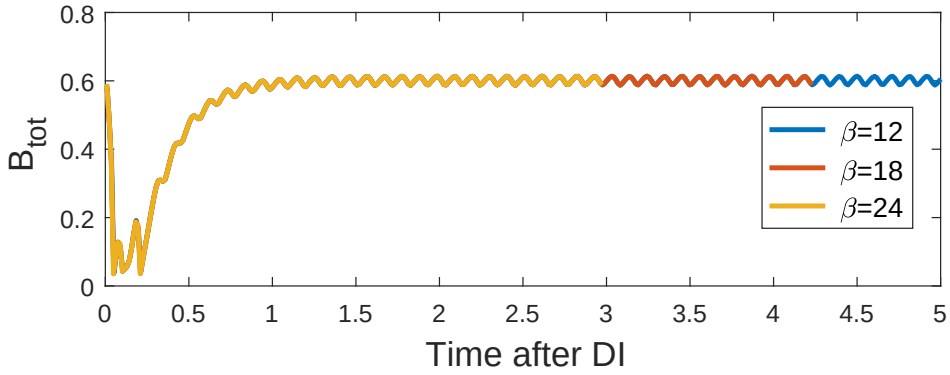


**Figure 4.22:** Overlayed timecourses of $B_{tot}$ (shifted by time $2\beta\pi/\omega$) from Fig. 4.21, showing identical recoveries of double-bound integrins after a DI.

For a non-zero deactivation rate, $k_D$, some of the $I_A$ integrins created during the initial DIs are deactivated instead of being readily available for rebinding. Timecourses of $A_{tot}$, $I_{A_{tot}}$ and $B_{tot}$ for $k_A = 1$ and $k_D = 4$ show a slowed recovery of $B_{tot}$ after the

initial DIs (Fig. 4.23) compared to Fig. 4.21. If subsequent DIs are taken during this initial recovery (Fig. 4.24), differing behaviours are seen for each value of $\beta$. This occurs since the system has not reached equilibrium as it had in Fig. 4.21, but we in fact see the opposite effect on recovery rate to that observed by Mailhot-Larouche *et al.* [95]. At earlier times (*e.g.* $\beta$=12), the total amount of $I_A + B$ is lower (reflected in higher $A$, where $A = 1 - I_A - B$) and rebinding is therefore slower. The differences we observe are only small; however, this effect will become more pronounced for more dramatic changes in $A$. In the overlayed timecourses (Fig. 4.24), the magnitude of recovery appears to be the same.

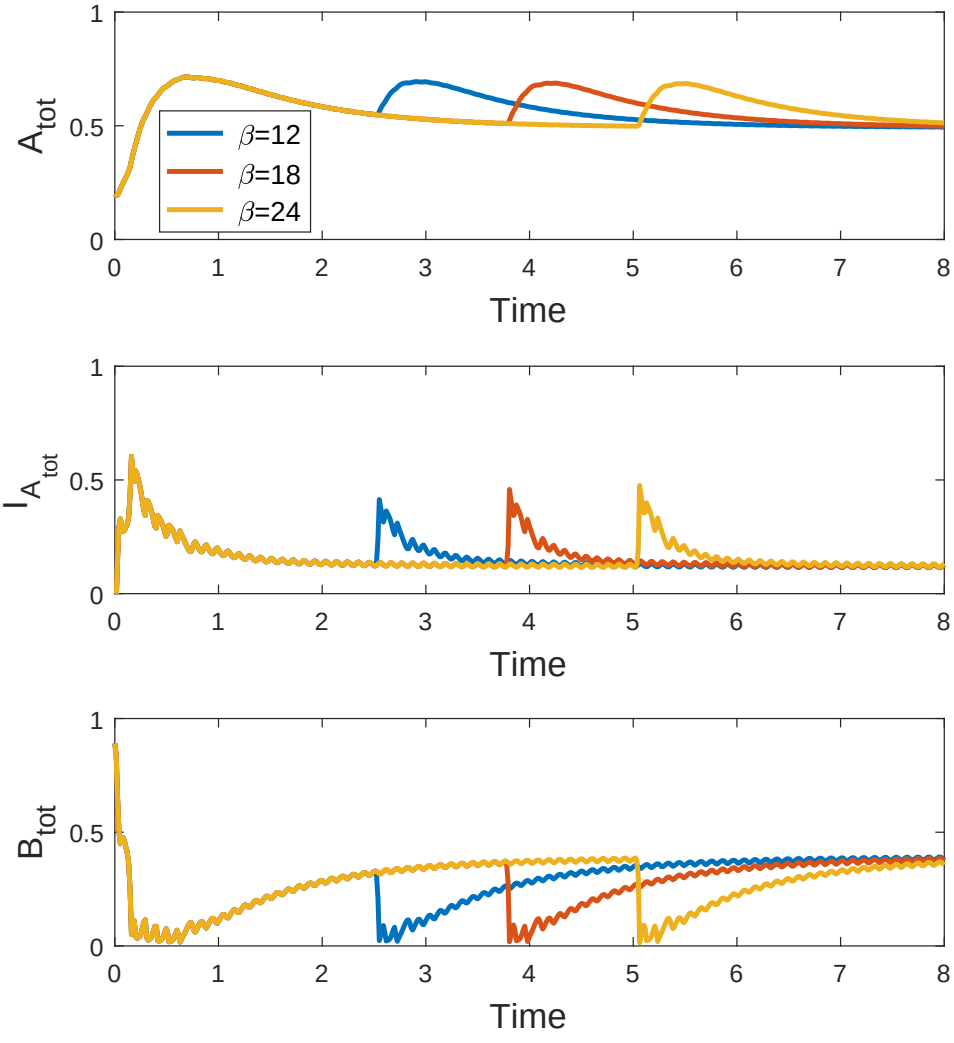


**Figure 4.23:** Timecourses for the total concentrations of adaptor proteins ($A$), actin-bound integrins ($I_A$) and double-bound ($B$) integrins when the ECM is subject to the boundary conditions in Eq. 4.3.1 and when $k_A = 1$, $k_D = 4$.

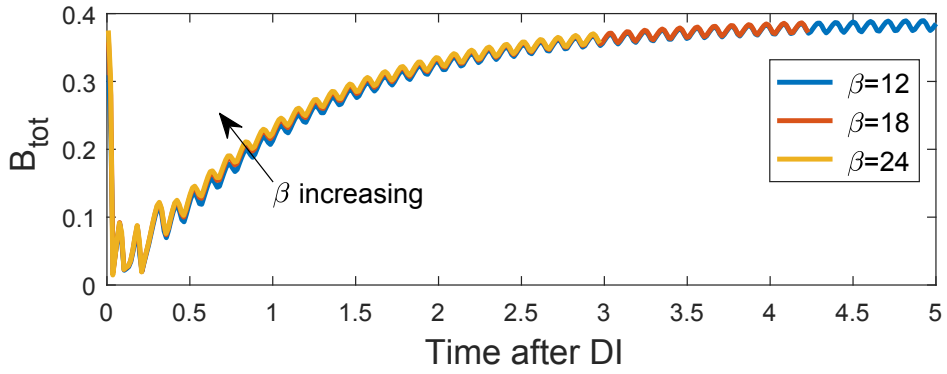


**Figure 4.24:** Overlayed timecourses of $B_{tot}$ (shifted by time $2\beta\pi/\omega$) from Fig. 4.23, showing a slightly faster recovery of $B_{tot}$ with an increased time interval between DIs.

By increasing the activation rate, $k_A$, for a fixed time interval ($\beta = 12$) between DIs (Fig 4.25), we observe that increased availability of $I_A$ integrins allows for a faster recovery of $B_{tot}$. Direct comparison for two different values of $k_A$ (Fig. 4.25) shows that the magnitude of the steady bound-integrin state also changes if this is modified. Alongside a faster recovery rate, a higher fraction of bound integrins is obtained when $k_A$ is larger.

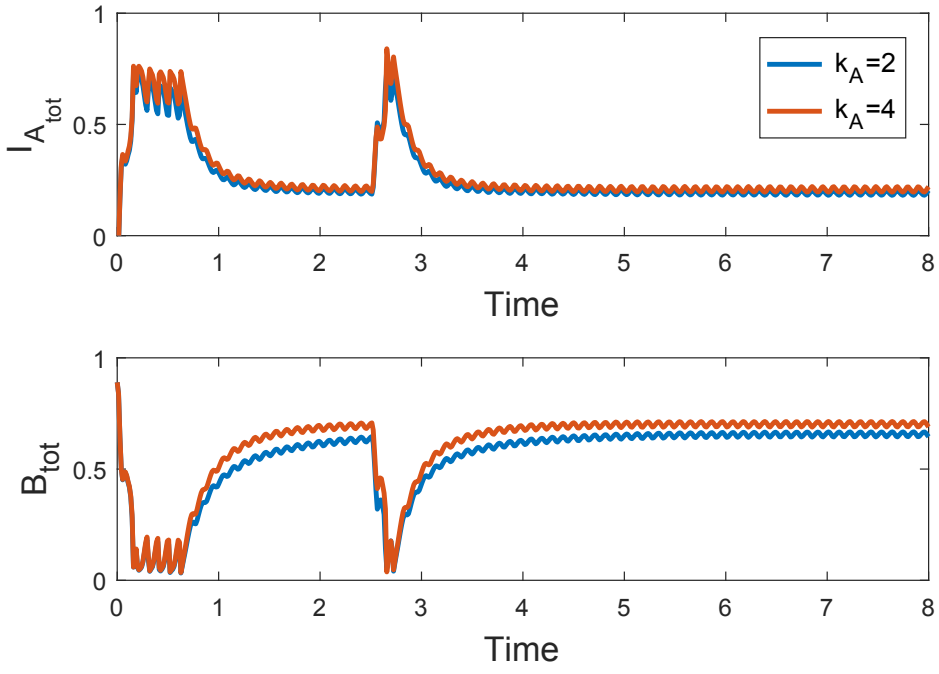


**Figure 4.25:** Timecourses for the total concentrations of actin-bound integrins ($I_A$) and double-bound ($B$) integrins when the ECM is subject to the boundary conditions in Eq. 4.3.1 with $\beta = 12$. The activation rate is $k_A = 2$ (blue) or $k_A = 4$ (orange), and deactivation is fixed at $k_D = 1$.

In the experimental results, the magnitude and rate of force recovery increased as the time interval, $T$, between DIs was reduced. Based on the results in Fig. 4.25 we hypothesise that a transient increase in activation rate, which then decays, could therefore produce this behaviour. As a simple test of this concept we consider a temporary increase in integrin activation rate, which could perhaps be triggered by the initial DIs (force can trigger inside-out integrin activation [3] and can also drive the recruitment and binding of adaptor proteins [84]). We use a time-dependent rate of the form

$$k_A(t) = 2 + c\left(\frac{b^a t^{a-1} e^{-bt}}{\Gamma(a)}\right) \tag{4.3.2}$$

where $\Gamma(a)$ is the Gamma function, defined by $\Gamma(a) = (a-1)!$, and a Gamma distribution is added to a baseline level of $k_A = 2$. This is shown in Fig. 4.26 for the parameters $a = 2.1$, $b = 1.5$ and $c = 12$, which yield a peak shortly after the initial DIs with a subsequent decay.

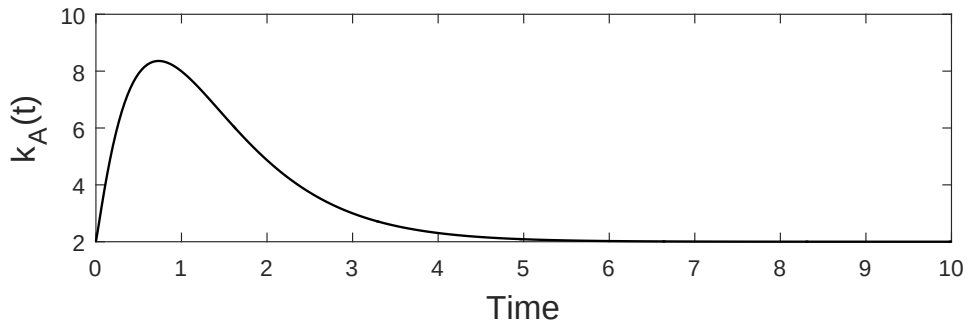


**Figure 4.26:** Time-dependent activation rate, given by Eq. 4.3.2 with $a = 2.1$, $b = 1.5$ and $c = 12$ .

Timecourses of $A_{tot}$, $I_{A_{tot}}$ and $B_{tot}$ (Fig. 4.27) show a dip in $A_{tot}$ due to the increased activation, which then slowly recovers. DIs taken during this time therefore have increased access to $I_A$ integrins, and moreso at earlier times. The bound integrin fraction therefore recovers more quickly for smaller time intervals (Fig. 4.28). The magnitude of bound integrin recovery is also greater at earlier times during this transient period. However, since there is a decay back to baseline (Fig. 4.26), the difference in the magnitudes of bound integrin recovery are reduced for $\beta = 18$ and $\beta = 24$; we additionally see that the magnitudes are approaching the same steady value over time. This is because the density of $I_A$ integrins eventually settles back to its baseline steady state, and once at a steady state (*e.g.* Fig. 4.22), changes in recovery cannot be obtained. Taken together, these results show that transient changes in the activation rate are a possible mechanism by which the experimentally observed behaviour can be explained. Moreover, if this is indeed a viable mechanism, the decay back

to a baseline activation rate would need to exceed 30 minutes for the experimental observations to be fully recapitulated.

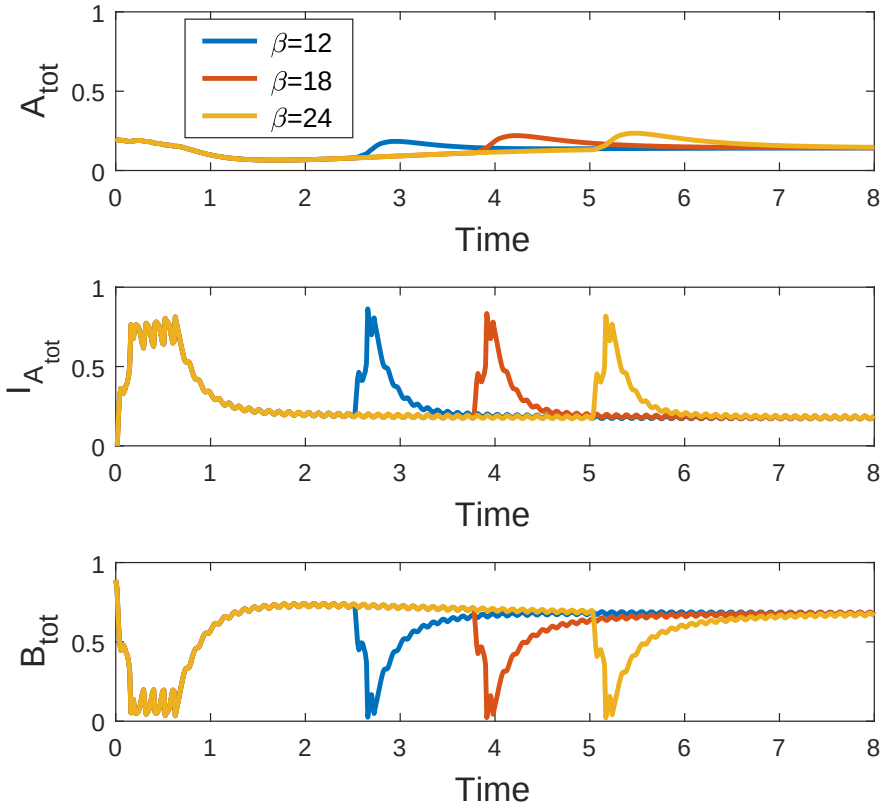


**Figure 4.27:** Timecourses for the total concentrations of adaptor proteins ($A$), actin-bound integrins ($I_A$) and double-bound ($B$) integrins with $k_D = 1$ and the time-dependent activation rate in Fig. 4.26.

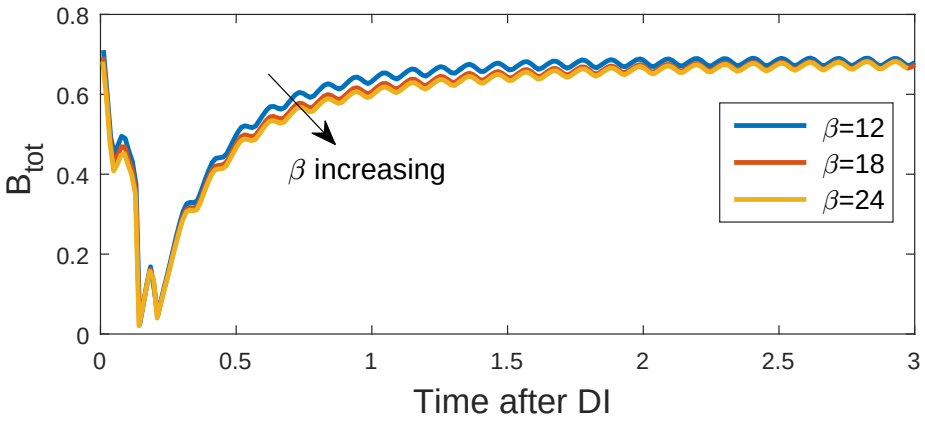


**Figure 4.28:** Overlayed timecourses of $B_{tot}$ (shifted by time $2\beta\pi/\omega$) from Fig. 4.27, showing slightly faster recovery of $B_{tot}$ with an reduced time interval between DIs.

## 4.4 Conclusions

In this chapter, we considered the activation, diffusion and strain-dependent reinforcement of integrins. This allowed us to investigate a wider range of adhesion behaviours, and demonstrates that our multiscale continuum framework (developed in Chapter 2) is amenable to both macroscale and microscale extensions.

Firstly, in Section 4.1, we extended the macroscale kinetic scheme (Fig. 4.1) to account for activation and diffusion of free integrins. We investigated the behaviour resulting from constant activation and deactivation rates and we further considered a time-dependent (Hill-type) activation rate, chosen as a phenomenological representation of intracellular signalling processes (Fig. 4.7). We observed that a transition between regimes where deactivation and then activation dominate can lead to a non-monotonic increase in adhesion strength (Fig. 4.8), which is behaviour that was observed to occur in experimental AFM data provided by Prof. Gerald Meininger, Dr. Leike Xie and Dr. Vladislav Glinsky, University of Missouri (Fig. 4.6). Within this modelling framework, detailed models of intracellular signalling pathways could be considered in future studies, allowing for more thorough investigations of these types of phenomena and the underlying mechanisms. Additionally, by including the diffusion of free integrins, our model now permits a wider range of macroscale spatio-temporal dynamics. Spatial patterning and integrin clustering are topics of wide interest and with a number of applications, such as in cell migration and tissue morphogenesis [4, 52]; this model could therefore be used and further developed to investigate these phenomena within a framework that also incorporates detailed microscale dynamics.

In Section 4.2 we extended the local microscale description to incorporate a known strain-dependent strengthening mechanism, occuring due to vinculin binding to cryptic sites on talin and reinforcing the integrin–cytoskeletal connection (Fig. 4.11). With the inclusion of this strengthening mechanism, we investigated the bound integrin response to both shear and oscillatory loading. In response to oscillatory loading we observed distinct high and low adhesion states (as seen in Chapter 3) and in each case, both the microscale and macroscale distributions exhibited qualitative differences (Figs. 4.15–4.18). Due to competition between adhesion rupture and reinforcement, we found that small amounts of deformation now encourage the persistence of adhesions (Fig. 4.14); there is a non-monotonic response to load, where adhe-

sions exhibit catch-bond like behaviour. Integrin-mediated adhesions are known to be sensitive to external environments and to develop differently on stiff and compliant substrates [32, 123]. Mechanosensitivity of integrins emerges naturally when strain-dependent strengthening is considered since matrix stiffness affects the transmission of load; for low amplitudes of load, we observe increased strengthening on stiffer substrates (Fig. 4.19). This is a factor likely to be relevant when comparing integrin dynamics in healthy and (stiffer) asthmatic airways.

An interesting area for future study would be whether the small fluctuations in the airway from tidal breathing can encourage a strengthening response, and thereby drive the system into a state of stronger adhesion. In Chapter 3, we discussed the bronchodilatory effect of DIs and how it differs in asthmatics and asthmatics. Depending on where the amplitudes of tidal breathing and DIs were in relation to the bistable window (Fig. 3.5), we observed either no change in adhesion state or transient or sustained switches from high to low adhesion states after a DI (Fig. 3.13). With the presence of force-dependent strengthening, it may be possible to observe a further outcome, in which a smaller DI (which is not sufficient to induce adhesion rupture) instead encourages adhesion strengthening. We previously hypothesised that the magnitude of the adhesion state could correlate with the extent of airway narrowing, and in some experimental studies DIs have in fact been observed to make bronchoconstriction worse [25, 94]. Furthermore, the absence of DIs is known to induce airway hyperresponsiveness in healthy subjects (Section 1.1.2), showing that regular, involuntary DIs (i.e. sighing) are crucial for maintaining normal lung function; the healthy airway is in a dynamic equilibrium [45]. If the fluctuations from tidal breathing can indeed drive the system toward a stronger adhesion state, it may be that regular DIs reset the balance by periodically initiating adhesion rupture. Although these ideas are speculative, it is worth considering how the force-dependent strengthening of integrin-mediated adhesions could factor into the airway response to DIs. The bronchodilatory ability of DIs has previously been attributed to disruptions in actomyosin crossbridges [47]; however, there are a number of unanswered questions under this hypothesis. We believe that both crossbridges and integrins could play a part. The force-dependent strengthening mechanism may be able to account for some of the more complicated dynamics, and could also be helpful in distinguishing between crossbridge and integrin contributions, since only the integrins have this trait.

The use of a local coordinate in the microscale model is crucial to capturing strain dependent reactions at the integrin level. As demonstrated by the results in this chapter, these reactions can introduce some interesting behaviours and can help to capture the known mechanosensing ability of integrins. This mechanosensitivity will be important when considering the effect of different material properties in healthy and asthmatic airways and of spatial variations in deformations across the lung; the multiscale model therefore provides a useful framework for future investigations.

In Section 4.3, we discussed an experimental result by Mailhot-Larouche *et al.* [95]. In their *in vitro* study they observed that a reduced duration between length oscillations representing deep inspirations (DIs) increased the rate and magnitude of contractile force recovery after a bronchodilatory DI. We simulated their oscillation protocol in some numerical experiments, where we explored different possible qualitative outcomes in the 4 species model (Section 4.1) as the activation rates were varied. Although there are likely to be many further mechanisms at play (such as crossbridge dynamics, intracellular signalling, diffusion and recruitment of adaptor proteins) this exploration highlighted some key points. The first is that, for the duration between DIs to have differing effects, the system cannot obtain steady state during the time period under investigation (such as occured in Fig. 4.21). This provides some information about the timescales involved with binding and activation reactions; we show that transient changes must be occuring over the full range of time intervals considered, which reached 30 minutes in the experiments. Secondly, increased rates and magnitudes of bound integrins required increased availability of $I_A$ integrins. In our model, there is conservation of the species $A + I_A + B = 1$, so this was only possible via an increased activation (or, equivalently, reduced deactivation) rate. In general, conservation is not guaranteed and recruitment via intracellular signalling and diffusion could yield the same result. The experimentally observed effect was captured using a transient increase in activation which then slowly decayed (Figs. 4.26, 4.28); this could perhaps be triggered by the initial DIs. Integrins respond to mechanical cues in many different ways; force can trigger inside-out integrin activation [3] and can also drive the recruitment and binding of adaptor proteins [84]. Both of these would have similar effects on the availability of $I_A$ integrins. Regardless of the underlying mechanism, our key observation is that, for the magnitude of recovery to be modulated, the change must be ongoing over the 30 minute time interval (Fig. 4.25).

# Chapter 5

# Vertical oscillations: models and experimental data

In this chapter we develop a model that allows for vertical motion between the cell and the ECM in order to replicate an experimental protocol where substrate-coated atomic force microscopy (AFM) probes are used to repeatedly approach and retract from the surface of a cell. The inclusion of vertical components will also be important in coupling our model of adhesion dynamics to descriptions of contractile force generation within the cell (Chapter 6). The model formulation is introduced in Section 5.1 and has two parts: a 3-spring model for material deformations, coupled to an adapted Lacker–Peskin model for the microscale integrin binding dynamics. The model for the integrin dynamics is similar to the microscale formulation introduced in Chapter 2, but has now been extended to allow for vertical separation between the cell and the ECM. The coupling to a 3-spring model for material deformations allows us to capture the two-way relation between cell-scale deformations and individual integrin binding and rupture events.

After some initial numerical tests, we use our model to simulate vertical oscillations applied to the ECM, replicating the AFM experiments described above. The experimental protocol is introduced fully in Section 5.2, and our model results are then compared to experimental data, provided by Prof. Gerald Meininger and Huang Huang (University of Missouri). In analysing the experimental data, we use cluster analysis techniques to classify different temporal patterns in force.

## 5.1 Model formulation

### 5.1.1 A 3-spring model for material deformations

We represent the cell, integrins and ECM by linear springs with spring constants $\hat{k}_A$, $\hat{k}_I(\hat{t})$ and $\hat{k}_E$, respectively, as depicted in Fig. 5.1. The cell and ECM spring constants, $\hat{k}_A$ and $\hat{k}_E$, are constant; however, the integrin spring constant, $\hat{k}_I(\hat{t})$, is designed to account for the collective strength of the bound integrins. It is therefore calculated as

$$\hat{k}_I(\hat{t}) = \rho\hat{\lambda}_b B(\hat{t}), \tag{5.1.1}$$

where $\rho$ is the total number of integrins expressed on the cell surface, $\hat{\lambda}_b$ is the individual integrin spring constant and $B(\hat{t}) \in [0,1]$ is the fraction of integrins that are bound to both the cell and the ECM. The underlying integrin dynamics evolve in time and $B(\hat{t})$ is calculated via a separate model, presented in Section 5.1.2. As in our previous models, the cell and ECM surfaces (green and red, respectively, in Fig. 5.1) that the integrins bind to are assumed to be locally rigid.

In the 3-spring model, each spring (representing the cell, integrins and ECM respectively) has a rest length of $\hat{L}_A$, $\hat{L}_I$, and $\hat{L}_E$ (Fig. 5.1(a)) and time-dependent deformed length of $\hat{L}_A'(\hat{t})$, $\hat{L}_I'(\hat{t})$, and $\hat{L}_E'(\hat{t})$ (Fig. 5.1(b)) respectively. We apply a displacement condition, $\hat{Y} = \hat{L}_T'(\hat{t})$, to the top of the ECM and use force-balance equations to determine the resulting deformed spring lengths. To carry out force balances, we consider separate cases depending on whether the fraction of bound integrins, $B$, is zero or non-zero, and whether the cell is under compression or tension. We assume integrins to be incompressible, meaning that when $\hat{L}_T' < \hat{L}_T$ they behave as rigid beams (i.e. we enforce $\hat{L}_I' = \hat{L}_I$).

Case 1: $B \neq 0$

In the case where some integrins are bound to the cell and the ECM ($B \neq 0$) and $\hat{L}_T' > \hat{L}_T$, force balance requires that the force in each spring at any point in time is given by

$$\hat{F}_{\hat{Y}} = \hat{k}_I(\hat{L}_I' - \hat{L}_I) = \hat{k}_E(\hat{L}_E' - \hat{L}_E) = \hat{k}_A(\hat{L}_A' - \hat{L}_A), \tag{5.1.2}$$

where the rest lengths $\hat{L}_I$, $\hat{L}_E$, and $\hat{L}_A$ are known parameters.

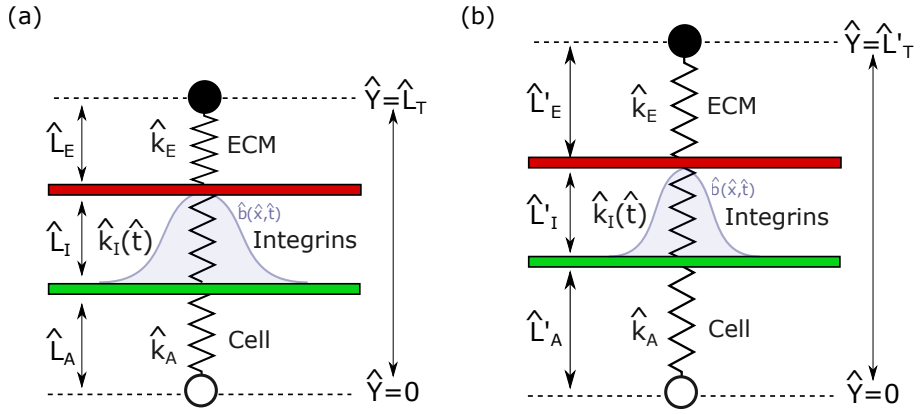


**Figure 5.1:** Schematic of the 3-spring model in (a) the rest configuration and (b) a deformed configuration. Hookean springs in series represent the cell, bound integrins and the ECM with spring constants $\hat{k}_A$, $\hat{k}_I(\hat{t})$ and $\hat{k}_E$ respectively. The cell, integrin, and ECM springs have rest lengths $\hat{L}_A$, $\hat{L}_I$, and $\hat{L}_E$ and time-dependent deformed lengths $\hat{L}'_A$, $\hat{L}'_I$, and $\hat{L}'_E$ respectively. The total deformed length is given by $\hat{L}'_T(\hat{t}) = \hat{L}'_A(\hat{t}) + \hat{L}'_I(\hat{t}) + \hat{L}'_E(\hat{t})$. The collective integrin spring constant, $\hat{k}_I(\hat{t})$, evolves in time according to the underlying distribution of integrins, $\hat{b}(\hat{x}, \hat{t})$, calculated using a separate model (Section 5.1.2), and is proportional to the fraction of double-bound integrins, $B \in [0, 1]$.

### Non-dimensionalisation

To non-dimensionalise the model equations, all lengths ($\hat{L}_T$, $\hat{L}'_T$, $\hat{L}_E$, $\hat{L}'_E$, $\hat{L}_I$, $\hat{L}'_I$, $\hat{L}_A$, $\hat{L}'_A$) are scaled by $\hat{h}$, the integrin binding range (Section 2.1). The spring constants ($\hat{k}_E$, $\hat{k}_A$ and $\hat{k}_I$) are scaled by $\rho\hat{\lambda}_b$ to obtain the dimensionless force balance equations

$$F_Y = k_I(L'_I - L_I) = k_E(L'_E - L_E) = k_A(L'_A - L_A), \tag{5.1.3}$$

where

$$k_E = \hat{k}_E/\rho\hat{\lambda}_b, \qquad k_A = \hat{k}_A/\rho\hat{\lambda}_b, \tag{5.1.4}$$

and

$$k_I = B. \tag{5.1.5}$$

The dimensionless force balance (Eq. 5.1.3) can be rewritten as two simultaneous equations

$$L'_I - L_I = \frac{k_E}{k_I}(L'_E - L_E) \quad \text{and} \quad \frac{k_E}{k_I}(L'_E - L_E) = \frac{k_A}{k_I}(L'_A - L_A). \tag{5.1.6}$$

Since $L'_T$ is known, we use the fact that the total length at any time is given by $L'_T = L'_A + L'_I + L'_E$ to eliminate $L'_E$. This leaves two equations with two unknowns ($L'_I$ and $L'_A$), which can be solved to give

$$L_I' = \frac{L_I}{1+\sigma_1\sigma_2} + \frac{\sigma_1\sigma_2}{1+\sigma_1\sigma_2}\left(L_T' - L_E - L_A\right), \tag{5.1.7}$$

and

$$L_A' = \frac{k_E(L_T' - L_I' - L_E) + k_A L_A}{(k_A + k_E)}, \tag{5.1.8}$$

where

$$\sigma_1 = \frac{k_A}{k_I} \quad \text{and} \quad \sigma_2 = \frac{k_E}{k_A + k_E}. \tag{5.1.9}$$

Using Eqs. 5.1.7 and 5.1.8, the deformed lengths of all three springs can be calculated for any applied time-dependent length fluctuation, $L_T'$, in terms of known parameters.

In the case where $L_T' \leq L_T$ (compression) we assume rigidity of the integrins ($L_I' = L_I$) and instead obtain

$$F_Y = k_E(L_E' - L_E) = k_A(L_A' - L_A). \tag{5.1.10}$$

We now have the relation $L_T' = L_A' + L_I + L_E'$ which gives

$$L_A' = \frac{k_E(L_T' - L_I - L_E) + k_A L_A}{(k_A + k_E)}. \tag{5.1.11}$$

Case 2: $B = 0$

When $B = 0$ there are no integrins bound to both the cell and the ECM; therefore the middle spring is no longer present (or, equivalently, $k_I = 0$ using Eq. 5.1.5). When $L_T' - L_E' > L_A'$ there is no contact between the cell and ECM; in this case there is no deformation and we simply have $L_E' = L_E$ and $L_A' = L_A$. This can also be obtained by considering Eqs. 5.1.7–5.1.9 in the limit as $B \to 0$ (i.e. as $\sigma_1 \to \infty$).

When $L_T' - L_E' \leq L_A$ there is contact and compression of the cell. We again consider dimensionless force balances to obtain the force in each spring

$$F_Y = k_E(L_E' - L_E) = k_A(L_A' - L_A). \tag{5.1.12}$$

This time we have $L_T' = L_E' + L_A'$, which gives

$$L_A' = \frac{k_E(L_T' - L_E) + k_A L_A}{(k_A + k_E)}, \tag{5.1.13}$$

and

$$L_E' = L_T' - L_A'. \tag{5.1.14}$$

In each of the above cases the three unknown spring deformations ($L'_A$, $L'_I$ and $L'_E$) can be calculated directly for any applied deformation, $L'_T$.

### 5.1.2 Model of integrin binding dynamics

The solution to the 3-spring model depends on knowing the fraction of bound integrins, $B$, via Eq. 5.1.5. In this section we present the dimensionless model for microscale integrin binding dynamics, which is an adaptation of the microscale model in Chapter 2, and employs the same scalings as in Eq. 2.2.26 and Section 5.1. Importantly, for the model to capture the two-way coupling between cell-scale deformations and integrin dynamics, the binding and rupture of integrins depends on the vertical extension $L = L'_I - L_I$ of the integrins, calculated from the 3-spring model. This introduces a coupling that is similar to our multiscale approach in Chapter 2.

As in previous sections, we model integrin binding and rupture events by considering state transitions of the integrins between actin-bound ($I_A$) and double-bound ($B$) states. Each integrin may therefore undergo the reactions

$$I_A \underset{k_u(d)}{\overset{k_b(d)}{\rightleftharpoons}} B, \tag{5.1.15}$$

where $k_b(d)$ and $k_u(d)$ are binding and unbinding rate functions respectively. These rates depend on a distance, $d \geq 0$, which is the distance from an unstressed position, given by $d = \sqrt{x^2 + L^2}$, for horizontal and vertical extensions of the integrin, $x$ and $L$, respectively. These rates are chosen so that the binding rate, $k_b(d)$, is highest when the distance from rest, $d$, is zero, and rupture rate, $k_u(d)$, increases as $d$ increases. The chosen rates in dimensionless form are

$$k_b(d) = \begin{cases} (1-d) & 0 < d \leq 1 \\ 0 & \text{otherwise,} \end{cases} \tag{5.1.16}$$

and

$$k_u(d) = \begin{cases} h_1 + h_2 d & 0 < d \leq s \\ h_3 & \text{otherwise,} \end{cases} \tag{5.1.17}$$

where $h_1$, $h_2$ and $h_3$ are dimensionless parameters as defined in Eq. 2.2.7. Here we use piecewise linear rates (similar to Eqs. 2.2.6, 2.2.7), and the rupture rate ($k_u$) increases with a linear gradient $h_2$ as the integrin extension increases. Furthermore, after a maximum extension of $s$, any remaining bound integrins are forced to unbind with a high rate $h_3$. The form of these rate functions is shown in Fig. 5.2.

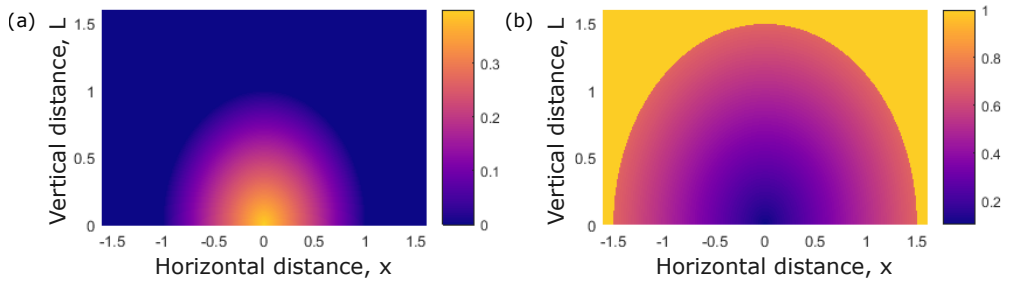


**Figure 5.2:** 2D reaction rates, indicated by colour, for binding ($k_b(x, L)$) and unbinding ($k_u(x, L)$). The binding propensity is highest at (0,0), when the integrin is in its rest position, whereas the unbinding propensity increases as distances increase. In Eq. 5.1.17, $s = \sqrt{1.5}$.

Since the vertical distance, $L$, is known at all times from the 3-spring model, we can adapt the Lacker–Peskin model [86], and track the horizontal extensions, $x$, of the integrins. This will allow us to determine the horizontal component of the traction forces generated by bound integrins. As in Chapter 2, we denote the fraction of bound integrins with horizontal extension $x$ by a distribution $b(x, t)$. If we only apply a vertical displacement to either surface, and if the binding and unbinding rates are symmetric in $x$, there is no horizontal relative velocity of the cell and the ECM. The equation for the distribution of integrins in this case has no advection term and is

$$\frac{\partial b(x,t)}{\partial t} = \eta k_b(d)\,(1 - B) - k_u(d)b(x,t), \tag{5.1.18}$$

which is the Lacker–Peskin model [86] with zero relative velocity between the two layers. This model originally only accounted for binding rates that are functions of the horizontal extensions, $x$, but since the distance $L$ is known from the 3-spring model, the binding rates can be rewritten as time-dependent functions of $x$ by using $d = \sqrt{x^2 + L^2}$ in Eqs. 5.1.16, 5.1.17. Note that, if the motion is not purely vertical, *i.e.* there is a non-zero horizontal component of relative velocity, an advection term is also needed in Eq. 5.1.18 (see Section 2.2.3). This is easily incorporated in the above, but is not considered here. In Eq. 5.1.18, the parameter $\eta$ is a dimensionless parameter which arises in the derivation of the model to allow for multiple binding sites (Eq. 2.2.27), and $B$ measures the bound fraction of integrins. As before, this is defined by

$$B(t) = \int_{-\infty}^{\infty} b(x,t)dx, \tag{5.1.19}$$

and takes a value between 0 and 1. The derivation of the original Lacker–Peskin model is discussed in detail in Chapter 2.

As previously, we treat the integrins as linear springs, each with spring constant $\lambda_b$. By Hooke's Law, we can calculate the total horizontal component of the force generated by integrins, which in dimensionless form is

$$F_X(t) = \int_{-\infty}^{\infty} xb(x,t)dx. \tag{5.1.20}$$

Since the binding rates are symmetric in $x$, if there is no imposed horizontal motion between the cell and the ECM then the distribution $b(x,t)$ will also be symmetric in $x$. In this case the integral, and therefore the horizontal force, will always be zero.

The vertical component of the force is found by using the vertical extensions, and since each of the integrins has the same extension, $L = L_I' - L_I$, this is given in dimensionless form by

$$F_Y(t) = BL. \tag{5.1.21}$$

This force is used in the 3-spring model, consistent with the definition of the integrin spring ($k_I$, Eq. 5.1.5) as $k_I = B$.

#### Summary and implementation

In summary, the equations to be evolved are a reaction equation for the integrin binding dynamics (Eq. 5.1.18) coupled to the deformed spring lengths ($L_E'$, $L_I'$ and $L_A'$). For a given displacement condition, $Y = L_T'(t)$, we have derived algebraic expressions for each of the deformed lengths, which take different forms determined by conditions on $B$ and $L_T'$. The different cases depend on whether there are a zero or non-zero bound fraction of integrins, and whether the cell is under tension or compression. To implement the model, we use the numerical techniques described in Section 2.2.4 to evolve the governing equation for the integrin distribution. Within this equation, we calculate the integrin extension, $L = L_I' - L_I$, based on the algebraic expressions for the deformed spring lengths. This is used in the modified binding rates (Eqs. 5.1.16 and 5.1.17) which, in contrast to the previous model, are now time-dependent.

### 5.1.3 Numerical results

To demonstrate the effect of vertical separation, we first consider some fixed displacements $L_T' > L_T$ that result in different integrin extensions, $L$, from their vertical rest length. The steady state distributions for bound integrins are shown in Fig. 5.3 for a

range of extensions and, as expected from the binding rates (Fig. 5.2), distributions decrease in both height and width as $L$ increases.

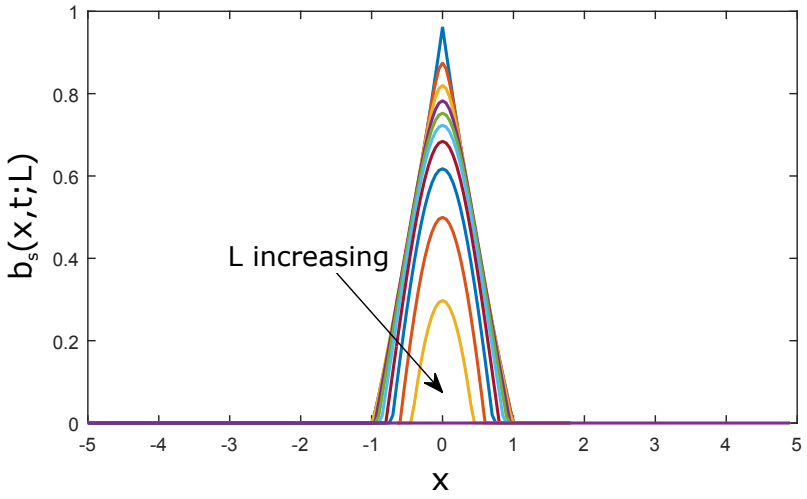


**Figure 5.3:** Steady states distributions, $b_s(x, t; L)$, of bound integrins for different extensions, $L$, of the integrins from their vertical rest length. As $L$ increases, the distributions decrease in both height and width. Here the value of $L$ is increased from 0 to 1 in steps of 0.1.

To further test our model, we replicate a common atomic force microscopy (AFM) experiment for measuring adhesion properties of cells (Section 1.2.3). Deflection of a metal cantilever is tracked as it approaches, indents and retracts from the surface of a cell (Fig. 1.6). The cantilever may be functionalised with ligands for the integrins to bind to, or be attached to a substrate-coated bead; its deflection is then used to calculate the adhesion force, commonly presented in 'approach–retract' curves (Fig. 1.6(b)). Experimental retraction curves contain information about the total adhesion force and also show individual rupture events via jumps in the retraction curve. Our equivalent model output, generated by imposing a linear time-dependent decrease and increase in $L_T'$ (Fig. 5.4), captures experimental adhesion characteristics well (Fig. 5.5). However, since the model is deterministic, a smooth retraction curve (Fig. 5.5(a)) is obtained rather than one that shows individual (stochastic) rupture events. Below the rest height ($L_T' < L_T$, *i.e.* when the cell is indented), we allow adhesions to form for a contact period, $c$, before retraction begins (Fig. 5.4). We can directly measure the adhesion force using Eq. 5.1.21 and find that the forces obtained in the retraction curves become larger and saturate (Fig. 5.5(a)) with increasing contact times. This has been observed in previous experimental studies for cell–ECM adhesion [137]; we also obtained this behaviour in a previous joint AFM and modelling study for the similar

process of cell–cell adhesion [73]. Our model shows that the change in adhesion force corresponds to an increasing bound fraction of integrins (Fig. 5.5); we do not consider activation mechanisms, and obtain a monotonic increase. We note that the similar experimental result presented by Taubenberger *et al.* [137] does not contradict the result we presented in Fig. 4.6. Their study considered contact times between 5 and 600 seconds, with relatively sparse timepoints, whereas the non-monotonic behaviour in Fig. 4.6 was detected during early adhesion formation, with several data points between 0.5 and 20 seconds.

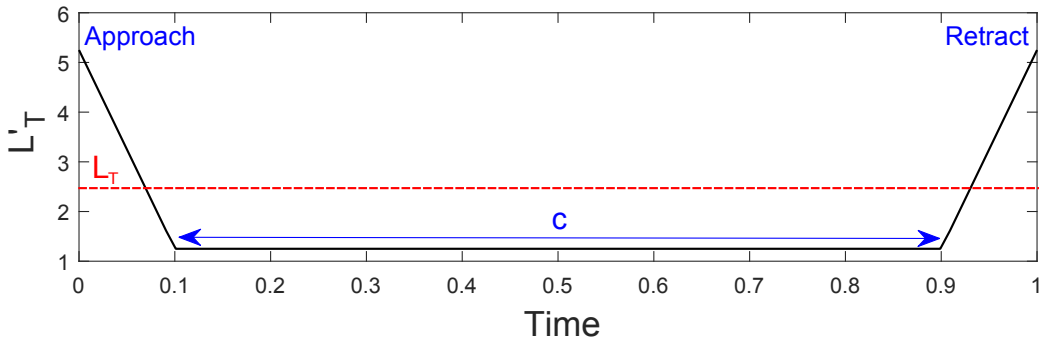


**Figure 5.4:** Schematic of the applied displacement to the ECM, $L_T'$, representing approach and retraction of an AFM probe from a cell. Adhesion forces are measured as the contact time before retraction, $c$, varies. There is indentation during the contact period, since $L_T' < L_T$ for rest length $L_T = 2.5$.

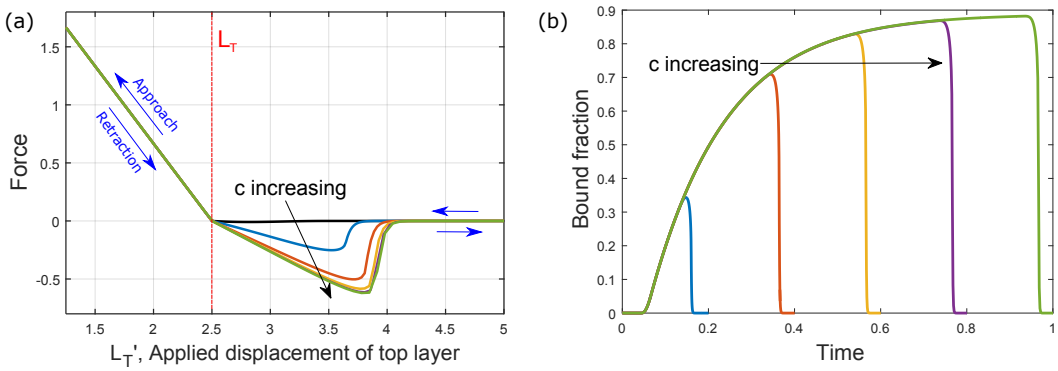


**Figure 5.5:** (a) Approach curve (black) and retraction curves for varying contact times, $c$, increasing from 0 to 0.8 in steps of 0.2. Retraction curves show an increase and saturation in maximum adhesion force. The rest length $L_T = 2.5$ and for $L_T' < L_T$ there is a positive (compressive) force. (b) As $c$ increases, the bound fraction of integrins reaches a higher maximum and saturates. The green line ($c = 0.8$) corresponds to the schematic for $L_T'$ in Fig. 5.4. Parameter values are provided in Appendix B.

### Vertical oscillatory loading

Motivated by the need to understand the integrin response to dynamic environments, we now consider an oscillatory loading of the ECM. This is similar to the loading considered in Chapter 3 but there are some key differences when the oscillations are perpendicular rather than parallel to the surface of the cell. Notably, in this vertical oscillation case, there can be times when the cell–ECM separation is larger than the integrin binding range, resulting in a zero bound fraction. In contrast, lateral oscillations (Chapter 3) allowed for continuous rebinding of integrins, even when the amplitude of oscillation was high. Vertical oscillations can therefore strongly affect the binding, as well as rupture, dynamics.

To match the experimental protocol, which will be presented in Section 5.2, we apply a vertical triangle-wave displacement (Fig. 5.6) to the top of the ECM. This is applied via $L_T'(t)$ (see Fig. 5.1), which is defined as

$$L_T'(t) = L_T - D + A\left(\frac{1}{2} + (-1)^{\lfloor 2\omega t+1\rfloor}\left(\frac{1}{2} + 2\omega t - \lfloor 2\omega t + 1\rfloor\right)\right), \tag{5.1.22}$$

where $A$ is the magnitude of the oscillation, $L_T - D$ is the minimum height of the top of the ECM (i.e. when the approach is complete, chosen to be independent of $A$), and $\omega$ is the frequency of oscillation. We refer to $D$ as the indentation depth, as this controls the amount of compression experienced. For extension to occur during the retraction phase, $A$ must be chosen so that $A > D$. As in Chapter 3, we will consider both zero and saturated initial conditions (Eq. 2.2.12) for the bound integrin distributions. In the case where the saturated initial condition is used the simulation is started at time $t = -1/2\omega$ (where $L_T'$ is at a minimum) instead of $t = 0$; the fully saturated condition is only applicable when the cell and ECM are in close proximity and simulating an initial 'retraction' period gives us the relevant initial distribution for when the first approach cycle begins at $t = 0$. Additionally, this is consistent with the experimental approach that will be presented in Section 5.2. In the numerical simulations, we track the timecourses of the fraction of bound integrins, $B$ (Eq. 5.1.19), and vertical adhesion forces (Eq. 5.1.21) as the amplitude $A$ varies. In addition, we can continuously track how each of the three layers deform. In the results that follow, we use parameter values as listed in Appendix B (unless otherwise stated in captions) to explore the possible qualitative model behaviours. Although here we use a triangular waveform, very similar model behaviours are obtained with a sinusoidal waveform (as will be used in Chapter 6).

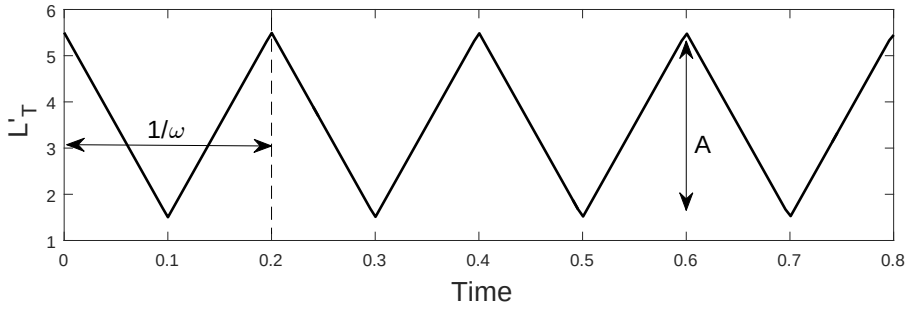


**Figure 5.6:** Triangular waveform used for $L_T'$ (Eq. 5.1.22), the vertical displacement applied to the top of the ECM. Here, the minimum height of the ECM is $L_T - D = 1.5$, the frequency is $\omega = 5$ and the amplitude is $A = 4$. The rest length $L_T = 2.5$ and the indentation depth is $D = 1$. Cycles of approach and retraction from the cell begin at time $t = 0$.

Applying low amplitude approach–retract oscillations (Fig. 5.7) results in an increase in the bound fraction from the zero initial condition (blue line) to a high steady state (Fig. 5.7(a)). The same steady state is reached when starting from a saturated initial condition (red line). Negative and positive values of force (Fig. 5.7(b)) correspond to adhesion and compression forces respectively, and the maximum adhesion forces at each cycle (i.e. the values at $t = 0, 0.2, \ldots$) are seen to saturate at the same rate as the bound fraction. The corresponding heights of each of the three layers for the zero initial condition are shown in Fig. 5.8. During the first approach ($t \in [0, 0.1]$), we observe a reduction in cell height (green line) due to indentation. As retraction ($t \in [0.1, 0.2]$) begins, the cell height increases. Due to adhesions that have formed, the cell is stretched upwards and closely follows the applied triangular waveform (black line). Later in the retraction ($t \approx 0.16$), a small number of bonds rupture and there is a slight rounding of the cell height.

Timecourses for the bound integrin fractions (for each initial condition) and the corresponding adhesion forces under high amplitude vertical oscillations, representing larger excursions being made in the approach–retract cycles, are shown in Fig. 5.9. In this case the zero and saturated initial conditions produce identical timecourses since all bonds have ruptured during the initial retraction (before $t = 0$) in the saturated case. Timecourses for the heights of each of the three layers, illustrate the corresponding cell deformations (Fig. 5.10). In contrast to Fig. 5.8, the cell deformation no longer closely follows the applied triangular waveform throughout the oscillation: there are small upward deformations during the initial phase of each retraction cycle, but once the bound fraction reaches zero the cell returns to its rest height.

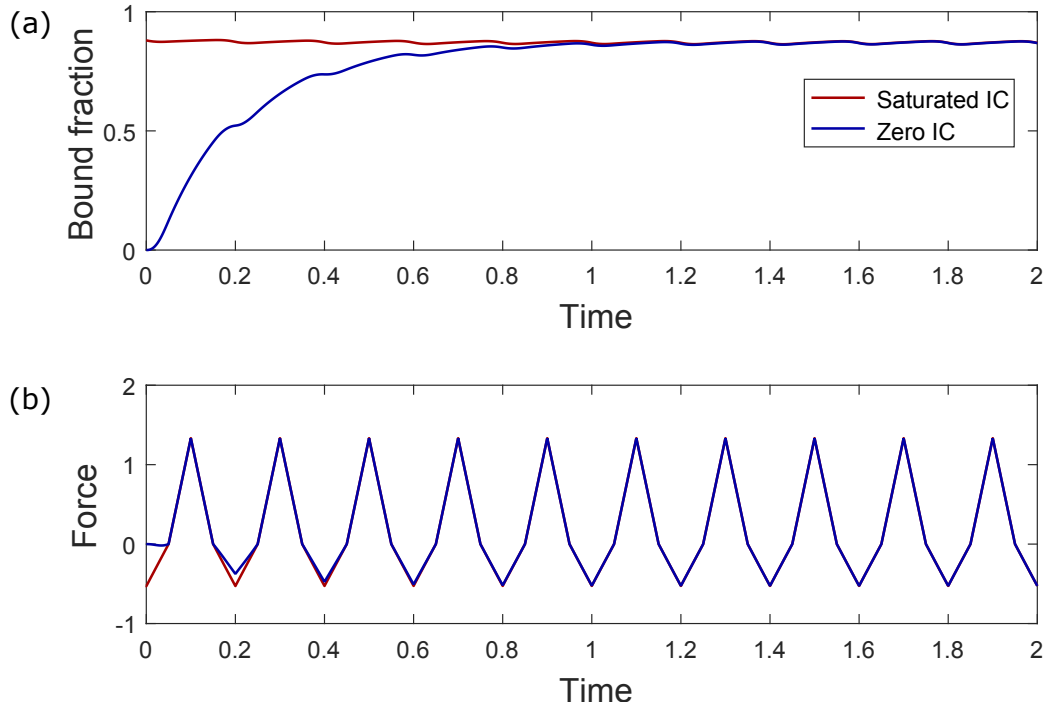


**Figure 5.7:** Timecourses for (a) the bound integrin fraction and (b) adhesion force in the presence of low amplitude ($A = 2$) approach–retract cycles. The red and blue lines show timecourses for saturated (Eq. 2.2.12) and zero initial conditions respectively.

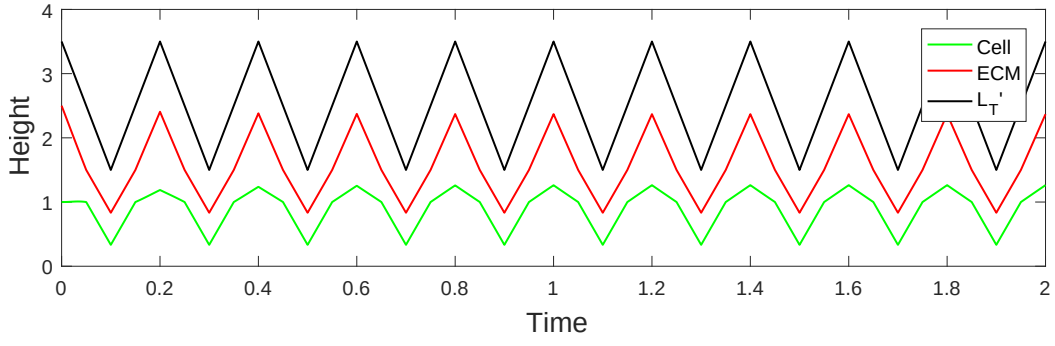


**Figure 5.8:** Timecourses for the heights of each of the three layers (Cell, ECM and $L_T'$), showing the deformations that occur under low amplitude ($A = 2$) approach–retract cycles when a zero initial bound fraction was used.

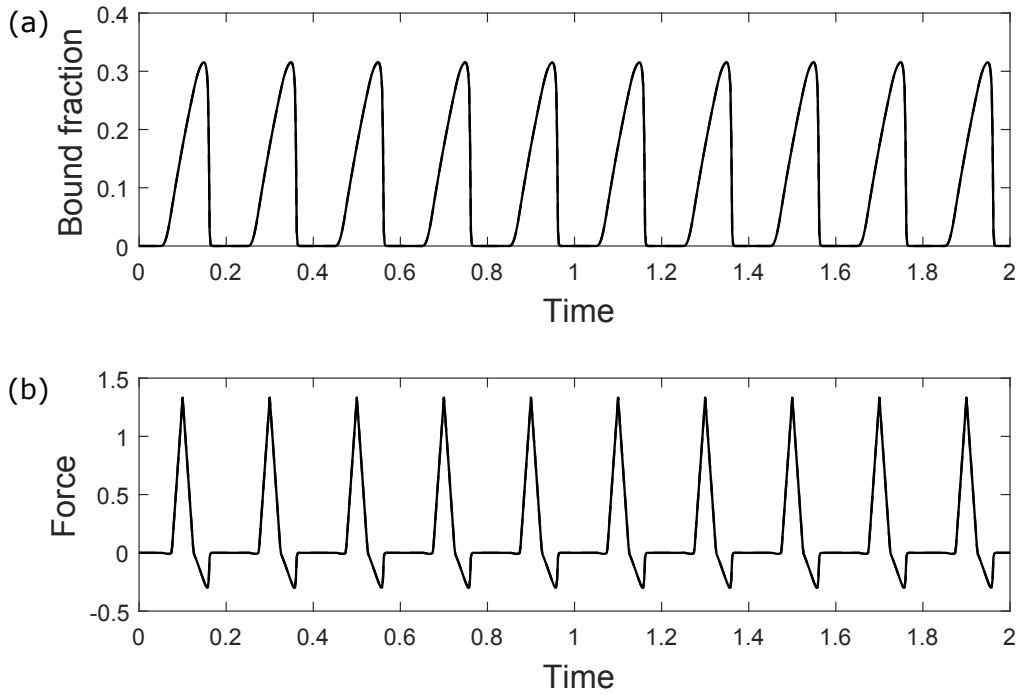


**Figure 5.9:** Timecourses for (a) the bound integrin fraction and (b) the corresponding adhesion force in the presence of high amplitude ($A = 4$) approach–retract cycles. Both the saturated (Eq. 2.2.12) and zero initial conditions produce these results.

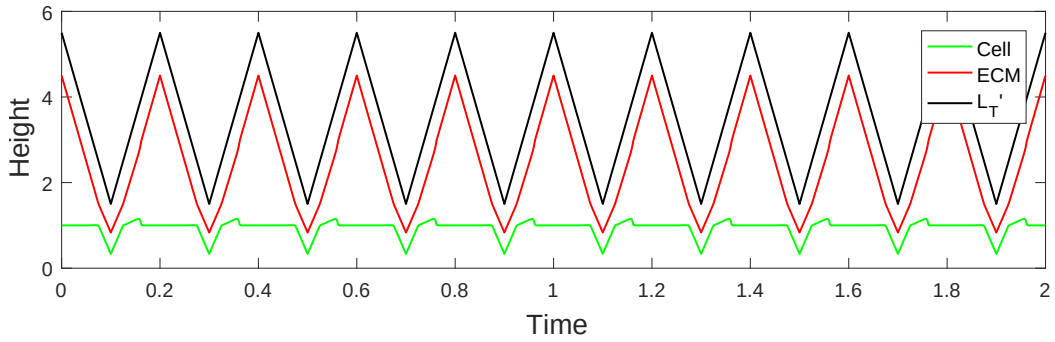


**Figure 5.10:** Timecourses for the heights of each of the three layers (Cell, ECM and $L_T'$), showing the deformations that occur under high amplitude ($A = 4$) approach–retract cycles. In this case a zero initial condition of bound integrins was used.

Bound fraction and adhesion force timecourses for an intermediate amplitude vertical oscillation (Fig. 5.11) suggest the existence of bistable behaviour due to mechanical cooperativity, similar to the lateral oscillation cases in Chapter 3. Since we also track the cell height as a function of time in this model (Fig. 5.12), the effect of mechanical cooperativity can be more clearly seen. With a saturated initial condition, the cell height (which is directly influenced by adhesion force, Fig. 5.11(b)) is increased during the retraction phase, which leads to reduced separation between the cell and ECM and allows the integrins to remain bound. This result shows that the bistability seen and analysed in Chapter 3 is a phenomenon that can be observed with vertical oscillations. Additionally it highlights the role of material stiffnesses: for cooperativity to be effective there must be sufficient deformation of the cell or ECM.

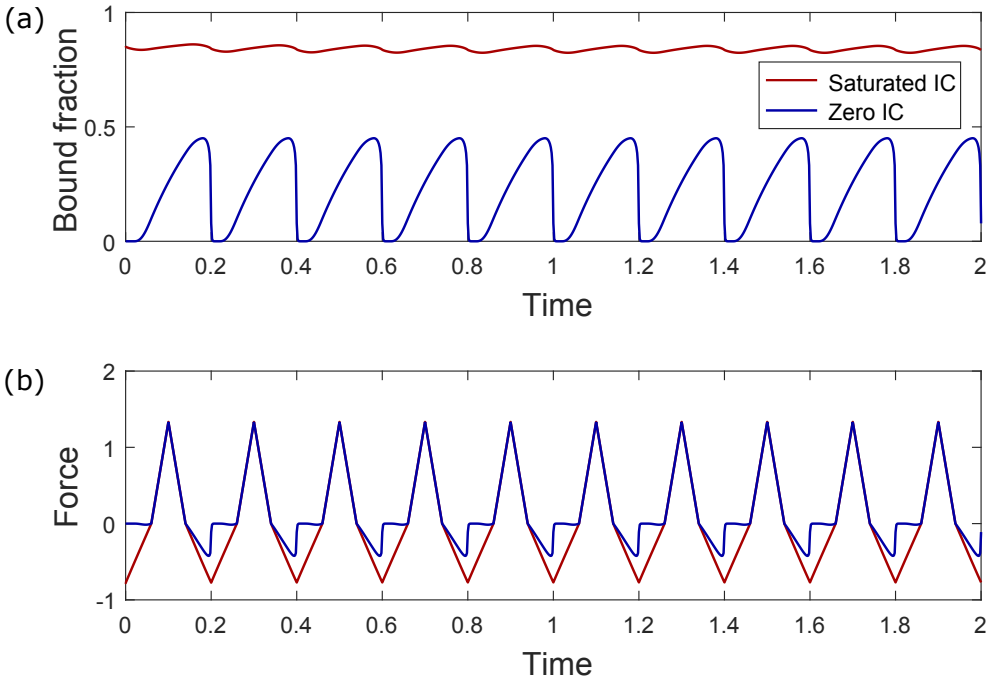


**Figure 5.11:** Timecourses for (a) the bound integrin fraction and (b) adhesion force in the presence of intermediate amplitude ($A = 2.5$) approach–retract cycles. Red and blue lines show timecourses for saturated (Eq. 2.2.12) and zero initial conditions respectively.

Although the bound fraction timecourses clearly show whether adhesion or rupture dominate, this information is not available in AFM experiments. However, in the two cases of adhesion and rupture, we also observed qualitative differences in the force timecourses, which can be measured by AFM. We will therefore focus on this aspect and use the force curves as a means of comparing model and experimental data.

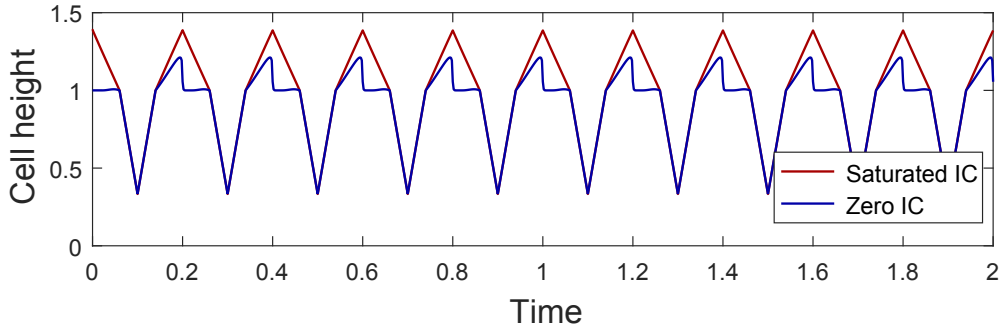


**Figure 5.12:** Timecourses for the cell height, showing the deformations that occur under intermediate amplitude ($A = 2.5$) approach–retract cycles with saturated (red line) and zero (blue line) initial conditions.

To show the typical behaviour of the adhesion force for each initial condition and for a range of oscillation amplitudes, we average the curves over each approach–retract cycle (Fig. 5.13). Additionally, the force curves have been normalised so that they all take values between 0 and 1. As the amplitude, $A$, increases there is a gradual narrowing of the force curves due to the increased speed of approach and retraction; this occurs in order to cover an increased distance within a fixed period of oscillation. More significantly, there is a change in the shape of the curves due to the transition between adhesion and rupture states. In the case of adhesion, the curves are approximately triangular with non-zero gradients throughout the approach ($t \in [0, 0.1]$) and retraction ($t \in [0.1, 0.2]$) phases. When there is rupture, the force curves exhibit regions of zero gradient due to periods of zero force when no bonds are present. In this case, the force curves are not symmetric about the turning point at $t = 0.1$. For $A = 2.2$, $A = 2.25$ and $A = 2.3$, which exhibit bistable behaviour, there are qualitative differences in the force curves for each initial condition due to the presence of both adhesion (red) and rupture (blue) states.

## 5.2 Experimental protocol for vertical oscillations

### 5.2.1 Vascular smooth muscle cells

In the experimental data we present in the next section, the experiments were carried out on aortic vascular smooth muscle cells (VSMCs). There are many similarities between vascular and airway smooth muscle cells, and integrins also have an important role in regulating mechanotransduction between VSMCs and the ECM. Changes in integrin signalling and expression are known to lead to altered vascular function

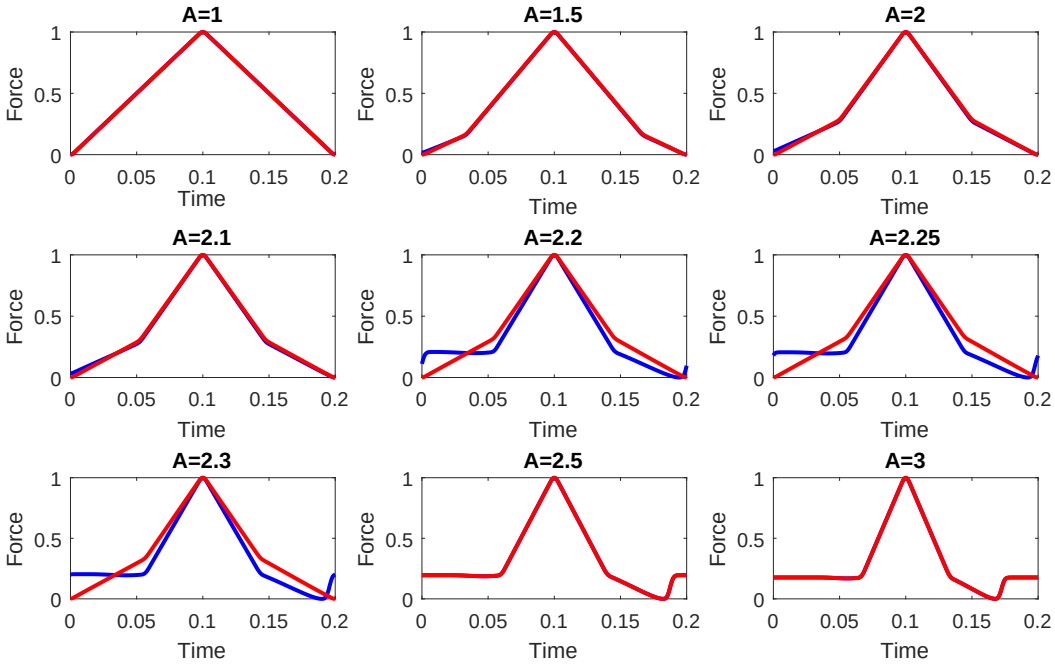


**Figure 5.13:** Force curves, normalised to take values between 0 and 1, and averaged over each approach–retract cycle. These show the typical behaviours of the adhesion force during approach ($t \in [0, 0.1]$) and retraction ($t \in [0.1, 0.2]$) for each amplitude, $A$, when using a saturated (red) and zero (blue) initial condition.

and have been associated with a range of cardiovascular diseases [23, 31, 63, 87]. A further similarity is that both smooth muscle cell types (airway and vascular) reside in, and must adapt to, dynamic environments. VSMCs are contained within the walls of blood vessels; they are affected by fluctuating mechanical forces due to both continuous blood flow and due to pulsatile changes in blood pressure and vessel diameter. As with ASM cells, the VSMC integrin response to dynamic environments is therefore an important area of study.

### 5.2.2 Experimental methods

The experimental data was obtained using atomic force microscopy (AFM) techniques and provided by Prof. Gerald Meininger and Huang Huang (University of Missouri). A vertical oscillatory displacement of varying amplitudes was applied to a fibronectin (FN)-coated AFM probe, which was used to repeatedly indent and retract from the surface of single live aortic VSMCs. For each experiment, force curves from 60 approach–retract cycles (at a frequency of 0.1Hz) were recorded as an indication of the time-dependent adhesion strength and dynamics.

In order to determine the effect of different amplitude oscillations on the adhesion characteristics between FN and the VSMCs, measurements were made with oscillation amplitudes varying between 200nm and 2000nm. In total, 13 oscillation amplitudes were applied and two protocols were followed for each amplitude: prebind and non-prebind. For the prebind protocol, the FN-coated beads were kept in contact with the cell surface for 20 minutes prior to the approach and retraction to allow stable focal adhesions to form. For the non-prebind protocol, approach and retraction cycles began immediately after the AFM probe engaged with the cell membrane. These two protocols correspond to the saturated and zero initial conditions considered in the model (Section 5.1.3).

For each amplitude and initial condition, repeat experiments were performed on between 5 and 9 cells. In total we have data from 173 cells: 84 from the non-prebind protocol and 89 from the prebind protocol. The raw data for each cell consisted of three continuously measured quantities: time, vertical displacement applied to the probe, and deflection of the probe. The force was calculated by multiplying the probe deflection by the known stiffness of the cantilever (18.1pN/nm). Note that the number (or bound fraction) of integrins cannot be measured in AFM experiments and the

cell deformation is not known continuously in time. For this reason we will analyse the force data, which is the output that is common to both model and experiment.

A schematic for the initial approach for the non-prebind protocol is shown in Fig. 5.14, where $A$ denotes the amplitude of oscillation and $z = C$ denotes the height of the cantilever when contact with the cell is made, measured from a reference height, $z = 0$. This is the minimum height of the end of the cantilever (occuring at the trough of the oscillation), which is controlled by the piezoelectric scanner (Fig. 1.6) and is fixed for each cell.

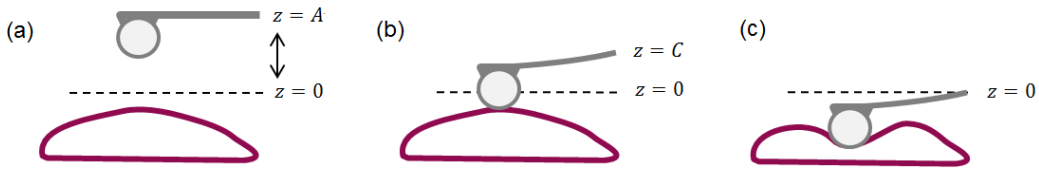


**Figure 5.14:** Schematic of the AFM protocol with no prebinding. (a) The cantilever begins to approach the cell from a height of $z = A$. (b) At $z = C$, contact with the cell is made. (c) Indentation of the cell occurs, and the cantilever continues to be lowered until a minimum height, $z = 0$. From this point, the process is reversed and then repeated for 60 cycles. The height, $z$, of the cantilever is controlled by a piezoelectric scanner (Fig. 1.6), and $z = 0$ is fixed for each cell.

### 5.2.3 Experimental results

We first show force data for a cell with no prebinding, which was subject to vertical oscillations with amplitude 400nm (Fig. 5.15). The triangular shape (Fig. 5.15(b)) follows the form of the applied displacement which, as in the model results, is behaviour indicative of adhesion (Figs. 5.7(b), 5.13). Note that here we plot the raw data; however, to obtain accurate values for the magnitude of force this measurement needs to be corrected to account for the initial deflection of the cantilever. In the experiments the cantilever is not guaranteed to be perfectly horizontal at the beginning of the experiment, meaning that there is initially a non-zero value of deflection even though there is no adhesion force. The correction is simple to make in this case since we know that at $t = 0$ the force should be identically zero due to the fact that there is no adhesion and no contact with the cell before the approach occurs; the force should therefore be shifted by its initial value. However, in the corresponding data with prebinding, correcting the force data is problematic since we do not have a point of

reference where force is known to be zero (or any other value). Since we cannot account for this shift consistently with prebinding, we focus on the qualitative aspects of the force data by considering the shape rather than the magnitude of the curves.

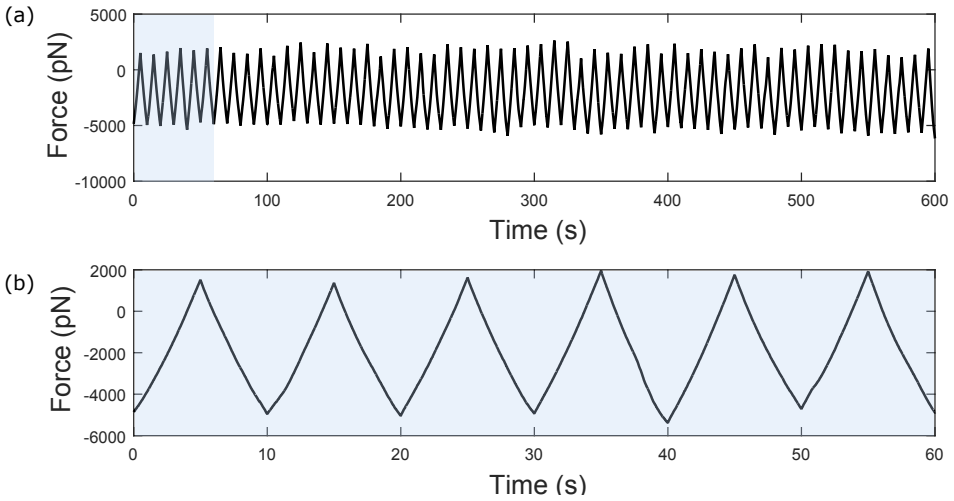


**Figure 5.15:** Raw AFM data for a cell with no prebinding, measured whilst the AFM probe was subject to vertical oscillations (with a triangular waveform) of amplitude 400nm over (a) 10 minutes and (b) the first 6 approach–retract cycles.

For larger amplitude oscillations (1400nm), we observe force curves (Fig. 5.16) qualitatively similar to our model results obtained in the rupture regime (cf. Fig. 5.16(b), Fig. 5.9(b)). The width of the curves appear narrower, and flat sections indicate full rupture and zero force. Before this occurs, there are adhesion formation and rupture events; however, this is less apparent than in Fig. 5.9(b) due to the relatively high magnitude of the compressive forces in the experiments. By focussing only on the bottom of the curves (Fig. 5.16(c)) rupture can be seen more clearly.

For a wider range of amplitudes, the normalised force curves, averaged over 60 cycles, over each cell (Fig. 5.17) show qualitatively similar behaviours to our model results (Fig. 5.13). As before, we observe a narrowing of force curves as the amplitude increases, and flattening at the ends as the behaviour transitions from adhesion to rupture. In extreme low and high amplitude cases there is very little difference in the non-prebind (blue) and prebind (red) data; however, we observe noticeable differences between the two protocols for $A = 1200$nm, $A = 1400$nm and $A = 1800$nm. We expect to see slight discrepancies due to the presence of noise in the experimental data, but since differences in the model indicated bistability we will examine these

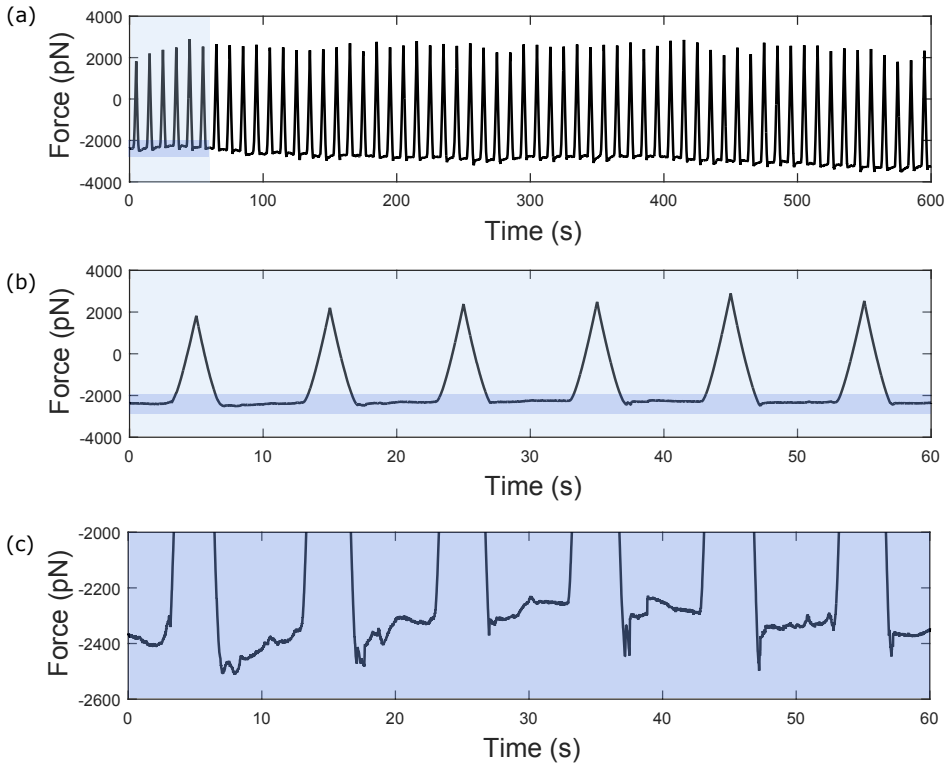


**Figure 5.16:** Raw AFM data for a cell with no prebinding, measured whilst the AFM probe was subject to vertical oscillations (with a triangular waveform) of amplitude 1400nm. We show the force over (a) 10 minutes, (b) the first 6 approach–retract cycles and (c) a limited range of force that allows us to see the rupture behaviour more clearly.

cases in more detail. For $A = 1400$nm and $A = 1800$nm, prebinding appears to encourage some increased adhesion. This is shown by an increased width of the prebind (red) curves, which indicates that contact between the bead and cell is sustained for a longer period. However, the overall shape of the curves (in particular, flatness at the ends) indicates that rupture still eventually occurs in both cases. For $A = 1200$nm, it is not clear if this is the case, and we examine this further below.

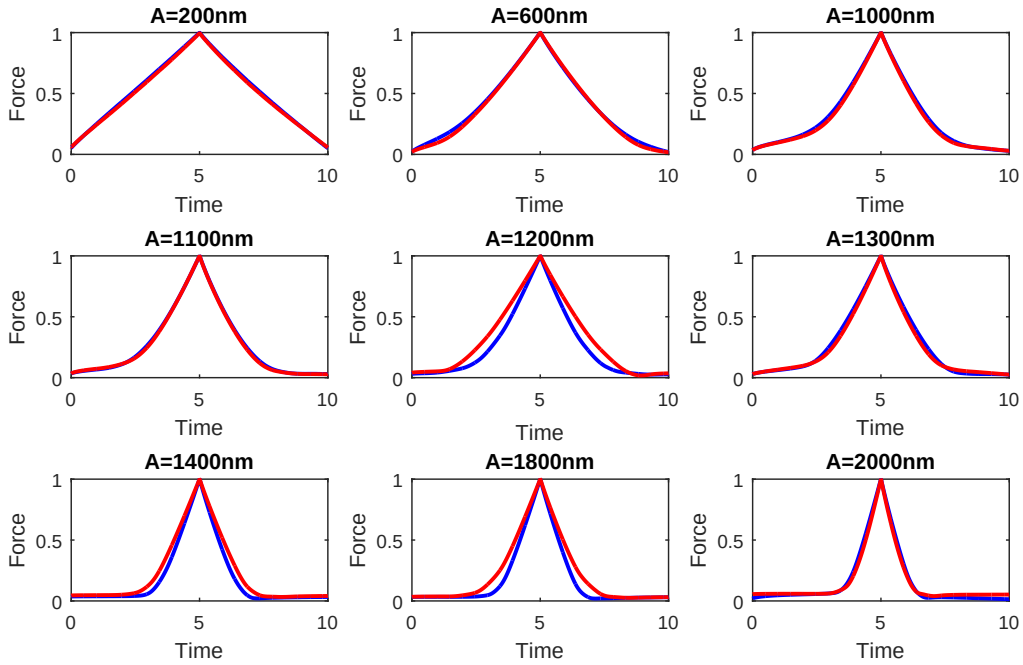


**Figure 5.17:** Force curves, normalised to take values between 0 and 1, and averaged over each approach–retract cycle and cell. These show the typical behaviours of the adhesion force during approach ($t \in [0, 5]$) and retraction ($t \in [5, 10]$) for amplitudes, $A$, with the prebind (red) and nonprebind (blue) protocols.

For 1200nm oscillations, from the complete force data for the individual cells (Figs. 5.18 and 5.19) we observe that, with no prebinding (Fig. 5.18), the behaviour is characteristic of rupture in all cases except for Cell 4. On the other hand, with prebinding (Fig. 5.19), for all cells except for Cell 2, we observe the wider, more triangular curves that are characteristic of adhesion. This is consistent with the model observations at intermediate amplitudes, where saturated and zero initial conditions resulted in adhesion or rupture states respectively (Fig. 5.11); however, there are still a number of factors (such as noise and intercellular variation) to consider in the experimental case before arriving at a conclusion about bistability.

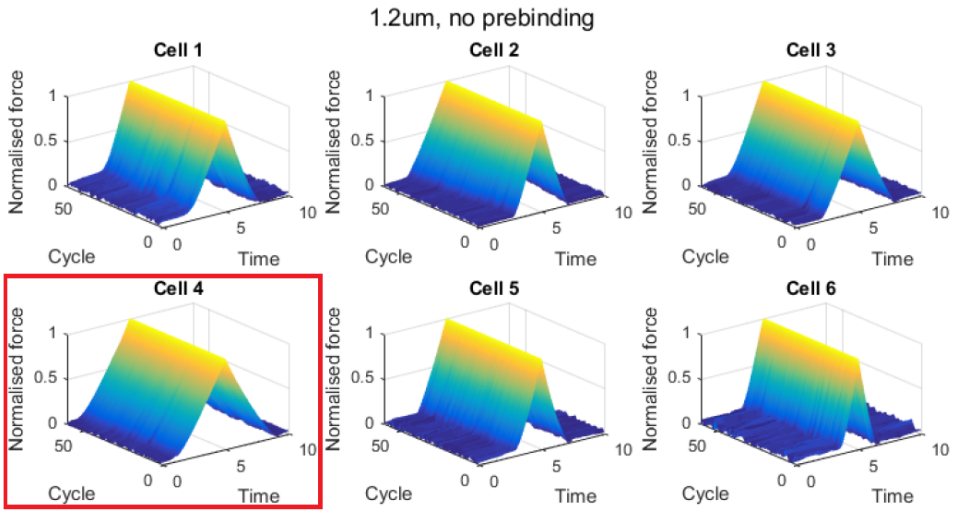


**Figure 5.18:** Normalised force curves for each cycle and each cell subject to 1200nm oscillations under the no-prebind protocol. Full rupture occurs in most cells, seen by the narrow width and flatness at the ends of the force curves (similarly to Fig. 5.16(b)). The more triangular force curve in Cell 4 differs, indicating adhesion (Fig. 5.15(b)).

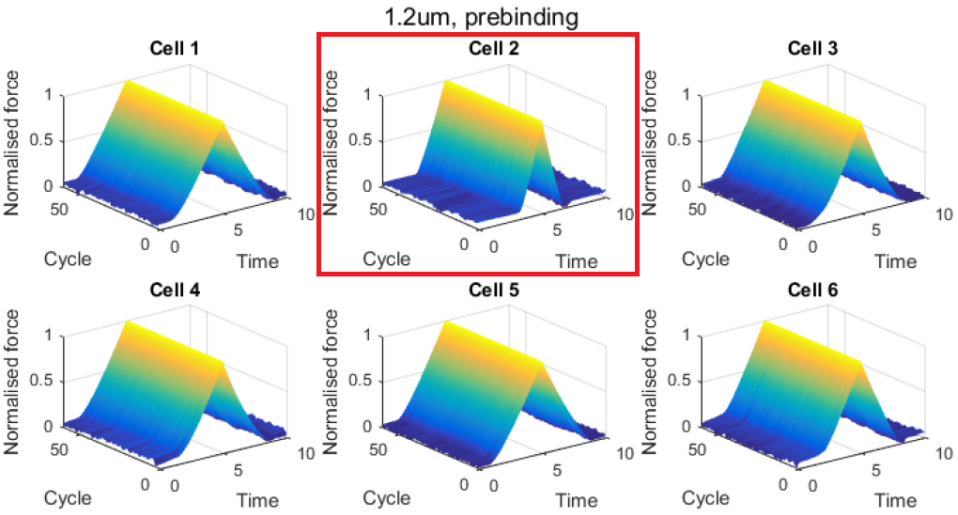


**Figure 5.19:** Normalised force curves for each cycle and each cell subject to 1200nm oscillations under the prebind protocol. Most of the force curves indicate adhesion, with a similar triangular shape to Fig. 5.15(b)). A larger amount of rupture is seen in Cell 2, which is similar in shape to Fig. 5.16(b)).

We now analyse the non-prebind data to see if the reason behind the different behaviour of Cell 4 can be identified. Although only the cantilever height and deflection over time are measured in the experiments, a number of quantities can be inferred. For example, the height of the cell can sometimes be estimated by analysis of the force curve. In the case where there is initially no adhesion and no contact between the bead and cell, the force starts at 0pN and increases sharply when contact is made. We estimate this contact point ($z = C$, Fig. 5.14) by calculating the height at which a 5% change in force occurs during the first approach cycle. We calculated this for each cell in Fig. 5.18 (Table 5.1), measured from a reference height of $z = 0$, which is the controlled height of the cantilever at the trough of the oscillation (see Fig. 5.14), and where maximum indentation of the cell occurs. Firstly we observe that there is a wide variation between these estimated heights, with a range spanning several hundred nanometres. The reference height, $z = 0$, is fixed between cells, which highlights that there must be variation in the cell heights, which had not been considered in the design of the experiment. This variation introduces limitations that will be discussed below. A further observation is that the 5% change in force occurs at a much larger height for Cell 4, meaning that there was a significantly reduced distance from the contact height to the peak of the oscillation (given by $A - C$, Fig. 5.14) for this cell. This reduced distance provides a likely reason for why this cell exhibited adhesion whilst the others showed rupture (Fig. 5.18).

| Cell index | 1 | 2 | 3 | 4 | 5 | 6 |
|---|---|---|---|---|---|---|
| 5% | 673nm | 493nm | 637nm | 875nm | 455nm | 289nm |

**Table 5.1:** The height (to the nearest nm) at which a 5% change in force occurs during the first approach cycle for each cell in Fig. 5.18. This height is relative to the point of maximum indentation ($z = 0$, Fig. 5.14) from which oscillations of amplitude 1.2$\mu$m are applied. The 5% change in force occurs at a significantly higher value for Cell 4 (red).

The same measure of height for the prebind data (Table 5.2) shows increased values (on average) compared to the non-prebind data. With prebinding, there is a possibility of adhesions being present at $t = 0$, meaning that the force does not necessarily start at 0pN. In these cases, a 5% change will occur relatively quickly since the force will begin to increase instantly, with no period of flatness due to a zero force. We observe that this does not occur for Cell 2, where the height is lower than for any of

the other cells. This means that an increased distance is travelled between the point of contact and the peak of the oscillation, which would again provide an explanation for the differing behaviour of Cell 2, where rupture was seen to occur rather than adhesion (Fig. 5.19).

| Cell index | 1 | 2 | 3 | 4 | 5 | 6 |
|---|---|---|---|---|---|---|
| 5% | 854nm | 368nm | 851nm | 801nm | 883nm | 1169nm |

**Table 5.2:** The $z-$height (to the nearest nm) at which a 5% change in force occurs during the first approach cycle for each cell in Fig. 5.19. This height is relative to the point of maximum indentation ($z = 0$) from which oscillations of amplitude 1.2$\mu$m are applied. The 5% change in force occurs at a significantly lower $z-$value for Cell 2 (red).

The variation detected between cells (Tables 5.1 and 5.2) highlights an important issue: each cell undergoes a different indentation depth, depending on its height. As a result, for cells originally classified under the same 'amplitude' category, there could be variation of up to several hundred nanometres in the distance between the cell surface and the peak of the oscillation. Classifying the data in this way therefore has limited use, since when comparing categories of *e.g.* 1100nm and 1200nm, individual cells could exhibit variations in height that negate the difference in amplitude. Moreover, the cell height can only be estimated in cases where the initial force during the approach is zero, which is not always the case in the prebind data. This means that we cannot always know, or correct for, the error. To improve accuracy, future experimental studies would ideally need to account for variations in cell height from the outset. This could either be through a carefully controlled selection of cells, or through adapting the amplitude applied by the piezoelectric scanner so that the distance from the cell surface to the peak of the oscillation (rather than the total distance) is the preserved quantity. In the prebind data, this would require using the initial approach data (*i.e.* from before the 20 minute period of prebinding) to infer the initial cell height. Currently, we do not have a record of this data, which would be needed in order to retrospectively correct for the intercellular variation.

Although there is a large variation between the individual cells in Tables 5.1 and 5.2, it appears that the mean height for the prebind cells is significantly increased. An increase in this measure seems to correlate with adhesion occuring over rupture, but

the key question is whether this a cause or an effect of the different adhesion outcomes. On the one hand, there is a relatively low number of cells, and it could be argued that an increase in cell height occurred by chance for the prebind cells, and that this led to increased adhesion due to a reduced distance between cell surface and peak of the oscillation. On the other hand, our model results (Fig. 5.12) show that an increase in cell height is to be expected in a bistable case with prebinding. The initial adhesions lead to an upward cell deformation during the initial retraction, and if the bead and cell stay attached, the cell height remains elevated (sketched in Fig. 5.20). Without a record of the initial cell heights, which would need to be measured from the approach before the 20 minutes of prebinding, we cannot identify which of these two cases occurred. It is therefore currently inconclusive whether or not bistability is behind the different observations in the prebind and non-prebind data.

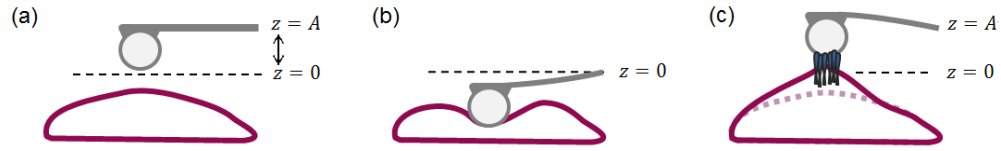


**Figure 5.20:** Schematic of possible cell deformation occuring during the prebind protocol. (a) Before the oscillations begin, the cantilever is lowered to the cell. (b) contact is maintained for 20 minutes to allow adhesions to form. (c) The cantilever is retracted upwards before the oscillation protocol begins (Section 5.2). Our model results (Fig. 5.12) show that prebinding leads to an upward cell deformation if the adhesions persist during retraction. This provides an explanation for the higher mean height for the prebind cells in Table 5.2; however, without further data, we cannot rule out the possibility of the increased mean being due to noise.

We now plot distributions of the $z-$height at which a 5% change in force occurs during the first approach for all cells in either the non-prebind and prebind protocols (Fig. 5.21); this consists of data points for 84 non-prebind cells and 89 prebind cells, which have been fitted to normal density functions using the MATLAB function `histfit`. If the differences were purely due to noise, we might expect the variations in cell heights to be similar over a larger number of cells, and for the distributions to therefore be similar in the prebind and non-prebind cases. However, we again observe a higher mean for the prebind cells, suggesting that prebinding could be influencing (rather than just coinciding with) the result. In addition, we carried out a two-sample Kolmorogov–Smirnov test on the two datasets, which tests the null hypothesis that they are drawn from the same distribution. The null hypothesis was rejected, with

p-value 0.0404. These results suggest that, whilst there is random variation in the cell heights, the variation is not independent of the prebind or non-prebind protocols. It is still not clear how we should account for this in the analysis of the data.

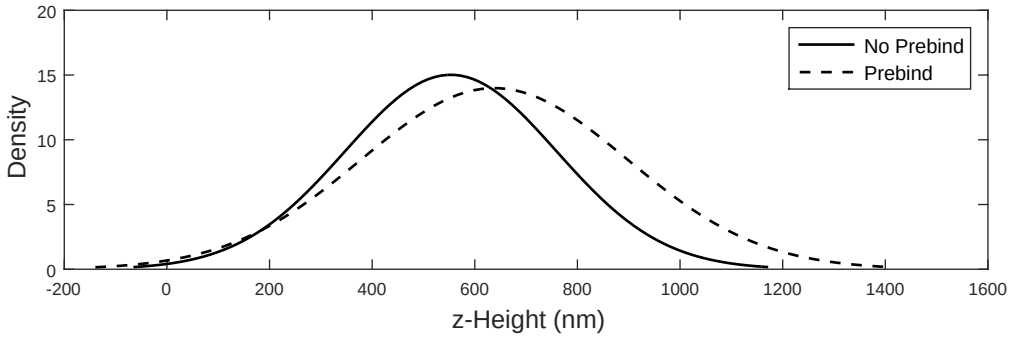


**Figure 5.21:** Fitted distributions of the $z-$height at which a 5% change in force occurs during the first approach, for 84 and 89 cells in the non-prebind (solid line) and prebind (dashed line) protocols respectively. The mean for the prebind cells is approximately 100nm higher than for the non-prebind cells. A two-sample Kolmorogov–Smirnov test on the original data rejects the null hypothesis (that the two datasets are drawn from the same distribution) with p-value 0.0404.

Due to the intercellular variability (discussed above), it is difficult to make direct comparisions between cells with any certainty. We therefore now examine some force data for individual cells. In several cases, timecourses from single experiments exhibit dramatic switches in behaviour. Switching is a phenomena associated with bistability in a stochastic system (see *e.g.* [96, 138] and our discrete model, Fig. 3.2); investigating these cases could therefore provide alternative evidence in support of bistability. In an example of such a force timecourse, for a cell subject to oscillations of amplitude 1000nm under the prebind protocol (Fig. 5.22), a sudden large drop in the amplitude of force appears to occur after 160 seconds. There are also qualitative differences, as seen in the normalised force curves overlayed for each cycle (Fig. 5.23(a)). We observe two distinct types of curves; wider curves that are characteristic of adhesion (Fig. 5.15) and narrower curves characteristic of rupture (Fig. 5.16). The reduced width corresponds to a reduced time with the bead and cell in contact. The same normalised force data as a surface plot (Fig. 5.23(b)) indicates that the change in width of the curves occurs at the same time as the switch in the timecourse (Fig. 5.22).

In a similar example (Fig. 5.24), the cell subject to oscillations of amplitude 1000nm again appears to undergo a transition from adhesion to rupture. In a contrasting

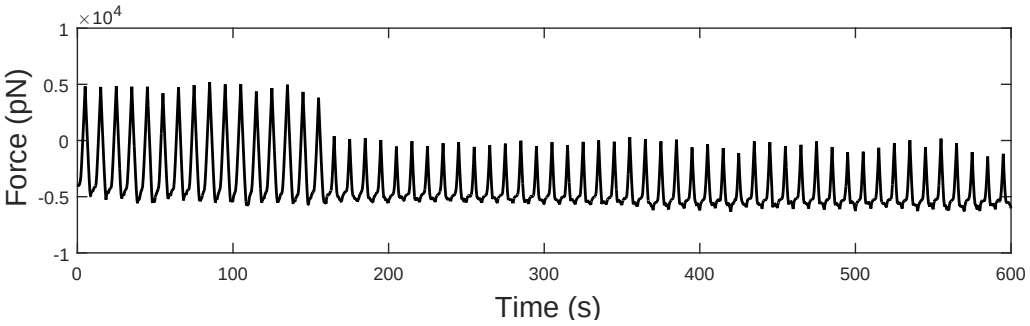


**Figure 5.22:** Example force timecourse that appears to undergo a sudden change at $t = 160s$. The cell was subject to oscillations of amplitude 1000nm under the prebind protocol. At earlier times, the force curves are characteristic of adhesion curves (Fig. 5.15). At later times, there is more rupture, characteristic of full detachment curves (Fig. 5.16).

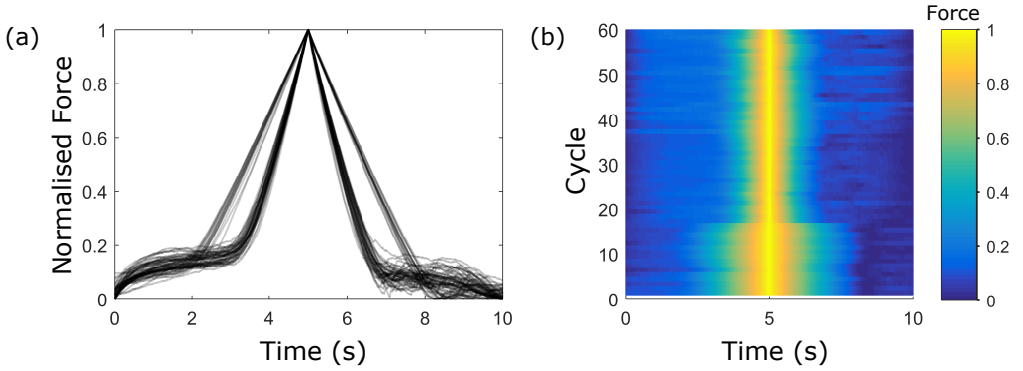


**Figure 5.23:** Normalised force curves from the timecourse in Fig. 5.22, shown (a) overlayed for each cycle and (b) in a surface plot. We observe two distinct types of curves, where a reduced width corresponds to a reduced time with the bead and cell in contact. A switch between the two types occurs suddenly after the 16th cycle.

example, for a cell subject to oscillations of amplitude 1150nm (Fig. 5.25) the switch appears to be in the opposite direction (*i.e.* to stronger adhesion).

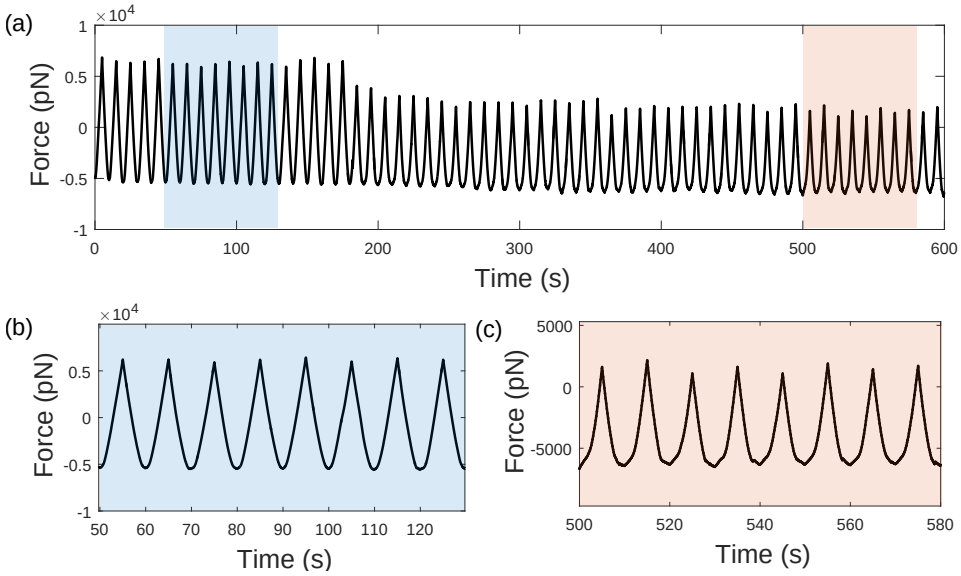


**Figure 5.24:** A further example of a force timecourse that appears to undergo a sudden change at $t = 180s$. This cell was also subject to oscillations of amplitude 1000nm under the prebind protocol (Fig. 5.22). At earlier times, the force curves are characteristic of adhesion curves (Fig. 5.15). At later times, there is increased rupture (Fig. 5.16) and a drop in magnitude.

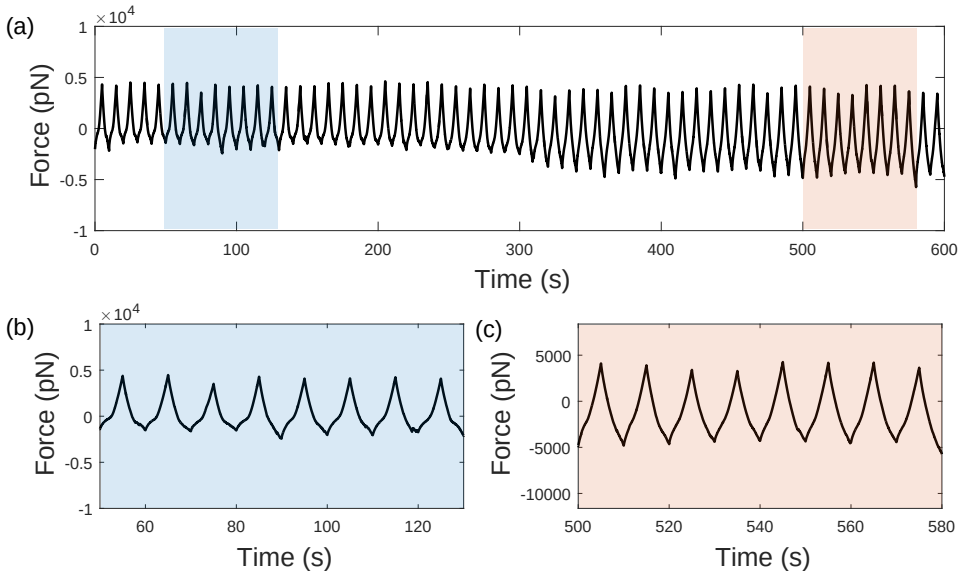


**Figure 5.25:** A force timecourse for a cell subject to oscillations of amplitude 1150nm under the prebind protocol. After $t = 300s$, there appears to be a switch in the opposite direction to Figs. 5.22 and 5.24, resulting in increased, rather than reduced, adhesion.

The above examples were identified by eye; however, if dealing with larger datasets in future, it may be useful to detect switches in the force curves automatically. Using the data in Fig. 5.22 as an example, we now show some possible approaches for quantifying and classifying the shape of the force curves. Firstly, we fit each normalised force curve in Fig. 5.23(a) to Gaussian functions of the form

$$f(t) = a_1 \exp\left(-\frac{(t-\mu)^2}{\sigma^2}\right), \tag{5.2.1}$$

where $a_1$, $\mu$ and $\sigma$ influence the peak height and position and the standard deviation respectively (Fig. 5.26). This fitting (Fig. 5.26(a)) only provides a coarse approximation of the shape of the curves in Fig. 5.23(a); however, the three parameters capture several key features that allow us to separate the data into two distinct families of curves. Visualising the $[a_1, \mu, \sigma]$ triplet that represents each fit (Fig. 5.26(b)), we observe a clear separation in the data points, and two distinct clusters of points.

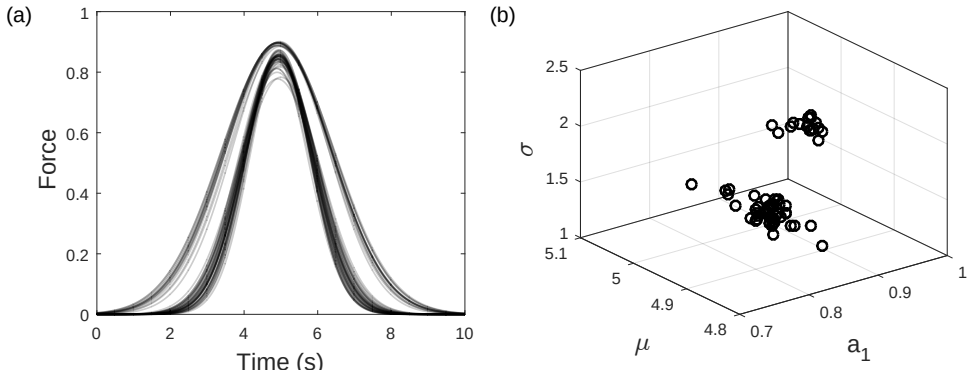


**Figure 5.26:** (a) Each normalised force curve in Fig. 5.23 has been fitted to a Gaussian function. (b) The three parameters uniquely defining the Gaussian (Eq. 5.2.1) can be plotted as points in $\mathbb{R}^3$. Two distinct clusters are seen, corresponding to the two distinct types of curves in (a).

Using the above technique, each force timecourse (consisting of 60 approach–retract cycles) is reduced to 60 points in $\mathbb{R}^3$ (Fig. 5.26), and we use standard cluster analysis techniques to detect cases where switching occurs. One of the simplest clustering methods is $k$–means clustering, which partitions the data points into $k$ clusters for a given value of $k$. Points are assigned to one of the clusters such that the within-cluster variances are minimised. A result of using the `kmeans` function in MATLAB, which relies on a $k$–means++ algorithm [6], applied to the data with $k = 2$ is shown in Fig. 5.27. The algorithm correctly separates the data into the two visible clusters, and provides positions for the centroids of each cluster (shown by blue and orange diamonds for the adhesion and rupture clusters, respectively). Typically, if the true number of

clusters is not known, this algorithm can be applied to the data for a range of $k$ values, and the optimal $k$ can be determined by analysis of the resulting partitions. An example would be to calculate 'silhouettes' of the data [121], which are measures based on within- and inter-cluster distances that quantify how well each data point fits into its given cluster. Further methods for selecting the optimal $k$–value are discussed in [139], but we find that these all require $k \geq 2$, so are not appropriate for determining whether our data exhibits a switch ($k = 2$) or not ($k = 1$).

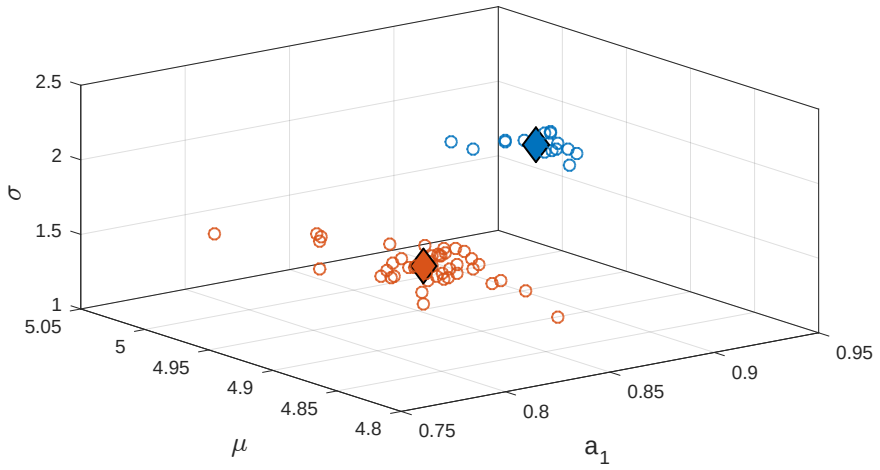


**Figure 5.27:** The result of a $k$–means algorithm applied to the data in Fig. 5.26(b) with $k = 2$. Centroids for the adhesion and rupture clusters are shown by the blue and orange diamonds respectively.

To overcome this, algorithms that do not require the number of clusters to be specified *a priori* could be considered. A possible alternative is a density-based approach called DBSCAN [38]. This algorithm requires two parameters to be specified: a minimum number of points, $m$, that is considered as a cluster and a maximum distance, $\varepsilon$, allowed between an element in a cluster and any other element. The advantage of this algorithm is that it can also classify points as outliers, depending on the minimum point specification, which is useful for noisy experimental data. The disadvantage, however, is that choosing $\varepsilon$ requires careful tuning if there is no intuitive threshold for what this value should be. We demonstrate the dependence of the output on these two parameters in Fig. 5.28. Using $m = 3$ and $\varepsilon = 0.4$ (Fig. 5.28(a)) we find that the data is grouped into one cluster. Reducing $\varepsilon$ (Fig. 5.28) generates two separate clusters as in Fig. 5.27; however, if $\varepsilon$ is reduced further (Fig. 5.28(c)), three clusters are formed. Depending on the choice of $m$, these further clusters could be disregarded as noise (Fig. 5.28(d)). The need for careful fitting of $m$ and $\varepsilon$ is a strong limitation; without a better understanding of what the correct choices should be, we find that

each result needs to be inspected individually anyway. Further work or alternative clustering algorithms should be considered for automatic classification of the data for a large collection of cells.

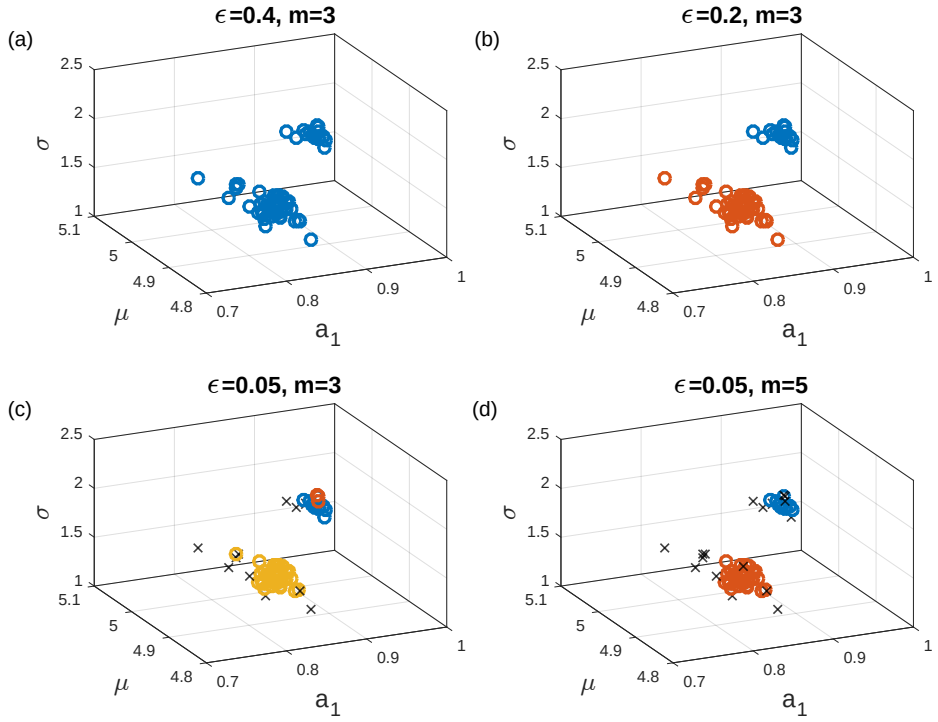


**Figure 5.28:** The result of a DBSCAN algorithm applied to the data in Fig. 5.26(b), with 4 different parameter combinations. In (a), $m = 3$ and $\varepsilon = 0.4$ and one cluster is detected (blue). (b) With a smaller radius, $\varepsilon = 0.2$, the data is partitioned into two clusters (blue and orange) as in Fig. 5.27. (c) If $\varepsilon$ is reduced further, e.g. $\varepsilon = 0.05$, the data is partitioned into three clusters (blue, orange, yellow) and additionally some points are identified as noise (black). (d) With an increase in $m$, the orange cluster in (c) is identified as noise.

An alternative to analysing fitted curves, that does not require transforming the data, could be to exploit the asymmetry of the rupture curves. From observations and model results (Fig. 5.13), force curves with strong adhesion are near-symmetric. However, when rupture dominates, the curves become increasingly asymmetric due to differences during approach and retraction. For each cycle, we have a vector of force values recorded at each timepoint, $F(t) = (F_1, \ldots, F_n)$. A skewness parameter, $S$, can be calculated from this via

$$S = \frac{\frac{1}{n}\sum_{i=1}^{n}(F_i - \mu)^3}{\left(\frac{1}{n-1}\sum_{i=1}^{n}(F_i - \mu)^2\right)^{3/2}}, \tag{5.2.2}$$

where $n$ is the number of data points and $\mu$ is the mean value of force. This measure is the normalised third central moment [77], and will be zero for symmetric data. We again consider the switching cell shown in Fig. 5.22 and determine $S$ for each cycle, tracking the change in skewness over time (Fig. 5.29). We find that each curve has a positive skew, due to higher values of force being obtained during the approach (first) half than the retraction (second) half. After the $16^{\text{th}}$ cycle, where the switch in curve types was previously observed to occur (Fig. 5.23(b)), we see a corresponding sudden increase in skewness. The data points are centered around two distinct means, and the skewness parameter could perhaps provide a one-dimensional alternative for cluster analysis. As in the analysis of the fitted curves, however, we find the need to specify (subjectively) a threshold value of separation that defines distinct clusters.

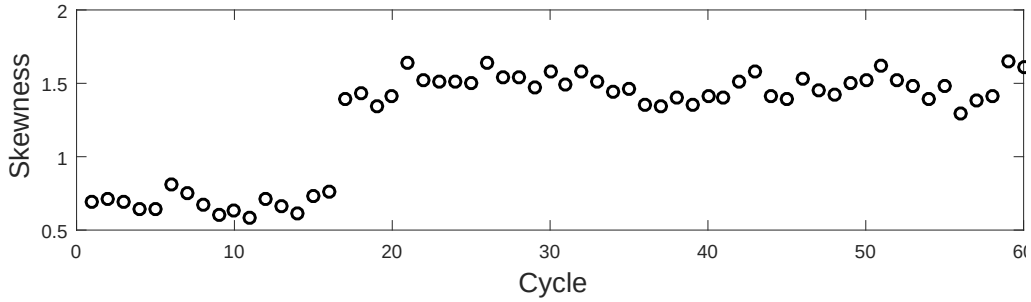


**Figure 5.29:** Skewness parameter (Eq. 5.2.2) calculated for each normalised force curve in Fig. 5.23(a). There is a sudden increase in skewness occurring at the transition (after Cycle 16) from adhesion to rupture curves, reflecting the more noticeable asymmetry of the rupture curves.

Whilst the above measures can visibly separate the data for the cell in Fig. 5.22 into two classes (one for cycles 1-16 and one for later times), quantifying the number of clusters via clustering algorithms requires careful tuning to the data. As part of this, the results must be verified by inspecting the original data and, for this reason, these methods are not yet any more efficient than simply inspecting each timecourse from the outset. We applied the DBSCAN algorithm to timecourses from other cells (results not shown), but did not find a consistent $m$ and $\varepsilon$ pairing to use to correctly predict the number of clusters for all cells. The examples of switching (Figs. 5.22–5.25) were therefore obtained simply by inspection; however, future refinement of the above ideas could perhaps provide a way of automating the detection of timecourses that exhibit switches. This would be useful in larger datasets, where it could be of interest to study the range of amplitudes in which switching behaviour occurs. If a stochastic switch occurs due to bistability, we would expect these amplitudes to lie near, and to

be especially likely near the boundaries of, the bistable region.

## 5.3 Conclusions

In this chapter, we extended the continuum integrin binding model introduced in Chapter 2 to allow for vertical motion between the cell and the ECM. We then incorporated this into a 3-spring model for the cell, integrins and ECM, which we used to simulate vertical oscillations applied to the ECM. The results are similar to those obtained for lateral oscillations in Chapter 3; low amplitude oscillations resulted in a high bound fraction of integrins (Fig. 5.9), and high amplitude oscillations resulted in a low bound fraction of integrins (Fig. 5.7). For intermediate amplitude oscillations, we observed bistability (Fig. 5.11) due to a mechanical cooperativity, showing that the result from Chapter 3 holds for vertical motion.

In Section 5.2 we presented experimental AFM data, which was provided by Prof. Gerald Meininger and Huang Huang (University of Missouri), and in which vertical oscillations were applied to vascular smooth muscle cells (VSMCs). To mimic the zero and saturated initial conditions used in the model, cells were either subjected to a 'prebind' procedure before the oscillations began, or not. For both low and high oscillation amplitudes, which produced distinct patterns in force, the experimentally measured force qualitatively matched the model force. The model therefore provided insight into the mechanisms behind these two distinct behaviours by revealing the corresponding patterns in bound integrin fractions and cell deformations. These are factors that cannot be measured by the experiments. For some amplitudes of oscillation, such as 1200nm (Fig. 5.17), prebinding appeared to make a qualitative difference to the shape of the force curves. When investigating this further (Figs. 5.18, 5.19), we observed behaviour mostly characteristic of adhesion when prebinding occured and behaviour mostly characteristic of rupture when there was no prebinding. However, we also noticed that individual cell heights could vary significantly (Table 5.1), and that this had not been considered in the design of the experiments. Due to this, there is a large amount of uncertainty when directly comparing cells, and we cannot know for sure if the differences seen in the prebind cells are due to bistability or due to intercellular variation. This result highlighted that the variation in cell heights is essential to consider in future AFM studies of this type.

Due to the difficulty in making direct comparisons between cells, we also analysed force timecourses from single cells. Several of these exhibited some interesting behaviour, where a sudden switch in both the magnitude and shape of the force curves were seen (Figs. 5.22–5.25). Although these examples were originally detected by inspecting the raw force data, we demonstrated the use of some data analysis methods that could be used and refined to classify force curves and detect switches automatically. One method was to fit the data to Gaussian functions (5.26), defined uniquely by three parameters. Plotting these parameters in three-dimensional space produces two visible and distinct clusters of points, corresponding to the adhesion- and rupture-type curves. To determine whether the data forms one or two clusters, and therefore whether a timecourse contains one or two types of curve, cluster analysis can be performed on these parameter sets. Note that different functions could also be used for fitting the data, such as polynomials. Many clustering algorithms can be used with high dimensional data, and would therefore still work for more than three parameters. Here we considered $k$–means clustering and a density-based clustering algorithm, DBSCAN, which provided a method for partitioning the data into clusters without first having to specify the number of clusters. DBSCAN requires two parameters to be carefully tuned to the data to ensure accuracy of the results. An alternative to fitting the data to Gaussian functions is to consider the skewness of the force curves (Fig. 5.29), which produces a single parameter for each curve. However, cluster analysis on this parameter still requires careful tuning. Both of these methods require validation by inspecting the original data; further work is therefore needed for automatic detection of the number of clusters for a large number of cells.

The combination of model and experimental data provides some strong evidence for bistability. The difference in prebind and non-prebind data in Figs. 5.18 and 5.19 could form a promising example if we were able to access information about the initial cell heights. This would allow us to infer whether the increased heights in the prebind data (Table 5.2) were a cause or effect of different adhesion states. Although this is currently undetermined, switching behaviour within individual experiments also provides a possible indicator of bistability since, in stochastic systems, bistability often results in switches. Further work is needed to conclusively determine if the bistability predicted by the model is present in cells *in vitro*; however, we have still gained insight through our model results. Our analysis also allowed us to highlight key factors that should be controlled or recorded in future experiments.

# Chapter 6

# Coupling cell–matrix adhesion to contractile force generation

We have so far been investigating the integrin response to oscillatory loading, which affects the transmission of contractile forces, generated by actomyosin crossbridges within ASM cells (Section 1.1.2), to the extracellular matrix. However, it is also known that the generation of contractile force itself can be modulated by oscillatory strain (Section 1.3.3). To fully understand the consequences for bronchoconstriction, there is therefore a need to consider both of these processes together and to couple models of integrin-mediated force transmission to descriptions of intracellular contractile force generation. In this chapter we address this by extending the 3-spring model introduced in Chapter 5. In our previous model, the cell was modelled as a passive material (Fig. 5.1); here we account for active processes within the cell by incorporating a well-established continuum model of contractile force generation. Using our coupled model, which accounts for actomyosin crossbridge dynamics within the cell, we investigate the interacting crossbridge and integrin dynamics that occur in response to oscillatory length fluctuations (Section 6.3).

## 6.1 Huxley–Hai–Murphy (HHM) model

To model intracellular crossbridge dynamics and the resultant contractile force generation, we use the Huxley–Hai–Murphy (HHM) model [47, 97]. This model extends the original Huxley crossbridge model [70] and has previously been incorporated into cell and airway level models [24, 64, 65, 112]. The HHM model accounts for myosin crossbridges as they transition between 4 possible states (illustrated in Fig. 6.1): un-

phosphorylated and unattached to actin ($M$), phosphorylated and unattached ($Mp$), phosphorylated and attached to actin ($AMp$) and unphosphorylated and attached to actin ($AM$). As depicted in the reaction schematic in Fig. 6.1, phosphorylation reactions are assigned constant reaction rates. However, following Huxley [70], the reaction rates for binding and unbinding from actin depend on a local spatial coordinate, $\hat{y}$, measuring a local displacement of the myosin head from its unstressed position.

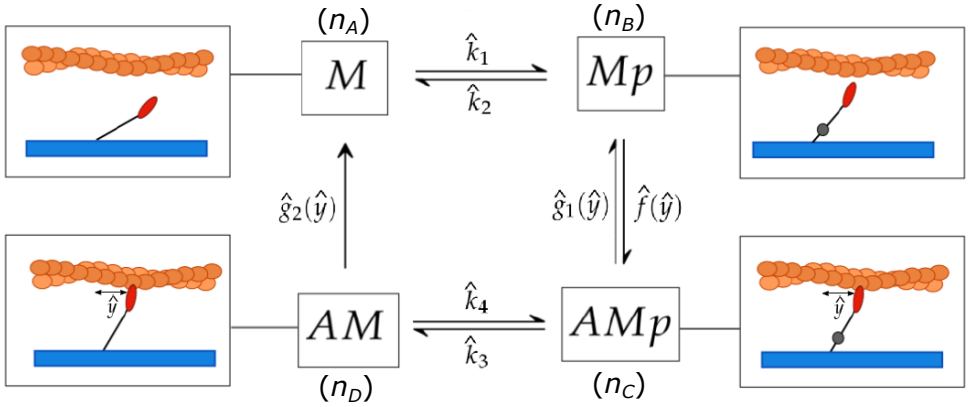


**Figure 6.1:** Myosin crossbridges transition between 4 possible states: unphosphorylated and unattached to actin ($M$), phosphorylated and unattached to actin ($Mp$), unphosphorylated and attached to actin ($AM$) and phosphorylated and attached to actin ($AMp$). The phosphorylation reactions are assigned constant reaction rates ($\hat{k}_1$–$\hat{k}_4$) whilst the binding and unbinding reactions rates ($\hat{f}, \hat{g}_1, \hat{g}_2$) are modelled as in the Huxley model [70] and depend on a local coordinate, $\hat{y}$. The four states will be represented by distributions, $n_A(\hat{y}, \hat{t})$–$n_D(\hat{y}, \hat{t})$, respectively.

Following a similar formulation to the model in Section 2.2.1, we consider distributions of each species: $n_A(\hat{y}, \hat{t})$, $n_B(\hat{y}, \hat{t})$, $n_C(\hat{y}, \hat{t})$ and $n_D(\hat{y}, \hat{t})$, which correspond to the fractions of crossbridges in the states $M$, $Mp$, $AMp$ and $AM$ respectively. As in our previous models, the governing equations are a system of advection–reaction equations given by

$$\frac{\partial n_A}{\partial \hat{t}} + \hat{v}(\hat{t})\frac{\partial n_A}{\partial \hat{y}} = \hat{k}_2 n_B - \hat{k}_1 n_A + \hat{g}_2(\hat{y}) n_D, \tag{6.1.1}$$

$$\frac{\partial n_B}{\partial \hat{t}} + \hat{v}(\hat{t})\frac{\partial n_B}{\partial \hat{y}} = -\hat{k}_2 n_B + \hat{k}_1 n_A - \hat{f}(\hat{y}) n_B + \hat{g}_1(\hat{y}) n_C, \tag{6.1.2}$$

$$\frac{\partial n_C}{\partial \hat{t}} + \hat{v}(\hat{t})\frac{\partial n_C}{\partial \hat{y}} = \hat{f}(\hat{y}) n_B - \hat{g}_1(\hat{y}) n_C - \hat{k}_3 n_C + \hat{k}_4 n_D, \tag{6.1.3}$$

$$\frac{\partial n_D}{\partial \hat{t}} + \hat{v}(\hat{t})\frac{\partial n_D}{\partial \hat{y}} = \hat{k}_3 n_c - \hat{k}_4 n_D - \hat{g}_2(\hat{y}) n_D, \tag{6.1.4}$$

where $\hat{v}(\hat{t})$ is the relative velocity of the actin and myosin filaments and the reaction

terms correspond to the state transitions shown in Fig. 6.1. Note that, in the original HHM model, $\hat{v}(\hat{t})$ (referred to as the shortening velocity) was defined to be positive in the direction of contraction. However, to ensure consistency with the directionality used in the 3-spring model, we choose to define $\hat{v}(\hat{t})$ to be negative in the direction of contraction as the two models will later be coupled. This results in a positive, rather than negative, advection term here. In this model the single-site binding assumption is used (discussed in Section 2.2.1), meaning that the conservation law $n_A + n_B + n_C + n_D = 1$ holds. We can therefore eliminate one variable and consider a reduced set of equations. In the simulations that follow, we evolve Eqs. 6.1.2–6.1.4.

Following the Huxley model [70, 97], the spatial binding rate functions, $\hat{f}(\hat{y})$, $\hat{g}_1(\hat{y})$ and $\hat{g}_2(\hat{y})$, are defined as

$$\hat{f}(\hat{y}) = \begin{cases} \hat{f}_A \hat{y}/\hat{h}_c & 0 \leq \hat{y} \leq \hat{h}_c \\ 0 & \text{otherwise,} \end{cases} \tag{6.1.5}$$

where $\hat{h}_c$ is the crossbridge binding range and $\hat{f}_A > 0$ is the maximum binding rate, obtained at $\hat{y} = \hat{h}_c$;

$$\hat{g}_1(\hat{y}) = \begin{cases} \hat{g}_A & \hat{y} < 0 \\ \hat{g}_B \hat{y}/\hat{h}_c & 0 \leq \hat{y} \leq \hat{h}_c \\ (\hat{g}_B + \hat{g}_C)\hat{y}/\hat{h}_c & \hat{y} > \hat{h}_c, \end{cases} \tag{6.1.6}$$

where $\hat{g}_A$, $\hat{g}_B$ and $\hat{g}_C$ are positive unbinding rate constants; and

$$\hat{g}_2(\hat{y}) = \begin{cases} \hat{\tilde{g}}_A & \hat{y} < 0 \\ \hat{\tilde{g}}_B \hat{y}/\hat{h}_c & 0 \leq \hat{y} \leq \hat{h}_c \\ (\hat{\tilde{g}}_B + \hat{\tilde{g}}_C)\hat{y}/\hat{h}_c & \hat{y} > \hat{h}_c, \end{cases} \tag{6.1.7}$$

where $\hat{\tilde{g}}_A$, $\hat{\tilde{g}}_B$ and $\hat{\tilde{g}}_C$ (all positive) are modified unbinding rate constants for the unphosphorylated crossbridges (Fig. 6.1). In contrast to the binding rates in our integrin model (Eqs. 5.1.16 and 5.1.17), these rates are asymmetric: crossbridges bind preferentially at positive distances, $\hat{y}$. The form of the rate functions are shown in Fig. 6.2.

Contractile force is generated by crossbridges in the attached ($AM$ and $AMp$) states. We assume that crossbridges have the same stiffness in both of these states; the force in each contractile unit is therefore given by

$$\hat{F}_{cu}(\hat{t}) = \hat{\rho}_c \hat{\lambda}_c \int_{-\infty}^{\infty} \hat{y}(n_C + n_D) d\hat{y}, \tag{6.1.8}$$

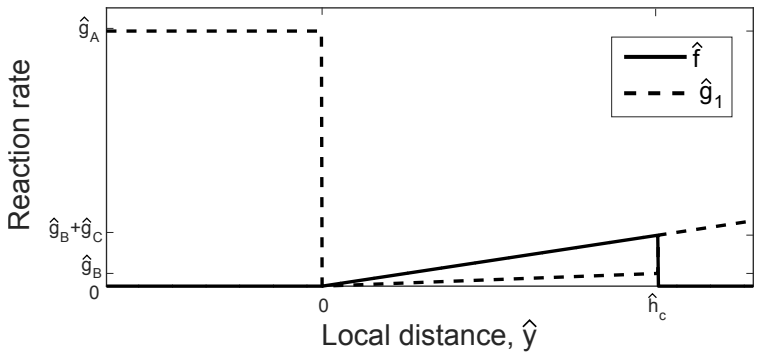


**Figure 6.2:** Sketch of the functional forms of the spatial binding rate function $\hat{f}(\hat{y})$ (Eq. 6.1.5) and the unbinding rate function $\hat{g}_1(\hat{y})$ (Eq. 6.1.6) for phosphorylated crossbridges. The modified unbinding rate function for unphosphorylated crossbridges, $\hat{g}_2(\hat{y})$ (Eq. 6.1.7), is of the same form as $\hat{g}_1(\hat{y})$ but with different rate constants (Appendix B).

where $\hat{\rho}_c$ is the total number of crossbridges (bound and unbound) per unit length of the contractile unit, and where $\hat{\lambda}_c$ is the crossbridge spring constant. The derivation of Eqs. 6.1.1–6.1.8 uses the methods presented in Section 2.2.1, and full details can be found in [47, 70, 97].

## 6.2 Coupling to the 3-spring framework

In this section we modify the 3-spring framework presented in Chapter 5 by extending the linear spring representation of the cell (Fig. 5.1) to include active contractile components, following the HHM description overviewed in Section 6.1. Contractile units are considered to act in parallel with the original spring (see schematic in Fig. 6.3); we therefore now account for both passive cytoskeletal stiffness and active contractile force generation via actomyosin crossbridges.

The HHM model introduced in Section 6.1 is used to model each of the contractile units. Since the contractile units are positioned in parallel, and the cell surface (green, Fig. 6.3) is assumed locally rigid (Section 5.1.1), the relative velocity, $\hat{v}(\hat{t})$, is identical for each of them; the governing equations for the crossbridge distributions are therefore the same in each contractile unit. The resulting coupled system is a system of five advection–reaction equations: four for the crossbridge distributions $n_A(\hat{y},\hat{t})$–$n_D(\hat{y},\hat{t})$ (Eqs. 6.1.1–6.1.4) and one for the integrin distribution $\hat{b}(\hat{x},\hat{t})$ (Eq. 5.1.18). To account for the force generated by parallel contractile units, the total contractile force is given

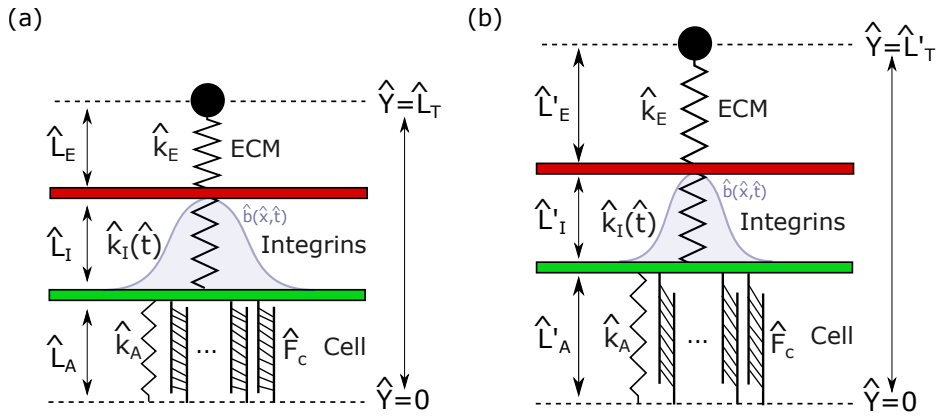


**Figure 6.3:** Schematic of the modified 3-spring model in (a) the rest configuration and (b) a deformed configuration. Hookean springs in series represent the (passive) cytoskeleton, bound integrins and the ECM with spring constants $\hat{k}_A$, $\hat{k}_I(\hat{t})$ and $\hat{k}_E$ respectively. Additional intracellular contractile units act in parallel to account for active contractile force generation, $\hat{F}_C(\hat{t})$, within the cell (Section 6.1). The cytoskeletal, integrin and ECM springs have rest lengths $\hat{L}_A, \hat{L}_I$ and $\hat{L}_E$ and time-dependent deformed lengths $\hat{L}'_A(\hat{t}), \hat{L}'_I(\hat{t})$ and $\hat{L}'_E(\hat{t})$ respectively. The collective integrin spring constant, $\hat{k}_I(\hat{t})$, evolves in time according to the underlying distribution of integrins, $\hat{b}(\hat{x}, \hat{t})$ (Section 5.1.2), and is proportional to the fraction of double-bound integrins, $B \in [0, 1]$.

by

$$\hat{F}_C(\hat{t}) = \hat{\rho}_c \hat{\lambda}_c N_{CU} \int_{-\infty}^{\infty} \hat{y}(n_C + n_D) d\hat{y}, \tag{6.2.1}$$

where $N_{CU}$ is the number of parallel contractile units. At each point in time, we assume all components are in equilibrium so that forces balance in a similar manner to Chapter 5. We define the relative velocity in the HHM model (Eqs. 6.1.1–6.1.4) to be

$$\hat{v}(\hat{t}) = \frac{\partial \hat{L}'_A}{\partial \hat{t}}, \tag{6.2.2}$$

where $\hat{L}'_A$ is the deformed height of the cell (Fig. 6.3). As in the 3-spring model, $\hat{L}'_E$ is the deformed ECM length (with rest length $\hat{L}_E$) and $\hat{L}'_I$ is the deformed integrin length (with rest length $\hat{L}_I$).

**Nondimensionalisation**

We nondimensionalise the ECM and integrin equations as in Chapter 5 (Section 5.1); all lengths are scaled by the integrin binding range, $\hat{h}$ (Eq. 2.1.2), and the spring constants are scaled by $\rho\hat{\lambda}_b$, where $\rho$ and $\hat{\lambda}_b$ are the number and spring constant of individual integrins, respectively (Eq. 5.1.1). The dimensionless total deformed length is given by

$$L'_T(t) = L'_E(t) + L'_I(t) + L'_A(t). \tag{6.2.3}$$

The HHM model equations and binding rate functions (Eqs. 6.1.1–6.1.8) are nondimensionalised with the scalings

$$y = \frac{\hat{y}}{\hat{h}}, \quad v = \frac{\hat{v}}{\hat{f}_1 \hat{h}}, \quad F_C = \frac{\hat{F}_C}{\hat{h}\rho\hat{\lambda}_b}, \quad h_c = \frac{\hat{h}_c}{\hat{h}}, \quad k_i = \frac{\hat{k}_i}{\hat{f}_1}, \quad t = \hat{t}\hat{f}_1, \tag{6.2.4}$$

where $i \in [1, ..., 4]$ and $\hat{f}_1$ is the maximum integrin binding rate (Eq. 2.1.2). This choice of scalings ensures consistency when coupling to the model of integrin binding dynamics (Eq. 5.1.18).

The dimensionless HHM model equations are

$$\frac{\partial n_A}{\partial t} + v(t)\frac{\partial n_A}{\partial y} = k_2 n_B - k_1 n_A + g_2(y) n_D, \tag{6.2.5}$$

$$\frac{\partial n_B}{\partial t} + v(t)\frac{\partial n_B}{\partial y} = -k_2 n_B + k_1 n_A - f(y) n_B + g_1(y) n_C, \tag{6.2.6}$$

$$\frac{\partial n_C}{\partial t} + v(t)\frac{\partial n_C}{\partial y} = f(y) n_B - g_1(y) n_C - k_3 n_C + k_4 n_D, \tag{6.2.7}$$

$$\frac{\partial n_D}{\partial t} + v(t)\frac{\partial n_D}{\partial y} = k_3 n_c - k_4 n_D - g_2(y) n_D, \tag{6.2.8}$$

where

$$v(t) = \frac{\partial L'_A}{\partial t}. \tag{6.2.9}$$

The dimensionless contractile force is

$$F_C(t) = \beta \int_{-\infty}^{\infty} y(n_C + n_D)dy, \tag{6.2.10}$$

for dimensionless parameter $\beta = \rho_c \lambda_c N_{CU}$, and where $\rho_c = \hat{\rho}_c \hat{h}$ and $\lambda_c = \hat{\lambda}_c / \rho \hat{\lambda}_b$. Additionally we scale each of the binding rates ($\hat{f}$, $\hat{g}_1$, $\hat{g}_2$) by $\hat{f}_1$ (Eq. 2.1.2), giving the dimensionless rate functions as

$$f(y) = \begin{cases} f_A y/\gamma & 0 \leq y \leq \gamma \\ 0 & \text{otherwise,} \end{cases} \tag{6.2.11}$$

$$g_1(y) = \begin{cases} g_A & y < 0 \\ g_B y/\gamma & 0 \leq y \leq \gamma \\ (g_B + g_C)y/\gamma & y > \gamma, \end{cases} \tag{6.2.12}$$

$$g_2(y) = \begin{cases} \tilde{g}_A & y < 0 \\ \tilde{g}_B y/\gamma & 0 \leq y \leq \gamma \\ (\tilde{g}_B + \tilde{g}_C)y/\gamma & y > \gamma, \end{cases} \tag{6.2.13}$$

where $\gamma = \hat{h}_c / \hat{h}$ is the ratio of crossbridge and integrin binding ranges (Eq. 6.1.5 and Eq. 2.1.2).

**Implementation**

As in Chapter 5, we mimic length changes due to tidal breathing by applying a displacement condition, $Y = L'_T(t)$, to the top of the ECM. To solve the system of equations, we need to be able to determine the three resulting deformed spring lengths ($L'_E$, $L'_I$, $L'_A$), the crossbridge distributions, $n_A(y,t)$–$n_D(y,t)$, the relative velocity, $v(t)$, and the integrin distribution, $b(x,t;L)$. From the above, we find that we currently have 7 equations (Eqs. 6.1.1–6.1.4, Eq. 5.1.18, Eq. 6.2.3 and Eq. 6.2.9) for 9 unknowns. As in Chapter 5, the remaining two equations are obtained by considering force balances.

To carry out force balances, we are required to consider separate cases (Fig. 6.4) depending on a number of factors. Firstly, in the presence of bound integrins we consider two cases depending on whether the system is under tension (Case 1A) or compression (Case 1B). The transition between tension and compression occurs when the

force in each component is zero, *i.e.* when

$$k_E(L'_E - L_E) = B(L'_I - L_I) = k_A(L'_A - L_A) + F_C = 0. \tag{6.2.14}$$

This requires $L'_E = L_E$, $L'_I = L_I$ and $L'_A = L_A - F_C/k_A$, which sum (using Eq. 6.2.3) to give

$$L'_T = L_T - F_C/k_A. \tag{6.2.15}$$

The conditions for the two cases are therefore

$$\begin{aligned} &\text{Case 1A:} \quad B \neq 0, \quad L'_T > L_T - F_C/k_A \\ &\text{Case 1B:} \quad B \neq 0, \quad L'_T \leq L_T - F_C/k_A. \end{aligned} \tag{6.2.16}$$

We assume that under compression (Case 1B) integrins are incompressible, meaning that they behave as rigid beams (*i.e.* we enforce $L'_I = L_I$). If there are no bound integrins, we consider two further cases: when there is separation between the cell and ECM (Case 2A) and when there is contact (Case 2B). The transition occurs when Eq. 6.2.14 holds and when $L'_T = L'_E + L'_A$. This gives

$$\begin{aligned} &\text{Case 2A:} \quad B = 0, \quad L'_T - L_E > L_A - F_C/k_A \\ &\text{Case 2B:} \quad B = 0, \quad L'_T - L_E \leq L_A - F_C/k_A. \end{aligned} \tag{6.2.17}$$

These four cases are illustrated in Fig. 6.4, and we now consider each of them in turn. In each case, we state the corresponding force balance conditions, and use these to find expressions for the unknowns $L'_E$, $L'_I$, $L'_E$ and $v(t)$. This closes the system of equations and allows us to evolve the model for any given displacement $L'_T(t)$.

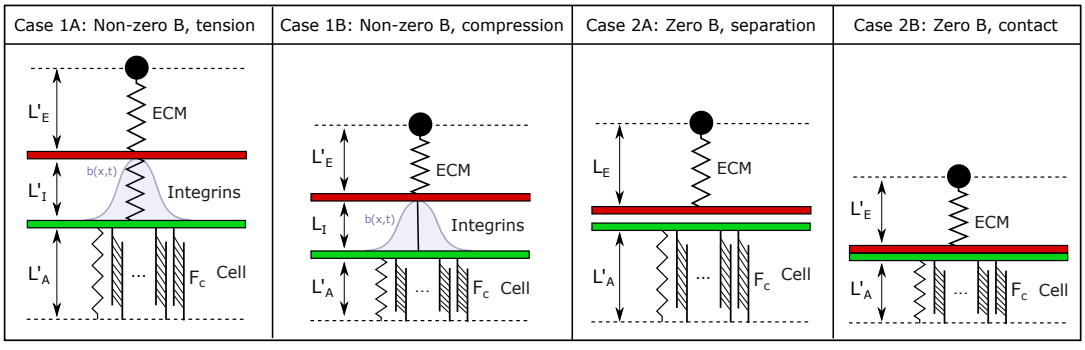


**Figure 6.4:** Illustration of the four cases considered when carrying out force balances. The cases are determined by the conditions in Eqs. 6.2.16 and 6.2.17, which account for a non-zero or zero fraction of bound integrins, respectively. We consider tension or compression (where integrins are assumed rigid) and separation or contact between the ECM and cell.

Case 1A: Non-zero B and tension

The dimensionless force balance equations are

$$k_E(L'_E - L_E) = B(L'_I - L_I) = k_A(L'_A - L_A) + \beta \int_{-\infty}^{\infty} y(n_C + n_D)dy, \tag{6.2.18}$$

which is Eq. 5.1.3 (from the 3-spring model) with an added term for the force generated in the HHM model (Eq. 6.2.10). These are used together with the Eq. 6.2.3 to calculate the deformed lengths. Eliminating $L'_I$ we obtain

$$L'_E = \frac{B(L'_T - L'_A - L_I) + k_E L_E}{k_E + B}, \tag{6.2.19}$$

which is substituted into Eq. 6.2.18 to give

$$L'_A = \frac{k_E B(L'_T - L_I - L_E) + k_A L_A(k_E + B) - \beta(k_E + B)\int_{-\infty}^{\infty} y(n_C + n_D)dy}{k_A(k_E + B) + k_E B}. \tag{6.2.20}$$

At a given point in time, each of the terms on the right hand side of Eq. 6.2.20 are known, allowing $L'_E$ and $L'_I$ to be calculated via Eq. 6.2.19 and Eq. 6.2.3, respectively.

To evolve the HHM governing equations, we additionally require an expression for $v(t) = \partial L'_A/\partial t$, which is found by differentiating Eq. 6.2.20 with respect to time. We then use Eqs. 5.1.18, 6.2.7 and 6.2.8 to eliminate the resulting time derivatives. The final expression is

$$v(t) = \frac{\partial L'_A}{\partial t} = \frac{\sigma \mathcal{F}_1 - (k_A + k_E)\mathcal{F}_2 \int_{-\infty}^{\infty} (\eta k_b(1 - B) - k_u b)\, dx}{\sigma^2 + \beta\,(k_E + B)\,\sigma N_{att}}, \tag{6.2.21}$$

where

$$\begin{aligned} \mathcal{F}_1 = \;& k_E B \frac{\partial L'_T}{\partial t} - \beta\,(k_E + B) \int_{-\infty}^{\infty} y\,(f n_B - g_1 n_C - g_2 n_D)\, dy \\ & + \left(k_E(L'_T - L_I - L_E) + k_A L_A - F_C\right) \int_{-\infty}^{\infty} (\eta k_b(1 - B) - k_u b)\, dx, \end{aligned} \tag{6.2.22}$$

$$\mathcal{F}_2 = k_E B(L'_T - L_I - L_E) + k_A L_A(k_E + B) - (k_E + B)F_C, \tag{6.2.23}$$

and

$$\sigma = k_A(k_E + B) + k_E B. \tag{6.2.24}$$

In addition, we have defined $N_{att} = N_C + N_D$ where (as in the definition for the bound fraction of integrins, $B$ in Eq. 5.1.19),

$$N_C = \int_{-\infty}^{\infty} n_C(y,t)dy, \qquad N_D = \int_{-\infty}^{\infty} n_D(y,t)dy. \tag{6.2.25}$$

The expression for $v(t)$ can now be substituted into the HHM governing equations (Eqs. 6.1.1–6.1.4), where we approximate the integrals numerically using the built-in MATLAB function, `trapz`.

Case 1B: Non-zero B and compression

Since we assume that integrins are incompressible we now assume rigidity of integrins and solve

$$F = k_E(L'_E - L_E) = k_A(L'_A - L_A) + \beta \int_{-\infty}^{\infty} y(n_C + n_D)dy. \tag{6.2.26}$$

This is solved alongside Eq. 6.2.3, leading to

$$L'_A = \frac{k_E(L'_T - L_E - L_I) - \beta \int_{-\infty}^{\infty} y(n_C + n_D)dy + k_A L_A}{k_A + k_E}, \tag{6.2.27}$$

$$L'_I = L_I, \tag{6.2.28}$$

$$L'_E = L'_T - L_I - L'_A. \tag{6.2.29}$$

As in Case 1A, differentiating Eq. 6.2.27 with respect to time and using Eqs. 6.2.7 and 6.2.8 gives the velocity

$$v(t) = \frac{\partial L'_A}{\partial t} = \frac{k_E \frac{\partial L'_T}{\partial t} - \beta \int_{-\infty}^{\infty} y\left(f n_B - g_1 n_C - g_2 n_D\right) dy}{k_A + k_E + \beta N_{att}}, \tag{6.2.30}$$

which is substituted into the HHM governing equations (Eqs. 6.1.1–6.1.4).

Case 2A: Zero B and separation

In this case the intermediate connection between cell and ECM is removed (Fig. 6.4). If there is no contact between cell and ECM we obtain

$$F = k_E(L'_E - L_E) = 0 = k_A(L'_A - L_A) + \beta \int_{-\infty}^{\infty} y(n_C + n_D)dy. \tag{6.2.31}$$

This is satisfied when $L'_E = L_E$ and

$$L'_A = L_A - \frac{\beta}{k_A} \int_{-\infty}^{\infty} y(n_C + n_D)dy, \tag{6.2.32}$$

which, with the use of Eqs. 6.2.7 and 6.2.8, gives

$$v(t) = \frac{\partial L'_A}{\partial t} = -\frac{\beta \int_{-\infty}^{\infty} y\left(f n_B - g_1 n_C - g_2 n_D\right) dy}{k_A + \beta N_{att}}. \tag{6.2.33}$$

Case 2B: Zero B and contact

If there are no bound integrins but there is contact between the ECM and cell (Fig. 6.4), we require

$$F = k_E(L'_E - L_E) = k_A(L'_A - L_A) + \beta \int_{-\infty}^{\infty} y(n_C + n_D)dy. \tag{6.2.34}$$

We use the relation $L'_E = L'_T - L'_A$ to obtain

$$L'_A = \frac{k_E(L'_T - L_E) + k_A L_A - \beta \int_{-\infty}^{\infty} y(n_C + n_D)dy}{k_A + k_E}, \tag{6.2.35}$$

which is differentiated with respect to time to give

$$v(t) = \frac{\partial L'_A}{\partial t} = \frac{k_E \frac{\partial L'_T}{\partial t} - \beta \int_{-\infty}^{\infty} y\,(f n_B - g_1 n_C - g_2 n_D)\,dy}{k_A + k_E + \beta N_{att}}, \tag{6.2.36}$$

where substitutions from Eqs. 6.2.7 and 6.2.8 have again been used.

**Summary**

In summary, the model is solved by evolving the system of advection–reaction equations in Eqs. 6.2.5–6.2.8 and Eq. 5.1.18. To do so, we additionally make use of algebraic expressions for the deformed spring lengths ($L'_E, L'_I, L'_A$) and a relative velocity $v(t)$. The expressions for these vary according to the four cases described above (illustrated in Fig. 6.4), and are determined by conditions on the bound fraction of integrins, $B$, and the applied displacement, $L'_T$. In Cases 2A and 2B, the length $L'_I$ is not required. To implement the model, we use the numerical techniques described in Section 2.2.4 to evolve the advection–reaction equations; the crossbridge distributions, $n_A(y,t)$–$n_D(y,t)$, are treated analogously to the integrin distribution, $b(x,t)$. We find that the explicit solver `ode45` provides sufficient stability for this model, and more efficiently produces the same results.

## 6.3 Coupled crossbridge and integrin dynamics

In this section, we present numerical results from the model introduced in Section 6.2. As in Section 5.1.3, we apply vertical oscillations to the ECM, and are now able to study the resulting actomyosin crossbridge dynamics and their interactions with the integrins. The relative importance of contractile force generation (via crossbridges) and contractile force transmission (via integrins) is key to understanding bronchoconstriction, and in Section 6.3.2 we conduct a parameter study to investigate this.

### 6.3.1 Crossbridge response to oscillatory loading

Throughout, we have been interested in how contractile force transmission (via integrins) is affected by dynamic loading, representing breathing. We now consider how the generation of those contractile forces is affected. To demonstrate the crossbridge response to oscillatory load, we first isolate the crossbridge dynamics from the adhesion dynamics by using a saturated initial condition for $B$ (Eq. 2.2.12) and setting the integrin binding rates, $k_b(d)$ and $k_u(d)$, to zero. The effective stiffness of the integrin springs therefore remains constant. We impose sinusoidal vertical oscillations via

$$L_T'(t) = L_T - D + A\left(1 + \sin\left(\omega t - \frac{3\pi}{2}\right)\right), \tag{6.3.1}$$

where the constants $A$, $L_T - D$ and $\omega$ are the amplitude, minimum height and frequency of oscillation, respectively.

The initial conditions for the crossbridges in each of the four states (Fig. 6.1) are

$$n_A(y,t) = 1, \qquad n_B(y,t) = 0, \qquad n_C(y,t) = 0, \qquad n_D(y,t) = 0, \tag{6.3.2}$$

and for the rate functions (Eqs. 6.1.5–6.1.7) we use the parameters given by Mijailovich *et al.* [97] (and listed here in Appendix B). In the following simulations, we use $\beta = 0.3$ as the dimensionless parameter that scales the contractile force (Eq. 6.2.10); we will demonstrate the effect of varying this in Section 6.3.2.

We first show timecourses for the fractions of the attached crossbridges ($N_C$, $N_D$, Eq. 6.2.25) for varying amplitudes of oscillatory loading (Fig. 6.5). As the amplitude increases, there is a rapid decrease in both types of attached crossbridges, which then converge to non-zero oscillatory states. The oscillations are more pronounced in $N_C$ (the $AMp$ crossbridges, Fig. 6.1) since both binding and unbinding are directly influenced by the spatial binding rates $f(y)$ and $g_1(y)$ (Eqs. 6.2.11 and 6.2.12).

We next examine the spatial distributions for each of the crossbridge states (Fig. 6.1) for $A = 1$ (Fig. 6.6) and for $A = 8$ (Fig. 6.7). Due to the form of the binding rates in Eq. 6.2.11, crossbridges attach at positive displacements, $y$. Distributions are then advected back and forth, with the attached crossbridges ($n_C(y,t)$ and $n_D(y,t)$) spanning a wider range of displacements as $A$ increases. As in Fig. 6.5, the peak heights of $n_C(y,t)$ and $n_D(y,t)$ are lower for $A = 8$ (Fig. 6.7(c, d)) compared to $A = 1$ (Fig. 6.6(c, d)), showing that there is greater disruption to attached crossbridges as $A$ increases.

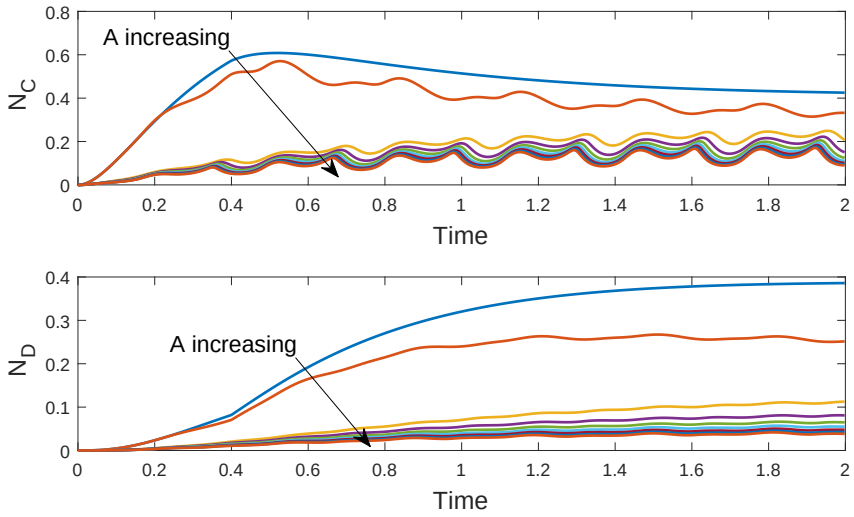


**Figure 6.5:** Timecourses for the densities of attached crossbridges ($N_C$, $N_D$; Eq. 6.2.25) as the amplitude, $A$, of oscillatory loading (Eq. 6.3.1) increases in integer values from $A = 0$ to $A = 8$. In Eq. 6.3.1, $D = 0$ and $\omega = 20$. A full list of parameter values is in Appendix B.

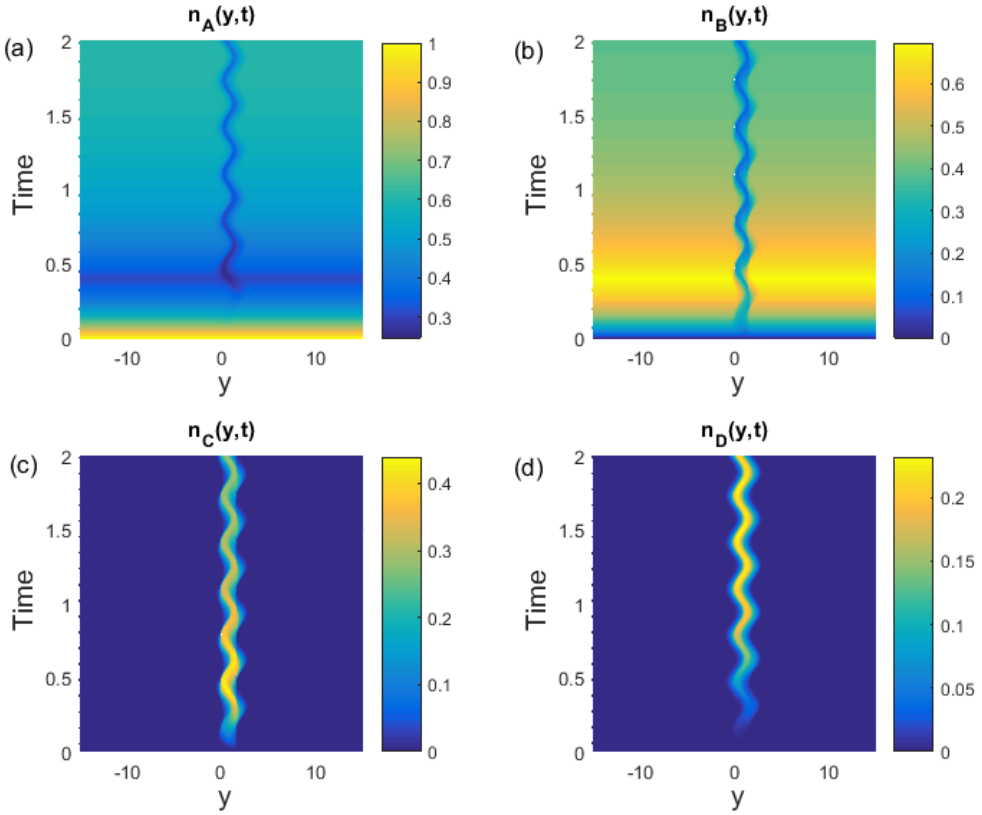


**Figure 6.6:** Spatial distributions of the crossbridge states, $n_A(y,t)$–$n_D(y,t)$ (Fig. 6.1), for $A = 1$ (Eq. 6.3.1). A full list of parameter values is in Appendix B.

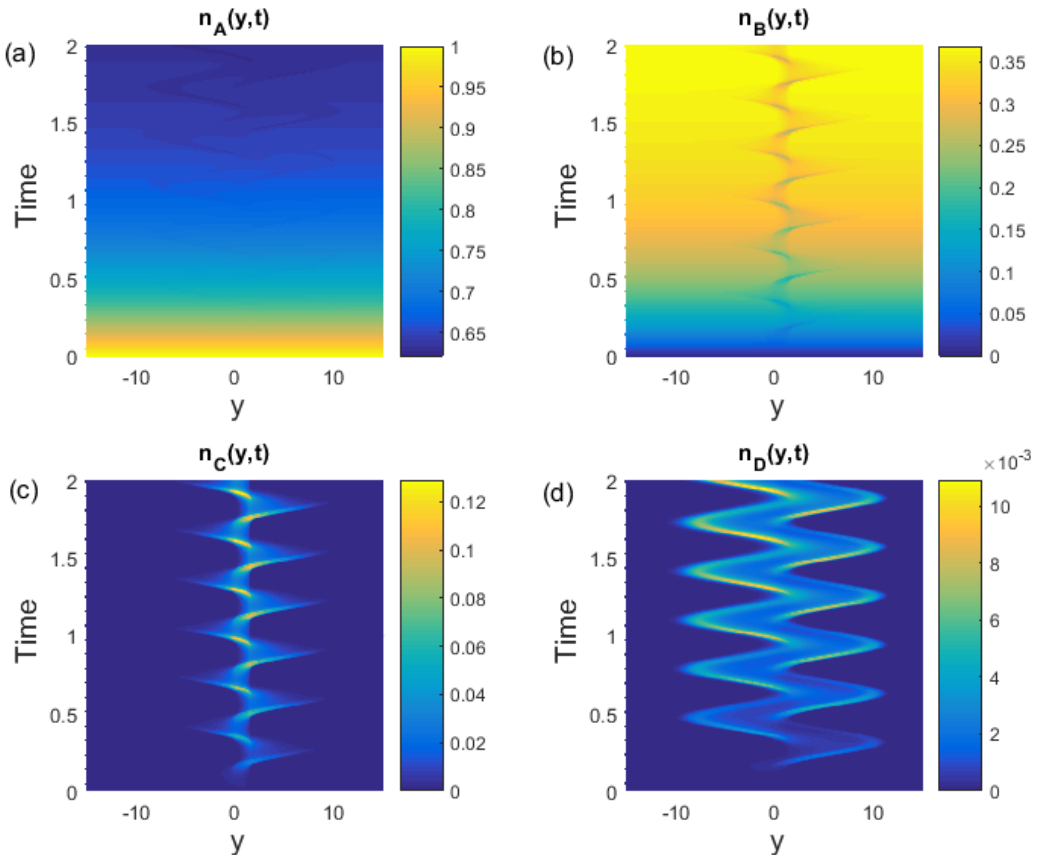


**Figure 6.7:** Spatial distributions of the crossbridge states, $n_A(y,t)$–$n_D(y,t)$ (Fig. 6.1), for $A = 8$ (Eq. 6.3.1). A full list of parameter values is in Appendix B.

The modified crossbridge distributions result in different total contractile forces (Eq. 6.2.10) generated for $A = 1$ (Fig. 6.6) cf. $A = 8$ (Fig. 6.7). Timecourses for the contractile force in each case (Fig. 6.8) confirm that lower peak and mean contractile forces are obtained for $A = 8$. We note also that the peak forces occur at earlier times for $A = 8$, and that there is an asymmetry in the shape of the oscillations. Although the frequency of oscillation is the same in each case, the shifted peak forces for $A = 8$ are a result of rupture occuring at earlier times. This also affects the shape of the oscillations, which deviate from the applied sinusoidal waveform.

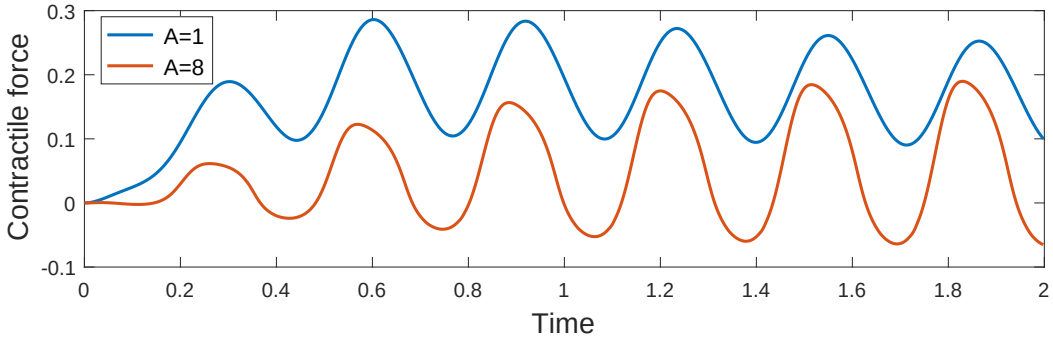


**Figure 6.8:** Timecourses for the contractile force generated by crossbridges when $A = 1$ (blue) and $A = 8$ (orange) in Eq. 6.3.1. These correspond to the crossbridge distributions in Fig. 6.6 and 6.7 respectively.

The results in this section (with constant bound fraction $B$) are consistent with previous studies using the HHM model, where length oscillations resulted in disruption of attached crossbridges and reduced mean contractile force [97]. Having recapitulated this behaviour, we will now consider our fully coupled system (Section 6.2) in which the crossbridges and integrins interact.

### 6.3.2 Interacting crossbridge and integrin dynamics

We now investigate the coupled crossbridge and integrin response to changes in the amplitude, $A$ (Eq. 6.3.1), which is increased and then decreased in gradual steps within the range $A = [0, 2]$. Timecourses for (a) the applied displacement, (b) the bound integrin fraction, (c) the attached crossbridge fraction and (d) the resulting cell height, are shown in Fig. 6.9, where different colours indicate changes in amplitude.

As the applied displacement (Fig. 6.9(a)) increases, we observe a decreasing density of bound integrins (Fig. 6.9(b)) and, at $t \approx 25$, there is a sudden collapse from high to low

oscillatory states. The applied displacement is reduced symmetrically; however, the bound integrin timecourse shows asymmetry in its response. The system therefore exhibits hysteresis, and we find that the behaviours for $A = 1$ (yellow) and $A = 1.25$ (purple) demonstrate bistability. This is behaviour that we previously observed in our discrete and continuum models with lateral oscillations (Figs. 3.1 and 3.5) and our 3-spring model for vertical oscillations, in the absence of crossbridge dynamics (Fig. 5.11). We now examine the corresponding crossbridge behaviour (Fig. 6.9(c)). Initially, whilst the integrins are in the highly bound oscillatory state, the attached crossbridge density, $N_{att}$, also decreases with increasing $A$. However, as the bound integrin fraction continues to decrease, we observe an increase in $N_{att}$. We note that, when displaced vertically, bound integrins induce deformation of the cell. For a high bound integrin fraction, the cell deformation is large, thus transmitting a large strain to the crossbridges. However, when the bound integrin fraction is reduced, there is less cell deformation which results in less disruption to the crossbridges. The system therefore demonstrates negative feedback, where changes in force transmission or force generation (via integrins or crossbridges, respectively) may be compensated in some way by an opposing response. This could have interesting consequences for the total contractile force, as it provides a mechanism for regulating the minimum and maximum attainable force.

We next examine the timecourse for the cell height (Fig. 6.9(d)). When the fraction of bound integrins is high (*e.g.* $t < 25$), the cell height closely follows the applied displacement, $L_T'$. When $B$ is low (*e.g.* $30 < t < 55$), the effect of the crossbridges can be more clearly seen. The cell height reaches its minimum value when $A = 2$ (light blue, $t \approx 35$) as a result of the high $N_{att}$ and correspondingly large contractile force generated by the crossbridges. Note, however, that this minimum does not coincide with the maximum value of $N_{att}$ over the entire timecourse, which occurs at $A = 0$ (dark blue) since, in this case, there is also a high fraction of bound integrins (Fig. 6.9(b)) which resists the contractile motion. This observation highlights that the crossbridges and integrins have a competing effect on cell height.

By repeating the procedure shown in Fig. 6.9, we now investigate the dependence of the dynamics on oscillation amplitude in more detail. We examine the time-averaged steady state densities of the bound integrins, attached crossbridges and total force (Fig. 6.10) and show these in bifurcation diagrams for the parameter $A$. In order to ensure the solutions were at their oscillatory steady state, we applied each oscillation

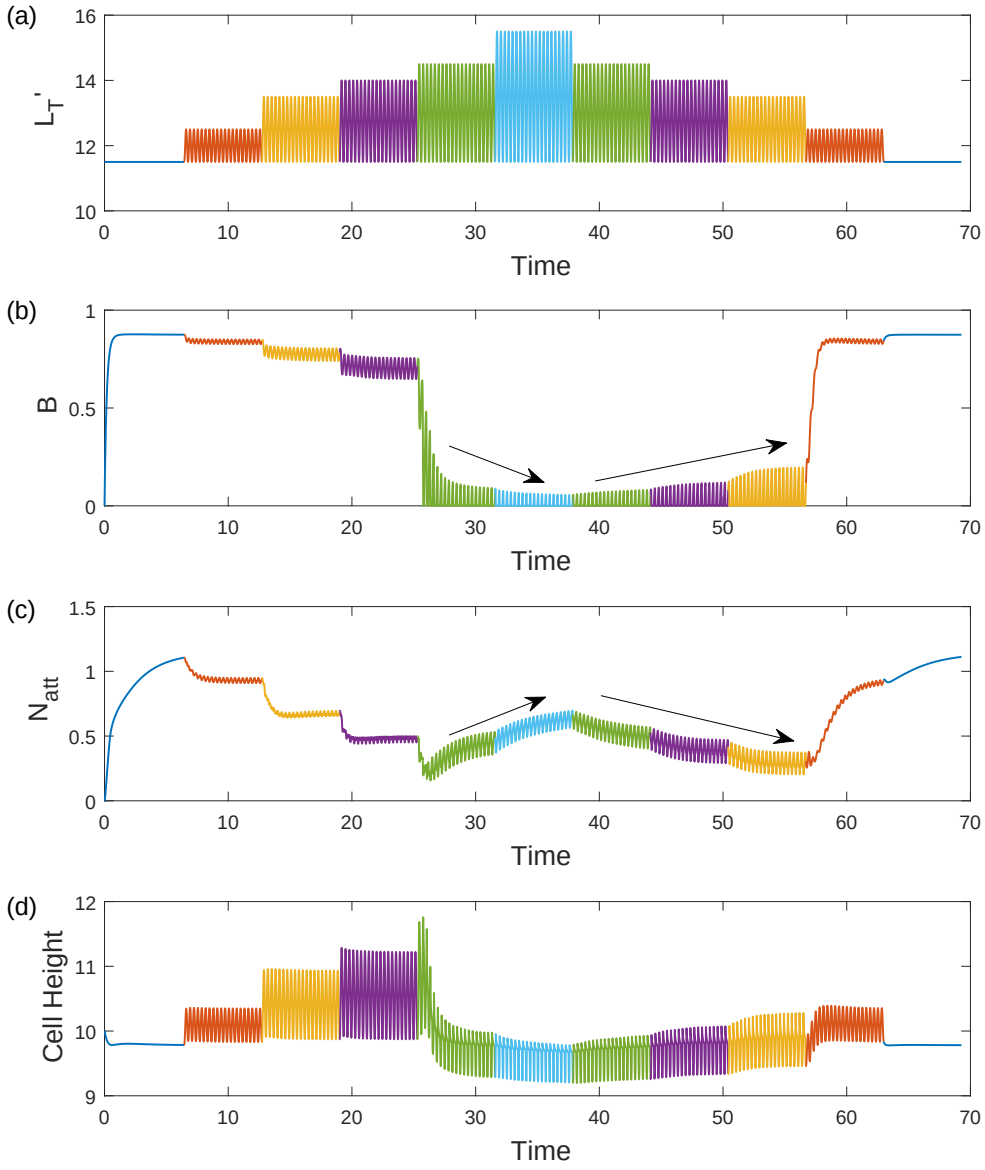


**Figure 6.9:** Timecourses for (a) the applied displacement, $L_T'$, (b) the bound integrin fraction, $B$, (c) the attached crossbridge fraction, $N_{att}$, and (d) the cell height, $L_A'$, in response to step changes in the amplitude, $A$, of oscillation (Eq. 6.3.1). Amplitudes are $A = 0$ (dark blue), 0.5 (orange), 1 (yellow), 1.25 (purple), 1.5 (green) and 2 (light blue), each applied for 20 cycles, in increasing and then decreasing order. A full list of parameter values is given in Appendix B.

amplitude for 20 cycles and averaged over the final cycle (shown by the points in Fig. 6.10). We observe bistable regions (shaded) and hysteresis loops (dashed lines) in each of these three variables.

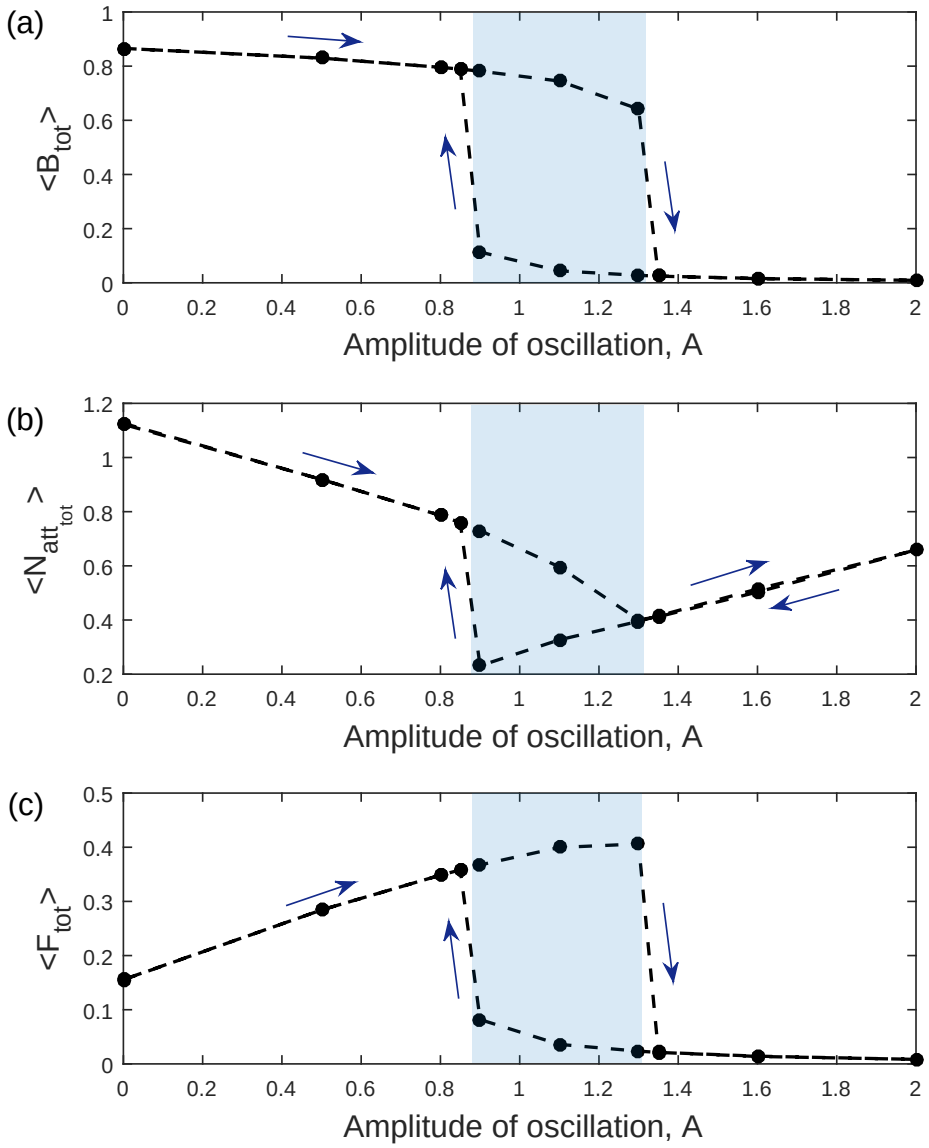


**Figure 6.10:** Time-averaged steady state densities of (a) the bound integrins, $\langle B_{tot} \rangle$, (b) the attached crossbridges, $\langle N_{att_{tot}} \rangle$, and (c) the total force, $\langle F_{tot} \rangle$, for different amplitudes of oscillation, $A$. We observe hysteresis loops (dashed lines) due to bistability (shaded regions).

As with the timecourses in Fig. 6.9, the density of bound integrins (Fig. 6.10(a)) decreases continually with increasing $A$ until a sudden transition from high to low adhesion states at $A = 1.35$. The corresponding crossbridge behaviour (Fig. 6.10(b))

as $A$ increases is non-monotonic. At first, there is a decrease in the density of attached crossbridges, but after $A = 1.35$ there is an increase in the attached crossbridges due to a reduction in cell deformation (as a result of fewer bound integrins). The corresponding force, determined via the tension in the ECM spring ($F_{tot} = k_E(L'_E - L_E)$), is shown in Fig. 6.10(c). Due to increased extension of the springs when larger displacements are applied, the force initially increases with $A$. However, as a result of the rupture of integrins and attached crossbridges, this increase in non-linear. Additionally, at the switch from high to low adhesion states ($A = 1.35$) the force drops significantly. After $A = 1.35$, the averaged force continues to decrease, showing that the reduction in bound integrin fraction has a more significant effect here than the increasing density of attached crossbridges. In the next section, we investigate how the dynamics change as the relative significance of integrins and crossbridges varies.

**Effect of varying $\beta$ and the passive cell stiffness**

In the previous results, the scale factor for the contractile force (Eq. 6.2.10) was chosen as $\beta = 0.3$. This dimensionless parameter, given by $\beta = \hat{\rho}_c\hat{\lambda}_c N_{CU}\hat{h}/\rho\hat{\lambda}_b$, is a ratio involving both the total number and the stiffnesses of integrins and crossbridges, thereby determining their relative strength. In the case where $\beta = 0$, we recover the model with passive cell stiffness only (Chapter 5). There is a natural variability in the dimensional parameter values involved; in particular, the relative numbers of crossbridges and integrins could vary significantly according to both the integrin density and the number and length of actin filaments connected (via adaptor proteins) to the integrin complexes. The ratios that these take are not known and, to account for this variability, we now vary $\beta$ through a range that allows us to observe the dynamics when integrins dominate (small $\beta$) through to where crossbridges dominate (large $\beta$).

We apply the same simulation protocol as in the previous section (Fig. 6.9), where the amplitude of oscillation is gradually increased and then decreased. First, we consider the time-averaged steady state densities of the bound integrins, attached crossbridges and total force for $A \in [0, 4]$. We show bifurcation diagrams (analogous to Fig. 3.5, where we considered bound integrins only) for each of these variables, for five different values of $\beta$ (Fig. 6.11). Discrete steps in amplitude were taken, each represented by a single point. For the lowest value of $\beta$ (Fig. 6.11(a)), we obtain similar behaviour to Fig. 6.10; increases in $A$ lead to a transition between high and low adhesion states and a decrease in attached crossbridges. We observe hysteresis, and a different path

is followed as $A$ is reduced. For larger $\beta$ (Fig. 6.11(b)), we observe a narrowing of the bistable window (shaded), which eventually disappears (Fig. 6.11(c)). This is consistent with the notion that we previously proposed (Chapters 3 and 5), that mechanical cooperativity is responsible for the bistability: as the cell stiffens, there is no longer sufficient cell deformation to enable a cooperative effect. Interestingly, as $\beta$ increases further (Fig. 6.11(d, e)), we observe a new type of bistable behaviour. Here the attached crossbridges initially sustain a high density and, during this period, we observe a decrease in bound integrins. When the attached crossbridge density drops, the bound integrin density temporarily increases, and the force drops. In contrast to the results for low $\beta$ (Fig. 6.10), in this case the decrease in attached crossbridges, rather than the increase in integrins, therefore dominates the contribution to the total force. Due to the hysteresis, each variable follows a different path for decreasing $A$; there is a lower density of attached crossbridges, the bound integrins reach higher values and the total force, $\langle F_{tot} \rangle$, is reduced. Note that, although the crossbridge and integrin behaviours change in each bistable regime ($\beta$ small or $\beta$ large), an interesting observation is that the total contractile force is reduced in both.

We now consider the time-averaged steady state densities for the bound integrins in a 2-parameter bifurcation diagram for $\beta$ and $A$ (Fig. 6.12(a)). Due to the bistability, there are areas where two steady state densities coexist; these regions are shown in white and illustrate the width of the bistable region. In addition, we show the difference, $B_{diff}$ between the value of $\langle B_{tot} \rangle$ obtained during the step increases and step decreases in $A$ (Fig. 6.12(b)); non-zero values highlight the regions of bistable behaviour, with the amplitude of $B_{diff}$ showing the difference in height of the two stable surfaces. As $\beta$ increases from zero, the first region of bistable behaviour gradually narrows and eventually collapses so that the transition between high and low bound integrin regimes becomes smooth (Fig. 6.12(a)). For large $\beta$ (as in Fig. 6.11(d)), we see the appearance of an additional bistable region for low amplitudes of oscillation.

The feedback between adhesion and contractile force generation (Fig. 6.11) is due to their competing effects on cell deformation; when under tension, integrins produce an upward force on the cell, whereas the crossbridges resist this motion with a downward contractile force. In both the very low or very high $\beta$ case, the bistability we observe (Figs. 6.11 and 6.12) is a result of mechanical cooperativity: a high initial density of either integrins or crossbridges can encourage their subsequent persistence by increasing cell deformation in the direction of the dominant force. Because of the

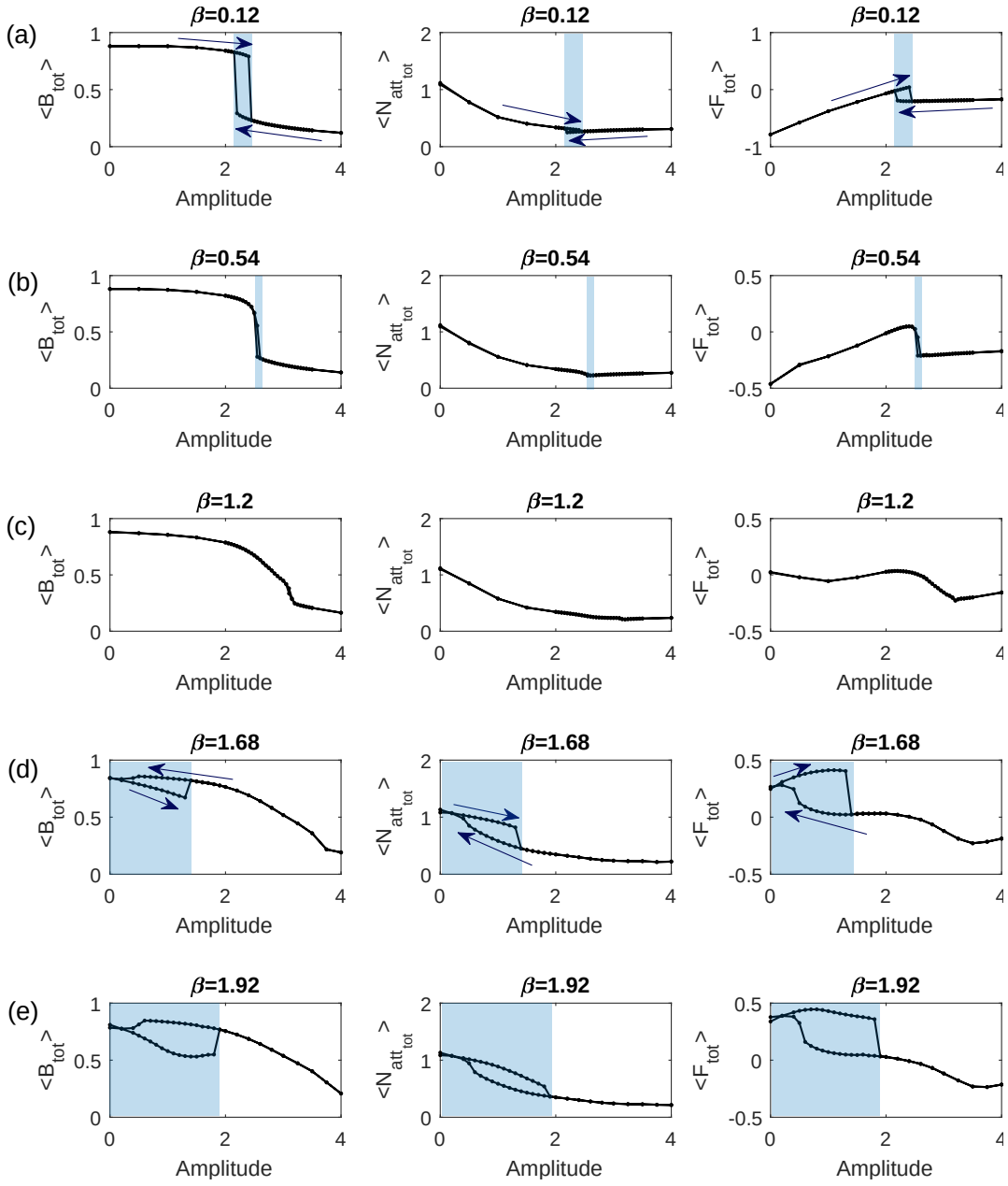


**Figure 6.11:** Time-averaged steady state densities of the bound integrins, attached crossbridges and total force for increasing values of $\beta$ (Eq. 6.2.10).

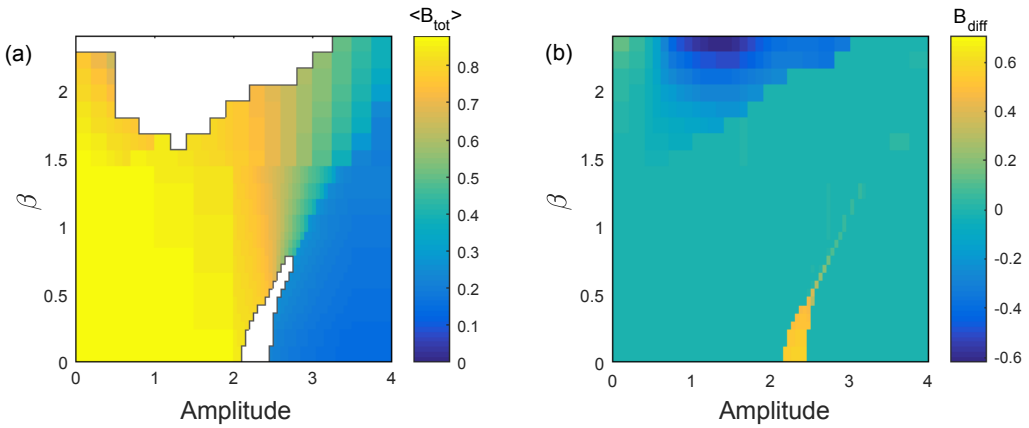


**Figure 6.12:** (a) Time-averaged steady state densities for the bound integrins for a range of amplitudes and $\beta$ values. Two steady state densities coexist in the bistable regions, and these regions are shaded in white. (b) The difference, $B_{diff}$ between $\langle B_{tot} \rangle$ for increasing and decreasing $A$. Non-zero values correspond to bistable regions and show the difference in height of the two stable surfaces. The passive cell stiffness is $k_A = 0.5$, and the remaining parameter values are given in Appendix B.

role of cell deformation in both the feedback and mechanical cooperativity, we expect the passive cell stiffness to also be important. We previously used the cell stiffness $k_A = 0.5$ (Fig. 6.12), and we now consider the equivalent result for a more compliant cell, $k_A = 0.25$ (Fig. 6.13). We firstly observe a widening of the first bistable window (for low $\beta$). In addition, the high bound integrin state persists for larger amplitudes than it did for the stiffer cell (Fig. 6.12). We further observe a decrease in the value of $\beta$ at which the transition between bistable and smooth behaviour occurs (Fig. 6.13(a)). When the passive cell stiffness is low, there is less resistance to the contractile force. As a result, the crossbridges begin to dominate at lower values of $\beta$. As a consequence of this, we see more extreme behaviour for large $\beta$ than we did in Fig. 6.12. At $\beta = 1.5$ we see that the bistable region spans the full range of $A$, indicating that the trend of the bistable region widening (seen in Figs. 6.11(d, e)) continues. The dip in bound integrins as $A$ increases also becomes progressively larger, and for $\beta > 1.8$ (Fig. 6.13(a)) we see that the bound fraction of integrins reaches zero. We show this in more detail for $\beta = 1.8$ in Fig. 6.14, where we observe that once $\langle B_{tot} \rangle$ reaches zero (Fig. 6.14(a)) there is no rebinding. Instead, the crossbridges reach a higher steady state (Fig. 6.14(b)) and, with no resistance from integrins, the cell height drops (Fig. 6.14(d)). This causes a separation between the cell and ECM that is larger than the integrin binding range. The height of the cell in this case is given by Eq. 6.2.32, which

will decrease for larger $\beta$; this behaviour will therefore continue for any $\beta > 1.8$. Finally we observe that, with no bound integrins, there is no transmission of contractile force (Fig. 6.14(c)). A complete separation of the cell and ECM does not occur *in vivo*, but could be relevant to consider in the *in vitro* studies we described in Section 5.2.

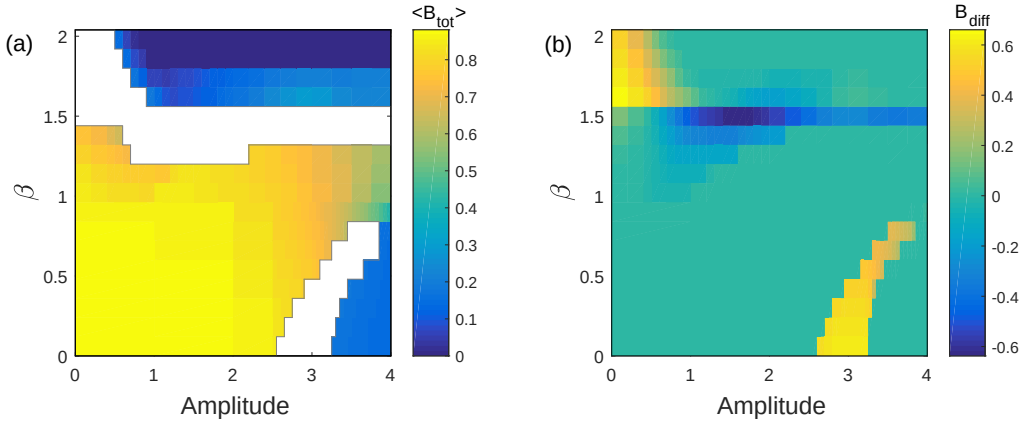


**Figure 6.13:** (a) Time-averaged steady state densities for the bound integrins for a range of amplitudes and $\beta$ values. Two steady state densities coexist in the bistable regions, and these regions are shaded in white. (b) The difference, $B_{diff}$ between $\langle B_{tot} \rangle$ for increasing and decreasing $A$. Non-zero values correspond to bistable regions and show the difference in height of the two stable surfaces. The passive cell stiffness is $k_A = 0.25$, and the remaining parameter values are given in Appendix B.

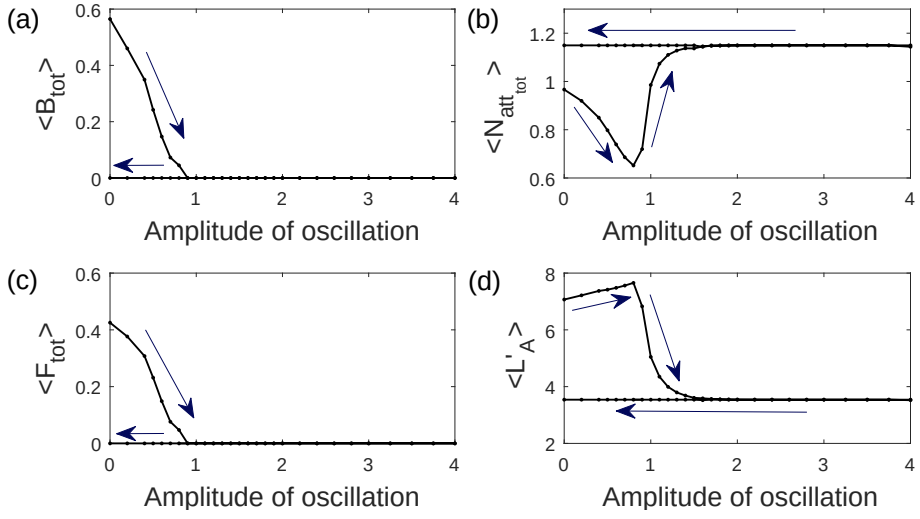


**Figure 6.14:** Time-averaged steady state densities for (a) bound integrins, (b) attached crossbridges (c) total contractile force, and (d) cell height as $A$ is increased and then decreased. The passive cell stiffness is $k_A = 0.25$ and $\beta = 1.8$; remaining parameter values are given in Appendix B.

## 6.4 Conclusions

In this chapter, we modified our 3-spring model from Chapter 5 to account for intracellular contractile force generation, mediated by actomyosin crossbridges. In parallel with a passive stiffness, we considered active contractile units within the cell, in which the crossbridge dynamics were governed by a Huxley–Hai–Murphy (HHM) description [97]. The HHM model is an advection–reaction system where crossbridges can undergo transitions between four states, accounting for attachment and detachment of myosin crossbridges to actin filaments, and phosphorylation and dephosphorylation of the crossbridges. We couple this to our model of material deformations through the advection term, which is driven by the cell deformation. By extending our previous model to include a HHM description, we are able to investigate the interacting dynamics of crossbridges and integrins in response to oscillatory length fluctuations. To our knowledge, the detailed interaction of contractile force generation and adhesion has not been investigated before.

The crossbridge dynamics in the absence of integrin dynamics recapitulated results from previous theoretical studies using the HHM model; we find that, for a fixed density of integrins (Section 6.3.1), increasing the amplitude of the oscillations leads to a strictly decreasing density of attached crossbridges (Fig. 6.5) with a corresponding decrease in mean and peak contractile force (Fig. 6.8). For the fully coupled system (Section 6.3.2) the crossbridges and integrins interact, and we see more complex behaviours. We find that, as a result of mechanical feedback between the integrins and the crossbridges, the density of attached crossbridges no longer strictly decreases with increasing oscillation amplitude (Fig. 6.9). For large amplitude oscillations, we observe negative feedback where a reduced density of bound integrins promotes crossbridge attachment (Fig. 6.10). This could provide a regulatory mechanism for the minimum and maximum attainable contractile force, as changes in integrin densities are compensated by opposing changes in the crossbridge attachment. Additionally, this result highlights the role of integrins in transmitting force bidirectionally; in addition to transmitting contractile force outwards to the ECM, they mediate the amount of force (due to environmental fluctuations) transmitted inwards to the crossbridges.

In the previous model (Chapter 5), where the cell was modelled as a passive material, we observed bistability in the bound fraction of integrins. In this chapter, we discover that this phenomenon persists in our extended model. Moreover, we observe corre-

sponding bistable behaviour in the attached crossbridges and total force (Fig. 6.10). We characterise this in detail via a 2-parameter bifurcation study for the parameter $\beta$, which controls the relative strength of the crossbridges and the integrins, and $A$, the oscillation amplitude. Consistent with the notion that bistability arises from mechanical cooperativity, we observe a narrowing of the bistable region as $\beta$ increases. With increased relative strength of the crossbridges, the downward contractile force that they generate resists the upward cell deformation required for integrin cooperativity, and we eventually lose bistability, resulting in a smooth transition between high and low adhesion states (Fig. 6.12(a)). Interestingly, as $\beta$ is increased further, we observe a second region of bistability. This is due to an analogous mechanism in which the crossbridges are cooperative: with a high initial condition of attached crossbridges, there is sufficient strength to deform the cell in favour of the crossbridges. As a result, the high attached state persists for larger amplitudes (Fig. 6.11(d,e)).

In the context of bronchoconstriction, it is important to quantify how the different integrin and crossbridge dynamics affect the total contractile force transmitted to the ECM. In Chapter 3, we showed how perturbations representing deep inspirations could result in a transition from high to low bound integrin states (Fig. 3.13). Although we have not simulated DIs specifically in this chapter, the identical bifurcation structure in *e.g.* Figs. 3.5 and 6.10 indicates that we will obtain the same behaviours for low $\beta$. Additionally, switches and hysteresis of this type were seen in Fig. 6.9 for gradual changes in amplitude. In Chapter 3, we hypothesised that the low bound integrin state could correspond to bronchodilation, and we have now shown that contractile force is indeed reduced in this state (Fig. 6.10). A further key observation is that a reduced contractile force can also be obtained in the second bistable region (for large $\beta$). In this case, the bound integrin density is increased after a large perturbation; however, due to the dominance of crossbridges, which are reduced, the net result is again a decrease in contractile force. This can be seen in the bifurcation diagrams for $\langle F_{tot} \rangle$ (Fig. 6.11). DIs are experimentally known to be able to induce bronchodilation in healthy individuals, but not in asthmatics, and we previously hypothesised that bistability could be the underlying mechanism behind sustained switches in behaviour. Our extended model provides further support for this hypothesis, as we now consider both of the key processes involved in regulating contractile force, and show that the bistability persists (and is in fact present for a large range of $\beta$). This is further strengthened by calculating that the total contractile force (in addition to just the density of bound integrins, cf. Fig. 3.13) is reduced (Fig. 6.11). The dominance of

crossbridges or integrins (and therefore the value of $\beta$) is currently unknown, but our model provides two plausible bistable regions.

Because of the importance of cell deformation in supporting mechanical cooperativity, we considered the effect of a reduced passive cell stiffness. This results in less resistance to the contractile force, meaning that the transition between integrin and crossbridge dominance, and the corresponding changes in behaviour (described above) occur at smaller values of $\beta$ (Fig. 6.13). For a fixed value of $\beta$, variations in cell stiffness could therefore result in different dynamics. As an example, taking $\beta = 1.3$ in Figs. 6.12 and 6.13, we observe bistability for the compliant cell (Fig. 6.13) but not for the stiffer cell (Fig. 6.12). A loss of bistability could be another factor to investigate when considering the different responses to DIs in non-asthmatics and asthmatics (who may have contracted cells at baseline and therefore stiffer cells). Under the hypothesis that the sustained reductions we observe in contractile force correspond to bronchodilation, a loss of bistability could have negative consequences for asthmatics as it would result in an inability of DIs to induce bronchodilation.

In future work, it will be crucial to gain better estimates for the model parameters and to validate the model predictions in experimental studies. In an *in vitro* set-up, it is possible to modulate cell contractility. An interesting AFM study could be to repeat the vertical oscillation protocol for cells in different contractile states. As in Chapter 5, there is a direct correspondence between our model set-up and the existing experimental protocol. We could therefore make use of this to investigate if the behaviours predicted by the model occur as cell contractility varies. Single cell studies could also be useful for estimating unknown parameters, as these cannot currently be measured *in vivo*.

# Chapter 7

# Conclusions

In this thesis, we have developed a series of mathematical models of airway smooth muscle (ASM) cell–matrix adhesion. The study was motivated by asthma, and in particular by the associated narrowing of the airways known as bronchoconstriction. Because of their role in transmitting contractile forces (which are generated within ASM cells), integrin-mediated adhesions play a pivotal role in regulating the extent of airway narrowing during bronchoconstriction. Our aim was to investigate how the dynamic mechanical environment of the *in vivo* airway could affect integrin dynamics and hence force transmission from ASM cells to the tissue. We used our mathematical models to investigate the integrin response to oscillatory loading, which represented mechanical fluctuations due to tidal breathing and deep inspirations (DIs). The effect of tidal breathing and DIs on contractile force generation has previously been well-studied; however, their effect on contractile force transmission, via integrins, had been neglected. The interacting dynamics of cell–matrix adhesion and contractile force generation had also not been studied in detail before, and we investigated this here. In addition to theoretical results from our models, we presented and analysed experimental data from atomic force microscopy experiments (with data provided by Prof. Gerald Meininger, University of Missouri). We summarise our main findings in Section 7.1, and discuss potential areas for future work in Section 7.2.

## 7.1 Summary of main findings

In Chapter 1, we reviewed the biological background and the existing modelling literature relevant to cell–matrix adhesion. We found stochastic simulations to be a common approach for modelling cell–matrix adhesion as these methods allow for

detailed consideration of individual integrin binding kinetics. Some continuum models accounting for integrin binding had previously been developed [20, 28, 29, 144]; however, there remained a need to capture the detailed response of the integrins to local mechanical cues. Continuum models provide computational advantages over large-scale stochastic simulations. Developing continuum frameworks that are capable of accurately capturing integrin binding kinetics therefore allow for more efficient consideration of integrin dynamics in higher scale (*e.g.* tissue level) models.

In Chapter 2, we began by developing a discrete stochastic–elastic model of cell–matrix adhesion (Section 2.1). Our discrete approach consisted of an evolving network of linear springs, in which the binding and unbinding of integrins from the ECM (modelled by the addition and removal of springs in the network) were governed by stochastic reactions. Within this framework, we enforced local spatial constraints on the integrin binding reactions; in addition, the mechanical response of the cell and the ECM to the bound integrins was captured. To model this in a more efficient manner, we then developed a novel multiscale model (Section 2.2). In order to capture the integrin-level detail described by our discrete model, we used a two-scale approach. At the microscale, we adapted the Huxley crossbridge model [70], which allowed us to define integrin binding and rupture rates based on a spatial coordinate, local to each integrin. We then coupled this description to a macroscale model of cell and ECM deformation. Our multiscale formulation allowed us to account for detailed integrin binding rate functions (of the type typically implemented in stochastic simulations) alongside material deformations at the cell level.

In Chapter 3, we used both the discrete model and the multiscale continuum model to investigate the effect of a lateral oscillatory loading of the ECM, representing mechanical fluctuations due to tidal breathing and DIs, on the adhesion dynamics. There was strong qualitative agreement between our discrete and continuum model results, and our results illustrated that strain transmission (via integrins) could be a highly dynamic process. We observed two distinct regimes where either adhesion formation or adhesion rupture dominated; these depended on the amplitude of loading and resulted in large differences in the steady state densities of bound integrins (Fig. 3.1). Furthermore, we observed a region of bistability for intermediate loading amplitudes (Fig. 3.5), which occured due to mechanical cooperativity; shared loading between pre-existing adhesions allowed the high density state to persist when rupture would otherwise dominate. This behaviour generated a hysteresis loop, meaning that the

loading history could significantly alter the future adhesion dynamics.

Using our continuum model, we demonstrated the importance of loading history by considering perturbations in the amplitude of oscillatory loading, representing DIs (Fig. 3.13). After large DI-like perturbations, our results showed either persistence of the high adhesion state or a transition from the high to the low adhesion states. We expect these high and low adhesion densities to significantly affect the level of contractile force that can be transmitted between intracellular and extracellular domains during ASM cell contraction. Our model therefore suggests a possible mechanism underlying experimental observations, in which the bronchodilatory effect after a DI is transient in asthmatics yet sustained in non-asthmatic subjects [33, 78, 125]. We found that the ability of a DI to induce a switch between states was influenced by differences in either: (i) the position of the bistable region, which shifted in response to changes in material parameters such as oscillation frequency, material stiffnesses and binding affinities (Fig. 3.8); (ii) the amplitude of the unperturbed oscillatory displacement, which we used to represent the magnitude of tidal breathing; or (iii) the magnitude of the DI. All of these are factors that could differ between individuals, as well as between asthmatics and non-asthmatics. We observed robustness of these dynamics when investigating the effect of varying the model parameters (Fig. 3.8) and of varying the input waveform (Fig. 3.11).

In Chapter 4, we considered both macroscale and microscale extensions of the multiscale continuum model. At the macroscale, we used a reaction–diffusion scheme to incorporate the activation and diffusion of free integrins (Section 4.1). In atomic force microscopy (AFM) experiments, a non-monotonic increase in adhesion strength had been observed (Fig. 4.6). We showed that a transition between regimes where deactivation and then activation dominated (through the use of a time-dependent activation rate) could lead to similar non-monotonic behaviour in the bound integrin fraction (Fig. 4.8). The time-dependent activation rate represented a delay due to intracellular signalling processes. We then extended the microscale integrin model (Section 4.2) to account for a known strain-dependent strengthening mechanism, occuring due to vinculin binding to cryptic sites on talin. By including this reaction, which reinforces the connection between integrins and the actin cytoskeleton, we observed that small deformations could encourage the persistence of adhesions (Fig. 4.14); there is competition between strengthening and rupture that introduces a non-monotonic response to load and the adhesions exhibit catch-bond like behaviour. In

response to oscillatory loading, we again observed distinct high and low adhesion states (Figs. 4.15–4.18). In addition to qualitative differences in the microscale bound integrin distributions, the strain-dependent strengthening resulted in differences in the spatial distributions of the macroscale species due to the differing propagations of load across the macroscale domain. Since the strengthening is strain dependent, and since matrix stiffness affects the transmission of load, we also considered the adhesion response for different substrate stiffnesses (Fig. 4.19). For low amplitudes of oscillatory load, we observed increased strengthening on stiffer substrates. Integrin-mediated adhesions are known to be mechanosensitive, and to develop differently on stiff and compliant substrates [32, 123]. This is likely to be relevant in the context of asthma, where healthy and asthmatic airways exhibit different stiffnesses; our ability to model these mechanisms is therefore useful for future studies.

In Section 4.3 we discussed an experimental observation by Mailhot-Larouche *et al.* [95], where a reduced time interval between large length oscillations (representing DIs) of isolated bronchi increased both the rate and magnitude of contractile force recovery. The mechanism behind this result is unknown. We simulated their oscillation protocol in our model, where we explored the different possible qualitative outcomes as activation and deactivation rates varied (Section 4.1). Our exploration highlighted that, for the time between DIs to have differing effects on bound integrin recovery, the macroscale species cannot obtain a steady state during the time period under investigation (Fig. 4.21). We also observed that increased recovery rates and magnitudes required increased availability of active, unbound integrins. In our model, this was only possible via an increased activation (or reduced deactivation) rate, due to conservation of integrins and adaptor proteins. However, in general, the increased availability of active integrins could also be induced by recruitment (via intracellular signalling) or diffusion of integrins and adaptor proteins. Regardless of the underlying mechanism, we found that, if the magnitude of recovery is to be affected, the change must be ongoing over the time intervals considered (Fig. 4.26), which reached 30 minutes in the experiments. The experimentally observed effect was captured using a transient increase in activation, with a slow decay to baseline (Figs. 4.26, 4.28). Increases in activation could perhaps be triggered by mechanical cues from the DIs; force can induce integrin activation and conformal changes [3], or the recruitment and binding of adaptor proteins [84]. The model therefore gives candidate mechanisms to be investigated; a particular consideration will be the timescales involved.

In Chapter 5, we extended our microscale model to allow for vertical motion. We coupled this to a '3-spring' description of material deformations, in which an effective spring (with time-dependent stiffness determined by the underlying integrin dynamics) represented the integrins and connected the cell to the ECM. We simulated vertical oscillations applied to the ECM and, as we found for lateral oscillations in Chapter 3, distinct high and low adhesion states were obtained for low and high amplitude oscillations, respectively (Figs. 5.7 and 5.9). For intermediate amplitude oscillations, we observed bistability (Fig. 5.11) due to a mechanical cooperativity, showing that the theoretical result from Chapter 3 holds for vertical motion. We then presented experimental data from AFM experiments, provided by Prof. Gerald Meininger and Huang Huang (University of Missouri), where a substrate-coated bead was repeatedly lowered and retracted from a cell. The amplitude of these vertical oscillations was varied under two experimental protocols. In the first, the cell and bead were initially separated so that no adhesions between the substrate and cell existed; in the second, cells were allowed a period of 'prebinding' to the bead prior to the oscillations. We interpreted these as zero and high initial conditions for the number of adhesions, analogous to the zero and saturated initial conditions used in the model. In both the model and experimental data, we obtained two qualitatively distinct patterns in adhesion force, corresponding to the high and low adhesion states. The model provided insight into the underlying integrin dynamics, as well as illustrating the temporal changes in cell height, which cannot be measured with the current technology. For the amplitude of 1200nm (Fig. 5.17), prebinding appeared to change the qualitative form of the force curves. When investigating this further (Figs. 5.18 and 5.19), we observed behaviour mostly characteristic of adhesion in the prebinding protocol, and behaviour mostly characteristic of rupture when there was no prebinding. However, we also noticed that individual cell heights could vary significantly (Table 5.1), making it difficult to compare cells directly. We therefore could not determine for sure whether the differences seen in the prebind cells were due to bistability or due to intercellular variation. This result highlighted that the variation in cell heights is essential to consider in the future design of AFM studies of this type. Since cells were difficult to compare directly, we also analysed force timecourses from single cells. Several of these exhibited a sudden switch in both the magnitude and shape of the force curves (Figs. 5.22–5.25). Although we identified these examples by inspection of the original force data, we discussed several approaches that could be developed to classify force curves and detect switches automatically. These relied on techniques from cluster analysis, where we considered separating curves into clusters according

to their shape (*e.g.* Figs. 5.26 and 5.29). Togther with our model results, the effect of prebinding and the switching behaviour in individual cells provided some strong indication of bistability. However, to conclusively determine whether this is the case, further experimental data is needed. In particular, further investigation into whether differences in initial cell heights (Tables 5.1 and 5.2) are a cause or effect of different adhesion states (Figs. 5.18 and 5.19) is essential.

Finally, in Chapter 6, we extended the model from Chapter 5 to account for contractile force generation occuring within the cell. The cell was previously modelled as a passive material and here we include active contractile components to describe contractile force generation via actomyosin crossbridges. The contractile components were modelled using the Huxley–Hai–Murphy (HHM) model [97], which accounts for attachment and detachment of myosin crossbridges to actin filaments, and phosphorylation and dephosphorylation of the crossbridges. The successful coupling of the two models allowed us to investigate the interacting dynamics of integrins and crossbridges, which has not been considered at this level of detail before. We considered the effect of applying length fluctuations and found that both force transmission (via integrins) and force generation (via crossbridges) were modulated. Moreover, we observed feedback between the two processes (Fig. 6.9); for large oscillation amplitudes we observed a regulatory mechanism due to negative feedback, where reductions in the bound integrin density induced an opposing change in the attached crossbridge density (Fig. 6.10). In addition to this, we observed two bistable regions with hysteresis in the bound fraction of integrins, attached crossbridges and total force (Fig. 6.10). As we increased the parameter $\beta$, which controls the relative strength of the crossbridges and the integrins, the first bistable region began to narrow until there was a smooth transition between high and low adhesion states (Fig. 6.12(a)). Further increases in $\beta$ lead to the emergence of a new region of bistability. A high initial condition of attached crossbridges induced a cooperative effect in favour of the crossbridges, and allowed the high attached state to persist for a larger range of amplitudes. There was a resulting decrease in bound integrins and a larger total force (Fig. 6.11(d, e)). For both cases of bistability (small and large values of $\beta$), the bistability occured due to mechanical cooperativity, where high initial conditions induced cell deformation in favour of the dominant process. In the two bistable regions we found that, after large amplitude oscillations, the bound integrin density could either be reduced (small $\beta$) or increased (large $\beta$). A crucial observation, however, is that in both of these cases the net result was a decrease in total contractile force (Fig. 6.11).

In extension to the results in Chapter 3 we therefore see that large perturbations, such as those mimicking DIs, have the ability to induce a switch to a lower contractile state (rather than just to a lower density of integrins, cf. Fig. 3.13). For intermediate values of $\beta$, and as the passive cell stiffness varies, we observed that the bistability could be lost. Under our proposed hypothesis, this could have negative consequences for asthmatics as it would result in an inability of DIs to induce sustained reductions in contractile force.

## 7.2 Scope for future work

There are many potential directions for future work, which we divide into three areas: model validation, model extensions and alternative applications. Each of these are discussed below. To conclude, we discuss the importance of our models and results for the future study of asthma.

An important area for future work is model validation. Our models predict a number of qualitative behaviours, but experimental studies are now needed to determine which of these are physiologically relevant. At the level of single cells, we compared our model results to data from AFM experiments (Chapter 5). The preliminary results are promising, and further use of these techniques could verify whether all of the behaviours predicted by the model occur *in vitro*. In particular, a priority would be to investigate the existence of bistability due to mechanical cooperativity, since this could have interesting physiological consequences. AFM experiments provide high precision measurements of adhesion forces and mechanical properties of the cell. In future studies, these techniques could perhaps be used to provide parameter values to be used in the models. This could either be through direct calculation (of *e.g.* cell stiffness) or through parameter inference (*e.g.* to estimate the integrin binding and rupture rate functions) by fitting our model to the data. After obtaining estimates for unknown or uncertain parameters, a subsequent challenge is to validate model predictions against tissue-level *in vitro* measurements (such as measurements of contractile force obtained during length oscillations applied to ASM tissue strips) and, eventually, *in vivo* observations. Integrin dynamics cannot be measured for these experiments, so this will require predicting emergent behaviours. A possible starting point is our coupled model of integrin and crossbridge dynamics, with which we can calculate the total contractile force from a single cell when the cell is subject to length

fluctuations.

There is plenty of scope to extend the current models, and this should be considered in parallel with model validation. The multiscale continuum model is amenable to both macroscale and microscale extensions, as demonstrated in Chapter 4. From a mechanical point of view, there are several simplifications in this model that could be addressed. Notably, we model the cell and ECM as linearly elastic materials. In order to accurately study the effect of larger deformations, nonlinear or viscoelastic descriptions at the macroscale could be considered. At the microscale, there is flexibility to investigate different functional forms for the integrin binding and rupture rates. There is also a vast amount of physiological detail that could be included, for example by explicitly modelling the signalling pathways involved in integrin activation, or by including additional diffusible species for the various adaptor proteins. For the purposes of understanding the mechanical effects relevant to bronchoconstriction, when a suitable level of detail has been obtained in the cell level models, a primary focus should be on incorporating these models into tissue-level descriptions.

Additionally, our modelling frameworks could be used in a number of other contexts. Cell–matrix adhesion plays an important role in a wide range of processes, and it is often important to understand and account for the local integrin behaviour (such as binding kinetics and conformal changes of integrins). This level of detail has been lacking in previous continuum models; however, our multiscale framework provides a way of accounting for them. A particularly interesting trait that integrins exhibit is the ability to detect and induce cellular changes in response to environmental stimuli. Based on the properties of the ECM, these so-called mechanosensing abilities allow integrins to send the appropriate mechanical and chemical signals to components within the cell, acting to regulate processes such as cell migration and tissue remodelling and development. Failures in mechanosensing have previously been suggested to lead to abnormalities in tissue-level properties and function; understanding cell–matrix interactions, and the mechanisms behind their mechanosensing abilities (at a level local to the integrins), is therefore relevant to many diseases and tissue types. Furthermore, the interest in tissue-level effects in these contexts means that continuum models will be beneficial.

Finally, our models highlight the need to consider ASM cell–matrix adhesion as a dy-

namic process in future studies of asthma and bronchoconstriction. We have demonstrated that integrin–mediated adhesion can be modulated by oscillatory loading, and that this has a significant effect on the total contractile force transmitted from ASM cells to the tissue. This should be acknowledged in future tissue level models if we are to fully understand experimental observations. Subcellular crossbridge dynamics have previously been considered in airway models via coupling to the HHM model [64, 65], and we propose that future work should aim to incorporate the interacting crossbridge and integrin dynamics. Here we have developed such a model of this crossbridge–integrin interaction.

Important future work will be to more fully investigate how the material properties of the airways influence adhesion dynamics. Much is still to be understood about the mechanosensitive nature of integrins; however, understanding how integrin dynamics depend on substrate stiffness will be relevant to modelling healthy (compliant) and asthmatic (stiffer) airways.

# Appendix A

# Analytical solutions for the single-site microscale model

## A.1 Steady state distributions with a constant relative velocity

At steady state, the piecewise linear binding and unbinding functions (Eqs. 2.2.6, 2.2.7) suggest consideration of Eq. 2.2.5 in each of six regions. For a non-zero, constant and positive $V(X,t)$, the steady state is obtained by solving

$$\text{(i)} \quad x < -s \qquad \frac{db}{dx} = -\frac{h_3}{V}b, \tag{A.1.1}$$

$$\text{(ii)} \quad -s \leq x < -1 \qquad \frac{db}{dx} = -\frac{(h_1 - h_2 x)}{V}, \tag{A.1.2}$$

$$\text{(iii)} \quad -1 \leq x < 0 \qquad V\frac{db}{dx} = (1+x) - (1 + h_1 + (1-h_2)x)b, \tag{A.1.3}$$

$$\text{(iv)} \quad 0 \leq x \leq 1 \qquad V\frac{db}{dx} = (1-x) - (1 + h_1 - (1-h_2)x)b, \tag{A.1.4}$$

$$\text{(v)} \quad 1 < x \leq s \qquad \frac{db}{dx} = -\frac{(h_1 + h_2 x)}{V}b, \tag{A.1.5}$$

$$\text{(vi)} \quad x > s \qquad \frac{db}{dx} = -\frac{h_3}{V}b. \tag{A.1.6}$$

In regions (i) and (vi) there is no binding and a constant high unbinding rate, $h_3$. The ODEs are separable and can be solved to give

$$\text{(i)} \quad x < -s \qquad b(x) = Ae^{-\frac{h_3}{V}x}, \tag{A.1.7}$$

$$\text{(vi)} \quad x > s \qquad b(x) = Be^{-\frac{h_3}{V}x}, \tag{A.1.8}$$

for constants $A$ and $B$.

For regions (ii) and (v) there is linear unbinding (Eq. 2.2.7) but no binding. The equations are again separable and we find

$$\text{(ii)} \quad -s \leq x < -1 \qquad b(x) = Ce^{-\frac{1}{V}\left(h_1 x - \frac{h_2}{2}x^2\right)}, \tag{A.1.9}$$

$$\text{(v)} \quad 1 < x \leq s \qquad b(x) = De^{-\frac{1}{V}\left(h_1 x + \frac{h_2}{2}x^2\right)}, \tag{A.1.10}$$

for constants $C$ and $D$ to be determined.

In regions (iii) and (iv), there is both binding and unbinding (Eqs. 2.2.6, 2.2.7). Rearranging, in region (iii) we have

$$\frac{db}{dx} + \frac{1}{V}\left((1+h_1) - (1-h_2)x\right)b = \frac{1}{V}(1+x). \tag{A.1.11}$$

Using an integrating factor $e^{\frac{1}{V}\int ((1+h_1)+(1-h_2)x)\ dx} = e^{\frac{1}{V}\left((1+h_1)x + \frac{1-h_2}{2}x^2\right)}$ this becomes

$$\frac{d}{dx}\left(be^{\frac{1}{V}\left((1+h_1)x+\frac{1-h_2}{2}x^2\right)}\right) = \frac{1}{V}e^{\frac{1}{V}\left((1+h_1)x+\frac{1-h_2}{2}x^2\right)}(1+x). \tag{A.1.12}$$

We integrate both sides to obtain

$$\begin{aligned} b(x)\exp\left(\left(\frac{(1+h_1)}{V}x + \frac{1-h_2}{2V}x^2\right)\right) =& \frac{1}{V}\int \exp\left(\left(\frac{(1+h_1)}{V}x + \frac{1-h_2}{2V}x^2\right)\right)dx \\ &+ \frac{1}{V}\int x\ \exp\left(\left(\frac{(1+h_1)}{V}x + \frac{1-h_2}{2V}x^2\right)\right)dx, \end{aligned} \tag{A.1.13}$$

where we will rewrite the exponentials as

$$\begin{aligned} \exp\left(\left(\frac{(1+h_1)}{V}x + \frac{1-h_2}{2V}x^2\right)\right) &= \exp\left(\frac{1-h_2}{2V}\left(x^2 + 2\frac{1+h_1}{1-h_2}x\right)\right) \\ &= \exp\left(\frac{1-h_2}{2V}\left(\left(x + \frac{1+h_1}{1-h_2}\right)^2 - \left(\frac{1+h_1}{1-h_2}\right)^2\right)\right) \\ &= \alpha_1\ \exp\left(\beta\left(x + \frac{1+h_1}{1-h_2}\right)^2\right), \end{aligned} \tag{A.1.14}$$

where $\alpha_1 = \exp\left(\frac{-(1+h_1)^2}{2V(1-h_2)}\right)$ and $\beta = \frac{1-h_2}{2V}$. Using a substitution $u = x + \frac{1+h_1}{1-h_2}$, the first integral on the right hand side of Eq. A.1.13 is then

$$\frac{1}{V}\int \alpha_1 e^{\beta\left(x+\frac{1+h_1}{1-h_2}\right)^2}dx = \frac{\alpha_1}{V}\int e^{\beta u^2}du = \frac{\alpha_1}{2V}\sqrt{\frac{\pi}{\beta}}\text{erfi}(\sqrt{\beta}u) + c_1, \tag{A.1.15}$$

where $c_1$ is a constant and $\text{erfi}(\sqrt{\beta}u)$ is the imaginary error function, a standard integral defined by

$$\text{erfi}(z) = \frac{2}{\sqrt{\pi}}\int e^{z^2}dz. \tag{A.1.16}$$

The second integral on the right hand side of Eq. A.1.13 is

$$\begin{aligned}\frac{1}{V}\int \alpha_1 x e^{\beta\left(x-\frac{1+h_1}{1-h_2}\right)^2} dx &= \frac{\alpha_1}{V}\int \left(u-\frac{1+h_1}{1-h_2}\right) e^{\beta u^2} du \\ &= \frac{\alpha_1}{V}\int u e^{\beta u^2} du - \frac{\alpha_1}{V}\left(\frac{1+h_1}{1-h_2}\right)\int e^{\beta u^2} du \\ &= \frac{\alpha_1}{2\beta V} e^{\beta u^2} - \frac{\alpha_1}{2V}\left(\frac{1+h_1}{1-h_2}\right)\sqrt{\frac{\pi}{\beta}}\text{erfi}(\sqrt{\beta}u) + c_2\end{aligned} \tag{A.1.17}$$

where $c_2$ is a constant. Combining these and dividing through by $\alpha_1 e^{\beta u^2}$ gives the steady solution in (iii) to be

$$b(x) = \frac{1}{2V}\left(1-\frac{1+h_1}{1-h_2}\right)\sqrt{\frac{\pi}{\beta}}\text{erfi}(\sqrt{\beta}u)\ \ e^{-\beta u^2} + Ee^{-\beta u^2} + \frac{1}{2\beta V} \tag{A.1.18}$$

where $E$ is a constant, $\beta = \frac{1-h_2}{2V}$ and $u = x + \frac{1+h_1}{1-h_2}$.

In terms of the original variables we have

$$b(x) = \frac{1-\gamma}{2V}\sqrt{\frac{\pi}{\beta}}\text{erfi}(\sqrt{\beta}(x+\gamma))e^{-\beta(x+\gamma)^2} + Ee^{-\beta(x+\gamma)^2} + \frac{1}{2\beta V}, \tag{A.1.19}$$

where $\gamma = \frac{1+h_1}{1-h_2}$ and $E$ is a constant to be determined. Note that here we have assumed $\beta$ to be positive, *i.e.* $h_2 = g_2/f_1 < 1$. If this is not the case, some minor modifications will be needed and the imaginary error function, $\text{erfi}(z)$, will be replaced by the error function, defined by

$$\text{erf}(z) = \frac{2}{\sqrt{\pi}}\int e^{-z^2} dz. \tag{A.1.20}$$

The solution for region (iv) is similar; the steady state ODE is

$$V\frac{db}{dx} = (1-x) - (1+h_1-(1-h_2)x)b, \tag{A.1.21}$$

which is rearranged to

$$\frac{db}{dx} + \frac{1}{V}(1+h_1-(1-h_2)x)b = \frac{1}{V}(1-x). \tag{A.1.22}$$

The integrating factor is $e^{\frac{1}{V}\int((1+h_1)-(1-h_2)x)\ \ dx} = e^{\frac{1}{V}\left((1+h_1)x-\frac{1-h_2}{2}x^2\right)}$ and gives

$$\frac{d}{dx}\left(b(x)e^{\frac{1}{V}\left((1+h_1)x-\frac{1-h_2}{2}x^2\right)}\right) = \frac{1}{V}e^{\frac{1}{V}\left((1+h_1)x-\frac{1-h_2}{2}x^2\right)}(1-x). \tag{A.1.23}$$

Integrating both sides leads to

$$b(x)e^{\frac{1}{V}\left((1+h_1)x-\frac{1-h_2}{2}x^2\right)} = \frac{1}{V}\int e^{\frac{1}{V}\left((1+h_1)x-\frac{1-h_2}{2}x^2\right)} dx - \frac{1}{V}\int x e^{\frac{1}{V}\left((1+h_1)x-\frac{1-h_2}{2}x^2\right)} dx, \tag{A.1.24}$$

where we now use

$$\exp\left(\frac{1}{V}\left((1+h_1)x-\frac{1-h_2}{2}x^2\right)\right)=\alpha_2\ \exp\left(-\beta\left(x-\frac{1+h_1}{1-h_2}\right)^2\right), \tag{A.1.25}$$

for $\alpha_2 = \exp\left(\frac{(1+h_1)^2}{2V(1-h_2)}\right)$ and $\beta = \frac{1-h_2}{2V} > 0$ as before. A similar substitution $u = x - \frac{1+h_1}{1-h_2}$ is made and the first integral on the right hand side of A.1.24 becomes

$$\frac{1}{V}\int \alpha_2 e^{-\beta\left(x-\frac{1+h_1}{1-h_2}\right)^2}dx=\frac{\alpha_2}{V}\int e^{-\beta u^2}du=\frac{\alpha_2}{2V}\sqrt{\frac{\pi}{\beta}}\text{erf}(\sqrt{\beta}u)+d_1, \tag{A.1.26}$$

where $d_1$ is a constant and $\text{erf}(\sqrt{\beta}u)$ the error function (Eq. A.1.20). The second integral on the right hand side of Eq. A.1.24 is

$$\begin{aligned}\frac{1}{V}\int \alpha_2 x e^{-\beta\left(x-\frac{1+h_1}{1-h_2}\right)^2}dx &= \frac{\alpha_2}{V}\int\left(u+\frac{1+h_1}{1-h_2}\right)e^{-\beta u^2}du\\ &= \frac{\alpha_2}{V}\int ue^{-\beta u^2}du+\frac{\alpha_2}{V}\left(\frac{1+h_1}{1-h_2}\right)\int e^{-\beta u^2}du\\ &= -\frac{\alpha_2}{2\beta V}e^{-\beta u^2}+\frac{\alpha_2}{2V}\left(\frac{1+h_1}{1-h_2}\right)\sqrt{\frac{\pi}{\beta}}\text{erf}(\sqrt{\beta}u)+d_2\end{aligned} \tag{A.1.27}$$

where $d_2$ is a constant. Combining these and dividing through by $\alpha_2 e^{-\beta u^2}$ gives the steady solution in (iv) to be

$$b(x)=\frac{1}{2V}\left(1-\frac{1+h_1}{1-h_2}\right)\sqrt{\frac{\pi}{\beta}}\text{erf}(\sqrt{\beta}u)e^{\beta u^2}+Fe^{\beta u^2}+\frac{1}{2\beta V} \tag{A.1.28}$$

where $F$ is a constant, $\beta = \frac{1-h_2}{2V}$ and $u = x - \frac{1+h_1}{1-h_2}$.

In terms of the original variables

$$b(x)=\frac{1-\gamma}{2V}\sqrt{\frac{\pi}{\beta}}\text{erf}(\sqrt{\beta}(x-\gamma))e^{\beta(x-\gamma)^2}+Fe^{\beta(x-\gamma)^2}+\frac{1}{2\beta V}, \tag{A.1.29}$$

where $\gamma = \frac{1+h_1}{1-h_2}$ and $F$ is a constant to be determined.

In summary there are six general solutions, given above, with one for each of the regions defined by the binding and unbinding rate functions (Eqs. 2.2.6, 2.2.7). In each solution there is a constant to be determined by enforcing continuity at each boundary.

**Determining the constants**

With $V > 0$ advection is to the right. In this case the solution in (i) requires $A = 0$. Continuity is enforced at the boundaries, starting with $x = -s$ to give $C = 0$. This

then means that at $x = -1$ we need $b(-1) = 0$, giving

$$E = \frac{\gamma - 1}{2V}\sqrt{\frac{\pi}{\beta}}\text{erfi}(\sqrt{\beta}(\gamma - 1)) - \frac{1}{2\beta V}e^{\beta(\gamma-1)^2}. \tag{A.1.30}$$

Equating the solutions to (iii) and (iv) at $x = 0$ gives

$$F = \frac{1-\gamma}{2V}\sqrt{\frac{\pi}{\beta}}\text{erfi}(\sqrt{\beta}\gamma)e^{-2\beta\gamma^2} + Ee^{-2\beta\gamma^2} - \frac{1-\gamma}{2V}\sqrt{\frac{\pi}{\beta}}\text{erf}(-\sqrt{\beta}\gamma). \tag{A.1.31}$$

Continuity at $b = 1$ requires

$$De^{-\frac{1}{V}(h_1+\frac{h_2}{2})} = \frac{1-\gamma}{2V}\sqrt{\frac{\pi}{\beta}}\text{erf}(\sqrt{\beta}(1-\gamma))\ e^{\beta(1-\gamma)^2} + Fe^{\beta(1-\gamma)^2} + \frac{1}{2\beta V}, \tag{A.1.32}$$

which gives

$$D = \left(\frac{1-\gamma}{2V}\sqrt{\frac{\pi}{\beta}}\text{erf}(\sqrt{\beta}(1-\gamma))\ e^{\beta(1-\gamma)^2} + Fe^{\beta(1-\gamma)^2} + \frac{1}{2\beta V}\right)e^{\frac{1}{V}(h_1+\frac{h_2}{2})}, \tag{A.1.33}$$

where $F$ is as above.

At the final boundary, $x = s$, we have

$$De^{\frac{1}{V}(h_1 s+\frac{h_2}{2})s^2} = Be^{-\frac{h_3}{V}s}, \tag{A.1.34}$$

which leads to

$$B = De^{\frac{h_3 s}{V^2}(h_1 s+\frac{h_2}{2}s^2)}. \tag{A.1.35}$$

Note that the problem switches symmetrically if instead $V < 0$, where the process starts from $B = 0$.

## A.2 Method of characteristics for piecewise-linear binding rates

In this section we present the time-dependent solutions of the single-site microscale model (Eq. 2.2.5) when there is a constant, positive, non-zero relative velocity, $V$. Using piecewise-linear binding rates (Eqs. 2.2.6, 2.2.7), the method of characteristics can be used to find analytical solutions for $b(x,t)$. The governing equations must first be considered in each of six regions of $x$, dictated by the choice of rate functions and denoted by the regions (i)–(vi) below. The six PDEs to be solved are

$$\begin{aligned}
&\text{(i)} && x < -s && \frac{\partial b(x,t)}{\partial t} + V\frac{\partial b(x,t)}{\partial x} = -h_3 b(x,t),\\
&\text{(ii)} && -s \le x < -1 && \frac{\partial b(x,t)}{\partial t} + V\frac{\partial b(x,t)}{\partial x} = -(h_1 - h_2 x)b(x,t),\\
&\text{(iii)} && -1 \le x < 0 && \frac{\partial b(x,t)}{\partial t} + V\frac{\partial b(x,t)}{\partial x} = (1+x) - (1 + h_1 + (1-h_2)x)b(x,t),\\
&\text{(iv)} && 0 \le x \le 1 && \frac{\partial b(x,t)}{\partial t} + V\frac{\partial b(x,t)}{\partial x} = (1-x) - (1 + h_1 - (1-h_2)x)b(x,t),\\
&\text{(v)} && 1 < x \le s && \frac{\partial b(x,t)}{\partial t} + V\frac{\partial b(x,t)}{\partial x} = -(h_1 + h_2 x)b(x,t),\\
&\text{(vi)} && x > s && \frac{\partial b(x,t)}{\partial t} + V\frac{\partial b(x,t)}{\partial x} = -h_3 b(x,t).
\end{aligned}$$

Since there is an advection term, we must also take into account the regions that the solution has previously propagated through. After determining the characteristic curves, we will need to further partition the solution space as will be shown and explained in Fig. A.1. A simpler example of this technique (for binding rates with three piecewise-linear regions) can be found in [8].

To find the characteristic curves, we let $b(x,t) = b(x(r),t(r))$ and look for curves $(x(r),t(r))$, parameterised by $r$, along which the solutions to the above PDEs can be represented by ODEs. Using the chain rule on $b(x(r),t(r))$:

$$\frac{db}{dr} = \frac{\partial b}{\partial x}\frac{dx}{dr} + \frac{\partial b}{\partial t}\frac{dt}{dr},$$

and we find that the characteristics are defined by the following three ODEs

$$\frac{db}{dr} = f(x,b(x,t)), \qquad \frac{dx}{dr} = V, \qquad \frac{dt}{dr} = 1.$$

The function $f(x,b(x,t))$ varies according to which region ((i)–(vi)) is being considered, and is found by comparison to the six PDEs above.

In each region we have the same solutions for $x$ and $t$: the solutions are $t = t_0 + r = r$ and $x = x_0 + V(t - t_0)$, giving the characteristics in $x - t$ space as straight lines of gradient $V$. The behaviour along them is determined by integrating $f(x, b(x,t))$ and applying initial data:

$$b(x,t) = \int_0^{t-t_0} f(x, b(x,t'))dt' + b_0(x_0, t_0).$$

In each region, we will state $f(x, b(x,t))$ and perform the above integral.

When sketching the characteristic curves (Fig. A.1), we find that further regions in characteristic space need to be considered to properly track the behaviour as distributions propagate from one region to the next. The origin of the data as well as it's position in $x$ will define its evolution. Considering constant, strictly positive $V$ produces 21 distinct regions (Fig. A.1).

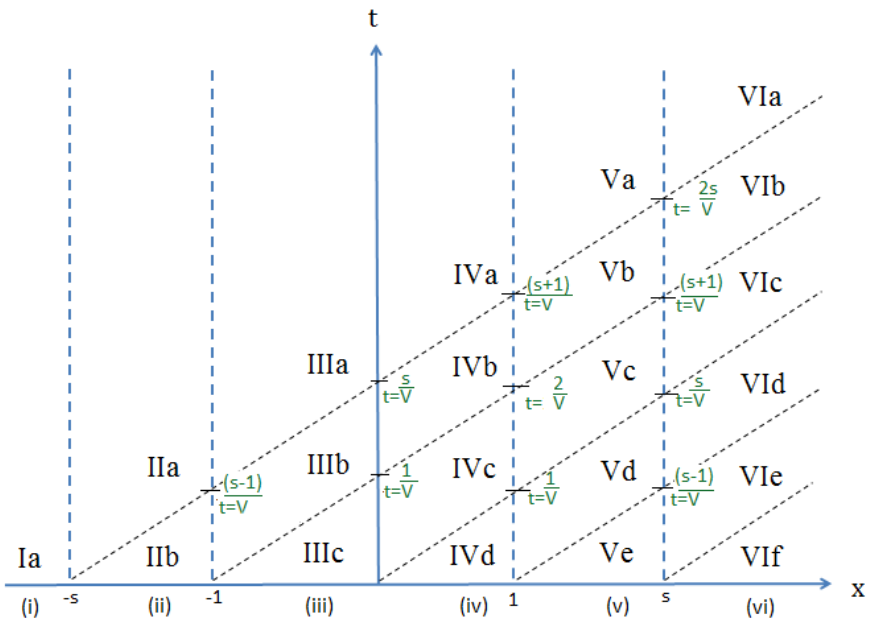


**Figure A.1:** The 21 distinct regions in $x - t$ space, where propogation of characteristics need to be carefully tracked. Vertical dotted lines separate the regions (i) to (vi). Diagonal dotted lines have gradient $1/V$ and subpartition these regions further.

The governing equations in regions (i) to (vi) do not change in the subpartitions but the initial data will. As an example, characteristics in region IIb (Fig. A.1) are in-

formed by initial data $b_0(x_0, 0)$ from region (ii): $b_0(x, 0)$ for $-s \leq x < -1$, but for IIa the information entering the region comes instead from the initial data of region (i), $b_0(x, 0)$ for $x < -s$, after it has been propagated along the characteristics in Ia to reach $x = -s$. As $V$ is positive and constant and the distances in $x$ are known we can define exactly where these transistions occur.

We will begin by solving the characteristic equations for the regions informed by the initial data at $t = 0$, which is the bottom row in Fig. A.1, and then work upwards through the diagram. A table giving the explicit boundaries in $x - t$ space that define these 21 regions is included in Table A.1 at the end of the section.

**Regions Ia and VIf**

Here, the ODEs are

$$\frac{db}{dr} = -h_3 b, \qquad \frac{dx}{dr} = V, \qquad \frac{dt}{dr} = 1.$$

Integrating directly, with respect to $r$, gives

$$b = b_0 e^{-h_3 r}, \qquad x = x_0 + Vr, \qquad t = t_0 + r,$$

where $t_0 = 0$ means that $t = r$ and the solutions can be written as

$$b(x, t) = b_0(x - Vt, 0)e^{-h_3 t},$$

for the initial distribution $b_0(x_0, 0) = b_0(x - Vt, 0)$. The distribution therefore travels as a wave from the initial condition, damped exponentially in time.

**Region IIb**

In this region, characteristic curves are given by

$$\frac{db}{dr} = -(h_1 - h_2 x)b, \qquad \frac{dx}{dr} = V, \qquad \frac{dt}{dr} = 1,$$

Integrating gives as before gives $t = r$ and $x = x_0 + Vt$. We substitute these into the equation for $b$ to obtain

$$\frac{db}{dt} = -(h_1 - h_2(x_0 + Vt))b,$$

which is solved by separation of variables to give

$$b(x, t) = b_0(x - Vt, 0)e^{-\left((h_1 - h_2 x_0)t - \frac{Vh_2}{2}t^2\right)},$$

for the initial distribution $b_0(x_0, 0)$.

**Region Ve**

The characteristic equations are very similar to in region IIb, and are given by

$$\frac{db}{dr} = -(h_1 + h_2 x)b, \qquad \frac{dx}{dr} = V, \qquad \frac{dt}{dr} = 1.$$

Similarly to the previous section, we arrive at $t = r$, $x = x_0 + Vt$ and

$$b(x,t) = b_0(x - Vt, 0)e^{-\left((h_1 + h_2 x_0)t + \frac{Vh_2}{2}t^2\right)},$$

for the initial distribution $b_0(x_0, 0)$ and where $x_0 = x - Vt$.

**Region IIIc**

The characteristic equations are

$$\frac{db}{dr} = (1 + x) - (1 + h_1 + (1 - h_2)x)b, \qquad \frac{dx}{dr} = V, \qquad \frac{dt}{dr} = 1.$$

Using $t = r$, $x = x_0 + Vt$ in the first equation gives

$$\frac{db}{dt} = (1 + x_0) + Vt - (1 + h_1 + (1 - h_2)x_0)b - (1 - h_2)Vtb,$$

which can be rearranged to

$$\frac{db}{dt} + ((1 + h_1 + (1 - h_2)x_0) + (1 - h_2)Vt)b = (1 + x_0) + Vt.$$

We define the constant $\alpha_1 = 1 + h_1 + (1 - h_2)x_0$ and use an integrating factor to obtain

$$\frac{d}{dt}\left(be^{\alpha_1 t + \frac{(1-h_2)V}{2}t^2}\right) = ((1 + x_0) + Vt)e^{\alpha_1 t + \frac{(1-h_2)V}{2}t^2}.$$

Integrating both sides leads to

$$be^{\alpha_1 t + \frac{(1-h_2)V}{2}t^2} = (1 + x_0)\int e^{\alpha_1 t + \frac{(1-h_2)V}{2}t^2}dt + V\int te^{\alpha_1 t + \frac{(1-h_2)V}{2}t^2}dt,$$

where the exponentials can be expressed as

$$\begin{aligned}
\exp\left(\alpha_1 t + \frac{(1-h_2)V}{2}t^2\right) &= \exp\left(\frac{(1-h_2)V}{2}\left(t^2 + \frac{2\alpha_1}{(1-h_2)V}t\right)\right) \\
&= \exp\left(\frac{(1-h_2)V}{2}\left(\left(t + \frac{\alpha_1}{(1-h_2)V}\right)^2 - \left(\frac{\alpha_1}{(1-h_2)V}\right)^2\right)\right) \\
&= \delta_1 \ \exp\left(\beta\left(t + \frac{\alpha_1}{(1-h_2)V}\right)^2\right),
\end{aligned}$$

where $\delta_1 = \exp\left(-\frac{\alpha_1^2}{2(1-h_2)V}\right)$ and $\beta = \frac{(1-h_2)V}{2}$. We can then use the substitution $u = t + \frac{\alpha_1}{(1-h_2)V}$, which leaves the equation to be solved, after some rearranging, as

$$be^{\beta u^2} = \left((1+x_0) - \frac{\alpha_1}{1-h_2}\right)\int e^{\beta u^2}du + V\int ue^{\beta u^2}du.$$

Integrating yields

$$be^{\beta u^2} = \frac{1}{2}\left((1+x_0) - \frac{\alpha_1}{1-h_2}\right)\sqrt{\frac{\pi}{\beta}}\text{erfi}(\sqrt{\beta}u) + \frac{V}{2\beta}e^{\beta u^2} + c_1,$$

for constant $c_1$ which will be determined by $b_0$. Dividing by the exponential, substituting in the original variables and with $\gamma_1 = \frac{1}{2}\left(-\frac{h_1+h_2}{1-h_2}\right)$, a constant, the solution in IIIc is given by

$$b(x,t) = \gamma_1\sqrt{\frac{\pi}{\beta}}\text{erfi}\left(\sqrt{\beta}\left(t + \frac{\alpha_1}{(1-h_2)V}\right)\right)e^{-\beta\left(t+\frac{\alpha_1}{(1-h_2)V}\right)^2} + \frac{V}{2\beta} + c_1e^{-\beta\left(t+\frac{\alpha_1}{(1-h_2)V}\right)^2},$$

where $c_1$ is determined by setting $t = 0$ and satisfying the initial condition $b(x_0, t_0) = b_0(x - Vt, 0)$. This gives

$$c_1 = b_0(x-Vt,0)e^{\beta\left(\frac{\alpha_1}{(1-h_2)V}\right)^2} - \gamma_1\sqrt{\frac{\pi}{\beta}}\text{erfi}\left(\sqrt{\beta}\left(\frac{\alpha_1}{(1-h_2)V}\right)\right) - \frac{V}{2\beta}e^{\beta\left(\frac{\alpha_1}{(1-h_2)V}\right)^2}.$$

**Region IVd**

In the final region on the bottom layer (Fig. A.1) the characteristic equations are

$$\frac{db}{dr} = (1-x) - (1+h_1-(1-h_2)x)b, \qquad \frac{dx}{dr} = V, \qquad \frac{dt}{dr} = 1.$$

Using $t = r$, $x = x_0 + Vt$ in the first equation

$$\frac{db}{dt} = (1-x_0-Vt) - (1+h_1-(1-h_2)(x_0+Vt))b.$$

The process for solving this is very similar to the steps in region IIIc (shown above), and requires an integrating factor and then a substitution. The resulting solution is

$$b(x,t) = \gamma_2\sqrt{\frac{\pi}{\beta}}\text{erf}\left(\sqrt{\beta}\left(t - \frac{\alpha_2}{(1-h_2)V}\right)\right)e^{\beta\left(t-\frac{\alpha_2}{(1-h_2)V}\right)^2} + \frac{V}{2\beta} + c_2e^{\beta\left(t-\frac{\alpha_2}{(1-h_2)V}\right)^2},$$

where $\alpha_2 = 1 + h_1 - (1-h_2)x_0$, $\beta = \frac{(1-h_2)V}{2}$ and $\gamma_2 = \frac{1}{2}\left(-\frac{h_1+h_2}{1-h_2}\right)$. The constant $c_2$ is determined by setting $t = 0$ and satisfying the initial condition $b(x_0, t_0) = b_0(x - Vt, 0)$, and is defined as

$$c_2 = b_0(x-Vt,0)e^{-\beta\left(-\frac{\alpha_2}{(1-h_2)V}\right)^2} - \gamma_2\sqrt{\frac{\pi}{\beta}}\text{erf}\left(\sqrt{\beta}\left(-\frac{\alpha_2}{(1-h_2)V}\right)\right) - \frac{V}{2\beta}e^{-\beta\left(-\frac{\alpha_2}{(1-h_2)V}\right)^2}.$$

**Higher layer partitions**

For the other partitions the general solutions will be of a similar form to the above (for their respective regions (i)–(vi), but initial data will need to be replaced by the data entering the regions from the left (lowest value of $x$) border. This will result in increasingly nested solutions. Taking region IIa as an example, the solution is calculated as follows.

**Region IIa**

Using the general solution from solving the characteristic equations in region IIb, we know that the information in region IIa propagates according to

$$b = B_0(-s, t_{1_a}) e^{-\left((h_1 - h_2 x_{1_a})(t - t_{1_a}) - \frac{Vh_2}{2}(t - t_{1_a})^2\right)},$$

where $B_0(-s, t_{1_a})$ is now the information arriving at the left hand boundary, $x_{1_a} = -s$, rather than the initial data at $t = 0$. This occurs at a time $t_{1_a}(x_0) \geq 0$, dependent on the initial $x_0$ in region (i). As $V$ is constant, $t_{1_a}$ is given by $t_{1_a} = (-s - x_0)/V$. The data arriving into IIa all originates from the initial distribution $b_0$ at time $t = 0$, so we know that $B_0(-s, t_{1_a}) = b_0(x - Vt, 0)e^{-h_3 t_{1_a}}$. It is then propagated according to the same rules as in IIb, but with the need to replace $t$ by $t - t_{1_a}$ and $x_0$ by $x_{1_a}$ in the exponential. Combining these results we have

$$b(x, t) = b_0(x - Vt, 0) e^{-h_3 t_{1_a}} e^{-\left((h_1 - h_2 x_0)(t - t_{1_a}) - \frac{Vh_2}{2}(t - t_{1_a})^2\right)}.$$

This replacement of $t$ by $t - t_{1_a}$ and $x_0$ by $x_{1_a}$ is seen by considering the characteristics. Integrating gives $t = r + t_{1_a}$ and $x = x_{1_a} + Vr$. The $x$ equation reduces back to $x = x_0 + Vt$, but as we are integrating for $b$ with respect to $r$ (=$t - t_{1_a}$) rather than $t$, the $x_0$ from the IIb solution is replaced by $x_{1_a}$.

The remaining solutions for IIIb, IVc, Vd and VIe use the same method and are listed in their final form. As a general rule, we will use the solution from the six above regions for the region (k) under consideration, but with $t$ replaced by $t - t_k$, where $t_k(x_0)$ is the time that the region is entered, and with $x_0$ replaced by $x_k$, the left boundary coordinate at time $t_k$. The initial condition $B_k$ is determined by continuity and by propagating $b_0(x - Vt, 0)$ according to the region (k-1) solution for a time $t_k$. We see that as we progress upwards in the diagram these solutions will become increasingly nested.

**Region IIIb**

Distributions enter IIIb from IIb after a time $t_{1_b} = \frac{-1-x_0}{V}$. They propagate according to:

$$b(x,t) = \left(\gamma_1\sqrt{\frac{\pi}{\beta}}\text{erfi}\left(\sqrt{\beta}\left((t-t_{1_b}) + \frac{\hat{\alpha}_1}{(1-h_2)V}\right)\right) + \hat{c}_1\right) e^{-\beta\left((t-t_{1_b})+\frac{\hat{\alpha}_1}{(1-h_2)V}\right)^2} + \frac{V}{2\beta},$$

where $\hat{c}_1$ is given by

$$\hat{c}_1 = B_{1_b}(-1,t_{1_b})e^{\beta\left(\frac{\hat{\alpha}_1}{(1-h_2)V}\right)^2} - \gamma_1\sqrt{\frac{\pi}{\beta}}\text{erfi}\left(\sqrt{\beta}\left(\frac{\hat{\alpha}_1}{(1-h_2)V}\right)\right) - \frac{V}{2\beta}e^{\beta\left(\frac{\hat{\alpha}_1}{(1-h_2)V}\right)^2}.$$

for initial condition $B_{1_b}(-1,t_{1_b})$. This comes from region IIb after time $t_{1_b}$ and is defined as

$$B_{1_b}(-1,t_{1_b}) = b_0(x-Vt,0)e^{-\left((h_1-h_2x_0)t_{1_b}-\frac{Vh_2}{2}t_{1_b}^2\right)}.$$

The constants $\beta$ and $\gamma_1$ are as defined as before (region IIIc), and $\hat{\alpha}_1 = h_1 + h_2$ is similar to $\alpha_1$ but with $x_0$ replaced by $x_{1_b} = -1$.

**Region IVc**

Distributions enter IVc from region IIIc after a time $t_{1_c} = \frac{-x_0}{V}$ and are governed by

$$b(x,t) = \left(\gamma_2\sqrt{\frac{\pi}{\beta}}\text{erf}\left(\sqrt{\beta}\left((t-t_{1_c}) - \frac{\hat{\alpha}_2}{(1-h_2)V}\right)\right) + \hat{c}_2\right) e^{\beta\left((t-t_{1_c})-\frac{\hat{\alpha}_2}{(1-h_2)V}\right)^2} + \frac{V}{2\beta},$$

where $\hat{c}_2$ is:

$$\hat{c}_2 = B_{1_c}(0,t_{1_c})e^{-\beta\left(-\frac{\hat{\alpha}_2}{(1-h_2)V}\right)^2} - \gamma_2\sqrt{\frac{\pi}{\beta}}\text{erf}\left(\sqrt{\beta}\left(-\frac{\hat{\alpha}_2}{(1-h_2)V}\right)\right) - \frac{V}{2\beta}e^{-\beta\left(-\frac{\hat{\alpha}_2}{(1-h_2)V}\right)^2}.$$

The constant $\hat{\alpha}_2 = 1 + h_1$ is found similarly to $\alpha_2$ in region IVd, but where $x_0$ has been replaced by $x_{1_c} = 0$. The initial condition $B_{1_c}$ is given by the IIIc solution after time $t_{1_c}$ and is

$$B_{1_c}(0,t_{1_c}) = \left(\gamma_1\sqrt{\frac{\pi}{\beta}}\text{erfi}\left(\sqrt{\beta}\left(t_{1_c} + \frac{\alpha_1}{(1-h_2)V}\right)\right) + c_1\right) e^{-\beta\left(t_{1_c}+\frac{\alpha_1}{(1-h_2)V}\right)^2} + \frac{V}{2\beta}$$

where $c_1$ is as defined previously in the calculations for region IIIc.

**Region Vd**

Initial data from IVd enters Vd at time $t_{1_d} = \frac{1-x_0}{V}$. It then propagates according to

$$b(x,t) = B_{1_d}(1,t_{1_d})e^{-\left((h_1+h_2x_v)(t-t_{1_d})+\frac{Vh_2}{2}(t-t_{1_d})^2\right)},$$

where $x_v = 1$ is the initial value at the boundary (at time $t_{1_d}$) and $B_{1_d}(1, t_{1_d})$ is given by

$$B_{1_d}(1, t_{1_d}) = \gamma_2 \sqrt{\frac{\pi}{\beta}} \text{erf}\left(\sqrt{\beta}\left(t_{1_d} - \frac{\alpha_2}{(1-h_2)V}\right)\right) e^{\beta\left(t_{1_d} - \frac{\alpha_2}{(1-h_2)V}\right)^2} + \frac{V}{2\beta} + c_2 e^{\beta\left(t_{1_d} - \frac{\alpha_2}{(1-h_2)V}\right)^2},$$

for the constants $c_2$, $\alpha_2$, $\beta$ and $\gamma_2$ as previously defined (region IVd) and where $x_0 = x - Vt$.

**Region VIe**

In this region initial data from Ve enters VIe at time $t_{1_e} = \frac{s - x_0}{V}$. It then propagates according to

$$b(x,t) = b_0(x - Vt, 0) e^{-((h_1 + h_2 x_0)t_{1_e} + \frac{Vh_2}{2} t_{1_e}^2)} e^{-h_3(t - t_{1_e})}.$$

For the next layer (IIIa, IVb, Vc, VId) the initial condition will be informed by the two previous regions by using the last six solutions evaluated at times $t_{2_a}$ to $t_{2_d}$. As the width of the intervals are fixed, the $t_2 - t_1$ terms can be evaluated exactly and used to simplify the result. The solutions to the characteristic equations with a non-zero initial time will give terms involving $t - t_2$, similarly to before.

**Region IIIa**

This region is relevant after time $t_{2_a}$, given by $t_{2_a} = t_{1_a} + \frac{s-1}{V}$. Using $x_0 = x - Vt$, the solution follows

$$b(x,t) = \left(\gamma_1 \sqrt{\frac{\pi}{\beta}} \text{erfi}\left(\sqrt{\beta}\left((t - t_{2_a}) + \frac{\hat{\alpha}_1}{(1-h_2)V}\right)\right) + \tilde{c}_1\right) e^{-\beta\left((t - t_{2_a}) + \frac{\hat{\alpha}_1}{(1-h_2)V}\right)^2} + \frac{V}{2\beta},$$

where $\tilde{c}_1$ is

$$\tilde{c}_1 = B_{2_a}(-1, t_{2_a}) e^{\beta\left(\frac{\hat{\alpha}_1}{(1-h_2)V}\right)^2} - \gamma_1 \sqrt{\frac{\pi}{\beta}} \text{erfi}\left(\sqrt{\beta}\left(\frac{\hat{\alpha}_1}{(1-h_2)V}\right)\right) - \frac{V}{2\beta} e^{\beta\left(\frac{\hat{\alpha}_1}{(1-h_2)V}\right)^2},$$

and

$$B_{2_a}(-1, t_{2_a}) = b_0(x - Vt, 0) e^{-h_3 t_{1_a}} \exp\left(-\left(\frac{(s-1)(h_1 - h_2 x_{ii})}{V} - \frac{h_2(s-1)^2}{2V}\right)\right).$$

The constant $\hat{\alpha}_1$ is defined as before (IIIb) and $x_{ii} = -s$ is the position of the boundary that is crossed at time $t_{2_a}$. To simplify the solution, $t_{2_a} - t_{1_a} = \frac{s-1}{V}$ has been used.

**Region IVb**

Distributions enter IVb from region IIIb after a time $t_{2_b} = t_{1_b} + \frac{1}{V}$. They are governed by

$$b(x,t) = \left(\gamma_2\sqrt{\frac{\pi}{\beta}}\text{erf}\left(\sqrt{\beta}\left((t-t_{2_b}) - \frac{\hat{\alpha}_2}{(1-h_2)V}\right)\right) + \tilde{c}_2\right) e^{\beta\left((t-t_{2_b}) - \frac{\hat{\alpha}_2}{(1-h_2)V}\right)^2} + \frac{V}{2\beta},$$

where $\tilde{c}_2$ is

$$\tilde{c}_2 = B_{2_b}(0,t_{2_b})e^{-\beta\left(-\frac{\hat{\alpha}_2}{(1-h_2)V}\right)^2} - \gamma_2\sqrt{\frac{\pi}{\beta}}\text{erf}\left(\sqrt{\beta}\left(-\frac{\hat{\alpha}_2}{(1-h_2)V}\right)\right) - \frac{V}{2\beta}e^{-\beta\left(-\frac{\hat{\alpha}_2}{(1-h_2)V}\right)^2}.$$

The initial condition $B_{2_b}$ is given by the IIIb solution after time $t_{2_b}$

$$B_{2_b}(0,t_{2_b}) = \left(\gamma_1\sqrt{\frac{\pi}{\beta}}\text{erfi}\left(\sqrt{\beta}\left(\frac{1}{V} + \frac{\hat{\alpha}_1}{(1-h_2)V}\right)\right) + \hat{c}_1\right) e^{-\beta\left(\frac{1}{V} + \frac{\hat{\alpha}_1}{(1-h_2)V}\right)^2} + \frac{V}{2\beta},$$

where $\hat{c}_1$ is as defined in region IIIb. Additionally we have used $t_{2_b} - t_{1_b} = \frac{1}{V}$ and $x_0 = x - Vt$.

**Region Vc**

The distribution from IVc enters Vc at time $t_{2_c} = t_{1_c} + \frac{1}{V}$. It then propagates according to

$$b(x,t) = B_{2_c}(1,t_{2_c})e^{-\left((h_1+h_2x_v)(t-t_{2_c}) + \frac{Vh_2}{2}(t-t_{2_c})^2\right)},$$

where $B_{2_c}(1,t_{2_c})$ is given by

$$B_{2_c}(1,t_{2_c}) = \left(\gamma_2\sqrt{\frac{\pi}{\beta}}\text{erf}\left(\sqrt{\beta}\left(\frac{1}{V} - \frac{\hat{\alpha}_2}{(1-h_2)V}\right)\right) + \hat{c}_2\right) e^{\beta\left(\frac{1}{V} - \frac{\hat{\alpha}_2}{(1-h_2)V}\right)^2} + \frac{V}{2\beta}.$$

The constant $\hat{c}_2$ is as given previously, by the solution in region IVc. The difference $t_{2_c} - t_{1_c} = \frac{1}{V}$ has also been used and $x_0 = x - Vt$.

**Region VId**

In region VId the distribution (propogating from region Vd) is considered after a time $t_{2_d} = t_{1_d} + \frac{s-1}{V}$. It evolves according to

$$b(x,t) = B_{2_d}(s,t_{1_d})e^{-h_3(t-t_{2_d})},$$

where $B_{2_d}$ is from Vd at time $t_{2_d}$

$$B_{2_d} = B_{1_d}(1,t_{1_d})e^{-\left(\frac{(s-1)(h_1+h_2x_v)}{V} + \frac{h_2(s-1)^2}{2V}\right)},$$

and $B_{1_d}(1, t_{1_d})$ is as defined previously (region Vd) and $x_0 = x - Vt$. We have also used $t_{2_d} - t_{1_d} = \frac{s-1}{V}$ to simplify the expression for $B_{2_d}$.

The next layer (regions IVa, Vb, VIc) consists of regions that have passed through three regions already. Initial conditions will come from the solutions above (IIIa, IVb, Vc), evaluated at times $t_{3_a}$ to $t_{3_c}$ that correspond to arrival at $x = 0$, $x = 1$ and $x = s$, respectively.

**Region IVa**

In this region, we look for solutions at times $t - t_{3a}$. At time $t = t_{3_a}$ we denote the initial condition by $B_{3_a}$, which is found by evaluating the IIIa solution at $t = t_{3_a}$ and $x = 0$. The evolution of the distribution is governed by

$$b(x,t) = \left(\gamma_2\sqrt{\frac{\pi}{\beta}}\text{erf}\left(\sqrt{\beta}\left((t-t_{3_a}) - \frac{\hat{\alpha}_2}{(1-h_2)V}\right)\right) + c_2^*\right) e^{\beta\left((t-t_{3a}) - \frac{\hat{\alpha}_2}{(1-h_2)V}\right)^2} + \frac{V}{2\beta},$$

where $c_2^*$ is

$$c_2^* = B_{3_a}(0, t_{3_a}) e^{-\beta\left(-\frac{\hat{\alpha}_2}{(1-h_2)V}\right)^2} - \gamma_2\sqrt{\frac{\pi}{\beta}}\text{erf}\left(\sqrt{\beta}\left(-\frac{\hat{\alpha}_2}{(1-h_2)V}\right)\right) - \frac{V}{2\beta}e^{-\beta\left(-\frac{\hat{\alpha}_2}{(1-h_2)V}\right)^2}.$$

The initial condition is calculated as

$$B_{3_a}(0, t_{3_a}) = \left(\gamma_1\sqrt{\frac{\pi}{\beta}}\text{erfi}\left(\sqrt{\beta}\left(\frac{1}{V} + \frac{\hat{\alpha}_1}{(1-h_2)V}\right)\right) + \tilde{c}_1\right) e^{-\beta\left(\left(\frac{1}{V} + \frac{\hat{\alpha}_1}{(1-h_2)V}\right)\right)^2} + \frac{V}{2\beta},$$

where $\tilde{c}_1$ and $B_{2_a}$ are as defined in region IIIa. The relations $t_{2_a} - t_{1_a} = \frac{s-1}{V}$ and $t_{3_a} - t_{2_a} = \frac{1}{V}$ have also been used.

**Region Vb**

In this region, solutions are for the times $t - t_{3_b}$. At time $t_{3_b}$, we denote the initial condition by $B_{3_b}$. This gives

$$b(x,t) = B_{3_b}(1, t_{3_b}) e^{-\left((h_1 + h_2 x_v)(t-t_{3_b}) + \frac{Vh_2}{2}(t-t_{3_b})^2\right)},$$

with initial condition

$$B_{3_b}(1, t_{3_b}) = \left(\gamma_2\sqrt{\frac{\pi}{\beta}}\text{erf}\left(\sqrt{\beta}\left(\frac{1}{V} - \frac{\hat{\alpha}_2}{(1-h_2)V}\right)\right) + \tilde{c}_2\right) e^{\beta\left(\frac{1}{V} - \frac{\hat{\alpha}_2}{(1-h_2)V}\right)^2} + \frac{V}{2\beta}.$$

The constant $\tilde{c}_2$ is as defined in region IVb. Additionally $t_{2_b} - t_{1_b} = t_{3_b} - t_{2_b} = \frac{1}{V}$ have been used.

**Region VIc**

This region begins at time $t_{3_c} = t_{1_c} + \frac{s}{V}$, and has solution

$$b(x,t) = B_{3_c}(s, t_{3_c}) e^{-h_3(t-t_{3_c})},$$

for $B_{3_c}(s, t_{3_c})$ given by

$$B_{3_c}(s, t_{3_c}) = B_{2_c}(1, t_{2_c}) e^{-\left(\frac{(s-1)(h_1+h_2 x_v)}{V} + \frac{(s-1)^2 h_2}{2V}\right)}.$$

The initial condition $B_{2_c}(1, t_{2_c})$ is defined as in region Vc. Relations including $t_{3_c} - t_{2_c} = \frac{s-1}{V}$ and $t_{2_c} - t_{1_c} = \frac{1}{V}$ have also been used.

Initial conditions for the penultimate layer (regions Va, VIb) will come from evaluation the IVa and Vb solutions at $x = 1$ and $x = s$ respectively, at corresponding times $t_{4_a}(x_0)$ and $t_{4_b}(x_0)$.

**Region Va**

The solution in Va is given by

$$b(x,t) = B_{4_a}(1, t_{4_a}) e^{-\left((h_1+h_2 x_v)(t-t_{4_a}) + \frac{Vh_2}{2}(t-t_{4_a})^2\right)},$$

for

$$B_{4_a}(1, t_{4_a}) = \left(\gamma_2 \sqrt{\frac{\pi}{\beta}} \text{erf}\left(\sqrt{\beta}\left(\frac{1}{V} - \frac{\hat{\alpha}_2}{(1-h_2)V}\right)\right) + c_2^*\right) e^{\beta\left(\frac{1}{V} - \frac{\hat{\alpha}_2}{(1-h_2)V}\right)^2} + \frac{V}{2\beta},$$

where $c_2^*$ is given in region IVa. The relations $t_{2_a} - t_{1_a} = \frac{s-1}{V}$ and $t_{3_a} - t_{2_a} = t_{4_a} - t_{3_a} = \frac{1}{V}$ have been used.

**Region VIb**

The solution in VIb is

$$b(x,t) = B_{4_b}(s, t_{4_b}) e^{-h_3(t-t_{4_b})},$$

where

$$B_{4_b}(s, t_{4_b}) = B_{3_b}(1, t_{3_b}) e^{-\left(\frac{(s-1)(h_1+h_2 x_v)}{V} + \frac{h_2(s-1)^2}{2V}\right)},$$

and the initial condition $B_{3_b}(1, t_{3b})$ has been defined in region Vb. Additionally $t_{2_b} - t_{1_b} = t_{3_b} - t_{2_b} = \frac{1}{V}$ and $t_{4_b} - t_{3_b} = \frac{s-1}{V}$ have been used.

The final region, VIa, tracks initial data from Ia after it has passed through each of the other five 'a' regions. The initial condition is determined by requiring continuity with the solution of region Va evaluated at $x = s$ and time $t_{5_a}(x_0)$ .

**Region VIa**

The solution in VIa is given by

$$b(x,t) = B_{5_a}(s, t_{5_a})e^{-h_3(t-t_{5_a})},$$

where

$$B_5(s, t_{5_a}) = B_{4_a}(1, t_{4_a})e^{-\left(\frac{(h_1+h_2x_v)(s-1)}{V} + \frac{h_2(s-1)^2}{2V}\right)},$$

and where $B_{4_a}(1, t_{4_a})$ is defined as in region Va. This solution contains information that has propagated through each of the other five 'a' regions; the general solutions for regions (i)–(vi) have therefore all been used and are nested within this result.

The boundaries of each of the 21 regions in characteristic space (Fig. A.1), which give the constraints for where the above solutions are valid, are listed in Table A.1.

**Time-dependent relative velocities, $V(t)$**

In the above solutions we assumed that $V$ was constant in time, which led to characteristics that were straight lines. If $V = V(t)$ now varies in time, this is no longer the case, and the relation $x = x_0 + Vt$ from the previous section must be replaced by $x = x_0 + \int_{t_0}^{t} V(t)\mathrm{dt}$. An example of this method, applied to a problem with 3 (rather than 6) piecewise linear regions, is found in [8].

In our example, the solutions in regions Ia and VIf will remain the same (except for this replacement of $Vt$ by $\int_{t_0}^{t} V(t)\mathrm{dt}$), but the boundaries and the solutions in the remaining regions will need to be reconsidered. For some choices of time-dependent $V(t)$ it will be possible to use a similar method as above; however, the partitions in characteristic space will become more difficult to track since the characteristics are no longer straight lines. A further consideration, if choosing the form of the function $V(t)$, is that $V(t)$ will appear in several of the integrals (and sometimes as products with other functions of $t$) and these will therefore need to be integrable. A simpler possibility could be to choose a piecewise constant function for $V$, and make repeated use of the above solutions. Alternatively, as shown in Fig. 2.15, numerical solutions can be sufficiently accurate and in many cases may be the preferred approach.

| Region | $x$-domain | $t$-domain |
|---|---|---|
| Ia | $x < -s$ | $t \geq 0$ |
| IIb | $-s \leq x < -1,$ | $0 \leq t < \frac{s+x}{V}$ |
| IIa | $-s \leq x < -1,$ | $t \geq \frac{s+x}{V}$ |
| IIIc | $-1 \leq x < 0,$ | $0 \leq t < \frac{1+x}{V}$ |
| IIIb | $-1 \leq x < 0,$ | $\frac{1+x}{V} \leq t < \frac{s+x}{V}$ |
| IIIa | $-1 \leq x < 0,$ | $t \geq \frac{s+x}{V}$ |
| IVd | $0 \leq x < 1$ | $0 \leq t < \frac{x}{V}$ |
| IVc | $0 \leq x < 1$ | $\frac{x}{V} \leq t < \frac{1+x}{V}$ |
| IVb | $0 \leq x < 1$ | $\frac{1+x}{V} \leq t < \frac{s+x}{V}$ |
| IVa | $0 \leq x < 1$ | $t \geq \frac{s+x}{V}$ |
| Ve | $1 \leq x < s$ | $0 \leq t < \frac{x-1}{V}$ |
| Vd | $1 \leq x < s$ | $\frac{x-1}{V} \leq t < \frac{x}{V}$ |
| Vc | $1 \leq x < s$ | $\frac{x}{V} \leq t < \frac{1+x}{V}$ |
| Vb | $1 \leq x < s$ | $\frac{1+x}{V} \leq t < \frac{s+x}{V}$ |
| Va | $1 \leq x < s$ | $t \geq \frac{s+x}{V}$ |
| VIf | $x \geq s$ | $0 \leq t < \frac{x-s}{V}$ |
| VIe | $x \geq s$ | $\frac{x-s}{V} \leq t < \frac{x-1}{V}$ |
| VId | $x \geq s$ | $\frac{x-1}{V} \leq t < \frac{x}{V}$ |
| VIc | $x \geq s$ | $\frac{x}{V} \leq t < \frac{1+x}{V}$ |
| VIb | $x \geq s$ | $\frac{1+x}{V} \leq t < \frac{s+x}{V}$ |
| VIa | $x \geq s$ | $t \geq \frac{s+x}{V}$ |

**Table A.1:** The $x - t$ values corresponding to the 21 partitions in characteristic space, where the above solutions are valid, and as shown in Fig. A.1.

# Appendix B

# Parameter values

## B.1 Parameter values for Chapter 3

### B.1.1 Dimensionless parameter values

The dimensionless parameter values used in the continuum and discrete simulations, unless otherwise stated in figure captions, are given below.

| Parameter | Description | Value |
|---|---|---|
| $K_A$ | Cell Stiffness | 2 |
| $K_E$ | ECM Stiffness | 4 |
| $h$ | Integrin binding range | 1 |
| $s$ | Maximum integrin range | 1.5 |
| $h_1$ | Dimensionless unbinding parameter (Eq. 2.2.7) | 0.5 |
| $h_2$ | Dimensionless unbinding parameter (Eq. 2.2.7) | 0.4 |
| $h_3$ | Dimensionless unbinding parameter (Eq. 2.2.7) | 5000 |
| $\delta$ | Ratio of microscale binding range, $\hat{h}$, to macroscale lengthscale $\hat{L}$ | 0.05 |
| $\nu$ | Ratio of microscale binding range, $\hat{h}$, to microscale characteristic length, $\hat{l}$. | 5 |
| $\omega$ | Frequency of oscillatory loading | 20 |

**Table B.1:** Dimensionless parameter values for the continuum simulations in Chapter 3, unless otherwise stated in figure captions.

| Parameter | Description | Value |
|---|---|---|
| $N_{I_A}$ | Number of $I_A$ nodes | 300 |
| $N_E$ | Number of $E$ nodes | 500 |
| $\kappa_a$ | Cell Spring Constant | 2($N_{I_A}$-1) |
| $\kappa_r$ | Restoring Spring Constant | 2($N_{I_A}$-1) |
| $\kappa_e$ | ECM Spring Constant | 4($N_E$-1) |
| $\kappa_b$ | Integrin Spring Constant | 1.8 |
| $h$ | Integrin binding range | 1 |
| $s$ | Maximum integrin range | 1.5 |
| $h_1$ | Dimensionless unbinding parameter (Eq. 2.2.7) | 0.5 |
| $h_2$ | Dimensionless unbinding parameter (Eq. 2.2.7) | 0.4 |
| $h_3$ | Dimensionless unbinding parameter (Eq. 2.2.7) | 5000 |
| $\delta$ | Ratio of microscale binding range, $\hat{h}$, to macroscale lengthscale $\hat{L}$ | 0.05 |
| $\omega$ | Frequency of oscillatory loading | 20 |

**Table B.2:** Parameter values for the discrete simulations in Chapter 3, unless otherwise stated in figures. Note that the cell and ECM spring constants are scaled by ($N_{I_A}$-1) and ($N_E$-1), respectively, which are the number of cell and ECM springs that act in series between $X = 0$ and $X = 1$ (see Fig. 2.2).

### B.1.2 Dimensional parameter values

The above dimensionless parameters were obtained, where possible, by using dimensional values from the literature (see below). Some parameters were unknown or widely variable in the literature (denoted by $^{**}$) and are discussed further below.

| Parameter | Description | Range of values | Sources | Chosen value |
|---|---|---|---|---|
| $\hat{T}$ | Breathing cycle duration | $2.7 - 5.8$s | [145] | 3.9s |
| $\hat{\omega}$ | Frequency (angular) of oscillatory loading | $1.08 - 2.33\text{s}^{-1}$ | $\hat{\omega} = 2\pi/\hat{T}$ | $1.6\text{s}^{-1}$ |
| $\hat{g}_1$ | Unstressed unbinding rate | $0.012 - 0.04\text{s}^{-1}$ | [92], [127] | $0.04\text{s}^{-1}$ |

| | | | | |
|---|---|---|---|---|
| $\hat{g}_2$ | Unbinding parameter | | | $0.032\text{s}^{-1**}$ |
| $\hat{g}_3$ | Forced unbinding rate | Instantaneous | Model choice | $400\text{s}^{-1}$ |
| $\hat{f}_1$ | Unstressed binding rate | $0.015 - 1.5\text{s}^{-1}$ | [127], [144] | $0.08\text{s}^{-1**}$ |
| $\hat{h}$ | Integrin binding range | $0 - 28\text{nm}$ | [101] | 20nm |
| $\hat{s}$ | Maximum integrin range before unbinding | 28nm+ | [101] | 30nm |
| $\hat{\lambda}_b$ | Integrin spring constant | $0.15 - 2\text{pN/nm}$ | [34], [48], [108] | 0.15pN/nm |
| $\hat{\rho}$ | Number of integrins per unit length | $0 - 0.2\text{nm}^{-1}$ | [91] | $0.1\text{nm}^{-1**}$ |
| $\hat{l}$ | Characteristic length | | | 4nm |
| $\hat{L}$ | Characteristic length | | | 400nm |

**Table B.3:** Dimensional parameter values used to obtain the dimensionless values in Table B.1. Parameters that were unknown or widely variable in the literature are denoted by ** and are discussed further below.

The unstressed binding rate $\hat{f}_1$ varies widely in the literature, as it depends on a number of factors including integrin affinity, integrin density and ligand density. Here we have chosen a rate based on [127, 144]; however, higher values have also been used in the simulations of [82, 108]. The unbinding parameter, $\hat{g}_2$, used in the piecewise linear rates (Eq. 2.1.3) does not have an equivalent in the literature, and was chosen to be of the same order of magnitude as the other reaction rates, $\hat{g}_1$ and $\hat{f}_1$. Some parameter values were estimated from known properties of integrins. The integrin binding ranges, $\hat{h}$ and $\hat{s}$ are estimates based on the length of integrins. An upper bound for $\hat{\rho}$ is estimated based on integrin diameters, which are typically between 5-10nm [91]. This suggests a maximum value of $\hat{\rho} = 0.2\text{nm}^{-1}$; however, the integrin density will vary up to this value depending on the extent of integrin clustering.

The constants $\hat{K}_A$ and $\hat{K}_E$ in Eq. 2.2.23 are given values (240pN and 480pN respectively) such that the dimensionless stiffness parameters, $K_A$ and $K_E$ in Eq. 2.2.31, are $\mathcal{O}(1)$. We make this choice so that the drag arising from bound integrins, $F(X,t)$, influences the macroscale dynamics via Eq. 2.2.31, since integrins are known to be able

to influence cell and ECM deformation.

Naturally there is some uncertainty associated with the above parameters, and we have investigated the effect of varying some of these (Chapter 3). We find that the qualitative behaviours remain similar for a range of parameter values.

## B.2 Parameter values for Chapter 4

### B.2.1 Integrin diffusion and activation

In Section 4.1 we considered an extended reaction sequence to include integrin diffusion and activation reactions. The dimensionless governing equations are given in Eqs. 4.1.2–4.1.4, along with Eqs. 2.2.28, 2.2.29 and 2.2.31. To nondimensionalise the system we employ the scalings of Eq. 2.2.26. In addition, we have obtained dimensionless activation and deactivation rates, $k_A$ and $k_D$ respectively, and a dimensionless diffusion constant, $D$, through the scalings

$$k_A = \hat{k}_A/\hat{f}_1, \qquad k_D = \hat{k}_D/\hat{f}_1, \qquad D = \hat{D}/\hat{f}_1\hat{L}^2. \tag{B.2.1}$$

Each macroscale species has been scaled by the total adaptor protein concentration, $\hat{A}_{tot}$, which is conserved across it's different states to give the dimensionless relation $I_A + A + B = 1$.

The dimensionless parameter values used in Section 4.1, unless otherwise stated, are

| Parameter | Description | Value |
|---|---|---|
| $K_A$ | Cell Stiffness | 2 |
| $K_E$ | ECM Stiffness | 4 |
| $h$ | Integrin binding range | 1 |
| $s$ | Maximum integrin range | 1.5 |
| $h_1$ | Dimensionless unbinding parameter (Eq. 2.2.7) | 0.5 |
| $h_2$ | Dimensionless unbinding parameter (Eq. 2.2.7) | 0.4 |
| $h_3$ | Dimensionless unbinding parameter (Eq. 2.2.7) | 5000 |
| $\delta$ | Ratio of microscale binding range, $\hat{h}$, to macroscale lengthscale $\hat{L}$ | 0.05 |
| $\nu$ | Ratio of microscale binding range, $\hat{h}$, to microscale characteristic length, $\hat{l}$. | 5 |

| | | |
|---|---|---|
| $\omega$ | Frequency of oscillatory loading | 20 |
| $k_A$ | Dimensionless activation rate | 2 |
| $k_D$ | Dimensionless deactivation rate | 0.1 |
| $D$ | Dimensionless diffusion constant | 0.05 |

**Table B.4:** Dimensionless parameter values for simulations in Section 4.1, unless otherwise stated in figure captions

### B.2.2 Force-dependent strengthening

In Section 4.2 we considered the extended reaction sequence, which includes integrin diffusion and activation reactions, and a strain-dependent strengthening of integrins due to reinforcement by vinculin. The dimensionless governing equations are given in Eqs. 4.2.3–4.2.6, along with Eqs. 2.2.28, 2.2.29, 2.2.31, 4.2.8 and 4.2.9. To nondimensionalise the system we employ the scalings of Eq. 2.2.26. In addition, we have obtained dimensionless activation and deactivation rates, $k_A$ and $k_D$ respectively, and a dimensionless diffusion constant, $D$, through the scalings

$$k_A = \hat{k}_A/\hat{f}_1, \qquad k_D = \hat{k}_D/\hat{f}_1, \qquad D = \hat{D}/\hat{f}_1\hat{L}^2. \tag{B.2.2}$$

Dimensionless strengthening and weakening rate parameters (in $k_s(x)$ and $k_w(x)$ respectively) are obtained from the scalings

$$s_1 = \hat{s}_1/\hat{f}_1, \qquad w_1 = \hat{w}_1/\hat{f}_1. \tag{B.2.3}$$

Each macroscale species has been scaled by the total adaptor protein concentration, $\hat{A}_{tot}$, which is conserved across it's different states to give the dimensionless relation $I_A + A + B + B_V = 1$.

The dimensionless parameter values used in Section 4.1, unless otherwise stated, are

| Parameter | Description | Value |
|---|---|---|
| $K_A$ | Cell Stiffness | 2 |
| $K_E$ | ECM Stiffness | 4 |
| $h$ | Integrin binding range | 1 |
| $s$ | Maximum integrin range | 1.5 |
| $h_1$ | Dimensionless unbinding parameter (Eq. 2.2.7) | 0.5 |
| $h_2$ | Dimensionless unbinding parameter (Eq. 2.2.7) | 0.4 |

| | | |
|---|---|---|
| $h_3$ | Dimensionless unbinding parameter (Eq. 2.2.7) | 5000 |
| $\delta$ | Ratio of microscale binding range, $\hat{h}$, to macroscale lengthscale $\hat{L}$ | 0.05 |
| $\nu$ | Ratio of microscale binding range, $\hat{h}$, to microscale characteristic length, $\hat{l}$. | 5 |
| $\omega$ | Frequency of oscillatory loading | 20 |
| $k_A$ | Dimensionless activation rate | 2 |
| $k_D$ | Dimensionless deactivation rate | 0.1 |
| $D$ | Dimensionless diffusion constant | 0.05 |
| $s_1$ | Dimensionless strengthening parameter (Eq. 4.2.8) | 50 |
| $w_1$ | Dimensionless weakening parameter (Eq. 4.2.9) | 0.05 |
| $\kappa$ | Relative strength of $b_v$ spring constant (Eq. 4.2.10) | 2 |

**Table B.5:** Dimensionless parameter values for simulations in Section 4.2, unless otherwise stated in figure captions.

## B.3 Parameter values for Chapter 5

### B.3.1 Retraction curves

The dimensionless parameter values used in the approach–retraction curves (replicating a common AFM protocol) are given below. These correspond to the results in Figs. 5.4 and 5.5.

| Parameter | Description | Value |
|---|---|---|
| $L_A$ | Dimensionless cell rest length | 1 |
| $L_I$ | Dimensionless integrin rest length | 0.5 |
| $L_E$ | Dimensionless ECM rest length | 1 |
| $k_A$ | Dimensionless cell stiffness | 2 |
| $k_E$ | Dimensionless ECM stiffness | 4 |
| $h$ | Dimensionless integrin binding range | 1 |
| $s$ | Dimensionless maximum integrin range | $\sqrt{1.5}$ |
| $h_1$ | Dimensionless unbinding parameter (Eq. 2.2.7) | 0.5 |
| $h_2$ | Dimensionless unbinding parameter (Eq. 2.2.7) | 0.4 |
| $h_3$ | Dimensionless unbinding parameter (Eq. 2.2.7) | 1000 |

| | | |
|---|---|---|
| $\nu$ | Ratio of microscale binding range, $\hat{h}$, to microscale characteristic length, $\hat{l}$. | 5 |
| $D$ | Dimensionless indentation depth | 1.25 |

**Table B.6:** Dimensionless parameter values for the approach–retraction study in Figs. 5.4 and 5.5

### B.3.2 Vertical oscillations: qualitative study

The dimensionless parameter values used in the qualitative study (Section 5.1.3) for vertical oscillations are given below.

| Parameter | Description | Value |
|---|---|---|
| $L_A$ | Dimensionless cell rest length | 1 |
| $L_I$ | Dimensionless integrin rest length | 0.5 |
| $L_E$ | Dimensionless ECM rest length | 1 |
| $k_A$ | Dimensionless cell stiffness | 2 |
| $k_E$ | Dimensionless ECM stiffness | 4 |
| $h$ | Dimensionless integrin binding range | 1 |
| $s$ | Dimensionless maximum integrin range | $\sqrt{1.5}$ |
| $h_1$ | Dimensionless unbinding parameter (Eq. 2.2.7) | 0.5 |
| $h_2$ | Dimensionless unbinding parameter (Eq. 2.2.7) | 0.4 |
| $h_3$ | Dimensionless unbinding parameter (Eq. 2.2.7) | 1000 |
| $\nu$ | Ratio of microscale binding range, $\hat{h}$, to microscale characteristic length, $\hat{l}$. | 5 |
| $\omega$ | Dimensionless frequency of oscillatory loading | 5 |
| $D$ | Dimensionless indentation depth | 1 |

**Table B.7:** Dimensionless parameter values for the qualitative study in Section 5.1.3, unless otherwise stated in figure captions

## B.4 Parameter values for Chapter 6

The dimensional parameter values for the spatial rates functions in the HHM model (Eqs. 6.1.5–6.1.7) are listed below.

| Parameter | $\hat{f}_A$ | $\hat{g}_A$ | $\hat{g}_B$ | $\hat{g}_C$ | $\hat{\tilde{g}}_A$ | $\hat{\tilde{g}}_B$ | $\hat{\tilde{g}}_C$ |
|---|---|---|---|---|---|---|---|
| Value | 0.88 | 4.4 | 0.22 | 0.66 | 0.2 | 0.1 | 0.03 |

**Table B.8:** Dimensional rate constants used spatial rate functions (Eqs. 6.1.5–6.1.7) in the HHM model. Values are taken from Mijailovich *et al.* [97] and Hiorns *et al.* [65].

For the remaining rate constants, $\hat{k}_{1-4}$ (Fig. 6.1), we use $\hat{k}_2$=$\hat{k}_3$=0.1 and either $\hat{k}_1$=$\hat{k}_4$=0.35 (t<5) or $\hat{k}_1$=$\hat{k}_4$=0.06 (t>5). All of these have units $s^{-1}$, and follow Mijailovich *et al.* [97] with one exception; for $\hat{\tilde{g}}_B$ we follow Hiorns *et al.* [65] and use $0.1s^{-1}$ instead of $0.01s^{-1}$. In addition to rate parameters, the crossbridge binding range must be specified. We use $\hat{h}_c = 15.6$nm [70, 97]. These parameters are nondimensionalised using the scalings in Eq. 6.2.4; each of the rate parameters is scaled by the dimensional integrin binding rate, $\hat{f}_1$ (Eq. 2.1.2), where $\hat{f}_1 = 0.08s^{-1}$.

The remaining dimensionless parameter values used in Section 6.3.1 and Section 6.3.2 are given below. Note that, in Section 6.3.1, we first consider the case where there is no integrin binding or rupture. In this case, the rate parameters $h_1$–$h_3$ are zero. In Section 6.3.1, we additionally use an indentation depth (Eq. 6.3.1) of $D = 0$.

| Parameter | Description | Value |
|---|---|---|
| $L_A$ | Dimensionless cell rest length | 10 |
| $L_I$ | Dimensionless integrin rest length | 0.5 |
| $L_E$ | Dimensionless ECM rest length | 1 |
| $k_A$ | Dimensionless passive cell stiffness | 0.5 |
| $k_E$ | Dimensionless ECM stiffness | 4 |
| $h$ | Dimensionless integrin binding range | 1 |
| $s$ | Dimensionless maximum integrin range | $\sqrt{1.5}$ |
| $h_1$ | Dimensionless integrin unbinding parameter (Eq. 2.2.7) | 0.5 |
| $h_2$ | Dimensionless integrin unbinding parameter (Eq. 2.2.7) | 0.4 |
| $h_3$ | Dimensionless integrin unbinding parameter (Eq. 2.2.7) | 1000 |
| $\nu$ | Ratio of microscale binding range, $\hat{h}$, to microscale characteristic length, $\hat{l}$. | 5 |
| $\omega$ | Dimensionless frequency of oscillatory loading | 20 |
| $D$ | Dimensionless indentation depth (Eq. 6.3.1) | 2 |

| | | |
|---|---|---|
| $\beta$ | Dimensionless scale factor for contractile force (Eq. 6.2.10) | 0.3 |
| $\gamma$ | Dimensionless crossbridge binding range | 1.56 |

**Table B.9:** Dimensionless parameter values for Section 6.3.1 and Section 6.3.2, unless otherwise stated in figure captions

The dimensionless parameter $\beta$ (Eq. 6.2.10) is defined as $\beta = \hat{\rho}_c \hat{\lambda}_c \hat{h} N_{CU} / \rho \hat{\lambda}_b$, where $\hat{\rho}_c$ is the number of crossbridges per unit length of a contractile unit, $\hat{\lambda}_c$ is the individual crossbridge stiffness, $\hat{h}$ is the integrin binding range, $N_{CU}$ is the number of parallel contractile units, $\rho$ is the number of integrins (bound and unbound) and $\hat{\lambda}_b$ is the individual integrin spring constant. Overall, this parameter controls the relative strength of the crossbridges to integrins. From the literature we have a range of $1 < \hat{\lambda}_c < 2.2$pN/nm for the dimensional crossbridge stiffness [10] and $0.15 < \hat{\lambda}_b < 2$pN/nm for the dimensional integrin stiffness [34], [48], [108]. There could be wide variability in the relative numbers of integrins and crossbridges, due to changes both the integrin density and the number and length of actin filaments connected (via adaptor proteins) to the integrin complexes. The values that these take are not known, and our approach in Section 6.3 is to vary $\beta$ through a range that allows us to observe the full range of dynamics, from when integrins dominate to when crossbridges dominate. Estimating or measuring these parameters will be important in future work.

# References


[1] Adair, B. D. , Xiong, J. P. , Maddock, C. , Goodman, S. L. , Arnaout, M. A. and Yeager, M. , 2005. Three-dimensional EM structure of the ectodomain of integrin aVb3 in a complex with fibronectin. *Journal of Cell Biology*, 168(7):1109–1118.

[2] Alberts, B. , Johnson, A. , Lewis, J. , Morgan, D. , Raff, M. , Roberts, K. and Walter, P. , 2014. *Molecular Biology of the Cell, Sixth Edition*. Taylor & Francis Group. ISBN 9781317563754.

[3] Alon, R. and Dustin, M. L. , 2007. Force as a facilitator of integrin conformational changes during leukocyte arrest on blood vessels and antigen-presenting cells. *Immunity*, 26(1):17–27.

[4] Alt, W. , Bock, M. and Möhl, C. , 2010. Coupling of cytoplasm and adhesion dynamics determines cell polarization and locomotion. *Cell Mechanics: From Single-Scale Based Models to Multiscale Modeling*, pages 86–125.

[5] Aplin, A. E. , Howe, A. , Alahari, S. K. and Juliano, R. L. , 1998. Signal transduction and signal modulation by cell adhesion receptors: the role of integrins, cadherins, immunoglobulin-cell adhesion molecules, and selectins. *Pharmacological Reviews*, 50(2): 197–264.

[6] Arthur, D. and Vassilvitskii, S. , 2007. k-means++: The advantages of careful seeding. In *Proceedings of the Eighteenth Annual ACM-SIAM Symposium on Discrete Algorithms*, pages 1027–1035. Society for Industrial and Applied Mathematics.

[7] Asthma, UK , 2017. Asthma facts and statistics. *www.asthma.org.uk (Nov. 2017)*.

[8] Avanzolini, G. and Cappello, A. , 1984. The characteristics method applied to the study of muscle dynamics. *Bulletin of Mathematical Biology*, 46(5-6):827–844.

[9] Banno, A. and Ginsberg, M. H. , 2008. Integrin activation. *Biochemical Society Transactions*, 36(2):229–234.

[10] Barclay, C. J. , 1998. Estimation of cross-bridge stiffness from maximum thermodynamic efficiency. *Journal of Muscle Research & Cell Motility*, 19(8):855–864.

[11] Bateman, E. D. , Hurd, S. S. , Barnes, P. J. , Bousquet, J. , Drazen, J. M. , Fitzgerald, M. , Gibson, P. , Ohta, K. , O'Byrne, P. , Pedersen, S. E. *et al.*, 2008. Global strategy for asthma management and prevention: Gina executive summary. *European Respiratory Journal*, 31 (1):143–178.

[12] Bates, J. , 2015. Modeling the impairment of airway smooth muscle force by stretch. *Journal of Applied Physiology*, 118(6):684–691.

[13] Bates, J. , Bullimore, S. R. , Politi, A. Z. , Sneyd, J. , Anafi, R. C. and Lauzon, A.-M. , 2009. Transient oscillatory force-length behavior of activated airway smooth muscle. *American Journal of Physiology-Lung Cellular and Molecular Physiology*, 297(2):L362–L372.

[14] Bell, G. I. , 1978. Models for the specific adhesion of cells to cells. *Science*, 200(4342): 618–627.

[15] Bendas, G. and Borsig, L. , 2012. Cancer cell adhesion and metastasis: selectins, integrins, and the inhibitory potential of heparins. *International Journal of Cell Biology*, 2012.

[16] Bennett, M. , Cantini, M. , Reboud, J. , Cooper, J. M. , Roca-Cusachs, P. and Salmeron-Sanchez, M. , 2018. Molecular clutch drives cell response to surface viscosity. *Proceedings of the National Academy of Sciences*, page 201710653.

[17] Beste, M. T. , Lee, D. , King, M. R. , Koretzky, G. A. and Hammer, D. A , 2012. An integrated stochastic model of "inside-out" integrin activation and selective t-lymphocyte recruitment. *Langmuir*, 28(4):2225–2237.

[18] Bhella, D. , 2015. The role of cellular adhesion molecules in virus attachment and entry. *Phil. Trans. R. Soc. B*, 370(1661):20140035.

[19] Binnig, G. , Quate, C. F. and Gerber, C. , 1986. Atomic force microscope. *Physical Review Letters*, 56(9):930.

[20] Block, M. R. , Destaing, O. , Petropoulos, C. , Planus, E. , Albigès-Rizo, C. and Fourcade, B. , 2015. Integrin-mediated adhesion as self-sustained waves of enzymatic activation. *Physical Review E*, 92(4):042704.

[21] Bousquet, J. , Jeffery, P. K. , Busse, W. W. , Johnson, M. and Vignola, A. M. , 2000. Asthma: from bronchoconstriction to airways inflammation and remodeling. *American Journal of Respiratory and Critical Care Medicine*, 161(5):1720–1745.

[22] Boxall, C. , Holgate, S. T. and Davies, D. E. , 2006. The contribution of transforming growth factor-beta and epidermal growth factor signalling to airway remodelling in chronic asthma. *The European Respiratory Journal*, 27(1):208–229.

[23] Brancaccio, M. , Hirsch, E. , Notte, A. , Selvetella, G. , Lembo, G. and Tarone, G. , 2006. Integrin signalling: the tug-of-war in heart hypertrophy. *Cardiovascular Research*, 70(3): 422–433.

[24] Brook, B. S. , 2014. Emergence of airway smooth muscle mechanical behavior through dynamic reorganization of contractile units and force transmission pathways. *Journal of Applied Physiology*, 116(8):980–997.

[25] Brown, R. H. , Scichilone, N. , Mudge, B. , Diemer, F. B. , Permutt, S. and Togias, A. , 2001. High-resolution computed tomographic evaluation of airway distensibility and the effects of lung inflation on airway caliber in healthy subjects and individuals with asthma. *American Journal of Respiratory and Critical Care Medicine*, 163(4):994–1001.

[26] Burridge, K. and Chrzanowska-Wodnicka, M. , 1996. Focal adhesions, contractility, and signaling. *Annual Review of Cell and Developmental Biology*, 12:463–518.

[27] Campbell, I. D. and Ginsberg, M. H. , 2004. The talin–tail interaction places integrin activation on ferm ground. *Trends in Biochemical Sciences*, 29(8):429–435.

[28] Cao, X. , Ban, E. , Baker, B. M. , Lin, Y. , Burdick, J. A. , Chen, C. S. and Shenoy, V. B. , 2017. Multiscale model predicts increasing focal adhesion size with decreasing stiffness in fibrous matrices. *Proceedings of the National Academy of Sciences*, page 201620486.

[29] Cao, X. , Lin, Y. , Driscoll, T. P. , Franco-Barraza, J. , Cukierman, E. , Mauck, R. L. and Shenoy, V. B. , 2015. A chemomechanical model of matrix and nuclear rigidity regulation of focal adhesion size. *Biophysical Journal*, 109(9):1807–1817.

[30] Chan, C. E. and Odde, D. J. , 2008. Traction dynamics of filopodia on compliant substrates. *Science*, 322(5908):1687–1691.

[31] Chen, C. , Li, R. , Ross, R. S and Manso, A. M. , 2016. Integrins and integrin-related proteins in cardiac fibrosis. *Journal of Molecular and Cellular Cardiology*, 93:162–174.

[32] Choquet, D. , Felsenfeld, D. P. and Sheetz, M. P. , 1997. Extracellular matrix rigidity causes strengthening of integrin–cytoskeleton linkages. *Cell*, 88(1):39–48.

[33] Crimi, E. , Pellegrino, R. , Milanese, M. and Brusasco, V. , 2002. Deep breaths, methacholine, and airway narrowing in healthy and mild asthmatic subjects. *Journal of Applied Physiology*, 93(4):1384–1390.

[34] Deshpande, V. S. , Mrksich, M. , McMeeking, R. M. and Evans, A. G. , 2008. A bio-mechanical model for coupling cell contractility with focal adhesion formation. *Journal of the Mechanics and Physics of Solids*, 56(4):1484–1510.

[35] Erban, R. , Chapman, J. and Maini, P. , 2007. A practical guide to stochastic simulations of reaction-diffusion processes. *arXiv preprint arXiv:0704.1908*.

[36] Erdmann, T. and Schwarz, U. S. , 2004. Stability of adhesion clusters under constant force. *Physical Review Letters*, 92(10):108102.

[37] Erdmann, T. and Schwarz, U. S. , 2006. Bistability of cell-matrix adhesions resulting from nonlinear receptor-ligand dynamics. *Biophysical Journal*, 91(6):L60–L62.

[38] Ester, M. , Kriegel, H.-P. , Sander, J. , Xu, X. *et al.*, 1996. A density-based algorithm for discovering clusters in large spatial databases with noise. In *Kdd*, volume 96, pages 226–231.

[39] Etzioni, A. , 1996. Adhesion molecules-their role in health and disease. *Pediatric Research*, 39(2):191–198.

[40] Evans, E. , Berk, D. and Leung, A. , 1991. Detachment of agglutinin-bonded red blood cells. i. forces to rupture molecular-point attachments. *Biophysical Journal*, 59(4):838–848.

[41] Evans, E. and Ritchie, K. , 1997. Dynamic strength of molecular adhesion bonds. *Biophysical Journal*, 72(4):1541–1555.

[42] Filippov, A. E. , Klafter, J. and Urbakh, M. , 2004. Friction through dynamical formation and rupture of molecular bonds. *Physical Review Letters*, 92(13):135503–1.

[43] Franck, C. , Maskarinec, S. A. , Tirrell, D. A. and Ravichandran, G. , 2011. Three-dimensional traction force microscopy: a new tool for quantifying cell-matrix interactions. *PloS One*, 6(3):e17833.

[44] Franz, C. M. , Taubenberger, A. , Puech, P. and Muller, D. J. , 2007. Studying integrin-mediated cell adhesion at the single-molecule level using afm force spectroscopy. *Sci. Stke*, 2007(406):pl5.

[45] Fredberg, J. J. , 1998. Airway smooth muscle in asthma: flirting with disaster. *European Respiratory Journal*, 12(6):1252–1256.

[46] Fredberg, J. J. , Inouye, D. , Miller, B. , Nathan, M. , Jafari, S. , Raboudi, S. H. , Butler, J. P. and Shore, S. A. , 1997. Airway smooth muscle, tidal stretches, and dynamically determined contractile states. *American Journal of Respiratory and Critical Care Medicine*, 156(6):1752–1759.

[47] Fredberg, J. J. , Inouye, D. S. , Mijailovich, S. M. and Butler, J. P. , 1999. Perturbed equilibrium of myosin binding in airway smooth muscle and its implications in bronchospasm. *American Journal of Respiratory and Critical Care Medicine*, 159(3):959–967.

[48] Gao, H. , Qian, J. and Chen, B. , 2011. Probing mechanical principles of focal contacts in cell-matrix adhesion with a coupled stochastic-elastic modelling framework. *Journal of the Royal Society, Interface / the Royal Society*, 8(62):1217–1232.

[49] Gillespie, D. T. , 1977. Exact Stochastic Simulation of Coupled Chemical Reactions. *The Journal of Physical Chemistry*, 81(25):2340–2361.

[50] Golias, C. H. , Chralabopoulos, A. , Peschos, D. , Maritsi, D. , Charalabopoulos, P. and Batistatou, A. , 2005. Adhesion molecules in cancer invasion and metastasis. *Hippokratia*, 9(1):106–114.

[51] Grainge, C. L. , Lau, L. C. K. , Ward, J. A. , Dulay, V. , Lahiff, G. , Wilson, S. , Holgate, S. , Davies, D. E. and Howarth, P. H. , 2011. Effect of bronchoconstriction on airway remodeling in asthma. *New England Journal of Medicine*, 364(21):2006–2015.

[52] Gumbiner, B. M. , 1996. Cell adhesion: the molecular basis of tissue architecture and morphogenesis. *Cell*, 84(3):345–357.

[53] Gunst, S. J. , 1983. Contractile force of canine airway smooth muscle during cyclical length changes. *Journal of Applied Physiology*, 55(3):759–769.

[54] Gunst, S. J. , Tang, D. D. and Saez, A. O. , 2003. Cytoskeletal remodeling of the airway smooth muscle cell: a mechanism for adaptation to mechanical forces in the lung. *Respiratory Physiology & Neurobiology*, 137(2):151–168.

[55] Hai, C. M. and Murphy, R. A. , 1988. Cross-bridge phosphorylation and regulation of latch state in smooth muscle. *American Journal of Physiology-Cell Physiology*, 254(1): C99–C106.

[56] Hai, C. M and Murphy, R. A. , 1988. Regulation of shortening velocity by cross-bridge phosphorylation in smooth muscle. *American Journal of Physiology-Cell Physiology*, 255 (1):C86–C94.

[57] Halwani, R. , Al-Muhsen, S. , Al-Jahdali, H. and Hamid, Q. , 2011. Role of transforming growth factor–$\beta$ in airway remodeling in asthma. *American Journal of Respiratory Cell and Molecular Biology*, 44(2):127–133.

[58] Hammer, D. A. , 2014. Adhesive dynamics. *Journal of Biomechanical Engineering*, 136(2): 021006.

[59] Hammer, D. A. and Apte, S. M. , 1992. Simulation of cell rolling and adhesion on surfaces in shear flow: general results and analysis of selectin-mediated neutrophil adhesion. *Biophysical Journal*, 63(1):35–57.

[60] Harburger, D. S. and Calderwood, D. A. , 2009. Integrin signalling at a glance. *Journal of Cell Science*, 122:159–163.

[61] Harvey, B. C. , Parameswaran, H. and Lutchen, K. R. , 2013. Can tidal breathing with deep inspirations of intact airways create sustained bronchoprotection or bronchodilation? *Journal of Applied Physiology*, 115(4):436–445.

[62] Hill, T. L. , 1974. Theoretical formalism for the sliding filament model of contraction of striated muscle part i. *Progress in Biophysics and Molecular Biology*, 28:267–340.

[63] Hillis, G. S and Flapan, A. D , 1998. Cell adhesion molecules in cardiovascular disease: a clinical perspective. *Heart*, 79(5):429–431.

[64] Hiorns, J. E. , Jensen, O. E. and Brook, B. S. , 2014. Nonlinear compliance modulates dynamic bronchoconstriction in a multiscale airway model. *Biophysical Journal*, 107(12): 3030–3042.

[65] Hiorns, J. E. , Jensen, O. E. and Brook, B. S. , 2016. Static and dynamic stress heterogeneity in a multiscale model of the asthmatic airway wall. *Journal of Applied Physiology*, 121 (1):233–247.

[66] Hirata, H. , Tatsumi, H. , Lim, C. T. and Sokabe, M. , 2014. Force-dependent vinculin binding to talin in live cells: a crucial step in anchoring the actin cytoskeleton to focal adhesions. *American Journal of Physiology-Cell Physiology*, 306(6):C607–C620.

[67] Hoffman, B. D. , Grashoff, C. and Schwartz, M. A. , 2011. Dynamic molecular processes mediate cellular mechanotransduction. *Nature*, 475(7356):316–323.

[68] Hong, Z. , Sun, Z. , Li, Z. , Mesquitta, W. T. , Trzeciakowski, J. P. and Meininger, G. A. , 2012. Coordination of fibronectin adhesion with contraction and relaxation in microvascular smooth muscle. *Cardiovascular Research*, 96(1):73–80.

[69] Hughes, P. E. and Pfaff, M. , 1998. Integrin affinity modulation. *Trends in Cell Biology*, 8 (9):359–364.

[70] Huxley, A. F. , 1957. Muscle structure and theories of contraction. *Progress in Biophysics and Biophysical Chemistry.*, 7:255–318.

[71] Hynes, R. O. , 2002. Integrins: bidirectional, allosteric signaling machines. *Cell*, 110(6): 673–687.

[72] Irons, L. , Owen, M. R. , O'Dea, R. D. and Brook, B. S. , 2018. Effect of loading history on airway smooth muscle cell–matrix adhesions. *Biophysical Journal*, 114(11):2679–2690.

[73] Irons, L. , Xie, L. , Owen, M. , Hill, M. A , Martinez-Lemus, L. A. , Glinski, O. , Glinsky, V. V , O'Dea, R. , Brook, B. and Meininger, G. A. , 2017. Utilization of mechano-biological models to predict cell adhesion interactions between bone marrow endothelial cells and breast cancer cells. *The FASEB Journal*, 31(1_Supplement):860–1.

[74] Jafer, A. T. , Mahmood, A. A. , Fatah, M. A. and Jasim, M. A. , 1997. Guidelines for the diagnosis and management of asthma.

[75] Jarjour, N. N. , Calhoun, W. J. , Kelly, E. A. , Gleich, G. J. , Schwartz, L. B. and Busse, W. W. , 1997. The immediate and late allergic response to segmental bronchopulmonary provocation in asthma. *American Journal of Respiratory and Critical Care Medicine*, 155(5): 1515–1521.

[76] Ji, B. and Huo, B. , 2013. Probing the mechanosensitivity in cell adhesion and migration: experiments and modeling. *Acta Mechanica Sinica*, 29(4):469–484.

[77] Joanes, D. N. and Gill, C. A. , 1998. Comparing measures of sample skewness and kurtosis. *Journal of the Royal Statistical Society: Series D (The Statistician)*, 47(1):183–189.

[78] Kapsali, T. , Permutt, S. , Laube, B. , Scichilone, N. and Togias, A. , 2000. Potent bronchoprotective effect of deep inspiration and its absence in asthma. *Journal of Applied Physiology*, 89(2):711–720.

[79] Kariyawasam, H. H. , Aizen, Ma. , Barkans, J. , Robinson, D. S. and Kay, A. B. , 2007. Remodeling and airway hyperresponsiveness but not cellular inflammation persist after allergen challenge in asthma. *American Journal of Respiratory and Critical Care Medicine*, 175(9):896–904.

[80] Keener, J. P. and Sneyd, J. , 1998. *Mathematical Physiology*, volume 1. Springer.

[81] Kong, D. , Ji, B. and Dai, L. , 2008. Stability of adhesion clusters and cell reorientation under lateral cyclic tension. *Biophysical Journal*, 95(8):4034–44.

[82] Kong, D. , Ji, B. and Dai, L. , 2010. Stabilizing to disruptive transition of focal adhesion response to mechanical forces. *Journal of Biomechanics*, 43(13):2524–2529.

[83] Kong, F. , García, A. J. , Mould, A. P. , Humphries, M. J. and Zhu, C. , 2009. Demonstration of catch bonds between an integrin and its ligand. *The Journal of Cell Biology*, 185 (7):1275–1284.

[84] Kuo, J.-C. , 2013. Mechanotransduction at focal adhesions: integrating cytoskeletal mechanics in migrating cells. *Journal of Cellular and Molecular Medicine*, 17(6):704–712.

[85] Kuznetsova, T. G. , Starodubtseva, M. N. , Yegorenkov, N. I. , Chizhik, S. A. and Zhdanov, R. I. , 2007. Atomic force microscopy probing of cell elasticity. *Micron*, 38(8): 824–833.

[86] Lacker, H. M. and Peskin, C. S. , 1986. A mathematical method for unique determination of crossbridge properties from steady-state mechanical and energetic experiments on macroscopic muscle. In *Some Mathematical Questions in Biology–Muscle Physiology*, volume 16, pages 121–153. The American Mathematical Society, Providence, RI.

[87] Lal, H. , Verma, S. K. , Foster, D. M. , Golden, H. B. , Reneau, J. C. , Watson, L. E. , Singh, H. and Dostal, D. E , 2009. Integrins and proximal signaling mechanisms in cardiovascular disease. *Frontiers in Bioscience*, 14(6):2307–2334.

[88] LaPrad, A. S. , Szabo, T. L. , Suki, B. and Lutchen, K. R. , 2010. Tidal stretches do not modulate responsiveness of intact airways in vitro. *Journal of Applied Physiology*, 109(2): 295–304.

[89] Latourelle, J. , Fabry, B. and Fredberg, J. J. , 2002. Dynamic equilibration of airway smooth muscle contraction during physiological loading. *Journal of Applied Physiology*, 92(2):771–779.

[90] Le Grimellec, C. , Lesniewska, E. , Giocondi, M. , Finot, E. , Vié, V. and Goudonnet, J. , 1998. Imaging of the surface of living cells by low-force contact-mode atomic force microscopy. *Biophysical Journal*, 75(2):695–703.

[91] Lepzelter, D. , Bates, O. and Zaman, M. , 2012. Integrin clustering in two and three dimensions. *Langmuir*, 28(12):5379–5386.

[92] Li, F. , Redick, S. D. , Erickson, H. P. and Moy, V. T. , 2003. Force measurements of the $\alpha 5\beta 1$ integrin–fibronectin interaction. *Biophysical Journal*, 84(2):1252–1262.

[93] Li, P. and Yackle, K. , 2017. Sighing. *Current Biology*, 27(3):R88–R89.

[94] Lim, T. K. , Pride, N. B. and Ingram, R. H. , 1987. Effects of volume history during spontaneous and acutely induced air-flow obstruction in asthma. *American Review of Respiratory Disease*, 135(3):591–596.

[95] Mailhot-Larouche, S. , Lortie, K. , Marsolais, D. , Flamand, N. and Bossé, Y. , 2017. An in vitro study examining the duration between deep inspirations on the rate of renarrowing. *Respiratory Physiology & Neurobiology*, 243:13–19.

[96] McAdams, H. H. and Arkin, A. , 1999. It's a noisy business! genetic regulation at the nanomolar scale. *Trends in genetics*, 15(2):65–69.

[97] Mijailovich, S. M. , Butler, J. P. and Fredberg, J. J. , 2000. Perturbed equilibria of myosin binding in airway smooth muscle: bond-length distributions, mechanics, and atp metabolism. *Biophysical Journal*, 79(5):2667–2681.

[98] Moore, B. J. , Verburgt, L. M. , King, G. G. and Pare, P. D. , 1997. The effect of deep inspiration on methacholine dose–response curves in normal subjects. *American Journal of Respiratory and Critical Care Medicine*, 156(4):1278–1281.

[99] Munevar, S. , Wang, Y. and Dembo, M. , 2001. Traction force microscopy of migrating normal and h-ras transformed 3t3 fibroblasts. *Biophysical Journal*, 80(4):1744–1757.

[100] Na, S. , Trache, A. , Trzeciakowski, J. , Sun, Z. , Meininger, G. A. and Humphrey, J. D. , 2008. Time-dependent changes in smooth muscle cell stiffness and focal adhesion area in response to cyclic equibiaxial stretch. *Annals of Biomedical Engineering*, 36(3):369–380.

[101] Nermut, M. V , Green, N. M. , Eason, P. , Yamada, S. S. and Yamada, K. M. , 1988. Electron microscopy and structural model of human fibronectin receptor. *The EMBO Journal*, 7(13):4093–4099.

[102] Neuman, K. C. and Nagy, A. , 2008. Single-molecule force spectroscopy: optical tweezers, magnetic tweezers and atomic force microscopy. *Nature Methods*, 5(6):491.

[103] Nunes, C. , Pereira, A. M. and Morais-Almeida, M. , 2017. Asthma costs and social impact. *Asthma Research and Practice*, 3(1):1.

[104] O'Byrne, P. M. and Inman, M. D. , 2003. Airway hyperresponsiveness. *Chest*, 123(3, Supplement):411S – 416S.

[105] Oenema, T. A. , Maarsingh, H. , Smit, M. , Groothuis, G. M. M. , Meurs, H. and Gosens, R. , 2013. Bronchoconstriction induces TGF$\beta$ release and airway remodelling in guinea pig lung slices. *PLoS ONE*, 8(6).

[106] Parsons, J. T. , Horwitz, A. R. and Schwartz, M. A. , 2010. Cell adhesion: integrating cytoskeletal dynamics and cellular tension. *Nature Reviews Molecular Cell Biology*, 11(9): 633–643.

[107] Pascual, R. M. and Peters, S. P , 2005. Airway remodeling contributes to the progressive loss of lung function in asthma: An overview. *Journal of Allergy and Clinical Immunology*, 116(3):477 – 486.

[108] Paszek, M. J. , Boettiger, D. , Weaver, V. M. and Hammer, D. A. , 2009. Integrin clustering is driven by mechanical resistance from the glycocalyx and the substrate. *PLoS Computational Biology*, 5(12).

[109] Patwa, A. and Shah, A. , 2015. Anatomy and physiology of respiratory system relevant to anaesthesia. *Indian Journal of Anaesthesia*, 59(9):533.

[110] Pelham, R. J. and Wang, Y. , 1997. Cell locomotion and focal adhesions are regulated by substrate flexibility. *Proceedings of the National Academy of Sciences*, 94(25):13661–13665.

[111] Petit, V. and Thiery, J. P. , 2000. Focal adhesions: Structure and dynamics. *Biology of the Cell*, 92.

[112] Politi, A. Z. , Donovan, G. M. , Tawhai, M. H. , Sanderson, M. J. , Lauzon, A. , Bates, J. H. and Sneyd, J. , 2010. A multiscale, spatially distributed model of asthmatic airway hyper-responsiveness. *Journal of Theoretical Biology*, 266(4):614–624.

[113] Postma, D. S. and Kerstjens, H. A. M. , 1998. Characteristics of airway hyperresponsiveness in asthma and chronic obstructive pulmonary disease. *American Journal of Respiratory and Critical Care Medicine*, 158(Supplement_2):S187–S192.

[114] Prechtel, K. , Bausch, A. R. , Marchi-Artzner, V. , Kantlehner, M. , Kessler, H. and Merkel, R. , 2002. Dynamic force spectroscopy to probe adhesion strength of living cells. *Physical Review Letters*, 89(2):028101.

[115] Qian, J. , Wang, J. , Lin, Y. and Gao, H. , 2009. Lifetime and strength of periodic bond clusters between elastic media under inclined loading. *Biophysical Journal*, 97(9):2438–2445.

[116] Ramos-Barbón, D. , Ludwig, M. S and Martin, J. G , 2004. Airway remodeling. *Clinical Reviews in Allergy & Immunology*, 27(1):3–21.

[117] Raqeeb, A. , Solomon, D. , Paré, P. D. and Seow, C. Y. , 2010. Length oscillation mimicking periodic individual deep inspirations during tidal breathing attenuates force recovery and adaptation in airway smooth muscle. *Journal of Applied Physiology*, 109(5): 1476–1482.

[118] Rayment, I. , Holden, H. M. , Whittaker, M. , Yohn, C. B. , Lorenz, M. , Holmes, K. C. and Milligan, R. A. , 1993. Structure of the actin-myosin complex and its implications for muscle contraction. *Science*, 261:58–58.

[119] Riveline, D. , Zamir, E. , Balaban, N. Q. , Schwarz, U. S. , Ishizaki, T. , Narumiya, S. , Kam, Z. , Geiger, B. and Bershadsky, A. D. , 2001. Focal contacts as mechanosensors. *The Journal of Cell Biology*, 153(6):1175–1186.

[120] Rosales, C. , O'Brien, V. , Kornberg, L. and Juliano, R. , 1995. Signal transduction by cell adhesion receptors. *Biochimica et Biophysica Acta (BBA)-Reviews on Cancer*, 1242(1): 77–98.

[121] Rousseeuw, P. J. , 1987. Silhouettes: a graphical aid to the interpretation and validation of cluster analysis. *Journal of Computational and Applied Mathematics*, 20:53–65.

[122] Schiesser, W. E. , 2012. *The Numerical Method of Lines: Integration of Partial Differential Equations*. Elsevier.

[123] Schwartz, M. A. , 2010. Integrins and extracellular matrix in mechanotransduction. *Cold Spring Harbor Perspectives in Biology*, 2(12):a005066.

[124] Schwartz, M. A. and DeSimone, D. W. , 2008. Cell adhesion receptors in mechanotransduction. *Current Opinion in Cell Biology*, 20(5):551–556.

[125] Scichilone, N. , Kapsali, T. , Permutt, S. and Togias, A. , 2000. Deep inspiration-induced bronchoprotection is stronger than bronchodilation. *American Journal of Respiratory and Critical Care Medicine*, 162(3):910–916.

[126] Seifert, U. , 2000. Rupture of multiple parallel molecular bonds under dynamic loading. *Physical Review Letters*, 84(12):2750–2753.

[127] Selhuber-Unkel, C. , Erdmann, T. , Lopez-Garcia, M. , Kessler, H. , Schwarz, U. S. and Spatz, J. P. , 2010. Cell adhesion strength is controlled by intermolecular spacing of adhesion receptors. *Biophysical Journal*, 98(4):543–551.

[128] Selhuber-Unkel, C. , López-García, M. , Kessler, H. and Spatz, J. P. , 2008. Cooperativity in adhesion cluster formation during initial cell adhesion. *Biophysical Journal*, 95(11): 5424–5431.

[129] Simard, B. , Turcotte, H. , Cockcroft, D. , Davis, B. E. , Boulay, M.-È. and Boulet, L.-P. , 2005. Deep inspiration avoidance and methacholine response in normal subjects and patients with asthma. *Chest*, 127(1):135–142.

[130] Skloot, G. , Permutt, S. and Togias, A. , 1995. Airway hyperresponsiveness in asthma: a problem of limited smooth muscle relaxation with inspiration. *The Journal of Clinical Investigation*, 96(5):2393–2403.

[131] Srinivasan, M. and Walcott, S. , 2009. Binding site models of friction due to the formation and rupture of bonds: State-function formalism, force-velocity relations, response to slip velocity transients, and slip stability. *Physical Review E - Statistical, Nonlinear, and Soft Matter Physics*, 80(4):1–15.

[132] Sun, Z. , Guo, S. and Fässler, R. , 2016. Integrin-mediated mechanotransduction. *The Journal of Cell Biology*, 215(4).

[133] Sun, Z. , Martinez-Lemus, L. A. , Trache, A. , Trzeciakowski, J. P. , Davis, G. E. , Pohl, U. and Meininger, G. A. , 2005. Mechanical properties of the interaction between fibronectin and $\alpha 5\beta 1$-integrin on vascular smooth muscle cells studied using atomic force microscopy. *American Journal of Physiology-Heart and Circulatory Physiology*, 289 (6):H2526–H2535.

[134] Takeichi, M. , 1988. The cadherins: cell-cell adhesion molecules controlling animal morphogenesis. *Development*, 102(4):639–655.

[135] Tan, J. L. , Tien, J. , Pirone, D. M. , Gray, D. S. , Bhadriraju, K. and Chen, C. S. , 2003. Cells lying on a bed of microneedles: an approach to isolate mechanical force. *Proceedings of the National Academy of Sciences*, 100(4):1484–1489.

[136] Tatler, A. L. , John, A. E. , Jolly, L. , Habgood, A. , Porte, J. , Brightling, C. , Knox, A. J. , Pang, L. , Sheppard, D. , Huang, X. and Jenkins, G. , 2011. Integrin $\alpha v\beta 5$-mediated TGF$\beta$ activation by airway smooth muscle cells in asthma. *The Journal of Immunology*, 187(11):6094–6107.

[137] Taubenberger, A. , Cisneros, D. A. , Friedrichs, J. , Puech, P.-H. , Muller, D. J. and Franz, C. M. , 2007. Revealing early steps of $\alpha 2\beta 1$ integrin-mediated adhesion to collagen type i by using single-cell force spectroscopy. *Molecular Biology of the Cell*, 18(5):1634–1644.

[138] Tian, T. and Burrage, K. , 2006. Stochastic models for regulatory networks of the genetic toggle switch. *Proceedings of the national Academy of Sciences*, 103(22):8372–8377.

[139] Tibshirani, R. , Walther, G. and Hastie, T. , 2001. Estimating the number of clusters in a data set via the gap statistic. *Journal of the Royal Statistical Society: Series B (Statistical Methodology)*, 63(2):411–423.

[140] Touhami, A. , Nysten, B. and Dufrêne, Y. F. , 2003. Nanoscale mapping of the elasticity of microbial cells by atomic force microscopy. *Langmuir*, 19(11):4539–4543.

[141] Walcott, S. , 2008. The load dependence of rate constants. *The Journal of Chemical Physics*, 128(21):06B601.

[142] Walcott, S. , Kim, D.-H. , Wirtz, D. and Sun, S. X. , 2011. Nucleation and decay initiation are the stiffness-sensitive phases of focal adhesion maturation. *Biophysical Journal*, 101 (12):2919–2928.

[143] Wang, M. D. , Schnitzer, M. J. , Yin, H. , Landick, R. , Gelles, J. and Block, S. M. , 1998. Force and velocity measured for single molecules of rna polymerase. *Science*, 282(5390): 902–907.

[144] Welf, E. S. , Naik, U. P. and Ogunnaike, B. A. , 2012. A spatial model for integrin clustering as a result of feedback between integrin activation and integrin binding. *Biophysical Journal*, 103(6):1379–1389.

[145] Williams, E. M. , Powell, T. , Eriksen, M. , Neill, P. and Colasanti, R. , 2014. A pilot study quantifying the shape of tidal breathing waveforms using centroids in health and COPD. *Journal of Clinical Monitoring and Computing*, 28(1):67–74.

[146] Wipff, P. J. , Rifkin, D. B. , Meister, J. J. and Hinz, B. , 2007. yofibroblast contraction activates latent TGF-$\beta$1 from the extracellular matrix. *The Journal of Cell Biology*, 179(6): 1311–1323.

[147] Wiseman, P. W. , Brown, C. M. , Webb, D. J. , Hebert, B. , Johnson, N. L. , Squier, J. A. , Ellisman, M. H. and Horwitz, A. F. , 2004. Spatial mapping of integrin interactions and dynamics during cell migration by image correlation microscopy. *Journal of Cell Science*, 117(23):5521–5534.

[148] Wolfenson, H. , Lavelin, I. and Geiger, B. , 2013. Dynamic regulation of the structure and functions of integrin adhesions. *Developmental Cell*, 24(5):447–458.

[149] Wozniak, M. A. , Modzelewska, K. , Kwong, L. and Keely, P. J. , 2004. Focal adhesion regulation of cell behavior. *Biochimica et Biophysica Acta*, 1692(2-3):103–119.

[150] Wu, P.-H. , Aroush, D. R.-B. , Asnacios, A. , Chen, W.-C. , Dokukin, M. E. , Doss, B. L. , Durand-Smet, P. , Ekpenyong, A. , Guck, J. , Guz, N. V. *et al.*, 2018. A comparison of methods to assess cell mechanical properties. *Nature Methods*, 15:491–498.

[151] Yuan, H. and Gao, H. , 2012. On the mechanics of integrin clustering during cell-substrate adhesion. *Acta Mechanica Solida Sinica*, 25(5):467–472.

[152] Zaidel-Bar, R. , Cohen, M. , Addadi, L. and Geiger, B. , 2004. Hierarchical assembly of cell-matrix adhesion complexes. *Biochemical Society Transactions*, 32(Pt3):416–420.

[153] Zhang, W. and Gunst, S. J , 2008. Interactions of airway smooth muscle cells with their tissue matrix: implications for contraction. *Proceedings of the American Thoracic Society*, 5(1):32–39.

[154] Zhurkov, S. N. , 1965. Thermofluctuation mechanism of fracture. *International Journal of Fracture Mechanics*, 1:311–323.